Filtering and localisation effects for elastic waves in periodic composite structures

Domenico Tallarico

Department of Mathematical Sciences
University of Liverpool

This dissertation is submitted for the degree of
Doctor of Philosophy

July 2017

To Ulrike, Miriam, Raffaella and
my parents, Luigi and Barbara

Declaration

I hereby declare that except where specific reference is made to the work of others, the contents of this dissertation are original and have not been submitted in whole or in part for consideration for any other degree or qualification in this, or any other university. This thesis is the result of my own research activity carried out in the Department of Mathematical Sciences at the University of Liverpool during the period of September 2014 until May 2017. The original results of this thesis are based on research articles previously published or under review.

Publications

- Tallarico, D., Movchan, N.V., Movchan, A.B., and Camposaragna, M. (2017) Propagation and filtering of elastic and electromagnetic waves in piezoelectric composite structures. *Math. Meth. Appl. Sci.*, **40**: 3202–3220. doi: 10.1002/mma.3893.

- Tallarico D., Movchan N.V., Movchan A.B., and Colquitt D.J. (2017) Tilted resonators in a triangular elastic lattice: chirality, Bloch waves and negative refraction, *Journal of the Mechanics and Physics of Solids*, **103**: 236-256, doi:10.1016/j.jmps.2017.03.007.

- Tallarico, D., Trevisan, A., Movchan, N.V., and Movchan, A.B. (2017) Edge waves and localisation in lattices containing tilted resonators, *Frontiers in Materials*, **4**:16 (18 pp.), doi:10.3389/fmats.2017.00016.

- Tallarico D., Movchan N.V., Movchan A.B., and Colquitt D.J. (2017) Bloch waves in a triangular lattice with tilted resonators: applications to focussing. Conference article to be presented at the international congress *Metamaterials 2017*, Marseille, France.

Domenico Tallarico
July 2017

Abstract

This PhD thesis is primarily concerned with the study of propagation - either enhanced or inhibited - of elastic and electromagnetic waves in composite structures governed by coupled equations. The introductory chapter of the thesis provides scientific and technological motivations of the aforementioned problems by means of a literature review. Chapter 1 is concerned with the mathematical methodologies and illustrative examples useful in the subsequent chapters. In particular, the governing equations for piezoelectric materials are discussed. Quasi-periodicity Bloch-Floquet conditions are presented and used to study periodic isotropic and piezoelectric layered structures as well as structured discrete lattices in one and two dimensions. In chapter 2, we formulate and solve the scattering of shear elastic and TM electromagnetic waves from a finite stack of piezoelectric layers via a recurrence procedure approach. The reflectance and transmittance are evaluated for pass- and stop-bands of the corresponding periodic problem. Particular attention is given to the so called "cross-term" transmittance, *i.e.* to the quantification of the conversion efficiency of electromagnetic energy into elastic energy and vice versa. Chapter 3 is dedicated to the analysis of the dispersive properties of a doubly-periodic piezoelectric composite material. Different frequency regimes are identified: a low-frequency regime where the material behaves isotropically, and a higher frequency regime in which the material exhibits dynamic anisotropy. Attention is given to the role of the piezoelectricity on the aforementioned phenomena. Chapter 4 introduces a triangular lattice whose unit cell contains a geometrically chiral inclusion, *i.e.* a triangular resonator which is tilted by an angle ϑ_0 with respect to the hosting unit cell. The Newton equations for the structured unit cell are solved together with Bloch-Floquet boundary conditions. The physical implications of the geometric chirality are identified and discussed both via the analysis of the dispersion diagram and through illustrative examples, including Bloch-Floquet displacement fields and forced problems of elasticity. Chapter 5 is devoted to several applications of the lattice structure introduced in chapter 4: focussing of elastic waves through a "flat lens" is achieved using the novel tunable dispersive properties of the triangular lattice with tilted resonators; structural interfaces containing tilted resonators are implemented and analysed in the context of edge wave-guiding and wave-defect interaction; finally the role of resonators on the initiation and advance of a crack in a thermoelastic lattice is investigated. In chapter 6 we provide our conclusions and outline future work.

Contents

List of figures

List of tables

Acknowledgements

Nearly three years have flown away very quickly. Looking back, this is a distinctive sign that I deeply enjoyed my time in Liverpool. I would like therefore to spend a few words to acknowledge all the wonderful people that made it possible.

First of all, my deepest and sincerest gratitude goes to my supervisors, Profs Natasha and Sasha Movchan that gave me such an amazing opportunity and provided me with such a far-sighted guidance. I would like to acknowledge Natasha's words of wisdom and her bright and teasing sense of humour, always welcome and appropriate. From her I learned - and I am still doing! - the attention to details in the formulation and solution of mathematical problems of physical interest. Life is never perfect and certainly losing details on the way does not make it easier. Sasha's vision as a whole of the research projects is something that strikes me the most, together with his comforting confidence and optimism - even when things do not look on the right track. Besides their top-class professional competence, that certainly does not need my emphasis, it is hard to find people so generous, welcoming and gentle.

I would like to acknowledge Enginsoft for the fruitful and stimulating six-months work placement between Trento and Padova, made possible by Dr Silvia di Rosa. The technical competence from Dr Michele Camposaragna and Dr Alessio Trevisan has certainly added value to this thesis.

I am grateful to Prof. Andrea Piccolroaz and Miss Irena Jatro from the University of Trento for their effort and time spent in the coordination of the Initial Training Network CERMAT-2 (People Programme of the European Union's Seventh Framework Programme FP7/2007-2013/ under REA grant agreement number PITN-GA-2013- 606878) which funded my Marie Curie fellowship in Liverpool. In this context, a big thanks goes to all the people I had the opportunity to meet all around Europe: Prof. Gennady Mishuris, Prof. Vladimir Buliak, Dr. Magdalena Gromada, Nicolai Gorbushin, Gennaro Vitucci, Nastya Vinokurova, Shwetank Pandey, Mojtaba Biglar, Daniel Kampen and Scot Swan. I hope that the current friendship is the starting point of future successful professional collaborations.

I would like to acknowledge Dr Daniel Colquitt for the fruitful research collaboration and technical advise. A special thanks goes to Dr Stewart Haslinger for his friendship

demonstrated during these three years and his genuine interest in my project. My gratitude goes as well to Dr Özgür Selsil, an enthusiastic and skilful swimmer, that dragged me back into the swimming pool after years of my absence from it. I would like to acknowledge as well my more experienced colleagues Dr Giorgio Carta, Dr Luca Argani and Dr Michael Nieves for their useful advice and words of kindness. I am grateful to Dr Gayane Piliposian for the useful discussions on piezoelectricity at the beginning of my PhD and for her genuine interest in my project throughout these three years. Thanks to my new friends Maria, Sara, Marta, Daria and Wojtek and to the PhD students at Maths department. A special thanks goes to Ulrike, my German squirrel, for the laughs together, the reciprocal support and our intercontinental adventure times.

You should never forget where you are coming from. That is why I would like to acknowledge my family, especially my grandma Vincenzina, my sisters Miriam and Raffaella and my parents Luigi and Barbara.

Introduction

The main focus of this thesis is the study of propagation, filtering and localisation of elastic waves in composite structures. Throughout the thesis we may equivalently refer to the investigated composite structures as elastic or phononic metamaterials. The elastic metamaterials presented and studied in this thesis belong to two main classes of structures:

- One-dimensional (1D) and two-dimensional (2D) continuous piezoelectric metamaterials;
- 2D discrete chiral metamaterials.

Mathematical methods for structured media. Periodic media can be modelled as discrete lattices or continue solids with a micro-structure. This choice is dictated by the scale and geometries of the problem. The monograph by Maradudin *et al.* [54] provides an important contribution to the band theory of the lattice dynamics of atomic nuclei in solids (the vibration modes and associated phononic branches), where the interaction between the nuclei was treated in the harmonic approximation with classical potentials. Discrete 1D problems in structural dynamics were considered by Mead [58], who studied the unit cell of 1D periodic continuous systems using a finite number of displacement coordinates. The work was later extended by Langley [46] whose main contribution was to incorporate the unit cell's boundary conditions within a functional used in a variational principle. The accurate descriptions of frame-like and truss-like elastic periodic 2D lattices were proposed by Martinsson and Movchan [56].

Ho *et al.* [29], Zhang *et al.* [104] and Plihal *et al.* [74] proposed the solution of the Maxwell equations in all-dielectric two-phases periodic media via the plane-wave expansion method. In [29], the existence of band gaps in an artificial 3D photonic[1] medium consisting of a periodic arrangement of spheres was shown. In [104] and [74] the focus was on a

[1] Phononic metamaterials are media where the dispersion of elastic waves can be influenced via the geometry and/or composition of the underlying micro-structure. Similarly, photonic metamaterials are used to influence the dispersive properties of electromagnetic waves.

2D photonic crystal and its dispersion properties. The method of plane-wave expansion in dielectric photonic crystals has been significantly improved, expecially after the work by Meade *et al.* [59] and Johnson and Joannopoulos [37]. These improvements were needed in order to reduce the number of plane wave terms in the expansion. Leung and Qiu [50] used the Korringa-Kohn-Rostoker method [42, 41] to obtain the band diagram of 2D photonic crystals with circular inclusions. The method was based on the Green's function representation of the scattered waves from spherical obstacles. Chan *et al.* [17] obtained a solution of Maxwell equations in 2D (both periodic and defective) photonic crystals. Their real space method, known as finite difference time-domain method, employs discretisation of the Maxwell equations in both the spatial and the time domain and the integration of the Maxwell equations in the time domain. The method scales linearly with the size of the system, while conventional plane-wave expansion methods scale with the third power. Finite difference and finite element methods were studied by Yang [98] and Dobson [26], respectively. Both authors addressed wave-guiding problems in 2D photonic crystals whose unit cell is irregular, *i.e.* it either contains multiple corners at the interface between the constituent materials or it is highly anisotropic. The multiple multipole method was used by Moreno *et al.* [63] to study periodic media containing metallic interfaces. The multiple multipole method is a numerical technique for performing electrodynamic field calculations in the frequency domain. It is particularly suitable for the study of media which include metallic interfaces, as they are computationally intensive due to frequency-dependent complex-valued dielectric functions. Busch *et al.* [13] provided a review of all the advantages and disadvantages of the methods mentioned above. Botten *et al.* [8, 9] used the multiple scattering method to study wave scattering by grating stacks made of cylindrical metallic and dielectric inclusions in a dielectric host. The method of multiple scattering was generalised by Botten *et al.* [10] to the study of phononic dispersion of periodic gratings.

The plane-wave expansion method was used by Sigalas and Economou [83, 82] to study continuous phononic metamaterials. The multipole representation of boundary conditions along the perimeter of circular inclusions/perforations in thin elastic plates was discussed by Movchan *et al.* [64] and analysed further by Poulton *et al.* [75]. McPhedran *et al.* [57] considered flexural waves in a thin elastic periodically pinned plate, as a special case of the inclusion radius being zero. The lattice Green's function was constructed to show localised vibrations at frequencies within the first zero-frequency band gap of the structure. Hussein [35] introduced the reduced Bloch-Floquet mode method based on the selection of modal Bloch-Floquet solutions of an elastic time-harmonic problem for a given phononic structure. The selection was performed at special high-symmetry points in the first Brillouin zone.

State of the art and challenges of piezoelectric technology. Piezoelectric transformers (both actuators and sensors) are used in sensitive measuring equipment, energy harvesting devices, electronics (MEMs), defence, security and medical equipment. We outline here the state-of-the-art of the technology based on piezoelectric components. Piezoelectric actuators, whose working principle is based on the "indirect piezoelectric effect" are widely used in scanning tunnelling and atomic force microscopy (Chen [18]). Piezoelectric sensors are based on the "direct piezoelectric effect" which governs the conversion of mechanical signmeals into electric signals. Their designs include piezoelectric ceramics combined with seismic masses.

The piezoelectric effect recently received attention in the context of energy harvesting research. Large networks of low-power electronic devices require self-powering mechanisms. The harvest of energy from mechanical vibrations using piezoelectric harvesters seems to be a sustainable, yet challenging, solution. A review which focuses on the piezoelectric energy harvesting is given by Anton and Sodano [2]. A review which compares piezoelectric, electromagnetic (inductive) and electrostatic (capacitive) energy harvesting is given in Wei *et al.* [96]. According to [96], piezoelectric materials are scalable, *i.e.* their technology is suitable to be transferred from macroscopic to microscopic scale and vice versa. Moreover, the piezoelectric coupling of piezoelectric ceramics and crystals is independent of ambient electromagnetic waves in contrast to electromagnetic and electrostatic mechanical harvesters. In addition, piezoelectric devices are passive, *i.e.* they do not require a source of external power, and they are light-weight. Finally, it is worthwhile mentioning that most piezoelectric ceramics are biologically compatible making them ideal candidates in biomechanical energy harvesting applications, such as for self-powering purposes of pacemakers [51].

The main drawback of energy harvesters based on piezoelectric ceramics and crystals is that their conversion efficiency is significantly lower compared with their electromagnetic and electrostatic counterparts. In addition, for a given poling direction, the mechanical-to-electric energy conversion spectrum is narrow around a characteristic frequency. However, both the conversion efficiency and the operational bandwidth can be improved by harnessing the geometry and poling direction in various piezoelectric materials [2]. Piezoelectric multi-layers, *i.e.* stacks comprising two or more piezoelectric materials,have superior conversion efficiency. The presence of interfaces, and the specific boundary conditions adopted, strongly influence the electromechanical coupling. For this reason, piezoelectric inhomogeneous composites that are made of piezoelectric ceramics and crystals are widely used in many applications in physics and engineering [100]. In the context of improving the energy conversion efficiency of piezoelectric devices (see Tallarico *et al.* [89]), we recently studied the scattering of elastic and electromagnetic waves from a layered piezoelectric structure

using the multiple scattering method. The literature on elastic or electromagnetic scattering by structured finite objects is vast, as pointed out earlier. This reflects the recent scientific and technological effort in moulding the flow of elastic and electromagnetic waves in structured media. However, the interaction between elastic and electromagnetic waves is often overlooked. Piezoelectric crystals and ceramics provide a natural platform to study such coupling effects. The main contribution of [89] has been the accurate evaluation of the scattered energy flux by a finite layered piezoelectric bi-material. In contrast to the earlier article by Shuvalov and Gorkunova [81], where the electromagnetic field is localised at the boundaries of a layered piezoelectric medium, our method is not limited to a low-frequency elastic-dominated scattering, but it is extended to frequencies where both elastic and electromagnetic propagating waves interact via the piezoelectric effect. Chapter 2 of this thesis is devoted to the discussion of this problem.

In the last two decades, the improvement in miniaturisation of electronic devices, have sparked also research interest in novel electromechanical coupling schemes beyond piezoelectricity. Piezoelectricity is based on the coupling of the electric polarisation and the elastic strain in non-centrosymmetric solids. Few atoms or atomically thin membranes exhibit flexoelectricity [79], based on the coupling between the gradients of strain and electric polarisation. At the nano-scale [88], flexoelectric electromechanical coupling dominates over the conventional piezoelectric effect which is based on the broken inversion symmetry of the unit cell. The electromechanical coupling considered in this thesis arises from piezoelectric effect at the *mm* scale.

Focussing of elastic waves. In the last two decades, significant progress has been made in gaining control of elastic waves at multiple scales. These advances are primarily due to recent improvements in micro- and nano-fabrication as well as novel theoretical breakthroughs, such as focussing through negative refraction. Negative refraction was predicted by Veselago [94] to occur at the interfaces between two electromagnetic media, one of which with simultaneously negative dielectric permittivity $\varepsilon(\omega)$ and negativity magnetic permeability $\mu(\omega)$. Pendry [69] theorised focusing based on negative refraction via a "double negative" indices flat lens. One of the most remarkable consequences of this exotic focussing is that it is almost lossless and goes beyond the Rayleigh resolution limit. Back in 1879, Lord Rayleigh [76] found that the image of two point sources of light passing through a circular lens of finite aperture (the diameter) D, cannot be resolved if their angular separation[2] is less

[2]The angular separation is defined as the angle between the two point sources as "seen" from the point of intersection between the optical axis and the lens.

than a threshold angular separation

$$\theta_{\text{th}} = 1.22\frac{\lambda}{D}, \tag{1}$$

where λ is the wavelength of the light coming from the point sources. The factor 1.22 is the approximate ratio of the first zero of the first-kind Bessel function $J_1(x)$ and π, and it denotes the radius of the first bright diffraction circle [7]. In order to reduce the resolution limit in Eq. (1), conventional super-resolving lenses have wide apertures - astronomical radio-telescopes are hundreds of meters wide [27]. The finest details of an optical image – those smaller than a wavelength of light – are carried by waves that decay exponentially as the light travels through a material. These "evanescent" waves cannot be focused in conventional materials characterised by positive dielectric permittivity and magnetic permeability . However, Pendry [69] has shown that these decaying waves would actually grow as they pass through a material with simultaneous negative dielectric permittivity and magnetic permeability, making a perfect lens possible.

As emphasised above, there are some practical limitations to the conversion efficiency of energy harvesting devices. More efficient energy focussing schemes provide a useful and viable way to circumvent these limits, by increasing the available incident flux of energy. Negative refraction of elastic or acoustic waves can arise from double negative materials, *i.e.* from locally resonant structures which exhibit a negative effective mass and negative bulk modulus [44, 80]. Luo *et al.* [53] exploited the dynamic anisotropy of a photonic crystal to achieve all-angle negative refraction and focussing without the effective refractive index being negative. Their scheme is based on Bragg scattering that induces bands with a negative group velocity. The same idea has been exploited in the context of phononic crystals for elastic waves by Ke *et al.* [39] and for water waves by Hu *et al.* [31]. Evidence of an acoustic super-lensing effect has been provided by Sukhovich *et al.* [86]. "Flat lenses" for elastic waves in simple discrete lattices were treated by Colquitt *et al.* [19, 20].

It is worthwhile emphasising that metamaterials and phononic crystals have complex dispersion surfaces. However, it is possible to design these systems such that, in a narrow frequency band, they act as double negative materials with an effective negative index of refraction.

We recently studied Bloch-Floquet waves in a lattice with geometrically chiral inclusions (see Tallarico *et al.* [90]) which is the main focus of chapter 4 of this thesis. The tunable properties of this lattice are traced back to a geometric parameter referred to as tilting angle. Harnessing the dispersion properties of the lattice, we were able to achieve negative refraction

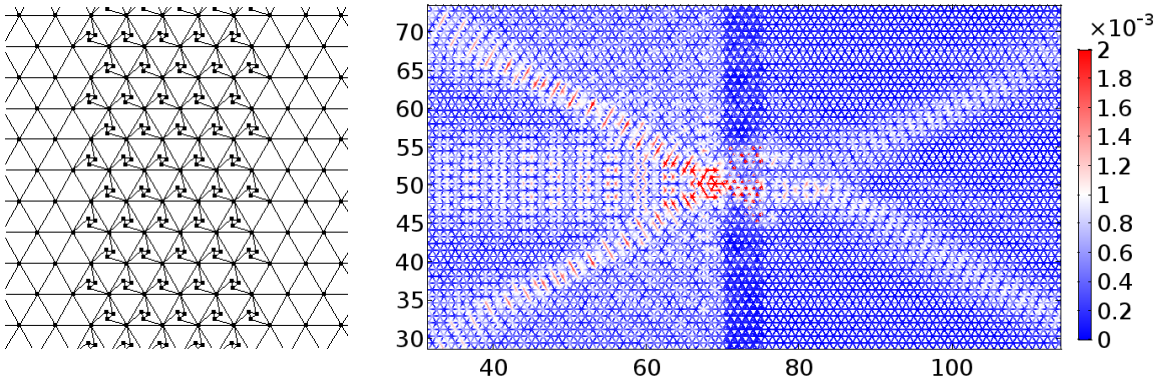

Fig. 1 *A structured interface (left panel) made of tilted resonators in a triangular elastic lattice exhibits focussing by negative refraction (right panel).*

[90]. An example of focussing via negative refraction is shown in Fig. 1 and further details can be found in chapter 5 of this thesis.

Piezoelectric metamaterials as dynamically coupled composite structures. The analysis of piezoelectric structures is often based on the quasi-static approximation as discussed in the monograph by Auld [3]. As a result, in this theory, although the mechanical equations are dynamic, the electromagnetic equations are static, the electric field being irrotational. When electromagnetic waves are involved, the complete set of Maxwell equations has to be taken into account, coupled to the mechanical equations of motion. The fully coupled equations of motion can be found in [3], Kyame [45] and Yang [99], among others. In this context, Darinskii *et al.* [25] discussed the role of electromagnetic waves in problems of reflection of acoustic waves at the interface between two semi-infinite piezoelectric materials. At quasi-normal incidence, *i.e.* for an angle of incidence $\theta_i \approx v_a/v_l$, where v_a and v_l are the typical speed of sound and light respectively, they found that according to the fully coupled electromagnetic description, the acoustic waves undergo total reflection while the quasi-electrostatic approximation predicts almost total transmission. The full set of Maxwell and Newton equations, for a very common symmetry class of piezoelectric materials, is assumed in this thesis and it is discussed in chapter 1.

Babiker *et al.* [5] studied the dynamic properties of 1D superlattices with metallic interfaces. This article paved the way to the study of polariton waves[3] in piezoelectric superlattices. As reported by Lu *et al.* [52] and Zhu *et al.* [105], a special type of polariton stems from the dynamical coupling of the Newton and Maxwell equations in layered piezoelectric

[3]Polaritons are waves arising from the collective excitation of photons with other resonant excitations (normal modes) of the structure, *e.g.* plasmons and phonons [1]. In this thesis the term "polariton" refers to the phonon-photon polariton in a similar sense as in [61].

periodic structures. This results in a polariton-induced band gap for Bloch-Floquet waves [103] and anomalous dielectric properties of the medium [105].

The coupling constant between electromagnetic and elastic wave equations in piezoelectric crystals is smaller compared to the one in ionic crystals, where the unit cell exhibits a net charge rather than a dipole moment. Huang [33] predicted polaritonic behaviour in bulk ionic crystals. In piezoelectric bulk materials, some components of the elastic displacement may decouple from the electromagnetic wave equations. However, even for those limit configurations Sabina and Movchan [78] have shown that the piezoelectric coupling strongly influences the interface conditions between two piezoelectric materials. More recently Piliposian *et al.* [70] have studied the dispersion diagram of out-of-plane shear waves in periodic piezoelectric bilayers. The dispersion equation derived in [70] is discussed in chapter 1. Inspired by [78], and [70], Tallarico *et al.* [89] have studied the scattering of elastic and electromagnetic waves by a finite layered structure. This topic is covered in chapter 2 of this thesis.

Before [78] and [70], photonic and phononic crystals made of piezoelectric materials were discussed by Zhang *et al.* [102], Wu *et al.* [97], Laude *et al. et al.* [48] and Hou *et al.* [30], among others. In particular, Zhang *et al.* [102] presented a model for the transmission problem in stratified media, emphasising applications in acoustics. The effects of electromechanical coupling in models of surface acoustic waves were discussed by Wu *et al.* [97] and Laude *et al.* [48]. Surface and bulk acoustic waves in two-dimensional phononic crystals were studied in [97]. A plane-wave expansion method for spectral problems in phononic piezoelectric crystals was presented in [30]. Sabina and Movchan [78] discussed the role of the electromechanical coupling on the dispersion properties of in-plane Bloch-Floquet waves within one- and two-dimensional phononic crystals. The non-centrosymmetry of the unit cell of piezoelectric materials is associated with anisotropic wave propagation. This makes their modelling challenging. However, many types of polarised piezoelectric crystals are orthotropic. In this case, the mathematical treatment of piezoelectricity greatly simplifies, and the formulation can be split in a 2D in-plane problem and a 1D out-of-plane problem.

Many out-of-plane problems are mathematically simple and can often be solved analytically, thus clearly showing the physics involved. Moreover, out-of-plane problems in piezoelectric materials are of great technological interest as outlined by Yang *et al.* [100]. Piliposian *et al.* [70] analytically derived and solved the dispersion equation for shear elastic Bloch-Floquet waves in 1D layered piezoelectric materials. The effects of the electromechanical coupling and filling fraction on the dispersion of Bloch-Floquet waves were investigated there. Polaritonic effects were investigated in a similar periodic piezoelectric waveguide by

Piliposyan *et al.* [71]. The dynamical coupling of Maxwell and Newton equations arises in [71] because of the finite size of the wave-guide in one of the spatial dimensions. More recently, the study of the effects of polaritons on the dispersion of Bloch-Floquet waves and on the transmission properties has been extended to piezoelectric layered structures with metallised interfaces by Piliposyan *et al.* [72].

Discrete lattices. The recent technological progress in etching and milling by three-dimensional (3D) printing at the mesoscopic scale (see Truby and Lewis [93] and Fu *et al.* [28], among others), alongside the usual mathematical tractability and physical clarity, have reignited research interest in discrete elastic composite structures. Elastic discrete lattices have always attracted the attention of mathematics and physics research communities. Elastic 1D and 2D lattices whose unit cells are made of mass-spring structures, have been chosen by Brillouin [11] to illustrate the theory of Bloch-Floquet waves. Moreover, phononic metamaterials designed with discrete structures have applications in fields including bridge design [15], bones modelling and fluid-structure interaction in blood vessels. One of the most appealing features of discrete elastic structures is the versatility of their unit cell topology which allows novel mechanisms to control and tune the dispersive properties of elastic waves.

Recently, unit cells with geometrically chiral topologies have been extensively studied (see *e.g.* [12, 6, 14, 95, 85, 84], among others). A geometric figure is said to be chiral if "its image in a plane mirror, ideally realised, cannot be brought to coincide with itself" [91]. Typical examples are the hands which are either "left-handed" or "right-handed". Indeed, the etymological origin of the word "chiral" derives from the ancient Greek for hand: $\chi\varepsilon\acute{\iota}\rho$. Brun *et al.* [12] introduced an analytical model for chiral elastic media, which takes into account internal rotations induced by gyroscopes. These structured media act as polarisers of elastic waves and also have very interesting dispersive properties in the context of the Bloch-Floquet waves in multi-scale periodic solids possessing internal rotations. Further studies of chiral structures have led to the exciting and novel results by Bigoni *et al.* [6], Carta *et al.* [14] and Wang *et al.* [95]. Hexagonal chiral lattices were studied by Spadoni *et al.* [85, 84]. Their numerical results highlighted the influence of chirality on the dynamic anisotropy of elastic in-plane waves and on the auxetic behaviour of the structure under static loads. The observation of dynamic chirality in structured elastic materials has been reported by Süsstrunk and Huber [87]. In particular it has been demonstrated that left and right propagating collective edge waves are not equivalent, *i.e.* the system is dynamically chiral. The seminal experiment conducted in [87] led to the newly established research field of "topological mechanics" which is the main focus of Huber [34].

An elastic lattice with the inertia concentrated at the nodal points is a highly attractive object for the study of Bloch-Floquet waves, as the dispersion equations can be expressed as polynomials with respect to a spectral parameter. In this context, Martinsson and Movchan [56] presented a unified analytical approach for studies of Bloch-Floquet waves in multi-scale truss and frame structures, which included the design of lattices whose stop bands were around pre-defined frequencies. In particular, low-frequency rotational waveforms were identified in some of the standing waves at the boundaries of the stop bands in the spectrum.

The asymptotic analysis of eigenvalue problems for degenerate and non-degenerate multi-structures was systematically presented in the monograph by Kozlov *et al.* [43], where rotational modes were studied in the context of the asymptotic analysis of the eigenvalues and corresponding eigenfunctions of multi-structures consisting of components of different limit dimensions.

Dirac systems, *i.e.* lattices where the phononic, photonic or electronic dispersive properties are locally linear, have recently attracted considerable attention. The interest began with the discovery of graphene [67], a 2D honeycomb lattice of carbon atoms, and the discovery of a plethora of unusual physical phenomena occurring in it [16]. There are other physical systems, such as phononic and photonic metamaterials, which exhibit linear dispersion at a given point in the first Brillouin zone. The so-called "$\boldsymbol{k}_0 \cdot \hat{\boldsymbol{p}}$" method [101], where $\hat{\boldsymbol{p}}$ is a differential operator proportional to the spatial gradient and $\boldsymbol{k}_0$ is a given Bloch-Floquet wave vector, has been successfully used to grasp the leading order corrections to the dispersion around $\boldsymbol{k}_0$ and at frequencies corresponding to the edges of band gaps in semiconductors [101] and at Dirac points in semi-metals [16]. More recently, Craster *et al.* [24, 23] and Colquitt *et al.* [21], developed high frequency homogenisation techniques, a mathematical algorithm to derive partial differential equations for a long scale variable beyond the leading order approximation underlying the "$\boldsymbol{k}_0 \cdot \hat{\boldsymbol{p}}$" method. High frequency homogenisation is suitable to investigate resonance points of the locally hyperbolic or locally parabolic type, as recently shown by Colquitt *et al.* [22]. Using the "$\boldsymbol{k}_0 \cdot \hat{\boldsymbol{p}}$" method applied to phononic crystals, Mei *et al.* [60] identified two classes of Dirac systems, where one is characterised by doubly-degenerate dispersion at the boundary of the first Brillouin zone and the other is occurring at the centre of the first Brillouin zone as a result of triple-degeneracy. The latter class is said to exhibit "Dirac-like" dispersion which happens because of "accidental degeneracy", *i.e.* the careful tuning of the eigenvalues of the system. The former class is referred to as "Dirac" dispersion and it is associated with the symmetry of the lattice. Examples of "Dirac points" and "Dirac-like points" are presented in chapter 4 of this thesis for a triangular lattice containing tilted resonators. Dirac-like dispersion is investigated in chapter 5 in the context of wave-defect interaction.

Structure of the thesis. In chapter 1 we discuss the Maxwell and Newton equations coupled by the piezoelectric tensor. We specialize to a very common type of anisotropy, *i.e.* the 6*mm* symmetry class. We introduce the Bloch-Floquet quasi-periodicity conditions and the dispersion diagrams for 1D discrete and continuous structures and 2D discrete lattices. Some important mathematical quantities and their physical meaning, such as group velocity and effective mass tensor, are reviewed. We present the dispersion diagrams for 1D periodic piezoelectric laminates, for both in-plane and out-of-plane elasticity, using traction-free and electrically insulating interfaces. Finally, we introduce the dynamic lattice Green's function for a simple 1D example.

In chapter 2 we derive the reflection and transmission coefficients at the interface between two piezoelectric materials whose polarisation is parallel to the interface. We compare these results with the well known Fresnel formulae [7]. We study the scattering problem of a multi-layered piezoelectric structure by taking into account the contribution of both the elastic and electromagnetic waves. This is done by the construction of a recurrence procedure associated with the "multiple bouncing" of waves at every interface. A comparison is made between the results of the scattered spectrum and the dispersion diagram predictions in terms of band gaps. Special attention is paid to the cross-term component of the transmitted spectrum, *i.e.* to the conversion of electromagnetic energy into elastic energy (and vice versa) mediated by the piezoelectric coupling in multi-layered structures.

In chapter 3 our main focus is on a 2D checkerboard-like periodic structures containing piezoelectric materials. The Bloch-Floquet problem of in-plane elasticity (plane strain) is considered for piezoelectric materials where the polarisation is out-of-plane. The full three-dimensional problem of elasticity is considered for a 2D checkerboard-like structure where the polarisation vectors lie in-plane. The boundary conditions are similar to those used for the 1D structure of chapter 2. The effect of the piezoelectric polarisation together with its magnitude is related to the position of standing wave frequency and Dirac points in the dispersion diagram. These results have been published in Tallarico *et al.* [89].

The 2D elastic discrete structure presented in chapter 4 is a vibrating triangular mass-truss lattice whose unit cell contains a tilted resonator of triangular shape. We present and solve the dispersion equation for elastic Bloch-Floquet waves and focus on the novel properties of the dispersion diagram. Attention is given to the coupling of pressure and shear waves induced by the presence of the rotational resonators. An oblique lattice containing two resonators per unit cell is also investigated in chapter 4 and its dispersive properties are compared to those of the triangular lattice possessing a single resonator.

In chapter 5, the dispersive properties of the triangular lattice containing tilted resonators are used to design a structured interface which exhibits negative refraction and focussing,

as in a "flat elastic lens". In addition, a Dirac-like cone arising at $\boldsymbol{k} = \mathbf{0}$ for a special set of parameters is used to generate edge waves propagating along structured interfaces. We also investigate the effect of a coating made of tilted resonators on finite 1D cracks. Finally, we study the propagation of a 1D crack sandwiched between rows of tilted resonators in a thermoelastic lattice.

In chapter 6 we present main conclusions and outline possible directions of future research.

Chapter 1

Theory of wave propagation in periodic composite structures

In section 1.1 we review several results concerning the propagation of elastic waves within bulk piezoelectric materials belonging to the hexagonal symmetry class ($6mm$). We assume that the spontaneous electric polarisation of such a material points along the z axis of a given Cartesian coordinate system. Under this assumption the in-plane problem of elasticity, *i.e.* the governing equations of the displacement components $u_x \equiv u_x(x,y)$ and $u_y \equiv u_y(x,y)$, fully decouples from the out-of-plane problem which governs $u_z \equiv u_z(x,y)$. We show that the elastic in-plane governing equations are dynamically coupled with the electric field whilst such a coupling disappears when considering the out-of-plane component of the displacement. The theory of Bloch-Floquet waves in periodic composite structures in presented in section 1.2. The basic equations are given in the context of benchmark 1D monatomic and biatomic discrete and continuous periodic structures (section 1.3) and 2D monatomic and biatomic discrete periodic structures (section 1.4). In section 1.5 the theory is extended to the case of layered 1D piezoelectric structures for both the out-of-plane and in-plane components of the displacement field. Finally, in section 1.6 we study properties of the dynamic lattice Green's function for a 1D biatomic chain.

1.1 Governing equations of bulk piezoelectric materials

From classical electrodynamics and elasticity, the displacement and the electromagnetic vector fields are described by the second Newton law and Maxwell equations, respectively. The second Newton law in its stress-displacement form is

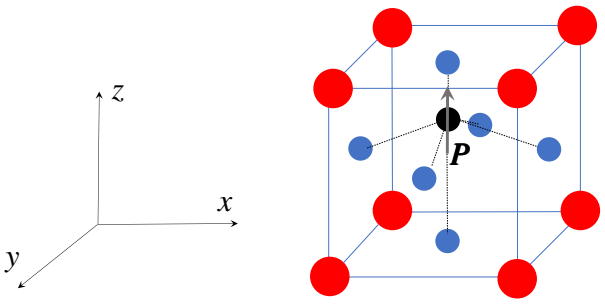

Fig. 1.1 *Illustration of the unit cell of perovskite piezoelectric material. The black circle and each of the red circles represent two different cations. Each of the blue circles denotes anions. The non-centrosimmetry of the unit cell produces a dipole moment per unit volume* $\boldsymbol{P}$ *(grey vector). A Cartesian coordinate has been chosen is such a way that* $\boldsymbol{P}$ *is oriented along the* $z-$*axis.*

$$\begin{aligned}
\frac{\partial \sigma_{xx}}{\partial x}+\frac{\partial \sigma_{yx}}{\partial y}+\frac{\partial \sigma_{zx}}{\partial z}&=\rho\frac{\partial^2 u_x}{\partial t^2},\\
\frac{\partial \sigma_{xy}}{\partial x}+\frac{\partial \sigma_{yy}}{\partial y}+\frac{\partial \sigma_{zy}}{\partial z}&=\rho\frac{\partial^2 u_y}{\partial t^2},\\
\frac{\partial \sigma_{xz}}{\partial x}+\frac{\partial \sigma_{yz}}{\partial y}+\frac{\partial \sigma_{zz}}{\partial z}&=\rho\frac{\partial^2 u_z}{\partial t^2},
\end{aligned} \tag{1.1}$$

where σ_{ij}, $i,j=\{x,y,z\}$, are the components of the stress tensor

$$\hat{\sigma}=\begin{pmatrix}\sigma_{xx} & \sigma_{xy} & \sigma_{xz}\\ \sigma_{yx} & \sigma_{yy} & \sigma_{yz}\\ \sigma_{zx} & \sigma_{zy} & \sigma_{zz}\end{pmatrix}, \tag{1.2}$$

ρ is the uniform mass density, u_i, $i=\{x,y,z\}$, denotes a component of the displacement vector field $\boldsymbol{u}=(u_x,u_y,u_z)^{\mathrm{T}}$ and "T" denotes transposition. The electromagnetic field is governed by the Maxwell equations

$$\begin{aligned}
\nabla\cdot\boldsymbol{D}=0,\quad \nabla\cdot\boldsymbol{B}=0,\\
\nabla\times\boldsymbol{E}=-\frac{\partial\boldsymbol{B}}{\partial t},\qquad \nabla\times\boldsymbol{H}=\frac{\partial\boldsymbol{D}}{\partial t},
\end{aligned} \tag{1.3}$$

where $\nabla(\cdot)=(\partial_x,\partial_y,\partial_z)^{\mathrm{T}}=(\partial/\partial x,\partial/\partial y,\partial/\partial z)^{\mathrm{T}}$, $\boldsymbol{D}=(D_x,D_y,D_z)^{\mathrm{T}}$ and $\boldsymbol{E}=(E_x,E_y,E_z)^{\mathrm{T}}$ are the electric displacement and electric field, $\boldsymbol{B}=(B_x,B_y,B_z)^{\mathrm{T}}$ and $\boldsymbol{H}=(H_x,H_y,H_z)^{\mathrm{T}}$ are the magnetic induction and magnetic fields. The absence of free volume charge and current densities is assumed in Eqs (1.3).

Boundary conditions. At a plane interface between two dielectric media, denoted by the subscripts 1 and 2, the interface conditions for the electromagnetic fields are [36]:

$$\begin{aligned}(\boldsymbol{D}_2-\boldsymbol{D}_1)\cdot\boldsymbol{n}_{12}&=\rho_s,\\(\boldsymbol{B}_2-\boldsymbol{B}_1)\cdot\boldsymbol{n}_{12}&=0,\\\boldsymbol{n}_{12}\times(\boldsymbol{E}_2-\boldsymbol{E}_1)&=\boldsymbol{0},\\\boldsymbol{n}_{12}\times(\boldsymbol{H}_2-\boldsymbol{H}_1)&=\boldsymbol{j}_s,\end{aligned}\tag{1.4}$$

where "$\times$" denotes cross-product of two vectors, $\boldsymbol{n}_{12}$ is the vector normal to the interface pointing from material 1 into material 2, ρ_s and $\boldsymbol{j}_s$ are surface free charge density and surface free current density, respectively.

Perfect contact conditions are

$$\boldsymbol{u}_1=\boldsymbol{u}_2,\quad\text{and}\quad(\hat{\sigma}_1-\hat{\sigma}_2)\boldsymbol{n}_{12}=0,\tag{1.5}$$

where the first equation is the continuity of the displacement fields and the second equation represents continuity of tractions.

Constituitive relations. According to the linear theory of piezoelectric phenomena (see Chap. 8 of [3]), Eqs (1.1) and (1.3) are coupled through the following stress-charge constituitive relations:

$$\sigma_{ij}=c_{ijkl}s_{kl}-e_{ijk}\mathrm{E}_k,\qquad D_i=e_{ijk}s_{jk}+\varepsilon_{ij}\mathrm{E}_j,\tag{1.6}$$

where summation over repeated indices $i,j,k,l=\{x,y,z\}$ is understood, $s_{kl}=(\partial_k u_l+\partial_l u_k)/2$ is the strain tensor and ∂_i denotes a component of the gradient ∇, c_{ijkl} is the stiffness tensor, e_{ijk} the piezoelectric tensor, and the dielectric permittivity matrix ε_{ij}. Since we are interested in a non magnetic material the additional constituitive relation is

$$\boldsymbol{B}=\mu\boldsymbol{H},\tag{1.7}$$

where μ is the magnetic permeability of the vacuum.

A special class of piezoelectric material. In this thesis we study piezoelectric materials belonging to the 6*mm* (hexagonal) symmetry class. Let us consider a Cartesian orthonormal coordinates system $\{x,y,z\}$. Without loss of generality we can assume that the 6-fold axis points along positive z. The electro-elastic constituitive tensors which appear in Eq. (1.6)

can be written in the following matrix form [45]

$$\hat{c} = \begin{pmatrix} c_{11} & c_{12} & c_{13} & 0 & 0 & 0 \\ c_{12} & c_{11} & c_{13} & 0 & 0 & 0 \\ c_{13} & c_{13} & c_{33} & 0 & 0 & 0 \\ 0 & 0 & 0 & c_{44} & 0 & 0 \\ 0 & 0 & 0 & 0 & c_{44} & 0 \\ 0 & 0 & 0 & 0 & 0 & \frac{1}{2}(c_{11}-c_{12}) \end{pmatrix}, \quad \hat{\varepsilon} = \begin{pmatrix} \varepsilon_{11} & 0 & 0 \\ 0 & \varepsilon_{11} & 0 \\ 0 & 0 & \varepsilon_{33} \end{pmatrix},$$

$$\hat{e} = \begin{pmatrix} 0 & 0 & 0 & 0 & e_{15} & 0 \\ 0 & 0 & 0 & e_{15} & 0 & 0 \\ e_{31} & e_{31} & e_{33} & 0 & 0 & 0 \end{pmatrix}. \tag{1.8}$$

The components of the stiffness matrix $(\hat{c})_{IJ}$, $I,J = \{1,2,3,4,5,6\}$ are the independent components of the stiffness tensor $(\hat{c})_{IJ} = c_{ijkl}$, where $ij,kl = \{xx,yy,zz,yz,xz,xy\}$. For example $c_{13} = c_{xxzz}$ and $c_{14} = c_{xxyz} = 0$. Similarly, the components of the piezoelectric matrix $(\hat{e})_{iJ}$, with $i = \{1,2,3\}$ and $J = \{1,2,3,4,5,6\}$, are the independent components of the piezoelectric tensor $(\hat{e})_{iJ} = e_{ijk}$, with $i = \{1,2,3\}$ and $jk = \{11,22,33,23,13,12\}$. Finally the components of the dielectric matrix are $(\hat{\varepsilon})_{ij} = \varepsilon_{ij}$ for $i,j = \{1,2,3\}$. The strain and stress tensors can be represented by the six-dimensional vectors of their independent components, namely

$$\begin{aligned} \boldsymbol{s} &= (s_1,s_2,s_3,s_4,s_5,s_6)^{\mathrm{T}} = (s_{xx},s_{yy},s_{zz},2s_{yz},2s_{xz},2s_{xy})^{\mathrm{T}} \text{ and,} \\ \boldsymbol{\sigma} &= (\sigma_1,\sigma_2,\sigma_3,\sigma_4,\sigma_5,\sigma_6)^{\mathrm{T}} = (\sigma_{xx},\sigma_{yy},\sigma_{zz},\sigma_{yz},\sigma_{xz},\sigma_{xy})^{\mathrm{T}}. \end{aligned} \tag{1.9}$$

The representation of the constituitive tensors in (1.8) and of the strain and stress tensors (1.9) is also known as Voigt representation [3]. In the Voigt representation, the constituitive equations (1.6) become

$$\boldsymbol{\sigma} = \hat{c}\boldsymbol{s} - \hat{e}^{\mathrm{T}}\boldsymbol{E} \quad \text{and} \quad \boldsymbol{D} = \hat{e}\boldsymbol{s} + \hat{\varepsilon}\boldsymbol{E}. \tag{1.10}$$

The constituitive matrices (1.8) guarantee that the out-of-plane and in-plane problems of elasticity are decoupled. As follows we discuss the governing equations of elastic out-of-plane and in-plane problems. The problems are, in principle, coupled to the electromagnetic fields via the constituitive equation (1.10). Our final aim is to study wave propagation in piezoelectric structures with the assumption that the wave vector $\boldsymbol{k}$ lies in the xy plane, for both out-of-plane and in-plane problems. The in-plane components of the vector fields belong to the xy plane of Fig. 1.1. The out-of-plane components of the vector fields are parallel to

the z-axis in Fig. 1.1. In the following, we assume

$$\partial/\partial z(\cdot) = 0, \tag{1.11}$$

for every elastic and electromagnetic physical quantity.

1.1.1 Out-of-plane equations in piezoelectric bulk materials: shear elastic and transverse magnetic waves

We focus here on a homogeneous piezoelectric material belonging to the 6*mm* symmetry class whose constituitive relations are given in Eq. (1.10) and the constituitive tensors are given in Eqs (1.8). We write the equations which involve u_z, the out-of-plane component of the displacement, where the z-axis is schematically shown in Fig. 1.1. The Newton equation (1.1) relative to u_z is

$$\frac{\partial \sigma_{xz}}{\partial x} + \frac{\partial \sigma_{yz}}{\partial y} = \rho \frac{d^2 u_z}{dt^2}. \tag{1.12}$$

The Maxwell equations (1.3) for the in-plane components of the electric field and electric displacement, and for the out-of-plane component of the magnetic field are

$$\frac{\partial E_y}{\partial x} - \frac{\partial E_x}{\partial y} = -\mu \frac{\partial H_z}{\partial t}, \qquad \frac{\partial H_z}{\partial y} = \frac{\partial D_x}{\partial t}, \qquad \frac{\partial H_z}{\partial x} = -\frac{\partial D_y}{\partial t}. \tag{1.13}$$

The remaining Maxwell and Newton equations will be considered in subsection 1.1.2. From (1.10), the constituitive equations involving the physical quantities which appear in Eqs (1.12) and (1.13) are

$$\begin{aligned} \sigma_{xz} &= c_{44} \frac{\partial u_z}{\partial x} - e_{15} \mathrm{E}_x, \qquad \sigma_{yz} = c_{44} \frac{\partial u_z}{\partial y} - e_{15} \mathrm{E}_y, \\ D_x &= e_{15} \frac{\partial u_z}{\partial x} + \varepsilon_{11} E_x, \qquad D_y = e_{15} \frac{\partial u_z}{\partial y} + \varepsilon_{11} E_y. \end{aligned} \tag{1.14}$$

The substitution of the first row of equations (1.14) into (1.12) yields

$$c_{44} \nabla^2 u_z - e_{15} \nabla \cdot \boldsymbol{E} = \rho \frac{\partial^2 u_z}{\partial t^2}. \tag{1.15}$$

Considering the second row of constituitive equations in (1.14), together with the first of Maxwell equations (1.3), we get

$$\nabla \cdot \boldsymbol{E} = -\frac{e_{15}}{\varepsilon_{11}} \nabla^2 u_z, \tag{1.16}$$

where $\nabla^2 = \partial^2/\partial x^2 + \partial^2/\partial y^2 + \partial^2/\partial z^2$. The substitution of Eq. (1.16) into Eq. (1.15) yields

$$G\,\nabla^2 u_z - \rho \frac{\partial^2 u_z}{\partial t^2} = 0, \quad \text{with } G = c_{44} + \frac{e_{15}^2}{\varepsilon_{11}}. \tag{1.17}$$

We consider now the last two Maxwell equations (1.13). We take the derivative of the first one with respect to x and of the second one with respect to y and sum term by term the resulting equations. The result is

$$\nabla^2 H_z = \frac{\partial}{\partial t}\left(\frac{\partial D_x}{\partial y} - \frac{\partial D_y}{\partial x}\right). \tag{1.18}$$

In the right hand side of (1.18), we use the second row of the constituitive relations (1.14). After using the first equation (1.13), we get

$$\nabla^2 H_z - \varepsilon_{11}\mu \frac{\partial^2 H_z}{\partial t^2} = 0. \tag{1.19}$$

Eqs (1.17) and (1.19) show that H_z and u_z are decoupled. The magnetic field propagates at the speed of light in the material and the displacement field propagates at piezoelectric-stiffened velocity (see *e.g.* [70]). Explicit expressions for the two speeds are

$$c = \frac{1}{\sqrt{\varepsilon_{11}\mu}} \text{ and } v = \sqrt{\frac{G}{\rho}}, \tag{1.20}$$

where G has been given in Eq. (1.17).

1.1.2 In-plane equations in piezoelectric bulk materials: vector elasticity and transverse electric waves

The in-plane displacements u_x and u_y are coupled with the out-of-plane electric field E_z and with the in-plane magnetic field components H_x and H_y. When the displacement field is in the xy-plane, the Newton equations (1.1) become

$$\begin{aligned} \frac{\partial \sigma_{xx}}{\partial x} + \frac{\partial \sigma_{xy}}{\partial y} &= \rho \frac{\partial^2 u_x}{\partial t^2}, \\ \frac{\partial \sigma_{xy}}{\partial x} + \frac{\partial \sigma_{yy}}{\partial y} &= \rho \frac{\partial^2 u_y}{\partial t^2}. \end{aligned} \tag{1.21}$$

The constituitive equations for the stress tensor components which appear in Eq. (1.21) are

$$\sigma_{xx} = c_{11}\frac{\partial}{\partial x}u_x + c_{12}\frac{\partial}{\partial y}u_y - e_{13}E_z,\ \sigma_{yy} = c_{11}\frac{\partial}{\partial y}u_y + c_{12}\frac{\partial}{\partial x}u_x - e_{13}E_z,$$
$$\sigma_{xy} = \frac{c_{11}-c_{12}}{2}\left(\frac{\partial}{\partial y}u_x + \frac{\partial}{\partial x}u_y\right), \tag{1.22}$$

The substitution of Eqs (1.22) in (1.21) yields

$$\begin{pmatrix} c_{11}\frac{\partial^2}{\partial x^2} + c_-\frac{\partial^2}{\partial y^2} & c_+\frac{\partial^2}{\partial x\partial y} \\ c_+\frac{\partial^2}{\partial x\partial y} & c_{11}\frac{\partial^2}{\partial y^2} + c_-\frac{\partial^2}{\partial x^2} \end{pmatrix}\begin{pmatrix} u_x \\ u_y \end{pmatrix} - \rho\frac{\partial^2}{\partial t^2}\begin{pmatrix} u_x \\ u_y \end{pmatrix} = e_{13}\begin{pmatrix} \partial_x E_z \\ \partial_y E_z \end{pmatrix}, \tag{1.23}$$

where we have introduced $c_\pm = (c_{11} \pm c_{12})/2$. Note that Eq. (1.23) is symmetric with respect the x and y axis. After taking the curl of the third Maxwell equation in (1.3), and using the fourth Maxwell equation in (1.3) with the constituitive relation

$$D_z = e_{13}\left(\frac{\partial}{\partial x}u_x + \frac{\partial}{\partial y}u_y\right) + \varepsilon_{33}E_z, \tag{1.24}$$

the wave equation for the out-of-plane electric field becomes

$$\nabla^2 E_z - \mu\varepsilon_{33}\,\partial_t^2 E_z = \mu e_{13}\,\frac{\partial^2}{\partial t^2}\left(\frac{\partial}{\partial x}u_x + \frac{\partial}{\partial y}u_y\right). \tag{1.25}$$

Eqs (1.23) and (1.25) are a system of coupled partial differential equations for the in-plane problem of elasticity and the out-of-plane component of the electric field in a $z-$polarised bulk piezoelectric material.

Effect of coupling in the bulk. We consider here the propagation of time-harmonic plane waves along the x-axis of the crystal (*i.e.* $\partial/\partial x(\cdot) = ik_x$ and $\partial/\partial t(\cdot) = -i\omega$). This assumption makes the problem y-independent. Therefore, $\partial/\partial y(\cdot) = 0$ in Eqs (1.23) and (1.25). The Newton equation (1.23) becomes

$$\begin{pmatrix} -c_{11}k_x^2 & 0 \\ 0 & -c_-k_x^2 \end{pmatrix}\begin{pmatrix} u_x \\ u_y \end{pmatrix} + \rho\omega^2\begin{pmatrix} u_x \\ u_y \end{pmatrix} = ik_x e_{13}\begin{pmatrix} E_z \\ 0 \end{pmatrix}, \tag{1.26}$$

and the Maxwell equation (1.25) yields

$$-k_x^2 E_z + \mu\varepsilon_{33}\,\omega^2 E_z = -ik_x\omega^2\mu e_{13}u_x. \tag{1.27}$$

By substituting E_z obtained from Eq. (1.27) into Eq. (1.26) we get an homogeneous matrix equation for (u_x, u_y) which has non-trivial solutions if its determinant is zero, that is for ω such that

$$\left(\rho\frac{\omega^2}{k_x^2} - c_{11}\right)\left(\mu\varepsilon_{33}\frac{\omega^2}{k_x^2} - 1\right) = \mu e_{31}^2\frac{\omega^2}{k_x^2} \quad \text{or} \quad \omega^2\rho - k^2 c_- = 0. \tag{1.28}$$

The first Eq. (1.28) describes coupled dispersion of waves: a quasi-elastic (in-plane) wave and one quasi-electromagnetic (out-of-plane) wave. The second equation is the dispersion equation for an in-plane elastic wave. The prefix “quasi-" stems from the fact that, in the limit $e_{31} = 0$, the dispersion equations reduce to a purely electromagnetic and a purely elastic, with phase velocities being $(\mu\varepsilon_{11})^{-1/2}$ and $(c_{11}/\rho)^{1/2}$, respectively. For a non-zero e_{31}, the quasi-acoustic and quasi-electromagnetic phase velocities differ from the aforementioned phase velocities.

1.2 Bloch-Floquet waves

For illustrative purpose, let us begin our discussion with an example in one spatial dimension x. A scalar function $f(x)$ is said to be quasi-periodic of period β if

$$f(x+\beta) = e^{ik_0\beta} f(x), \tag{1.29}$$

where k_0 is the 1D Bloch parameter. The condition in Eq. (1.29) is known as “Floquet quasi-periodicity condition" among researchers in classical physics interested in elastic and/or electromagnetic periodic structures; researchers with a solid-state physics background may recognise it as “Bloch quasi-periodicity condition". In this thesis, we refer to Eq. (1.29) as Bloch-Floquet quasi-periodicity condition. The Bloch-Floquet quasi-periodicity condition is essential in the study of linear non-dissipative periodic structures governed by several physical equations, spanning from discrete and continuum elasticity to electromagnetism and quantum mechanics. It allows the complete description of a periodic physical system using information only about its unit cell. In two spatial dimensions identified by the vector of coordinates $\boldsymbol{r} = (x,y)^{\mathrm{T}}$, a quasi-periodic vector function $\boldsymbol{f}$ satisfies quasi-periodicity conditions

$$\boldsymbol{f}(\boldsymbol{r}+\boldsymbol{t}^{(\boldsymbol{n})}) = e^{i\boldsymbol{k}\cdot\boldsymbol{t}^{(\boldsymbol{n})}}\boldsymbol{f}(\boldsymbol{r}), \tag{1.30}$$

where

$$\boldsymbol{t}^{(\boldsymbol{n})} = n_1\boldsymbol{t}_1 + n_2\boldsymbol{t}_2, \;\; \boldsymbol{n} = (n_1,n_2)^{\mathrm{T}} \in \mathbb{Z}^2, \tag{1.31}$$

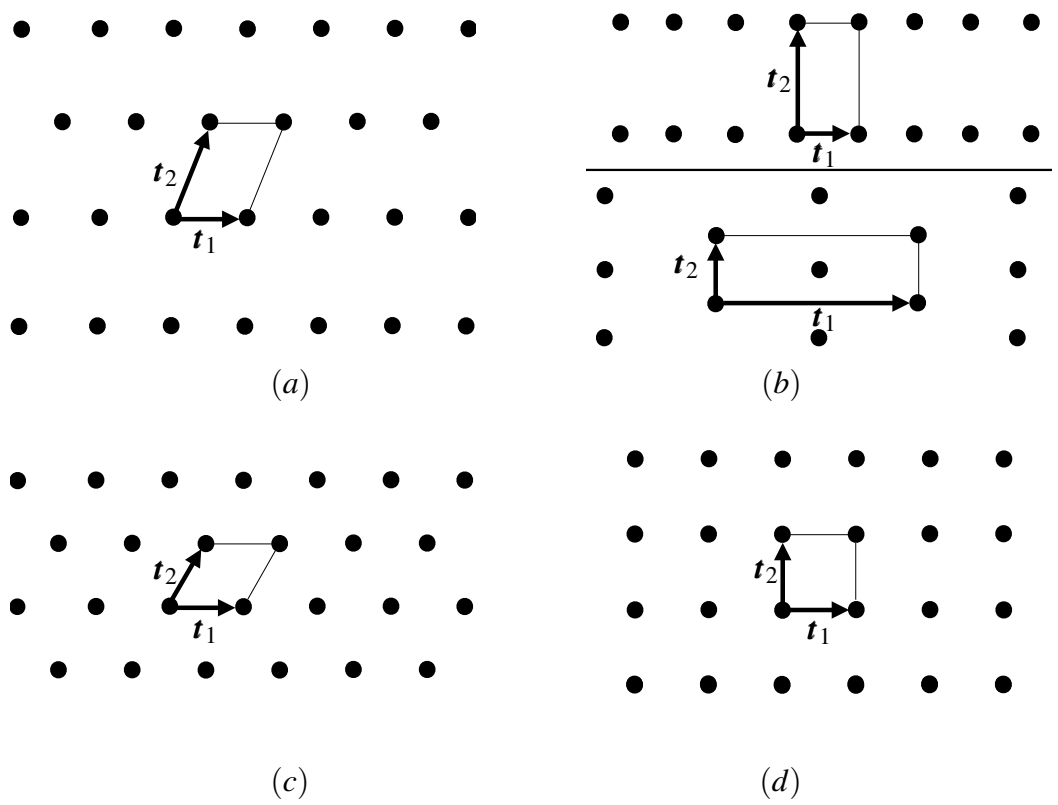

Fig. 1.2 *Bravais lattices in two dimensions whose nodal points are represented by black dots. Panel (a) is the oblique lattice. Panel (b) encloses rectangular (upper part) and centred rectangular (lower part). Panel (c) and (d) are triangular (hexagonal) and square lattices, respectively. The thick arrows represent a choice of the lattice vectors $\boldsymbol{t}_1$ and $\boldsymbol{t}_2$ which together with thin segments delimit choices of the unit cells of the lattices.*

is a position vectors identifying the $\boldsymbol{n}$ unit cell of the so-called Bravais lattice (also known as direct lattice). The vectors $\boldsymbol{t}_1$ and $\boldsymbol{t}_2$ in (1.31) are the lattice translation vectors. In Eq. (1.30) we introduced the 2D Bloch vector $\boldsymbol{k} = (k_x, k_y)^{\mathrm{T}}$. Linear waves which satisfy Bloch-Floquet quasi-periodicity conditions (such as the functions in Eqs (1.29) and (1.30)) are referred to as Bloch-Floquet waves.

1.2.1 Bravais lattice

In two spatial dimensions, five types of Bravais lattices can be identified (see *e.g.* [40], chapter 1). A graphical representation of the 2D Bravais lattices is provided in Fig. 1.2. The 2D Bravais lattices are the oblique (panel (a)), rectangular (panel (b), upper part), centred rectangular (panel (b), lower part), triangular (also known as hexagonal in panel (c)) and square (panel (d)). A unit cell of minimal area is called "primitive cell". Possible choices of the unit cell are represented in Fig. 1.2 by the parallelograms formed by the lattice

translation vectors $\boldsymbol{t}_1$ and $\boldsymbol{t}_2$ and the thin lines. Another example of minimal area unit cell is the "Wigner-Seitz unit cell". Given a nodal point $\boldsymbol{t}^{(\boldsymbol{m})}$, where $\boldsymbol{m}$ is a pair of integers, the Wigner-Seitz unit cell is the locus of points which are closer to $\boldsymbol{t}^{(\boldsymbol{m})}$ than to any other nodal point.

1.2.2 Reciprocal lattice

Let us consider Eq. (1.30) and expand the functions of $\boldsymbol{r}$ on the left-hand and right-hand side of the equality in Fourier series. The results are, respectively

$$\boldsymbol{f}(\boldsymbol{r}+\boldsymbol{t}^{(\boldsymbol{n})}) = \sum_{\boldsymbol{m}\in\mathbb{Z}^2} \tilde{\boldsymbol{f}}^{(\boldsymbol{m})} e^{i\boldsymbol{G}^{(\boldsymbol{m})}\cdot(\boldsymbol{r}+\boldsymbol{t}^{(\boldsymbol{n})})}, \quad \text{and} \quad \boldsymbol{f}(\boldsymbol{r}) = \sum_{\boldsymbol{m}\in\mathbb{Z}^2} \tilde{\boldsymbol{f}}^{(\boldsymbol{m})} e^{i\boldsymbol{G}^{(\boldsymbol{m})}\cdot\boldsymbol{r}}, \tag{1.32}$$

where

$$\boldsymbol{G}^{(\boldsymbol{m})} = m_1\boldsymbol{G}_1 + m_2\boldsymbol{G}_2, \;\; \boldsymbol{m} = (m_1, m_2)^{\mathrm{T}} \in \mathbb{Z}^2. \tag{1.33}$$

In order for the quasi-periodicity condition (1.30) to hold for every $\boldsymbol{k}$, the condition

$$\boldsymbol{G}_i \cdot \boldsymbol{t}_j = 2\pi\delta_{ij}, \;\; i,j = \{1,2\}, \tag{1.34}$$

needs to be satisfied, where δ_{ij} is a Kronecker delta. The vectors $\boldsymbol{G}_1$ and $\boldsymbol{G}_2$ in Eq. (1.34) are translation vectors for a Bravais lattice in two dimensions called reciprocal lattice. The Wigner-Seitz cell (see section (1.2.1)) for the reciprocal lattice is known as first Brillouin zone. The first Brillouin zone encloses all the Bloch vectors $\boldsymbol{k}$ which satisfy Eq. (1.30). Bloch vectors outside this minimal area region can be remapped in the first Brillouin zone via a translation vector $\boldsymbol{G}$ as in Eq. (1.33).

1.2.3 Group velocity

Time-harmonic linear problems in physics can be mathematically represented as systems of linear elliptic partial differential equations (PDEs). In the absence of external forces the system of PDEs is homogeneous. For high-contrast media, the governing equations simplify to linear algebraic equations coupling the displacements of the nodal points of the lattice. In a periodic medium, both discrete and continuum, quasi-periodicity conditions (1.30) hold, together with the boundary conditions required by a specific problem.

The solution of the time-harmonic Bloch-Floquet problem identifies the Bloch-Floquet frequencies $\omega(\boldsymbol{k})$, for which waves can propagate through the structure. The group velocity

for a Bloch-Floquet wave is

$$\boldsymbol{v}_g = \begin{pmatrix} \partial\omega(\boldsymbol{k})/\partial k_x \\ \partial\omega(\boldsymbol{k})/\partial k_y \end{pmatrix}, \tag{1.35}$$

where $\omega(\boldsymbol{k})$ is a permissible frequency. In general, Bloch-Floquet waves are dispersive so that their group velocity depends on the frequency ω. The group velocity identifies the direction of propagation of energy and therefore it gives useful insight into the dynamic properties of periodic media. In one dimension, the gradient in Eq. (1.35) is replaced by $\mathrm{d}/\mathrm{d}k(\cdot)$. Graphically, the group velocity in Eq. (1.35) is parallel to the normal directions to the slowness contours[1]. I

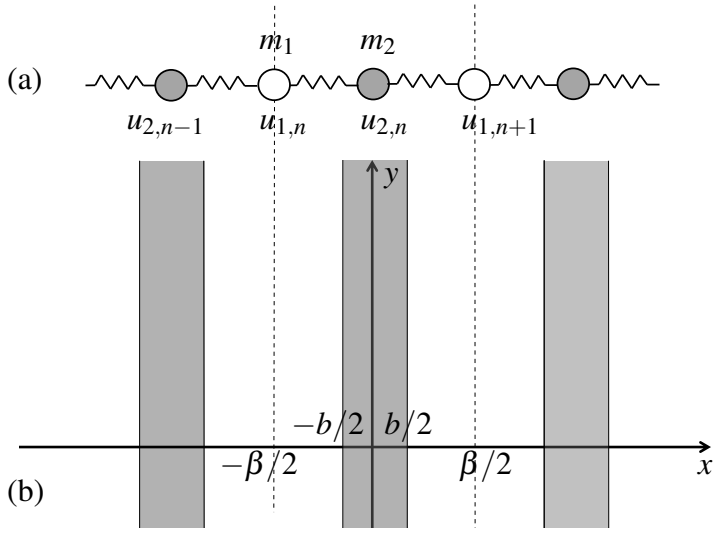

Fig. 1.3 *Schematic representation of a biatomic chain (panel (a)) and of a layered periodic material (panel (b)) whose unit cells are delimited by the vertical dashed lines $x = \pm\beta/2$. The white layers have width $a = (\beta - b)/2$ and the grey layers have width $a = b/2$. They correspond to different materials. The unit cell of the biatomic chain contains two masses, m_1 (white circles) and m_2 (grey circles). The masses are linked one another by trusses of stiffness C.*

1.3 One-dimensional composite structures

Let us consider a 1D chain of equidistant masses m_1 and m_2 as the one shown in Fig. 1.3(a). The masses are linked by massless springs of longitudinal stiffness C and infinite bending stiffness, so that the motion is confined to one dimension. The unit cell of the biatomic chain has width β and contains two masses. In this sense the chain represents the simplest example of a micro-structured material. Considering the unit cell $n \in \mathbb{Z}$, the equations of motion for

[1] The slowness contour for the Bloch-Floquet frequency $\omega(\boldsymbol{k})$ is the locus of points $\boldsymbol{k}$ such that $\omega(\boldsymbol{k}) = \text{const}$.

the displacements $u_{1,n}$ and $u_{2,n}$ are

$$\begin{aligned} -\Omega m_1 u_{1,n} &= C(u_{2,n} + u_{2,n-1} - 2u_{1,n}), \\ -\Omega m_2 u_{2,n} &= C(u_{1,n} + u_{1,n+1} - 2u_{2,n}), \end{aligned} \tag{1.36}$$

where $\Omega = \omega^2$.

Discrete periodic biatomic chain. We are interested in the propagation of Bloch-Floquet waves. Similarly to Eq. (1.30), the Bloch-Floquet condition for the displacements in Eq. (1.36) are

$$u_{i,n+1} = e^{ik_0\beta} u_{i,n}, \;\; i = \{1,2\}, \tag{1.37}$$

where k_0 is the 1D Bloch parameter

$$k_0 \in [-\frac{\pi}{\beta}, \frac{\pi}{\beta}], \tag{1.38}$$

and the interval $[-\pi/\beta, \pi/\beta]$ represents the first Brillouin zone in one dimension, as it follows from the considerations in section 1.2.2. Substituting Eq. (1.37) into (1.36) gives

$$\begin{aligned} -m_1 \Omega u_{1,n} &= C(u_{2,n} + u_{2,n} e^{-i\beta k_0} - 2u_{1,n}), \\ -m_2 \Omega u_{2,n} &= C(u_{1,n} + u_{1,n} e^{i\beta k_0} - 2u_{2,n}). \end{aligned} \tag{1.39}$$

We emphasise that the problem (1.39) is formulated within a single cell n, the cell index n being therefore superfluous. Non-trivial solutions $u_1 = u_{1,n}$ and $u_2 = u_{2,n}$ in Eq. (1.39) correspond to the values of k_0 and Ω for which the determinant of the associated matrix equation is equal to zero, *i.e.*

$$\frac{m_1 m_2}{C^2}\Omega^2 - 2\frac{(m_1 + m_2)}{C}\Omega + 2(1 - \cos(k_0\beta)) = 0. \tag{1.40}$$

For every k_0 as in Eq. (1.38), Eq. (1.40) has two solutions, where the lower one in frequency is the acoustic branch and the higher in frequency is called the optical branch [40]. Approximate solutions of Eq. (1.40) to leading order in $k_0 \to 0$ are [40]

$$\begin{aligned} \Omega_o &\approx 2C\left(\frac{1}{m_1} + \frac{1}{m_2}\right) \quad \text{for the optical branch,} \\ \Omega_a &\approx \frac{1}{2}\frac{C}{m_1 + m_2} k_0^2 \beta^2 \quad \text{for the acoustic branch.} \end{aligned} \tag{1.41}$$

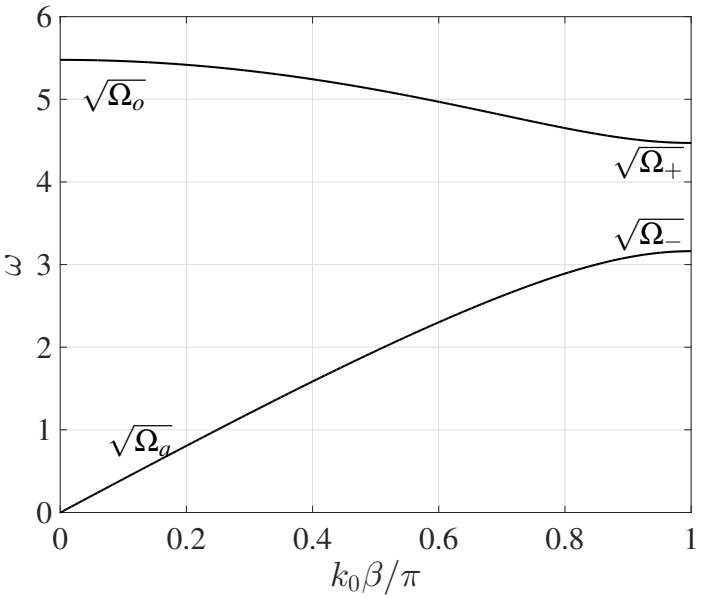

Fig. 1.4 *The figure shows the dispersion curves (optical and acoustic modes) for a bi-atomic 1D lattice whose dispersion equation is* (1.40)*. The parameters are* $C = 10$, $m_1 = 1$, $m_2 = 2$ *and the lattice spacing* $\beta = 1$.

Without loss of generality we can assume $m_2 > m_1$. At $k_0 = \pi/2$ the solutions of Eq. (1.40) take the form

$$\Omega_+ = \frac{2C}{m_1} \text{ and } \Omega_- = \frac{2C}{m_2}. \tag{1.42}$$

Fig. 1.4 shows the optical and acoustic branches for a biatomic chain obtained from Eq. (1.40). The parameters are $m_1 = 1$, $m_2 = 2$ and $C = 10$. The lattice spacing is $\beta = 1$. Fig. 1.4 illustrates that as $k_0 \to 0$, $\Omega(k_0)$ tends to the acoustic and optical asymptotic limits in Eq. (1.41). Moreover, since $m_1 \neq m_2$, with $m_2 > m_1$, a complete band gap appears at the Brillouin zone edge $k_0 = \pi/\beta$. From Eq. (1.42), the frequency width of the band gap is

$$\Delta\omega_G = \sqrt{\frac{2}{C}}\left(\frac{1}{\sqrt{m_1}} - \frac{1}{\sqrt{m_2}}\right). \tag{1.43}$$

Layered periodic medium made of isotropic materials. We consider the propagation of time-harmonic out-of-plane elastic waves through a periodic layered medium whose layers are made of homogeneous isotropic materials. Fig. 1.3(b) shows the layered medium. The displacement fields in the medium are governed by the following equation:

$$\mu_j \nabla^2 U_j^{(n)} + \rho_j \Omega U_j^{(n)} = 0, \quad x \in X_j^{(n)}, \quad \text{with } j = 1,2, \quad \text{and } y \in (-\infty, \infty), \tag{1.44}$$

where we do not invoke summation over repeated indices, $X_1^{(n)} = (-\beta - b/2 + n\beta, -b/2 + n\beta)$, $X_2^{(n)} = (-b/2 + n\beta, b/2 + n\beta)$, with n an integer, β the period of the structure and b

the width of grey layers. The coefficient μ_i and ρ_i are the shear modulus and the mass density of the $X_i^{(n)}$ layer. Consider a time-harmonic wave for which the displacement amplitude has the form

$$U_j^{(n)}(x,y) = u_j^{(n)}(x)e^{ik_y y}. \tag{1.45}$$

The substitution of Eq. (1.45) into Eq. (1.44) leads to

$$\frac{\mathrm{d}^2}{\mathrm{d}x^2}\left(u_j^{(n)}\right) + \kappa_j^2 u_j^{(n)} = 0, \quad x \in X_j^{(n)}, \text{ and } \kappa_j = \left(\frac{\omega^2}{v_{s,j}^2} - k_y^2\right)^{1/2}, \quad \text{with } j = 1,2, \tag{1.46}$$

where $v_{s,j} = \sqrt{\mu_j/\rho_j}$, $j = \{1,2\}$, is the shear wave speed in material (j). With reference to the unit cell in Fig. 1.3(b) and the unit cell represented therein, the Bloch-Floquet quasi-periodicity conditions are

$$u_1^{(2)}(x-\beta/2) = e^{ik_0\beta}u_1^{(1)}(x+\beta/2) \quad \text{and} \quad \frac{\mathrm{d}}{\mathrm{d}x}u_1^{(2)}(x-\beta/2) = e^{ik_0\beta}\frac{\mathrm{d}}{\mathrm{d}x}u_1^{(1)}(x+\beta/2). \tag{1.47}$$

The continuity of displacements and tractions at the interfaces $x = \pm b/2$ are

$$\begin{aligned} & u_1^{(1)}(x)\Big|_{x=-b^-/2} = u_2^{(1)}(x)\Big|_{x=-b^+/2}, \quad u_2^{(1)}(x)\Big|_{x=b^-/2} = u_1^{(2)}(x)\Big|_{x=b^+/2}, \\ \text{and} \quad & \mu_1\frac{\mathrm{d}}{\mathrm{d}x}u_1^{(1)}(x)\Big|_{x=-b^-/2} = \mu_2\,\frac{\mathrm{d}}{\mathrm{d}x}u_2^{(1)}(x)\Big|_{x=-b^+/2}, \\ & \mu_2\frac{\mathrm{d}}{\mathrm{d}x}\,u_2^{(1)}(x)\Big|_{x=b^-/2} = \mu_1\,\frac{\mathrm{d}}{\mathrm{d}x}u_1^{(2)}(x)\Big|_{x=b^+/2}, \end{aligned} \tag{1.48}$$

respectively, where the superscripts "+" and "-" denote limits from right and from left of the interface.

The general solution of Eq. (1.46) is

$$u_j^{(n)} = A_j^{(n)}e^{i\kappa_j x} + B_j^{(n)}e^{-i\kappa_j x}, \quad x \in X_j^{(n)}, \quad \text{with } j = 1,2, \tag{1.49}$$

where $A_j^{(n)}$, $B_j^{(n)}$, $j = 1,2$, are constant coefficients over the strip $X_j^{(n)}$, $j = \{1,2\}$. By substituting the Ansatz (1.49) in the Bloch-Floquet conditions (1.47) and in the boundary conditions (1.48), we obtain a linear system of six equations for six coefficients. The solvability condition of this system requires the

$$\begin{aligned} 4\cos(k_0\beta)\kappa_1\kappa_2\mu_1\mu_2 = \big[&(\kappa_1\mu_1 + \kappa_2\mu_2)^2\cos(a\kappa_1 + b\kappa_2) \\ &- (\kappa_1\mu_1 - \kappa_2\mu_2)^2\cos(a\kappa_1 - b\kappa_2)\big], \end{aligned} \tag{1.50}$$

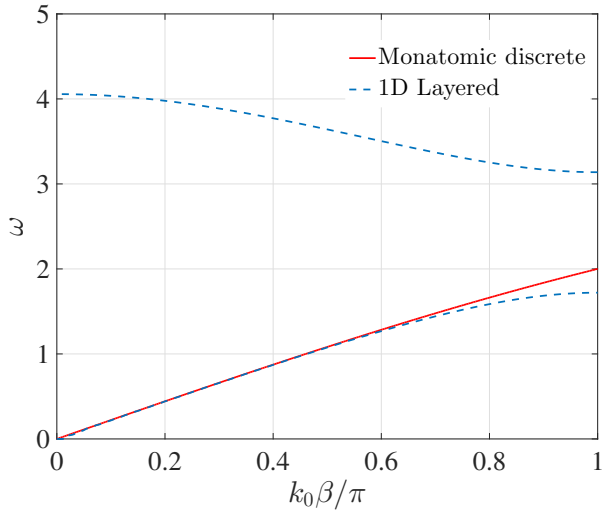

Fig. 1.5 *The blue dashed lines are the first two dispersion curves for a layered periodic 1D structure obtained using the dispersion equation* (1.50)*. The figure corresponds to $k_y = 0$. The parameters are $\mu_1 = 2$ and $\mu_2 = 10^{-3}\mu_1$, $a = b = 0.5$ and $\rho_1 = \rho_2 = 1$. As $\omega \to 0$ the dispersion tends to the one of an "equivalent monatomic chain" (red continuous line) with mass-to-stiffness ratio* (1.57)*.*

where $a = (\beta - b)/2$. We observe that the dispersion equation (1.50) is symmetric under simultaneous exchange of the triplets (a, κ_1, μ_1) and (b, κ_2, μ_2). When $a = b$, the equation is symmetric under exchange of materials, *i.e.* under exchange of the pairs (κ_1, μ_1) and (κ_2, μ_2). Moreover, Eq. (1.50) can be reduced to Eq. (39) in Ref. [70]. We emphasise that Bloch-Floquet quasi-periodicity conditions have allowed us to formulate the problem within the unit cell instead of considering an infinite set of layers $X_i^{(n)}$.

Asymptotically equivalent model problem. Let us assume that Bloch-Floquet waves, as those in Eq. (1.49), propagate along the $x-$ axis in Fig. 1.3(b), *i.e.* $\kappa_i = \omega/v_{s,i}$. We assume that the layered medium in Fig. 1.3(b) is made of materials with high-contrast stiffness ($\mu_1/\mu_2 = \xi \ll 1$), equal densities ($\rho_1 = \rho_2 = \rho$) and equal thickness of the layers ($a = b = \beta/2$). Under these assumptions, using the identities $v_{s,1} = \sqrt{\xi} v_{s,2}$ and $\kappa_2 = \sqrt{\xi}\kappa_1$, Eq. (1.50) becomes

$$4\sqrt{\xi}\cos(k_0\beta) = (1+\sqrt{\xi})^2\cos(a\kappa_1(1+\sqrt{\xi})) - (1-\sqrt{\xi})^2\cos(a\kappa_1(1-\sqrt{\xi})). \quad (1.51)$$

We assume that the thickness a of the layers is small compared to the wavelength, *i.e.*

$$\kappa_1 a \ll 1 \implies \omega \ll \frac{v_{s,1}}{a}. \quad (1.52)$$

Therefore, after the expansion of the trigonometric functions on the right hand-side, Eq. (1.51) can be recast in the following form

$$4\sqrt{\xi}\cos(k_0\beta) \approx (1+\sqrt{\xi})^2 - (1-\sqrt{\xi})^2 \\ -((1+\sqrt{\xi})^4 - (1-\sqrt{\xi})^4)\frac{(a\kappa_1)^2}{2} + ((1+\sqrt{\xi})^6 - (1-\sqrt{\xi})^6)\frac{(a\kappa_1)^4}{24}. \tag{1.53}$$

To the leading order in ξ, from Eq. (1.53), we get

$$p_1\Omega^2 - p_2\Omega + 2(1-\cos(k_0\beta)) = 0, \tag{1.54}$$

with the coefficient of the polynomial equation (1.54) given by

$$p_1 = \frac{a^4}{4}\frac{\rho^2}{\mu_1^2} \quad \text{and} \quad p_2 = 2a^2\frac{\rho}{\mu_1}. \tag{1.55}$$

We observe that (1.54) has the same form as the dispersion equation (1.40). With reference to Eq. (1.40), we introduce the notation

$$\tilde{p}_1 = \frac{m_1 m_2}{C^2} \quad \text{and} \quad \tilde{p}_2 = 2\,\frac{m_1+m_2}{C}, \tag{1.56}$$

where m_1 and m_2 are the masses , and C is the stiffness of the links. With reference to the relations in (1.55) and (1.56)

$$p_1 = \tilde{p}_1, p_2 = \tilde{p}_2 \iff \frac{m_1}{C} = \frac{m_2}{C} = \frac{p_2}{4} \pm \frac{1}{2}\sqrt{\frac{p_2^2}{4} - 4p_1} = \frac{p_2}{4}, \tag{1.57}$$

where the last equality follows from the expressions (1.55). Eq. (1.57) implies that, when $a = b$, $\mu_1/\mu_2 \ll 1$ and asymptotic condition (1.52) holds, a continuous layered medium can be approximated by a monatomic chain whose mass-to-stiffness ratio is given by Eq. (1.57). This fact is further illustrated in Fig. 1.5. In Movchan *et al.* [65], a uniform approximation was found over the frequency range corresponding to the two lowest dispersion curves. The approximation is in term biatomic lattice parameter m_1 and m_2, the masses of a biatomic chain. Their result assumes that a is the small parameter in Eq. (1.52) (instead of the frequency ω assumed here) and the resulting equivalent masses are $m_1 \neq m_2$, thus reproducing the band gap of the layered structure.

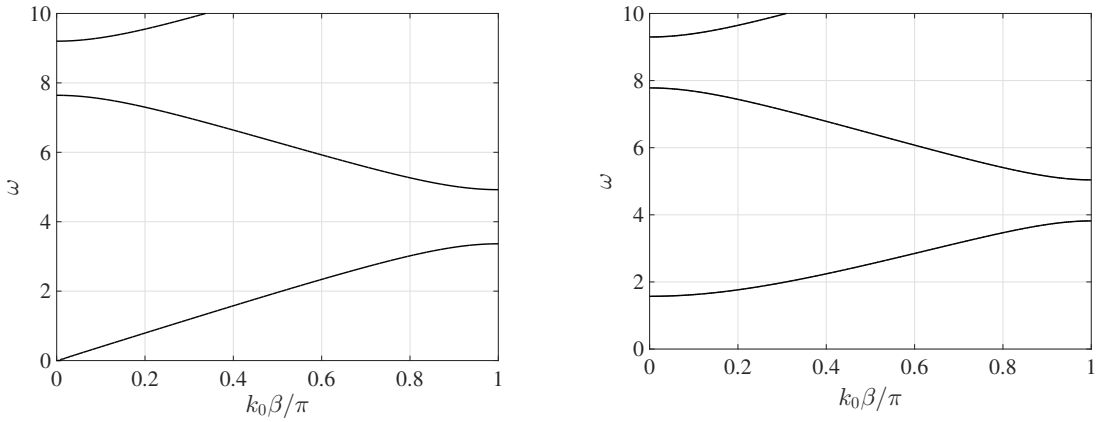

Fig. 1.6 *The panels show the dispersion curves of a layered periodic structure obtained solving Eq. (1.50) at normal incidence (panel (a)) and for $k_y = 1/\beta$ (panel (b)). The other parameters are $\mu_1 = 1$, $\mu_2 = 3$, $\rho_1 = \rho_2 = 1$, $a = \beta/2 = 1/2$.*

A zero-frequency band gap. We observe that the parameters κ_i, $i = \{1,2\}$, introduced in Eq. (1.49) are either real or imaginary depending on the frequency ω. When

$$\min(\kappa_1^2, \kappa_2^2) < 0, \tag{1.58}$$

the function in Eq. (1.49) has exponentially localised form. More specifically, if the condition (1.58) holds then Eq. (1.50) is not satisfied for any real Bloch parameter k_0. Therefore, assuming $v_{s,2} > v_{s,1}$, Eq. (1.58) implies that the interval

$$0 < \omega < v_{s,2} k_y, \tag{1.59}$$

is a complete stop band for the periodic layered medium. Since the interval (1.59) has $\omega = 0$ as lower bound, it is denoted as "zero-frequency band gap".

Dispersion diagram. We illustrate here the dispersion diagram of a layered periodic structure where only shear elastic waves can propagate. Fig. 1.6(a) shows the dispersion curves of a layered periodic structure obtained by solving Eq. (1.50) with $k_y = 0$. Fig. 1.6(b) shows the dispersion curves of a layered periodic structure obtained solving Eq. (1.50) with $k_y = 1/\beta$. The other parameters are $\mu_1 = 1$, $\mu_2 = 3$, $\rho_1 = \rho_2 = 1$, $a = \beta/2 = 1/2$ in both parts of the figure. We observe that Eq. (1.50) gives an infinite spectrum of frequencies for every value of the Bloch parameter k_0. In Figs (1.6)(a) and (1.6)(a) we show the first

two branches and the beginning of the third one. A zero-frequency band gap appears in Fig. 1.6(b), consistently with the prediction (1.59). In 1.6(a) the band gap disappears at $k_y = 0$.

1.4 Two-dimensional composite structures

Discrete lattice structures are particularly attractive because their dispersion equation is polynomial in ω, in contrast with the transcendental Eq. (1.50). The main focus of this section is to elucidate some general facts for 2D discrete lattices, with special focus on triangular and oblique lattices both monatomic and biatomic.

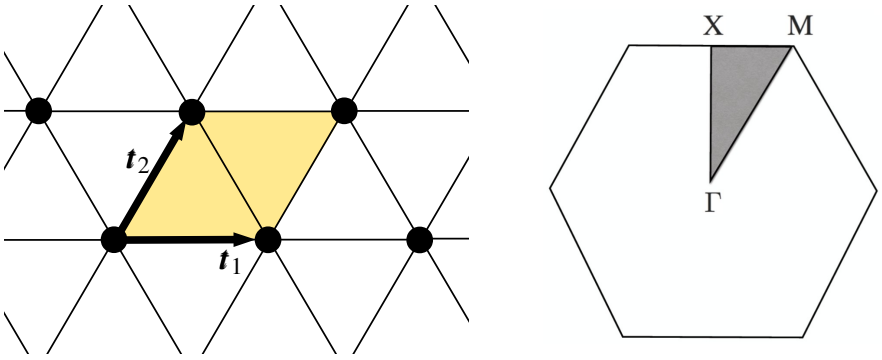

Fig. 1.7 *Schematic representations of the monatomic triangular lattice (panel (a)) and its first Brillouin zone (panel (b)).*

1.4.1 Triangular lattice

A schematic representation of the monatomic triangular lattice is shown in Fig. 1.7(a). Primitive vectors $\boldsymbol{t}_1$ and $\boldsymbol{t}_2$ are also shown, their expression being

$$\boldsymbol{t}_1 = \begin{pmatrix} 1 \\ 0 \end{pmatrix} L \text{ and } \boldsymbol{t}_2 = \begin{pmatrix} 1 \\ \sqrt{3} \end{pmatrix} \frac{L}{2}, \tag{1.60}$$

where L is the lattice spacing. It is convenient to introduce an auxiliary vector $\boldsymbol{t}_3 = \boldsymbol{t}_1 - \boldsymbol{t}_2$. The translation vectors for the reciprocal lattice follow from Eq. (1.34) and are

$$\boldsymbol{G}_1 = \frac{2\pi}{L} \begin{pmatrix} 1 \\ -1/\sqrt{3} \end{pmatrix} \text{ and } \boldsymbol{G}_2 = \frac{2\pi}{L} \begin{pmatrix} 0 \\ 2/\sqrt{3} \end{pmatrix}. \tag{1.61}$$

The first Brillouin zone associated with the lattice vectors (1.61) is shown in Fig. 1.7(b), together with the high symmetry points

$$\Gamma = \begin{pmatrix} 0 \\ 0 \end{pmatrix}, \quad \mathrm{M} = \frac{2\pi}{\sqrt{3}L}\begin{pmatrix} 1/\sqrt{3} \\ 1 \end{pmatrix} \text{ and } \mathrm{X} = \frac{2\pi}{\sqrt{3}L}\begin{pmatrix} 0 \\ 1 \end{pmatrix}. \tag{1.62}$$

Unless otherwise stated, dispersion surfaces for triangular lattices are presented as a function of the Bloch vector $\boldsymbol{k}$ such that

$$\boldsymbol{k} = \begin{pmatrix} k_x \\ k_y \end{pmatrix} \in \left[-\frac{4\pi}{3L}, \frac{4\pi}{3L}\right]^2. \tag{1.63}$$

The square region defined by Eq. (1.63) encloses the first Brillouin zone shown in Fig. 1.7(b).

Monatomic triangular lattice. We assume that the yellow semi-transparent area in Fig. 1.7(a) is the $\boldsymbol{n}$ unit cell, with $\boldsymbol{n} \in \mathbb{Z}^2$, its nodal point $\boldsymbol{n}$ being the bottom-left circle. The Newton equations for the time-harmonic linear elastic displacement $\boldsymbol{u}^{(\boldsymbol{n})}$ of the nodal point $\boldsymbol{n}$ is

$$\begin{aligned} -m_{\mathrm{TL}}\Omega\boldsymbol{u}^{(\boldsymbol{n})} = c_\ell\hat{\tau}_1\left(\boldsymbol{u}^{(\boldsymbol{n}+\boldsymbol{p}_1)} + \boldsymbol{u}^{(\boldsymbol{n}-\boldsymbol{p}_1)} - 2\boldsymbol{u}^{(\boldsymbol{n})}\right) + c_\ell\hat{\tau}_2\left(\boldsymbol{u}^{(\boldsymbol{n}+\boldsymbol{p}_2)} + \boldsymbol{u}^{(\boldsymbol{n}-\boldsymbol{p}_2)} - 2\boldsymbol{u}^{(\boldsymbol{n})}\right), \\ + c_\ell\hat{\tau}_3\left(\boldsymbol{u}^{(\boldsymbol{n}+\boldsymbol{p}_1+\boldsymbol{p}_2)} + \boldsymbol{u}^{(\boldsymbol{n}-\boldsymbol{p}_1-\boldsymbol{p}_2)} - 2\boldsymbol{u}^{(\boldsymbol{n})}\right), \end{aligned} \tag{1.64}$$

where we introduce $\boldsymbol{p}_1 = (1,0)^{\mathrm{T}}$ and $\boldsymbol{p}_2 = (0,1)^{\mathrm{T}}$ and m_{TL} is the mass of the nodal points. The rank-two tensors $\hat{\tau}_i$ in (1.64), with $i = \{1,2,3\}$, are projectors over the directions pointing the nearest neighbours from a given lattice nodal point, *i.e.*

$$\begin{aligned} \hat{\tau}_1 = \frac{1}{L^2}\boldsymbol{t}_1 \otimes \boldsymbol{t}_1 = \begin{pmatrix} 1 & 0 \\ 0 & 0 \end{pmatrix}, \quad \hat{\tau}_2 = \frac{1}{L^2}\boldsymbol{t}_2 \otimes \boldsymbol{t}_2 = \frac{1}{4}\begin{pmatrix} 1 & \sqrt{3} \\ \sqrt{3} & 1 \end{pmatrix}, \\ \text{and } \hat{\tau}_3 = \frac{1}{L^2}(\boldsymbol{t}_1 - \boldsymbol{t}_2) \otimes (\boldsymbol{t}_1 - \boldsymbol{t}_2) = \frac{1}{4}\begin{pmatrix} 1 & -\sqrt{3} \\ -\sqrt{3} & 1 \end{pmatrix}, \end{aligned} \tag{1.65}$$

where $\boldsymbol{v} \otimes \boldsymbol{w}$ denotes the dyadic product of two vector, $\boldsymbol{v}$ and $\boldsymbol{w}$. The Bloch-Floquet condition for the time-harmonic displacement $\boldsymbol{u}^{(\boldsymbol{n})}$ is

$$\boldsymbol{u}^{(\boldsymbol{n}+\boldsymbol{m})} = e^{i(m_1\boldsymbol{t}_1\cdot\boldsymbol{k} + m_2\boldsymbol{t}_2\cdot\boldsymbol{k})}\boldsymbol{u}^{(\boldsymbol{n})}, \tag{1.66}$$

where $\boldsymbol{m} = (m_1, m_2)^{\mathrm{T}} \in \mathbb{Z}^2$, $\boldsymbol{t}_1$ and $\boldsymbol{t}_2$ are given in Eq. (1.60) and $\boldsymbol{k}$ is the Bloch vector belonging to the first Brillouin zone in Fig. (1.7)(b). The substitution of (1.66) into (1.64)

yields

$$-m_{\mathrm{TL}}\Omega\boldsymbol{u}^{(\boldsymbol{n})} = 2c_\ell \sum_{i=1}^{3} (\cos(\boldsymbol{k}\cdot\boldsymbol{t}_i) - 1)\hat{\tau}_i \boldsymbol{u}^{(\boldsymbol{n})}. \tag{1.67}$$

Bloch-Floquet conditions have allowed us to reformulate the problem (1.64), where nearest-neighbours nodal points are involved, into the problem (1.67), where only the displacement $\boldsymbol{u}^{(\boldsymbol{n})}$ appears. Non trivial solutions of Eq. (1.67) can be obtained if and only if

$$\det\left(\hat{\Sigma}_{\boldsymbol{k}}^{(\mathrm{TL})} - m_{\mathrm{TL}}\Omega\hat{I}_2\right) = 0, \text{ with } \hat{\Sigma}_{\boldsymbol{k}}^{(\mathrm{TL})} = -\sum_{i=1}^{3} 2c_\ell(\cos(\boldsymbol{k}\cdot\boldsymbol{t}_i) - 1)\hat{\tau}_i, \tag{1.68}$$

where $\omega = \Omega^2$, $\hat{\tau}_i$ and $\boldsymbol{t}_i$, $i = 1,2,3$, are given in Eqs (1.60) and (1.65), respectively, and m_{TL} is the mass at the nodal points. The matrix $\hat{I}_2$ is the 2×2 identity matrix. The roots of (1.68) in units $L = 1$ are

$$\begin{aligned} m_{\mathrm{TL}}\Omega_{\pm}^2(\boldsymbol{k}) &= c_\ell(\cos k_x + 2\cos(k_x/2)\cos(\sqrt{3}ky/2) \pm \sqrt{C(\boldsymbol{k})} - 3), \\ C(\boldsymbol{k}) &= \cos^2(k_x/2)\cos^2(\sqrt{3}k_y/2) + 3\sin^2(k_x/2)\sin^2(\sqrt{3}k_y/2) \\ &\quad + \cos^2(k_x) - 2\cos(k_x)\cos(k_x/2)\cos(\sqrt{3}k_y/2). \end{aligned} \tag{1.69}$$

The Bloch frequencies (1.69) correspond to "shear dominated" ($\Omega_+(\boldsymbol{k})$) and "pressure dominated" ($\Omega_-(\boldsymbol{k})$) Bloch eigenmodes $\boldsymbol{u}^{(\boldsymbol{n})}$. This terminology is reminiscent of the low-frequency long-wavelength isotropic behaviour of the dispersion surfaces whose constant effective group velocities are [56]

$$v_{\mathrm{p}} = \sqrt{3}v_{\mathrm{s}} \text{ and } v_{\mathrm{s}} = \frac{1}{2}\sqrt{\frac{3}{2}}L\sqrt{\frac{c_\ell}{m}}, \tag{1.70}$$

where v_{p} and v_{s} are the pressure and shear velocity, respectively.

Fig. 1.8(a) shows the Bloch frequencies (1.69) as a function of the Bloch vector (1.63). Fig. 1.8(b) shows the slowness contours obtained from panel (a) at $\omega = 1$ (red solid curve) and $\omega = 0.5$ (blue dashed curve). For $\omega \to 0$ and $|\boldsymbol{k}| \to 0$, the Bloch frequency for pressure (shear) elastic waves is

$$\omega(\boldsymbol{k}) \approx v_{\mathrm{p}}\,|\boldsymbol{k}| \text{ and } \omega(\boldsymbol{k}) \approx v_{\mathrm{s}}\,|\boldsymbol{k}|, \tag{1.71}$$

where $|\boldsymbol{v}|$ denotes the norm of a vector $\boldsymbol{v}$, and the v_p and v_s are the pressure and shear group velocities introduced in Eq. (1.70). This is illustrated in Fig. 1.8(b) where the dashed blue curves are in fact isotropic and in good agreement with (1.71). At higher frequency (see *e.g.* the red curves in Fig. 1.8(b)) the approximations (1.71) for the Bloch frequencies no

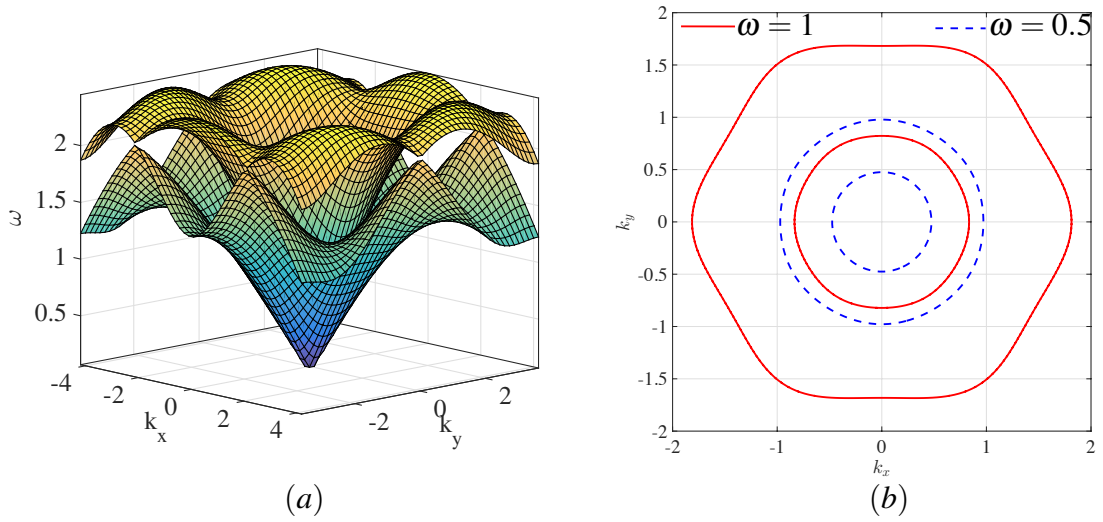

Fig. 1.8 *Panel (a) shows the Bloch frequencies of a monatomic triangular lattice (see Eq.* (1.69) *) as a function of the Bloch vector* (1.63)*. We use* $c_\ell = 1$ *and* $m_{\mathrm{TL}} = 1$*. Panel (b) shows the slowness contours obtained from panel (a) at* $\omega = 1$ *(red solid curve) and* $\omega = 0.5$ *(blue dashed curve).*

longer apply and dynamic anisotropy dominates wave propagation, *i.e.* waves propagating in different directions experience different group velocity. This is illustrated by the hexagon-like solid red curves corresponding to the shear-dominated mode at $\omega = 1$. The dynamic anisotropy for the monatomic triangular lattice has been quantified and used earlier in [19, 20], in focusing applications. All these facts will be further illustrated in the context of chapter 4.

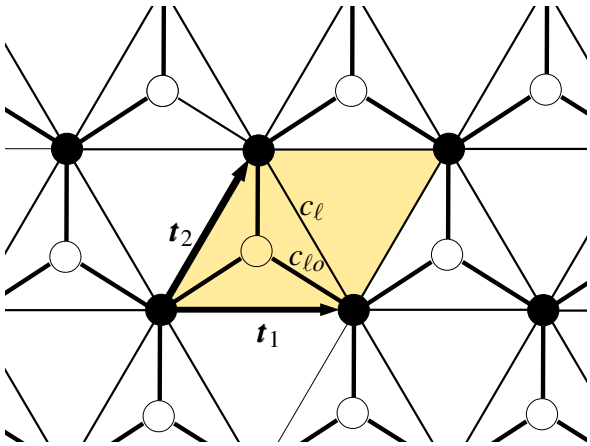

Fig. 1.9 *Schematic representation of a structured triangular lattice. The unit cell (yellow semitransparent area) contains a point resonator of mass* m_b *(white disks). Point masses* m_a *are assumed at the triangular lattice nodal points (black disks). Thin and thick lines represent massless trusses of stiffness* c_ℓ *and* $c_{\ell o}$*, respectively.*

A structured triangular lattice with a point mass resonator. In this section, we study a monatomic structured triangular lattice whose unit cell contains a point resonator (see Fig. 1.9). The triangular lattice nodal points (black circles in Fig. 1.9) have mass m_a, and the point-wise resonator has mass m_b (white circles in Fig. 1.9). The nodal points are connected one another by massless trusses of stiffness c_ℓ. Moreover, the resonator enclosed in the unit cell (yellow-highlighted region in Fig. 1.9) is located at

$$\tilde{\boldsymbol{r}}_{\rm cm} = \begin{pmatrix} 1 \\ 1/\sqrt{3} \end{pmatrix} \frac{L}{2}, \tag{1.72}$$

with respect to the nodal point at the bottom-left corner of the unit cell. The resonators are linked to the triangular lattice nodal points by trusses of stiffness $c_{\ell o}$. The dispersion equation for the structured triangular lattice in Fig. 1.9 is

$$\det\left(\hat{\Sigma}^{(\rm STL)}_{\boldsymbol{k}} - \omega^2 \hat{\mathscr{M}}^{(\rm STL)}\right) = 0, \tag{1.73}$$

where

$$\hat{\mathscr{M}}^{(\rm STL)} = \mathrm{diag}(m_a, m_a, m_b, m_b), \tag{1.74}$$

and the superscript “(STL)" stands for “Structured Triangular Lattice". The stiffness matrix is

$$\hat{\Sigma}^{(\rm STL)}_{\boldsymbol{k}} = \begin{pmatrix} \hat{\Sigma}_{aa}(\boldsymbol{k}) & \hat{\Sigma}_{ab}(\boldsymbol{k}) \\ \hat{\Sigma}_{ba}(\boldsymbol{k}) & \hat{\Sigma}_{bb} \end{pmatrix}, \tag{1.75}$$

where

$$\begin{aligned} \hat{\Sigma}_{aa}(\boldsymbol{k}) &= -\begin{pmatrix} 4c_\ell \mathrm{C}_x^2 - 3c_{\ell o}/2 - 5c_\ell + c_\ell \mathrm{C}_x\mathrm{C}_y & -\sqrt{3}c_\ell \mathrm{S}_x\mathrm{S}_y \\ -\sqrt{3}c_\ell \mathrm{S}_x\mathrm{S}_y & 3c_\ell \mathrm{C}_x\mathrm{C}_y - 3c_{\ell o}/2 - 3c_\ell \end{pmatrix}, \\ \hat{\Sigma}_{bb} &= \frac{3}{2} c_{\ell o} \hat{I}_2, \quad \text{and} \quad \hat{\Sigma}_{ab}(\boldsymbol{k}) = \hat{\Sigma}^{\dagger}_{ba}(\boldsymbol{k}) = \\ &= -\frac{c_{\ell o}}{2} \exp(-iLk_x/2) \begin{pmatrix} 3\mathrm{C}_x & i\sqrt{3}\ \mathrm{S}_x \\ i\sqrt{3}\ \mathrm{S}_x & \mathrm{C}_x + 2\exp(i\sqrt{3}Lk_y/2) \end{pmatrix}, \end{aligned} \tag{1.76}$$

and

$$\mathrm{C}_x = \cos(Lk_x/2), \ \ \mathrm{C}_y = \cos(\sqrt{3}Lk_y/2), \ \ \mathrm{S}_x = \sin(Lk_x/2) \ \text{ and } \ \mathrm{S}_y = \sin(\sqrt{3}k_y/2). \tag{1.77}$$

Equation (1.73) can be further simplified using the block partition of the stiffness matrix introduced in Eq. (1.76). The results is

$$\left(\omega^2-\omega_b^2\right)^2 \det\left(\hat{I}_2\omega^2-\frac{1}{m_a}\hat{\Sigma}_{aa}(\boldsymbol{k})\right)=\frac{1}{m_a m_b}\left|\det(\hat{\Sigma}_{ba}(\boldsymbol{k}))\right|^2, \tag{1.78}$$

where

$$\omega_b^2=\frac{3}{2}\frac{c_{\ell o}}{m_b}, \tag{1.79}$$

is the natural frequency for a single point resonator.

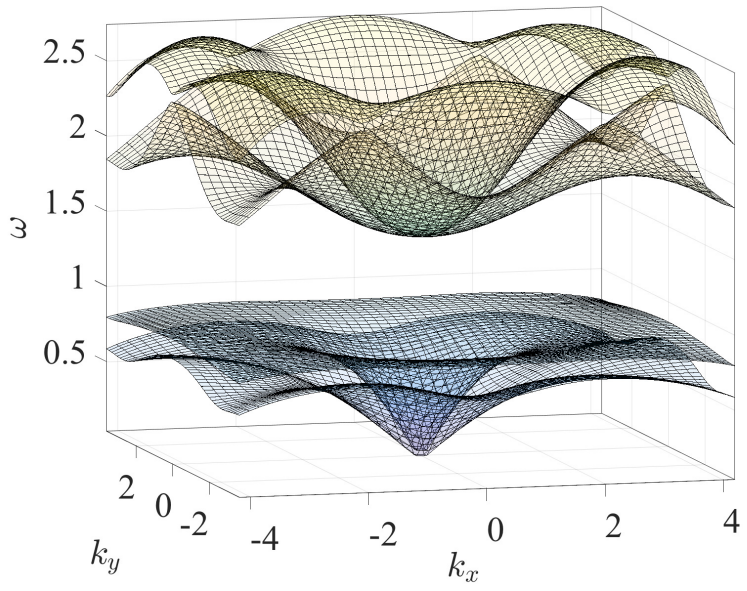

Fig. 1.10 *Dispersion surfaces for a triangular lattice with a point resonator, corresponding to the solution of Eq.* (1.73) *with* $L=1$, $c_{\ell o}=1$,$c_\ell=1$, $m_a=1$ *and* $m_b=2$.

Frequency band gap. Eq. (1.78) is never satisfied when $\omega=\omega_b$, which corresponds to the frequency of oscillation of a single resonator per unit cell. Physically, it implies that around $\omega=\omega_b$ a band gap is expected. Moreover, in writing Eq. (1.78) we implicitly assumed that

$$\det\left(\omega^2\hat{I}_2-\frac{1}{m_a}\hat{\Sigma}_{aa}(\boldsymbol{k})\right)\neq 0. \tag{1.80}$$

Fig. 1.10 shows the Bloch-Floquet frequency dispersion surface for a triangular lattice containing a single point-wise resonator. The results are obtained by solving Eq. (1.73) with $L=1$, $c_{\ell o}=1$,$c_\ell=1$, $m_a=1$ and $m_b=2$. We emphasise that a complete band gap occurs in the neighbourhood of the natural frequency ω_b for the single resonator (see Eq. (1.78)).

Differently from the dispersive properties of a monatomic triangular lattice (see *e.g.* Fig. 1.8(a)), we observe that the dispersion surfaces in Fig. 1.10 are four, consistently with the number of degrees of freedom of the structured unit cell in Fig. 1.9. The two lower and two upper surfaces are known as acoustic and optical branches, respectively.

1.4.2 Oblique lattice

In this section, we analyse a special "Oblique Lattice" (OL) which can be obtained from the triangular lattice in Fig. 1.7(a) by replacing a constant mass m with the masses m_1 and m_2. A schematic representation of the oblique lattice considered here is given in Fig. 1.11(a). We show two possible unit cells for the lattice: one is highlighted in yellow and delimited by the translation vectors

$$\tilde{\boldsymbol{t}}_1 = 2\boldsymbol{t}_1 \quad \text{and} \quad \tilde{\boldsymbol{t}}_2 = \boldsymbol{t}_2, \tag{1.81}$$

where $\boldsymbol{t}_i$, $i = \{1,2\}$, are given in Eq. (1.60). The second one is highlighted in orange and is delimited by the translation vectors

$$\boldsymbol{t}_1^* = 2\boldsymbol{t}_1 - \boldsymbol{t}_2 \quad \text{and} \quad \boldsymbol{t}_2^* = \boldsymbol{t}_2. \tag{1.82}$$

We assign the mass m_1 (black circles) to the nodes $\tilde{\boldsymbol{t}}_b^{(\boldsymbol{n})} = n_1\tilde{\boldsymbol{t}}_1 + n_2\tilde{\boldsymbol{t}}_2$, and m_2 (white circles) to the nodes $\tilde{\boldsymbol{t}}_w^{(\boldsymbol{n})} = \boldsymbol{t}_1 + n_1\tilde{\boldsymbol{t}}_1 + n_2\tilde{\boldsymbol{t}}_2$, where $\boldsymbol{n} = (n_1, n_2)^{\mathrm{T}} \in \mathbb{Z}^2$. Equivalently, nodal points located at $\boldsymbol{t}_b^{*(\boldsymbol{n})} = n_1\boldsymbol{t}_1^* + n_2\boldsymbol{t}_2^*$ and $\boldsymbol{t}_w^{*(\boldsymbol{n})} = \boldsymbol{t}_1 + n_1\boldsymbol{t}_1^* + n_2\boldsymbol{t}_2^*$, have masses m_1 and m_2, respectively.

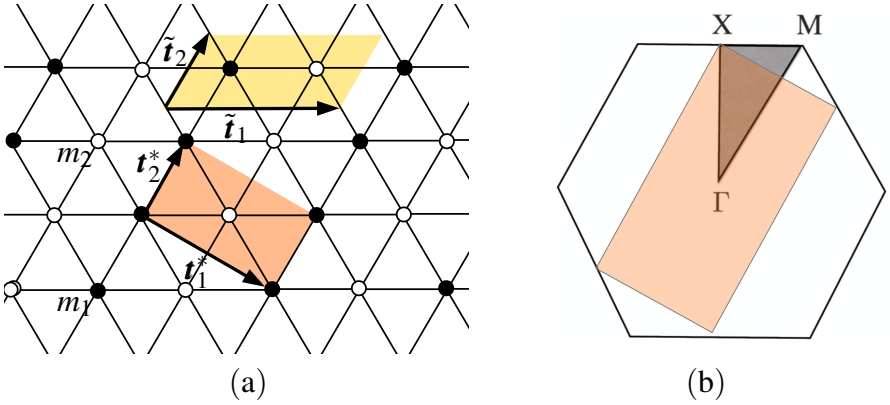

Fig. 1.11 *Schematic representations of a biatomic lattice (panel (a)) and its first Brillouin zone (orange semitransparent region in panel (b)). In panel (b) the first Brillouin zone for a triangular lattice (hexagon) is also shown for comparison.*

Equations of motion. In a given cell $\boldsymbol{n}$, *e.g.* the yellow region in Fig. 1.11(a), the linear elastic time-harmonic displacement $\tilde{\boldsymbol{u}}_1^{(\boldsymbol{n})}$ of the mass m_1 from the nodal point $\tilde{\boldsymbol{t}}_b^{(\boldsymbol{n})}$ is governed

by the equation of motion

$$\begin{aligned}-\Omega m_1 \tilde{\boldsymbol{u}}_1^{(\boldsymbol{n})} &= c_\ell \hat{\tau}_1 \left(\tilde{\boldsymbol{u}}_2^{(\boldsymbol{n})} + \tilde{\boldsymbol{u}}_2^{(\boldsymbol{n}-\boldsymbol{p}_1)} - 2\tilde{\boldsymbol{u}}_1^{(\boldsymbol{n})} \right) \\ &+ c_\ell \hat{\tau}_2 \left(\tilde{\boldsymbol{u}}_1^{(\boldsymbol{n}+\boldsymbol{p}_2)} + \tilde{\boldsymbol{u}}_1^{(\boldsymbol{n}-\boldsymbol{p}_2)} - 2\tilde{\boldsymbol{u}}_1^{(\boldsymbol{n})} \right) \\ &+ c_\ell \hat{\tau}_3 \left(\tilde{\boldsymbol{u}}_2^{(\boldsymbol{n}-\boldsymbol{p}_1)} + \tilde{\boldsymbol{u}}_2^{(\boldsymbol{n}+\boldsymbol{p}_2-\boldsymbol{p}_1)} - 2\tilde{\boldsymbol{u}}_1^{(\boldsymbol{n})} \right), \end{aligned} \tag{1.83}$$

where $\tilde{\boldsymbol{u}}_2^{(\boldsymbol{n})}$ are the displacement of the mass m_2 from the nodal points $\tilde{\boldsymbol{t}}_w^{(\boldsymbol{n})}$, and the 2×2 projectors $\hat{\tau}_i$, $i=1,2,3$, are given in (1.65). The displacement $\tilde{\boldsymbol{u}}_2^{(\boldsymbol{n})}$ satisfies the equation of motion

$$\begin{aligned}-\Omega m_2 \tilde{\boldsymbol{u}}_2^{(\boldsymbol{n})} &= c_\ell \hat{\tau}_1 \left(\tilde{\boldsymbol{u}}_1^{(\boldsymbol{n})} + \tilde{\boldsymbol{u}}_1^{(\boldsymbol{n}+\boldsymbol{p}_1)} - 2\tilde{\boldsymbol{u}}_2^{(\boldsymbol{n})} \right) \\ &+ c_\ell \hat{\tau}_2 \left(\tilde{\boldsymbol{u}}_2^{(\boldsymbol{n}+\boldsymbol{p}_2)} + \tilde{\boldsymbol{u}}_2^{(\boldsymbol{n}-\boldsymbol{p}_2)} - 2\tilde{\boldsymbol{u}}_2^{(\boldsymbol{n})} \right) \\ &+ c_\ell \hat{\tau}_3 \left(\tilde{\boldsymbol{u}}_1^{(\boldsymbol{n}+\boldsymbol{p}_2)} + \tilde{\boldsymbol{u}}_1^{(\boldsymbol{n}+\boldsymbol{p}_1-\boldsymbol{p}_2)} - 2\tilde{\boldsymbol{u}}_2^{(\boldsymbol{n})} \right). \end{aligned} \tag{1.84}$$

Bloch-Floquet conditions. The elastic displacements $\tilde{\boldsymbol{u}}_1^{(\boldsymbol{n})}$ and $\tilde{\boldsymbol{u}}_2^{(\boldsymbol{n})}$ in Eqs (1.83) and (1.84) satisfy Bloch-Floquet conditions

$$\tilde{\boldsymbol{u}}_i^{(\boldsymbol{n}+\boldsymbol{m})} = e^{i(m_1\tilde{\boldsymbol{t}}_1\cdot\boldsymbol{k}+m_2\tilde{\boldsymbol{t}}_2\cdot\boldsymbol{k})}\tilde{\boldsymbol{u}}_i^{(\boldsymbol{n})}, \quad i=1,2, \tag{1.85}$$

with $\boldsymbol{n},\boldsymbol{m}\in\mathbb{Z}^2$, $\boldsymbol{m}=(m_1,m_2)^{\mathrm{T}}$, and $\tilde{\boldsymbol{t}}_i$, $i=1,2$, as in Eq. (1.81). The vector $\boldsymbol{k}$ in Eq. (1.85) is the Bloch-Floquet wave vector in the first Brillouin zone of the structure. The translation vectors of the reciprocal lattice can be obtained from Eq. (1.34) using the translation vectors for the real space lattice in Eq. (1.81). The result is

$$\tilde{\boldsymbol{G}}_1 = \frac{1}{2}\boldsymbol{G}_1 \quad \text{and} \quad \tilde{\boldsymbol{G}}_2 = \boldsymbol{G}_2, \tag{1.86}$$

where $\boldsymbol{G}_i$, $i=1,2$, are given in Eq. (1.61). Similarly, the reciprocal lattice translation vectors corresponding to (1.82) are

$$\boldsymbol{G}_1^* = \frac{1}{2}\boldsymbol{G}_1 \quad \text{and} \quad \boldsymbol{G}_2^* = \frac{1}{2}\boldsymbol{G}_1 + \boldsymbol{G}_2, \tag{1.87}$$

where $\boldsymbol{G}_i$, $i=1,2$, are given in Eq. (1.61). We emphasise that the vectors (1.87) are orthogonal. Consequently, the first Brillouin zone obtained with the Wigner-Seitz method on the nodal points generated by the translation vectors (1.87) is rectangular. The dispersion equations and corresponding roots do not depend on equivalent choices of first Brillouin

zones. Therefore, we choose to present the dispersion properties of the lattice over the rectangular Brillouin zone

$$\boldsymbol{k} = \alpha_1 \boldsymbol{G}_1^* + \alpha_2 \boldsymbol{G}_2^*, \quad \text{with} \quad (\alpha_1, \alpha_2) \in [-1/2, 1/2]^2, \tag{1.88}$$

where $\boldsymbol{G}_i^*$, $i = 1,2$ are given in (1.87). The rectangular Brillouin zone in (1.88) is schematically represented Fig. 1.11(b) as an orange semi-transparent area. The first Brillouin zone for a triangular lattice (see Fig. 1.7(b)) is also shown for comparison.

After the substitution of the Bloch-Floquet conditions (1.85), Eqs (1.83) and (1.84) become

$$\begin{aligned} -\Omega m_1 \tilde{\boldsymbol{u}}_1(\boldsymbol{k}) = {} & c_\ell \hat{\tau}_1 \left(\tilde{\boldsymbol{u}}_2(\boldsymbol{k}) + \tilde{\boldsymbol{u}}_2(\boldsymbol{k}) e^{-i\boldsymbol{k}\cdot\tilde{\boldsymbol{t}}_1} - 2\tilde{\boldsymbol{u}}_1(\boldsymbol{k}) \right) \\ & + 2c_\ell \hat{\tau}_2 \left(\cos(\boldsymbol{k}\cdot\tilde{\boldsymbol{t}}_2) - 1 \right) \tilde{\boldsymbol{u}}_1(\boldsymbol{k}) \\ & + c_\ell \hat{\tau}_3 \left(\tilde{\boldsymbol{u}}_2(\boldsymbol{k}) e^{-i\boldsymbol{k}\cdot\boldsymbol{t}_2} + \tilde{\boldsymbol{u}}_2(\boldsymbol{k}) e^{-i\boldsymbol{k}\cdot(\tilde{\boldsymbol{t}}_1 - \tilde{\boldsymbol{t}}_2)} - 2\tilde{\boldsymbol{u}}_1(\boldsymbol{k}) \right), \end{aligned} \tag{1.89}$$

and

$$\begin{aligned} -\Omega m_2 \tilde{\boldsymbol{u}}_2(\boldsymbol{k}) = {} & c_\ell \hat{\tau}_1 \left(\tilde{\boldsymbol{u}}_1(\boldsymbol{k}) + \tilde{\boldsymbol{u}}_1(\boldsymbol{k}) e^{i\boldsymbol{k}\cdot\tilde{\boldsymbol{t}}_1} - 2\tilde{\boldsymbol{u}}_2(\boldsymbol{k}) \right) \\ & + 2c_\ell \hat{\tau}_2 \left(\cos(\boldsymbol{k}\cdot\tilde{\boldsymbol{t}}_2) - 1 \right) \tilde{\boldsymbol{u}}_2(\boldsymbol{k}) \\ & + c_\ell \hat{\tau}_3 \left(\tilde{\boldsymbol{u}}_1(\boldsymbol{k}) e^{i\boldsymbol{k}\cdot\boldsymbol{t}_2} + \tilde{\boldsymbol{u}}_1(\boldsymbol{k}) e^{i\boldsymbol{k}\cdot(\tilde{\boldsymbol{t}}_1 - \tilde{\boldsymbol{t}}_2)} - 2\tilde{\boldsymbol{u}}_2(\boldsymbol{k}) \right), \end{aligned} \tag{1.90}$$

where the cell nodal coordinates $\boldsymbol{n}$ have been omitted. The Bloch-Floquet amplitudes $\tilde{\boldsymbol{u}} = (\tilde{\boldsymbol{u}}_1^{\mathrm{T}}, \tilde{\boldsymbol{u}}_2^{\mathrm{T}})^{\mathrm{T}}$ in Eqs (1.89) and (1.90) are non-zero if and only if

$$\det\left(\hat{\Sigma}_{\boldsymbol{k}}^{(\mathrm{OL})} - \Omega \hat{\mathscr{M}}^{(\mathrm{OL})} \right) = 0, \tag{1.91}$$

where

$$\hat{\mathscr{M}}^{(\mathrm{OL})} = \mathrm{diag}(m_1, m_1, m_2, m_2), \tag{1.92}$$

and the superscript “(OL)" stands for “Oblique Lattice". The stiffness matrix is

$$\hat{\Sigma}_{\boldsymbol{k}}^{(\mathrm{OL})} = \begin{pmatrix} \hat{\Sigma}_{11}(\boldsymbol{k}) & \hat{\Sigma}_{12}(\boldsymbol{k}) \\ \hat{\Sigma}_{21}(\boldsymbol{k}) & \hat{\Sigma}_{22}(\boldsymbol{k}) \end{pmatrix}, \tag{1.93}$$

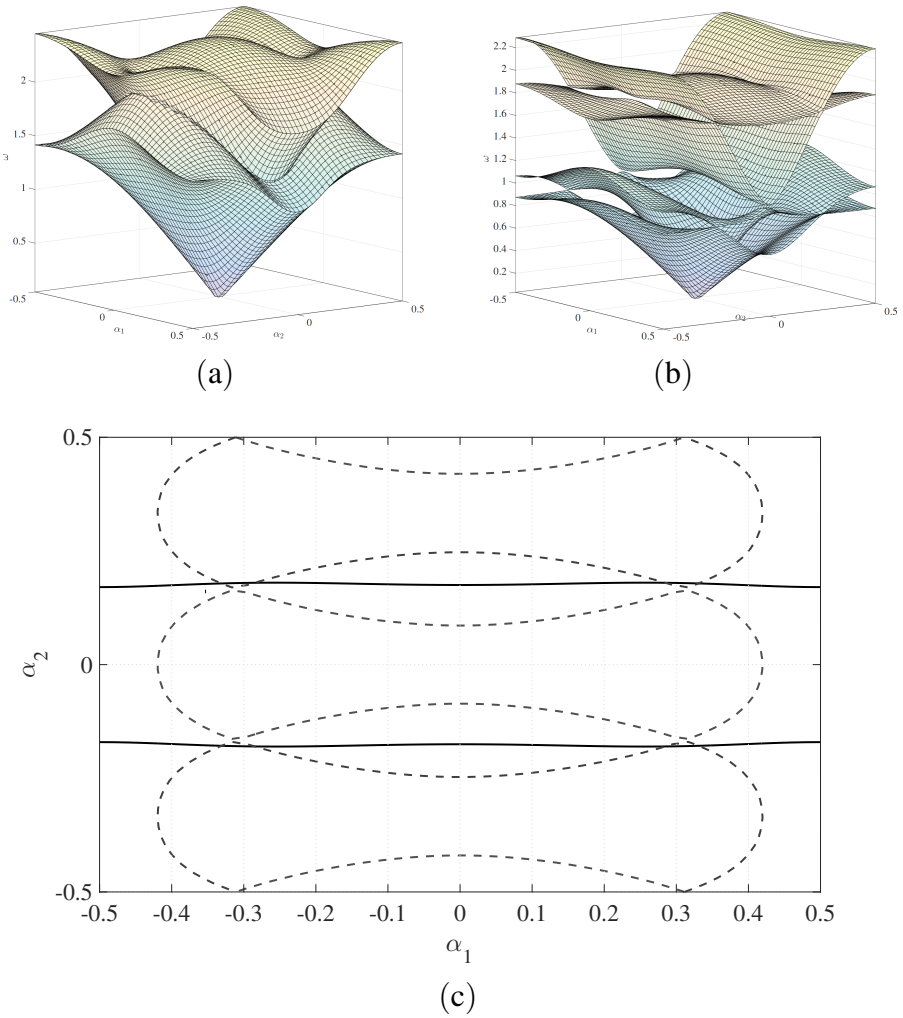

Fig. 1.12 *Dispersion diagrams over the first Brillouin zone for the oblique lattice represented in Fig. 1.11(a). In panel (a) we use $m_1 = m_2 = 1$, while in panel (b) we fix $m_1 = 1$ and $m_2 = 3$. The stiffness of the links is $c_\ell = 1$. Panel (c) shows a comparison of slowness contours obtained from panel (a) (dashed grey lines) and panel (b) (solid black lines) at $\omega = 1.5$.*

where

$$\hat{\Sigma}_{11}(\boldsymbol{k}) = \hat{\Sigma}_{22}(\boldsymbol{k}) = 2c_\ell \left[\hat{\tau}_1 + (1 - \cos(\boldsymbol{k}\cdot\tilde{\mathbf{t}}_2))\hat{\tau}_2 + \hat{\tau}_3\right], \tag{1.94}$$

$$\hat{\Sigma}_{12}(\boldsymbol{k}) = \hat{\Sigma}_{21}^{\dagger}(\boldsymbol{k}) = -c_\ell \left[\hat{\tau}_1(1 + e^{-i\boldsymbol{k}\cdot\tilde{\boldsymbol{t}}_1}) + \hat{\tau}_3(e^{-i\boldsymbol{k}\cdot\tilde{\boldsymbol{t}}_2} + e^{-i\boldsymbol{k}\cdot(\tilde{\boldsymbol{t}}_1 - \tilde{\boldsymbol{t}}_2)})\right]. \tag{1.95}$$

For every $\boldsymbol{k}$ in Eq. (1.88), the dispersion equation (1.91) has four solutions $\Omega = \omega^2$. The solutions $\omega \equiv \omega(\boldsymbol{k})$ of Eq. (1.91) are reported in Fig. 1.12(a) and 1.12(b). The parameters used in the computations are $c_{\ell o} = 1$, $m_1 = 1$ and $L = 1$. Fig. 1.12(a) corresponds to the case $m_2 = m_1$, *i.e.* monatomic lattice, while in Fig. 1.12(b) $m_2 = 3m_1$ is used. In order to compare

the dispersion properties we report in Fig. 1.12(c) the slowness contours of the Fig. 1.12(a) (grey dashed lines) and Fig. 1.12(b) (black full lines) evaluated at $\omega = 1.5$.

1.5 Layered piezoelectric periodic composite structures: coupled Bloch-Floquet waves

A layered periodic piezoelectric structure is considered in this section. With reference to Fig. 1.3(b), we assume that the grey and white layers are made of two different 6*mm* piezoelectric materials whose $6-$fold axis points in the out-of-plane z-direction. The aim is here to construct the dispersion diagram for Bloch-Floquet waves.

For out-of-plane elastic and transverse magnetic waves, the governing equations derived in the subsection 1.1.1 apply. In section 1.5.2 we outline the derivation of the dispersion equation for out-of-plane elastic waves, as done by Piliposyan *et al.* [71].

In section 1.5.3 we quantify polaritonic effects arising from the coupling of in-plane elastic waves and transverse electric waves in a layered piezoelectric structures. Following a method similar to the one used by Zhu *el. al.* [105], we obtain an asymptotic dispersion equations, valid at the boundary of the 1D first Brillouin zone.

In section 1.5.4, we present the dispersion diagrams for both out-of-plane and in-plane problems of elasticity in a 1D piezoelectric structures.

1.5.1 Representation of the fields across planar interfaces under the out-of-plane shear assumption

The out-of-plane assumption for the displacement field is

$$u_x(x,y) = 0, \quad u_y(x,y) = 0, \quad \text{and} \quad E_z(x,y) = 0. \tag{1.96}$$

The last condition is essential in order to ensure purely out-of-plane elastic waves, as it follows from Eq. (1.28). We assume that elastic and electromagnetic quantities are time-harmonic and have plane-wave dependence on the y spatial coordinate, *i.e.*

$$\begin{aligned} u_z(x,y;t) = u_{z,0}(x)e^{ik_y y - i\omega t}, \;\; H_z(x,y;t) = H_{z,0}(x)e^{ik_y y - i\omega t}, \\ \sigma_{xz}(x,y;t) = \sigma_{xz,0}(x)e^{ik_y y - i\omega t} \;\; \text{and} \;\; E_y(x,y;t) = E_{y,0}(x)e^{ik_y y - i\omega t}. \end{aligned} \tag{1.97}$$

We introduce the following vector function

$$\boldsymbol{\eta}(x) = \begin{pmatrix} -\omega u_{z,0}(x) \\ iE_{y,0}(x) \\ i\sigma_{xz,0}(x) \\ iH_{z,0}(x) \end{pmatrix}, \tag{1.98}$$

where the components have been introduced in (1.97). Using Eqs (1.12), (1.13) and (1.14) we deduce the differential equation

$$\frac{1}{i}\frac{\mathrm{d}}{\mathrm{d}x}\boldsymbol{\eta}(x) = \hat{S}\,\boldsymbol{\eta}(x), \tag{1.99}$$

with

$$\hat{S} = \begin{pmatrix} 0 & 0 & \omega/G & -e_{15}k_y/(G\varepsilon_{11}) \\ 0 & 0 & -e_{15}k_y/(G\varepsilon_{11}) & \left(\omega^2\varepsilon_{11}\mu - k_y^2 c_{44}/G\right)/(\omega\varepsilon_{11}) \\ \left(\omega^2\rho - k_y^2 c_{44}\right)/\omega & k_y e_{15} & 0 & 0 \\ k_y e_{15} & \omega\varepsilon_{11} & 0 & 0 \end{pmatrix}, \tag{1.100}$$

and $\boldsymbol{\eta}(x)$ introduced in Eq. (1.98). The eigenvalues of $\hat{S}$ are

$$s_1 = -q,\ \ s_2 = q,\ \ s_3 = -r,\ \ s_4 = r, \tag{1.101}$$

where

$$q = \sqrt{\omega^2\mu\varepsilon_{11} - k_y^2} \ \text{ and } \ r = \sqrt{\omega^2\rho/G - k_y^2}, \tag{1.102}$$

and corresponding eigenvectors, which are solutions of Eq. (1.99), are

$$\begin{aligned} \boldsymbol{e}_1(x) &= -2i\sqrt{\frac{\omega\varepsilon_{11}}{2q}}\begin{pmatrix} 0 \\ -q/(\varepsilon_{11}\omega) \\ e_{15}k_y/(\varepsilon_{11}\omega) \\ 1 \end{pmatrix} e^{-iqx},\ \ \boldsymbol{e}_2(x) = 2\sqrt{\frac{\omega\varepsilon_{11}}{2q}}\begin{pmatrix} 0 \\ q/(\varepsilon_{11}\omega) \\ e_{15}k_y/(\varepsilon_{11}\omega) \\ 1 \end{pmatrix} e^{+iqx}, \\ \boldsymbol{e}_3(x) &= 2i\sqrt{\frac{Gr}{2\omega}}\begin{pmatrix} -\omega/(Gr) \\ e_{15}k_y/(\varepsilon_{11}Gr) \\ 1 \\ 0 \end{pmatrix} e^{-irx},\ \ \boldsymbol{e}_4(x) = 2\sqrt{\frac{Gr}{2\omega}}\begin{pmatrix} \omega/(Gr) \\ -e_{15}k_y/(\varepsilon_{11}Gr) \\ 1 \\ 0 \end{pmatrix} e^{+irx}. \end{aligned} \tag{1.103}$$

The energy flux parallel to the $x-$direction is [3]

$$\mathscr{F}_x = \frac{1}{2}\mathrm{Re}\left(-\sigma_{xz}(x)v_z^*(x) + E_y(x)H_z^*(x)\right) = \frac{1}{4}\boldsymbol{\eta}(x)^\dagger\ \hat{\mathscr{E}}\ \boldsymbol{\eta}(x), \tag{1.104}$$

where $*$ denotes complex conjugation and † denotes Hermitian conjugation. The explicit form of $\boldsymbol{\eta}(x)$ is given in Eq. (1.98) and

$$\hat{\mathscr{E}} = \begin{pmatrix} 0 & 0 & 1 & 0 \\ 0 & 0 & 0 & 1 \\ 1 & 0 & 0 & 0 \\ 0 & 1 & 0 & 0 \end{pmatrix}. \tag{1.105}$$

The normalisation of the eigenmodes in Eq. (1.103) has been chosen in such a way that the right-propagating modes are

$$\boldsymbol{e}_i^\dagger(x)\ \hat{\mathscr{E}}\ \boldsymbol{e}_j(x) = \delta_{ij}, \quad i,j = \{1,3\}, \quad \text{with} \quad \mathrm{Im}(q) = \mathrm{Im}(r) = 0, \tag{1.106}$$

and left-propagating mode

$$\boldsymbol{e}_i^\dagger(x)\ \hat{\mathscr{E}}\ \boldsymbol{e}_j(x) = -\delta_{ij}, \quad i,j = \{2,4\}, \quad \text{with} \quad \mathrm{Im}(q) = \mathrm{Im}(r) = 0. \tag{1.107}$$

The non-propagating modes are such that

$$\boldsymbol{e}_i^\dagger(x)\ \hat{\mathscr{E}}\ \boldsymbol{e}_j(x) = 0, \quad i,j = \{1,2,3,4\}, \quad \text{with} \quad \mathrm{Re}(q) = \mathrm{Re}(r) = 0. \tag{1.108}$$

By requiring that both the wave-vectors in Eq. (1.102) are real, one can identify threshold frequencies above which electromagnetic and/or elastic waves propagate within a given piezoelectric material and at a given k_y, the y-component of the wave vector. The elastic and electromagnetic threshold frequencies are respectively

$$\omega_{\mathrm{T}}^{(\mathrm{EL})} = \sqrt{\frac{G}{\rho}}k_y \quad \text{and} \quad \omega_{\mathrm{T}}^{(\mathrm{EM})} = \frac{1}{\sqrt{\mu\varepsilon}}\ k_y\ . \tag{1.109}$$

In addition, two frequency regimes naturally arise from Eq. (1.109). For frequencies such that[2]

$$\omega_{\mathrm{T}}^{(\mathrm{EL})} < \omega < \omega_{\mathrm{T}}^{(\mathrm{EM})}, \tag{1.110}$$

[2]We observe that $\omega_{\mathrm{T}}^{(\mathrm{EL})} < \omega_{\mathrm{T}}^{(\mathrm{EM})}$,because $\omega_{\mathrm{T}}^{(\mathrm{EL})}/\omega_{\mathrm{T}}^{(\mathrm{EM})} = v/c$ where the speed of light c and the speed of shear waves v are introduced in Eq. (1.20).

only elastic displacement waves can propagate in the stack. We call this range elastic frequency regime. For frequencies such that

$$\omega > \omega_{\mathrm{T}}^{(\mathrm{EM})}, \tag{1.111}$$

both elastic and electromagnetic waves can propagate in the stack. We will refer to this interval as the electromagnetic frequency regime. Table 1.1 shows several threshold frequencies

	$\omega_{\mathrm{T}}^{(\mathrm{EL})}[10^6$ rad/s]	$\omega_{\mathrm{T}}^{(\mathrm{EM})}[10^9$ rad/s]
PZT	2.58	11.10
$BaTiO_3$	43.30	250.91

Table 1.1 *Examples of threshold elastic (EL) and electromagnetic (EM) frequencies calculated at* $k_y = 1/\beta$ *and* $\beta = 1$ mm *for two different materials: Lead Zirconate Titanate (PZT) and Barium Titanate (* $BaTiO_3$ *).*

(see Eq. (1.109)) for different materials at $k_y = 1/\beta$. The smallest threshold elastic and electromagnetic frequency is the one associated with PZT. Therefore PZT will be chosen as an hosting material for layered finite stack (see chapter 2).

1.5.2 Dispersion equation for out-of-plane elastic waves in piezoelectric composite structures

Bloch-Floquet conditions enable a formulation of the propagation problem in a periodic medium in term of its unit cell only. With reference to Fig. (1.3)(b), consider the unit cell delimited by the vertical dashed lines $x = \pm\beta/2$. The two white layers on the left and the right sides of the unit cell are denoted by superscripts "(2)" and "(3)", respectively. The central grey layer is denoted by "(1)". The vector function (1.98) can be written in terms of the eigenmodes (1.103) as

$$\boldsymbol{\eta}^{(j)}(x) = \sum_{i=1,4} \lambda_i^{(j)} \boldsymbol{e}_i^{(j)}(x), \tag{1.112}$$

where $\boldsymbol{e}_i^{(j)}(x)$ denote the eigenmodes evaluates in the the aforementioned layers $j = \{1,2,3\}$, and $\lambda_i^{(j)}$ is the amplitude of the i^{th} eigenmode in the $(j)-$layer. The continuity conditions at the interfaces $x = \pm b/2$ are

$$\boldsymbol{\eta}^{(2)}(-b^-/2) = \boldsymbol{\eta}^{(1)}(-b^+/2) \quad \text{and} \quad \boldsymbol{\eta}^{(1)}(b^-/2) = \boldsymbol{\eta}^{(3)}(b^+/2), \tag{1.113}$$

and the Bloch-Floquet conditions impose

$$\boldsymbol{\eta}^{(2)}(x-\beta/2) = \boldsymbol{\eta}^{(3)}(x+\beta/2)e^{i\beta k_0}, \tag{1.114}$$

for every x in the unit cell. We introduce the notation

$$\mathscr{C}_i = c_{44}^{(i)}, \quad e_i = e_{15}^{(i)}, \quad \varepsilon_i = \varepsilon_{11}^{(i)} \quad G_i = \mathscr{C}_i + \frac{e_i^2}{\varepsilon_i}, \quad i = \{1,2\} \tag{1.115}$$

where $c_{44}^{(i)}$, $e_{15}^{(i)}$ and $\varepsilon_{11}^{(i)}$ are components of the stiffness, piezoelectric and dielectric tensors, respectively, for material $i = \{1,2\}$ in the $i-$th layer. We emphasise that the aforementioned physical quantities are sufficient to describe the out-of-plane problem of elasticity. The Eqs (1.113) and (1.114) are written explicitly in what follows.

Continuity conditions. The continuity condition at $x = -b/2$ in (1.113) is

$$\begin{aligned}
&-i\lambda_1^{(2)}\sqrt{\frac{\omega\varepsilon_2}{2q_2}}\begin{pmatrix} 0 \\ -q_2/(\varepsilon_2\omega) \\ e_2k_y/(\varepsilon_2\omega) \\ 1 \end{pmatrix} e^{iq_2b/2} + \lambda_2^{(2)}\sqrt{\frac{\omega\varepsilon_2}{2q_2}}\begin{pmatrix} 0 \\ q_2/(\varepsilon_2\omega) \\ e_2k_y/(\varepsilon_2\omega) \\ 1 \end{pmatrix} e^{-iq_2b/2} \\
&+i\lambda_3^{(2)}\sqrt{\frac{G_2r_2}{2\omega}}\begin{pmatrix} -\omega/(G_2r_2) \\ e_2k_y/(\varepsilon_2G_2r_2) \\ 1 \\ 0 \end{pmatrix} e^{ir_2b/2} + \lambda_4^{(2)}\sqrt{\frac{G_2r_2}{2\omega}}\begin{pmatrix} \omega/(G_2r_2) \\ -e_2k_y/(\varepsilon_2G_2r_2) \\ 1 \\ 0 \end{pmatrix} e^{-ir_2b/2} \\
&= -i\lambda_1^{(1)}\sqrt{\frac{\omega\varepsilon_1}{2q_1}}\begin{pmatrix} 0 \\ -q_1/(\varepsilon_1\omega) \\ e_1k_y/(\varepsilon_1\omega) \\ 1 \end{pmatrix} e^{iq_1b/2} + \lambda_2^{(2)}\sqrt{\frac{\omega\varepsilon_1}{2q_1}}\begin{pmatrix} 0 \\ q_1/(\varepsilon_1\omega) \\ e_1k_y/(\varepsilon_1\omega) \\ 1 \end{pmatrix} e^{-iq_1b/2} \\
&+i\lambda_3^{(1)}\sqrt{\frac{G_1r_1}{2\omega}}\begin{pmatrix} -\omega/(G_1r_1) \\ e_1k_y/(\varepsilon_1G_1r_1) \\ 1 \\ 0 \end{pmatrix} e^{ir_1b/2} + \lambda_4^{(1)}\sqrt{\frac{G_1r_1}{2\omega}}\begin{pmatrix} \omega/(G_1r_1) \\ -e_1k_y/(\varepsilon G_1r_1) \\ 1 \\ 0 \end{pmatrix} e^{-ir_1b/2}.
\end{aligned} \tag{1.116}$$

The continuity condition at the interface $x = b/2$ in (1.113) is

$$
\begin{aligned}
&-i\lambda_1^{(1)}\sqrt{\frac{\omega_1\varepsilon_1}{2q_1}}\begin{pmatrix}0\\ -q_1/(\varepsilon_1\omega)\\ e_1k_y/(\varepsilon_1\omega)\\ 1\end{pmatrix}e^{-iq_1b/2}+\lambda_2^{(1)}\sqrt{\frac{\omega\varepsilon_1}{2q_1}}\begin{pmatrix}0\\ q_1/(\varepsilon_1\omega)\\ e_1k_y/(\varepsilon_1\omega)\\ 1\end{pmatrix}e^{iq_1b/2}\\
&+i\lambda_3^{(1)}\sqrt{\frac{G_1r_1}{2\omega}}\begin{pmatrix}-\omega/(G_1r_1)\\ e_1k_y/(\varepsilon_1G_1r_1)\\ 1\\ 0\end{pmatrix}e^{-ir_1b/2}+\lambda_4^{(1)}\sqrt{\frac{G_1r_1}{2\omega}}\begin{pmatrix}\omega/(G_1r_1)\\ -e_1k_y/(\varepsilon_1G_1r_1)\\ 1\\ 0\end{pmatrix}e^{ir_1b/2}
\end{aligned}
$$

$$
\begin{aligned}
&=-i\lambda_1^{(3)}\sqrt{\frac{\omega\varepsilon_2}{2q_2}}\begin{pmatrix}0\\ -q_2/(\varepsilon\omega)\\ e_2k_y/(\varepsilon_2\omega)\\ 1\end{pmatrix}e^{-iq_2b/2}+\lambda_2^{(3)}\sqrt{\frac{\omega\varepsilon_2}{2q_2}}\begin{pmatrix}0\\ q_2/(\varepsilon\omega)\\ e_2k_y/(\varepsilon_2\omega)\\ 1\end{pmatrix}e^{iq_2b/2}\\
&+i\lambda_3^{(3)}\sqrt{\frac{G_2r_2}{2\omega}}\begin{pmatrix}-\omega/(G_2r_2)\\ e_2k_y/(\varepsilon_2G_2r_2)\\ 1\\ 0\end{pmatrix}e^{-ir_2b/2}+\lambda_4^{(3)}\sqrt{\frac{G_2r_2}{2\omega}}\begin{pmatrix}\omega/(G_2r_2)\\ -e_2k_y/(\varepsilon_2G_2r_2)\\ 1\\ 0\end{pmatrix}e^{ir_2b/2}. \qquad (1.117)
\end{aligned}
$$

Bloch-Floquet conditions. The Bloch-Floquet conditions (1.114) evaluated at $x = 0$ yields

$$
\begin{aligned}
&-i\lambda_1^{(2)}\sqrt{\frac{\omega\varepsilon_2}{2q_2}}\begin{pmatrix}0\\ -q_2/(\varepsilon_2\omega)\\ e_2k_y/(\varepsilon_2\omega)\\ 1\end{pmatrix}e^{iq_2\beta/2}+\lambda_2^{(2)}\sqrt{\frac{\omega\varepsilon_2}{2q_2}}\begin{pmatrix}0\\ q_2/(\varepsilon_2\omega)\\ e_2k_y/(\varepsilon_2\omega)\\ 1\end{pmatrix}e^{-iq_2\beta/2}\\
&+i\lambda_3^{(2)}\sqrt{\frac{G_2r_2}{2\omega}}\begin{pmatrix}-\omega/(G_2r_2)\\ e_2k_y/(\varepsilon_2G_2r_2)\\ 1\\ 0\end{pmatrix}e^{ir_2\beta/2}+\lambda_4^{(2)}\sqrt{\frac{G_2r_2}{2\omega}}\begin{pmatrix}\omega/(G_2r_2)\\ -e_2k_y/(\varepsilon_2G_2r_2)\\ 1\\ 0\end{pmatrix}e^{-ir_2\beta/2}=
\end{aligned}
$$

$$= -i\lambda_1^{(3)}\sqrt{\frac{\omega\varepsilon_2}{2q_2}}\begin{pmatrix}0\\ -q_2/(\varepsilon_2\omega)\\ e_2k_y/(\varepsilon_2\omega)\\ 1\end{pmatrix}e^{-iq_2\beta/2+ik_0\beta}+\lambda_2^{(3)}\sqrt{\frac{\omega\varepsilon_2}{2q_2}}\begin{pmatrix}0\\ q_2/(\varepsilon_2\omega)\\ e_2k_y/(\varepsilon_2\omega)\\ 1\end{pmatrix}e^{iq_2\beta/2+ik_0\beta}$$
$$+i\lambda_3^{(3)}\sqrt{\frac{G_2r_2}{2\omega}}\begin{pmatrix}-\omega/(G_2r_2)\\ e_2k_y/(\varepsilon_2G_2r_2)\\ 1\\ 0\end{pmatrix}e^{-ir_2b/2+ik_0\beta}+\lambda_4^{(3)}\sqrt{\frac{G_2r_2}{2\omega}}\begin{pmatrix}\omega/(G_2r_2)\\ -e_2k_y/(\varepsilon_2G_2r_2)\\ 1\\ 0\end{pmatrix}e^{ir_2\beta/2+ik_0\beta}. \tag{1.118}$$

Dispersion equation. The twelve equations (1.116) (1.117) and (1.118) for the twelve unknowns $\lambda_i^{(j)}$, $i=1,2,3,4$ and $j=1,2,3$, have non-trivial solutions if the determinant of the associated matrix is equal to zero. The result is [70]

$$\cos(\beta k_0) = -\frac{1}{4}\left(f(k_y,\omega)+\sqrt{f^2(k_y,\omega)-4g(k_y,\omega)+8}\right), \tag{1.119}$$

where we have introduced the functions

$$f(k_y,\omega) = -2\cos(bq_1)\cos(aq_2)-2\cos(br_1)\cos(ar_2)+Q\sin(bq_1)\sin(aq_2)$$
$$+k_y^2\left(\frac{R_1^2\sin(aq_2)sin(br_1)}{G_1q_2r_1}+\frac{R_2^2\sin(bq_1)\sin(ar_2)}{G_2q_1r_2}\right)+G\sin(br_1)\sin(ar_2), \tag{1.120}$$

and

$$\begin{aligned}g(k_y,\omega) &= 2+2\cos(br_1)\cos(ar_2)\,(2cos(bq_1)\cos(aq_2)-Q\sin(bq_1)\sin(aq_2))\\ &+2k_y^2[K_1\sin(bq_1)\sin(br_1)-K_1\sin(bq_1)\sin(br_1)\cos(aq_2)\cos(ar_2)\\ &+K_2\sin(aq_2)\sin(ar_2)-K_3\cos(bq_1)\cos(ar_2)\sin(aq_2)\sin(br_1)\\ &-K_4\cos(aq_2)\cos(br_1)\sin(bq_1)\sin(ar_2)-K_2^2\cos(bq_1)\cos(br_1)\sin(aq_2)\sin(ar_2)]\\ &-2G\cos(bq_1)\cos(aq_2)\sin(br_1)\sin(ar_2)+QG\sin(bq_1)\sin(aq_2)\sin(br_1)\sin(ar_2)\\ &+k_y^4K_1K_2\sin(bq_1)\sin(aq_2)\sin(br_1)\sin(ar_2),\end{aligned} \tag{1.121}$$

where we emphasise that the parameters q_i, and r_i, $i=\{1,2\}$, introduced in Eq. (1.102) are functions of k_y. In Eqs (1.120) and (1.121) we have introduced the following notations

$$G=\frac{G_1r_1}{G_2r_2}+\frac{G_2r_2}{G_1r_1},\ \ Q=\frac{q_2^2\varepsilon_1^2+q_1^2\varepsilon_2^2}{q_1q_2\varepsilon_1\varepsilon_2},\ \ R_1=\frac{e_2\varepsilon_1-e_1\varepsilon_2}{\varepsilon_1\sqrt{\varepsilon_2}},\ \ R_2=\frac{e_2\varepsilon_1-e_1\varepsilon_2}{\varepsilon_2\sqrt{\varepsilon_1}},$$
$$K_1=\frac{R_2^2}{G_1q_1r_1},\ \ K_2=\frac{R_1^2}{G_2q_2r_2},\ \ K_3=\frac{R_1^2}{G_1q_2r_1}\ \ K_4=\frac{R_2^2}{G_2q_1r_2},\quad a=\beta-b. \tag{1.122}$$

1.5.3 Dynamical coupling in periodic layered structures

We illustrate here an important effect arising from the dynamic coupling of the elastic in-plane fields and transverse electric field, as those encountered in Eqs. (1.21) and (1.25). The method used here follows the one presented in Ref. [105]. We study a layered structure as the one represented in Fig. 1.3 and assume for simplicity $b=\beta/2$. The periodicity arise here from the periodic modulation of the polarisation vector, pointing in the positive z direction in the white layers and in the negative z direction in the grey layers. The periodic polarisation can be written as

$$e_{13}(x)=e_{13}\sum_{m\neq 0} i\frac{1-\cos(m\pi)}{m\pi}e^{iG_mx},\ \text{with}\ \ G_m=\frac{\pi m}{b}. \tag{1.123}$$

By taking into account the x dependence of the piezoelectric coupling (1.123) into the constituitive relations (1.22), the first row in the Newton matrix equation (1.23) yields

$$c_{11}\frac{\partial^2}{\partial x^2}u_x(x,t)-\rho\frac{\partial^2}{\partial t^2}u_x(x,t)=\frac{\partial}{\partial x}\left(e_{13}(x)E_z(x,t)\right), \tag{1.124}$$

where we have assumed propagation along the $x-$axis ($\partial/\partial y(\cdot)=0$). The form of the Maxwell equation (1.25) remains the same, although the spatial dependence of the piezoelectric coupling (1.123) should be taken into account. By introducing the Fourier transform representation of the time-harmonic fields

$$u_x(x,t)=\int_{-\infty}^{+\infty}\mathrm{d}\bar{k}\ \tilde{u}_x(\bar{k})\ e^{i\bar{k}x-i\omega t}\ \ \text{and}\ \ E_z(x,t)=\int_{-\infty}^{+\infty}\mathrm{d}\bar{q}\ \tilde{E}_z(\bar{q})\ e^{i\bar{q}x-i\omega t}, \tag{1.125}$$

Eq. (1.25) becomes

$$\int_{-\infty}^{+\infty}\mathrm{d}\bar{q}(-\bar{q}^2+\mu\varepsilon_{33}\omega^2)e^{i\bar{q}x}\ \tilde{E}_z(\bar{q})=\omega^2\mu e_{13}\int_{-\infty}^{+\infty}\mathrm{d}\bar{k}\ \bar{k}\ \sum_{m\neq 0}\frac{1-\cos(m\pi)}{m\pi}e^{i(G_m+\bar{k})x}\tilde{u}_x(\bar{k}). \tag{1.126}$$

The Newton equation (1.124) becomes

$$\int_{-\infty}^{+\infty} \mathrm{d}\bar{k}\ \left(c_{11}\bar{k}^2-\rho\omega^2\right)\tilde{u}(\bar{k})e^{i\bar{k}x} = e_{13}\int_{-\infty}^{+\infty}\mathrm{d}\bar{q}\ \sum_{n\neq 0}(\bar{q}+G_n)\ \frac{1-\cos(n\pi)}{n\pi}e^{i(G_n+\bar{q})x}\tilde{E}_z(\bar{q}). \quad (1.127)$$

In order for Eqs (1.126) and (1.124) to become identities we require that

$$(-\bar{q}^2+\mu\varepsilon_{33}\omega^2)\tilde{E}_z(\bar{q}) = \omega^2\mu e_{13}\sum_{m\neq 0}\ \bar{k}\ \frac{1-\cos(m\pi)}{m\pi}\tilde{u}_x(\bar{k}), \quad \text{with} \quad \bar{q}=\bar{k}+G_m, \quad (1.128)$$

and

$$\left(c_{11}\bar{k}^2-\rho\omega^2\right)\tilde{u}(\bar{k}) = e_{13}\sum_{n\neq 0}(\bar{q}+G_n)\ \frac{1-\cos(n\pi)}{n\pi}\tilde{E}_z(\bar{q}), \quad \text{with} \quad \bar{k}=\bar{q}+G_n, \quad (1.129)$$

respectively. We observe that $\bar{q}\ll G_1$, which implies that $\bar{q}$ can be simplified when compared to G_m. The second implication is that the conditions in the previous two equations become $\bar{k}=-G_m$ and $\bar{k}=G_n$, respectively. Introducing the notation

$$C_m = \frac{1-\cos(m\pi)}{m\pi}, \ \text{ with } \ m\in\mathbb{Z}/\{0\}, \quad (1.130)$$

Eqs (1.128) and (1.129) become

$$(\mu\varepsilon_{33}\omega^2-\bar{q}^2)\ \tilde{E}_z(\bar{q}) = \omega^2\mu e_{13}\sum_{m\neq 0}\ \delta_{\bar{k},-G_m}\ \bar{k}\ C_m\tilde{u}_x(\bar{k}), \quad (1.131)$$

and

$$\left(c_{11}\bar{k}^2-\rho\omega^2\right)\tilde{u}(\bar{k}) = e_{13}\sum_{n\neq 0}\delta_{\bar{k},G_n}G_n\ C_n\tilde{E}_z(\bar{q}), \quad (1.132)$$

respectively, where C_m has been introduced in Eq. (1.130). Substituting the expression for $\tilde{u}(k)$ (1.132) into (1.131) we get

$$\begin{aligned}(-\bar{q}^2+\mu\varepsilon_{33}\omega^2) &= -\omega^2\mu e_{13}^2\sum_{m,n\neq 0}\ \delta_{\bar{k},-G_m}\ \delta_{\bar{k},G_n}\ \bar{k}\ G_nC_mC_n\frac{1}{-c_{11}\bar{k}^2+\rho\omega^2}\\ &= \frac{4^2\omega^2\mu e_{13}^2}{\beta^2}\frac{1}{-c_{11}G_m^2+\rho\omega^2}, \ \text{ with, } \ m=1,3,5... \end{aligned} \quad (1.133)$$

Eq. (1.133) can be recast into

$$\frac{\bar{q}^2}{\varepsilon_{33}\mu\omega^2} = 1 + \frac{16e_{13}^2}{\rho\varepsilon_{33}\beta^2}\frac{1}{c_{11}G_m/\rho - \omega^2}, \quad \text{with} \quad m = 1,3,5,\ldots \tag{1.134}$$

which is the result of Zhu *et al.* [105].

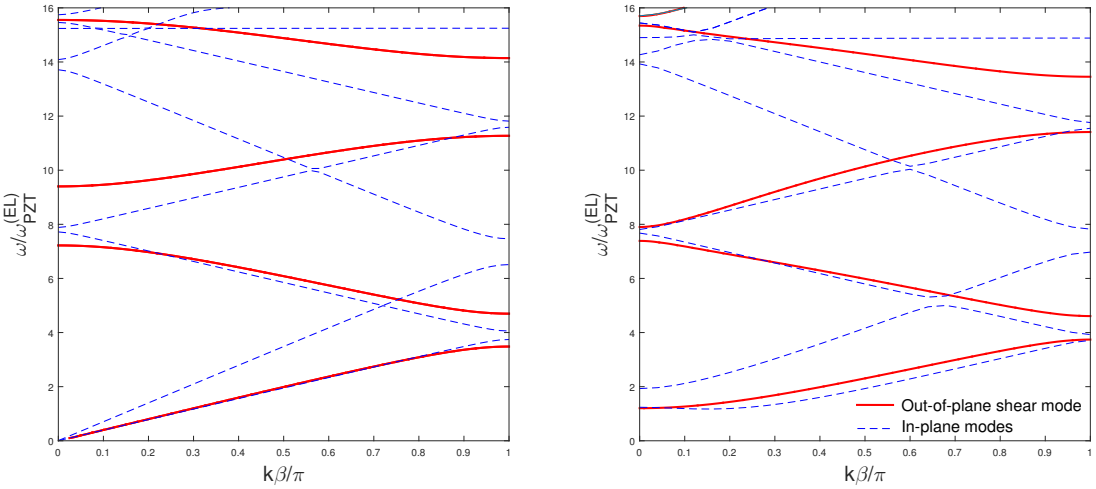

(a) (b)

Fig. 1.13 *In both panels the solid red lines correspond to eigenfrequencies for the out-of-plane shear displacement waves while the blue dashed lines represent the frequency for in-plane shear and pressure modes. The plane here considered is the xy plane of Fig. 1.3. With reference to the same picture, we fix the parameters to be* $\beta = 2$ mm, $b = 1/(3\beta)$. *Region (1) of the unit cell is occupied by PZT while regions (2) and (3) are occupied by the* $BaTiO_3$. *Panel (a) has been obtained at* $k_y = 0$ *while panel (b) has been obtained using* $k_y = 1/\beta$.

1.5.4 Dispersion of Bloch-Floquet waves in one-dimensional periodic piezoelectric structures

The dispersion equation (1.119) corresponds to out-of-plane elastic displacement in a piezoelectric layered structure. For illustrative purposes we here compare in-plane elastic wave propagation with those corresponding to out-of-plane waves (1.119). The comparison is provided in Fig. 1.13(a) and 1.13(b). The key assumption in dealing with the in-plane problem is

$$E_z(x,y) = 0, \tag{1.135}$$

which guarantees that elastic and electromagnetic partial differential equations are not dynamically coupled.

Panels (a) and (b) show dispersion diagrams for Bloch waves in a piezoelectric periodic structure with unit cell of length β and made of PZT and $BaTiO_3$. Panel (a) refers to normal incidence while panel (b) to oblique incidence ($k_y = 1/\beta$). The solid lines are the dispersion curves for out-of-plane Bloch-Floquet displacement waves while the dashed lines are the in-plane modes. In Fig. 1.13(b), we observe the formation of a zero frequency band gap.

	$c_{44}\,[10^{10}\mathrm{N/m^2}]$	$e_{15}\,[\mathrm{C/m^2}]$	$\varepsilon_{11}[10^{-11}\mathrm{F/m}]$	$\rho[10^3\mathrm{kg/m^3}]$
PZT	2.56	12.7	646	7.6
$BaTiO_3$	4.3	11.6	1.264	5.7

Table 1.2 *Piezoelectric materials:* Barium Titanate *(*$BaTiO_3$*) and* Lead-Zirconium Titanate *(PZT). We list from the left to the right the elastic constant, the piezoelectric constant, the dielectric permittivity constant and the mass density.*

1.6 Dynamic lattice Green's function

The Green's function is a useful tool for studying the dynamic response of continuous and discrete structures subject to an external excitation. For illustrative purposes, here we study the Green's function for a one dimensional biatomic lattice as the one depicted in Fig. 1.3(a). Time-harmonic wave propagation with angular frequency $\Omega = \omega^2$ yields

$$\begin{aligned} -\Omega m_1\, u_{1,n} &= C(u_{2,n} + u_{2,n-1} - 2u_{1,n}) + P_1\delta_{0,n}, \\ -\Omega m_2\, u_{2,n} &= C(u_{1,n+1} + u_{1,n} - 2u_{2,n}) + P_2\delta_{0,n}, \end{aligned} \tag{1.136}$$

where P_1 and P_2 are the moduli external forces whose directions are parallel to the biatomic chain in 1.3(a), and $\delta_{m,n}$, $m,n \in \mathbb{Z}$, is the Kroneker delta. We introduce the following discrete Fourier transform identities

$$u_{j,n} = \frac{1}{2\pi}\int_{-\pi}^{\pi} e^{in\eta}\tilde{u}_j(\eta)\,\mathrm{d}\eta \quad \text{and} \quad \delta_{0,n} = \frac{1}{2\pi}\int_{-\pi}^{\pi} e^{in\eta}\,\mathrm{d}\eta, \quad n\in\mathbb{Z} \quad \text{and} \quad j=\{1,2\}, \tag{1.137}$$

where $\delta_{0,n} = 1$ if $n = 0$ and zero otherwise. Upon the substitution of (1.137) into (1.136), and setting $C = 1$, for every wave number η we obtain

$$\begin{aligned} \tilde{u}_1 &= \frac{1}{Q(\eta,\omega)}\left[P_1(2-m_2\omega^2) + P_2(1+e^{-i\eta})\right], \\ \tilde{u}_2 &= \frac{1}{Q(\eta,\omega)}\left[P_2(2-m_1\omega^2) + P_1(1+e^{i\eta})\right]. \end{aligned} \tag{1.138}$$

The function $Q(\eta,\omega)$ in Eq. (1.138) is

$$Q(\eta,\Omega)=Q_0(\Omega)-2(1+\cos(\eta)),\ \text{and}\quad Q_0(\Omega)=(m_1\Omega-2)(m_2\Omega-2), \tag{1.139}$$

which coincides with the left-hand side of the dispersion equation (1.40). From Eqs (1.138), the discrete Fourier transform of the dynamic lattice Green's function $\hat{G}_{\rm F}(\Omega,\eta)$ for a biatomic chain can be expressed in the matrix form as

$$\begin{pmatrix}\tilde{u}_1\\ \tilde{u}_2\end{pmatrix}=\frac{1}{Q(\eta,\Omega)}\begin{pmatrix}2-m_2\Omega & 1+e^{-i\eta}\\ 1+e^{i\eta} & 2-m_1\Omega\end{pmatrix}\begin{pmatrix}P_1\\ P_2\end{pmatrix}, \tag{1.140}$$

Assuming $P_1=0$ and $P_2=1$ in Eqs (1.140), the Fourier transforms are

$$u_{1,n}=\frac{1}{2\pi}\int_{-\pi}^{\pi}\frac{1+e^{-i\eta}}{Q(\eta,\omega)}e^{in\eta}\mathrm{d}\eta,\quad\text{and}\quad u_{2,n}=\frac{2-m_2\Omega}{2\pi}\int_{-\pi}^{\pi}\frac{1}{Q(\eta,\omega)}e^{in\eta}\mathrm{d}\eta. \tag{1.141}$$

Localised vibration modes in the stop bands. We assume that $m_2>m_1$ and evaluate $u_{1,n}$ and $u_{2,n}$ in Eqs (1.141) at frequencies within the finite and infinite band-gaps, *i.e.* for $\Omega_-<\Omega<\Omega_+$ and $\Omega>\Omega_o$, respectively. The frequencies Ω_o, Ω_+ and Ω_- have been introduced in Eqs. (1.41) and (1.42). The expressions for the lattice displacements become

$$\begin{aligned}u_{1,n}&=-\frac{1}{2\pi}\int_{-\pi}^{\pi}\frac{1+e^{-i\eta}}{\cos(\eta)+1+(2-m_1\Omega)(m_2\Omega-2)/2}e^{in\eta}\mathrm{d}\eta,\quad\text{and,}\\ u_{2,n}&=-\frac{2-m_2\Omega}{2\pi}\int_{-\pi}^{\pi}\frac{1}{\cos(\eta)+1+(2-m_1\Omega)(m_2\Omega-2)/2}e^{in\eta}\mathrm{d}\eta.\end{aligned} \tag{1.142}$$

In the finite band gap where the Ω-dependent term in Eqs (1.142) is positive, the result of the integration is [62]

$$u_{1,n}=(-1)^n\frac{e^{-|n|z}-e^{-|n-1|z}}{\sinh z},\quad\text{and}\quad u_{2,n}=(-1)^n(2-m_2\Omega)\frac{e^{-|n|z}}{\sinh z}, \tag{1.143}$$

where $z\in\mathbb{R}$, and

$$\cosh z=1+(2-m_1\Omega)(m_2\Omega-2)/2>0.$$

Fig. 1.14 shows the displacements of the nodal points of a forced biatomic chain. The figure has been obtained evaluating Eqs (1.141). The horizontal axis shows the coordinates of the masses in the lattice with $m\in\mathbb{Z}$. The frequency has been chosen in such a way that $Q_0=-1/2$, and with $m_2=2m_1=2$. Fig. 1.14 illustrates exponentially localised vibrations

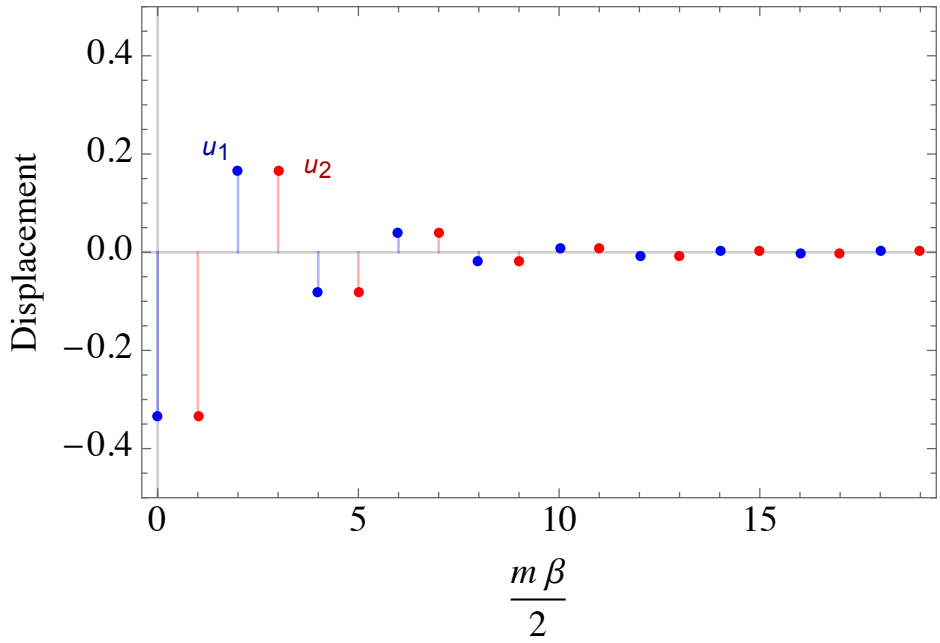

Fig. 1.14 *Localised vibrations of the nodal points of a forced biatomic chain with masses* $m_2 = 2$ *and* $m_1 = 1$ *and Eqs* (1.143)*. The frequency,* $\Omega = 1/m_2 + 1/m_1$*, is in the finite stop band.*

around the point where the load is applied. The specific choice of the frequency gives in-phase oscillations of the same amplitude for masses belonging to the same cell. Fig. 1.15

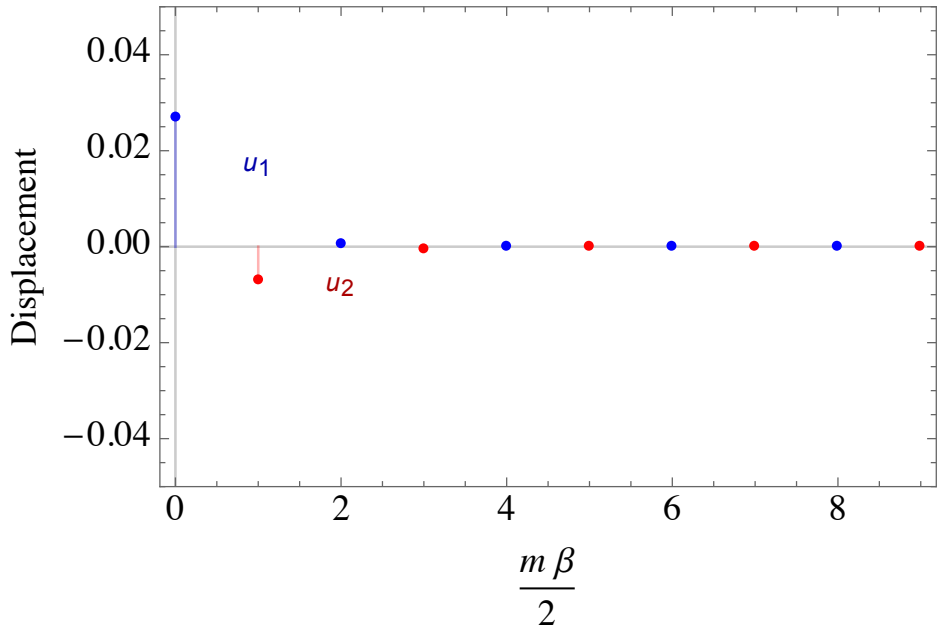

Fig. 1.15 *Localised vibrations of the nodal points of a biatomic chain with masses* $m_2 = 2m_1 = 2$ *and* $C = 1$ *for* $P_1 = 0$ *and* $P_2 = 1$*. The frequency,* $\Omega = 4(1/m_2 + 1/m_1)$*, is in the infinite stop band.*

illustrates localised vibrations around the point where the load is applied, at the frequency $\Omega = 4(1/m_1 + m_2)$, for which $Q_0 > 4$ (the frequency is in the infinite stop-band). At this frequency, the displacements of the masses in the same cell are out-of-phase.

Chapter 2

Scattering from layered piezoelectric finite stacks

In this chapter we study the reflection and transmission problem for a finite stack of piezoelectric layers. We model the stack as a finite repetition of the unit cell represented in Fig. 1.3, here denoted as "building block". The displacement field is assumed to be out-of-plane and thus the governing equations presented in section 1.1.1 apply. The total number of building blocks is denoted by $\mathscr{N}$.

The interest in studying the problem stated above is twofold. First of all, when $\mathscr{N}$ is sufficiently large, the reflection spectrum encapsulates some features of the well known periodic problem [70], already discussed in section 1.5.2. In fact, total reflection regions should match the stop bands for Bloch-Floquet waves. The second and most important source of interest comes from the fact that a finite stack exhibits interesting phenomena such as resonances for transmitted elastic and/or electromagnetic waves. The problem is made more intriguing because of the piezoelectric effect, as a mechanism to "convert" elastic energy into electromagnetic energy and vice versa. In this chapter, the transmitted energy flux is decomposed into an elastic and and electromagnetic contribution, already identified in section 1.5.1, Eq. (1.104).

2.1 Scattering from a single piezoelectric layer

Single interface. Before studying the scattering properties of the stack, we focus on the reflection and transmission by a planar interface $x = x_1$ separating two semi-infinite piezoelectric materials [25]. The materials on the left and on the right of the interface are denoted by (2) and (1), respectively. The materials are assumed to be perfectly matched at the

interface. The continuity of fields at the interface can be written in terms of the eigenmodes given in Eq. (1.103). We denote the eigenmodes in Eq. (1.103) by $\mathbf{e}_j^{(n)}(x) = \mathbf{e}_j^{(n)}\exp(+is_j x)$, with $j = \{1,2,3,4\}$ the index of the corresponding eigenvalues s_j in Eq. (1.101) and $n = \{1,2\}$ the material indices. The scattering problem for shear elastic waves incident from the left admits solution

$$\begin{aligned}
\boldsymbol{\eta}_{\mathrm{A}}^{(2),\ell}(x) &= \mathbf{e}_4^{(2)}e^{+ir_2x} + R_{\mathrm{EA}}^{(\ell)}\mathbf{e}_1^{(2)}e^{-iq_2x} + R_{\mathrm{AA}}^{(\ell)}\mathbf{e}_3^{(2)}e^{-ir_2x}, \ \text{for } x < x_1, \\
\boldsymbol{\eta}_{\mathrm{A}}^{(1),\ell}(x) &= T_{\mathrm{EA}}^{(\ell)}\mathbf{e}_2^{(1)}e^{+iq_1x} + T_{\mathrm{AA}}^{(\ell)}\mathbf{e}_4^{(1)}e^{+ir_1x}, \ \text{for } x > x_1.
\end{aligned} \tag{2.1}$$

The scattering problem for transverse magnetic waves incident from the left has solution

$$\begin{aligned}
\boldsymbol{\eta}_{\mathrm{E}}^{(2),\ell}(x) &= \mathbf{e}_2^{(2)}e^{+iq_2x} + R_{\mathrm{AE}}^{(\ell)}\mathbf{e}_3^{(2)}e^{-ir_2x} + R_{\mathrm{EE}}^{(\ell)}\mathbf{e}_1^{(2)}e^{-iq_2x}, \ \text{for } \mathrm{x} < \mathrm{x}_1, \\
\boldsymbol{\eta}_{\mathrm{E}}^{(1),\ell}(x) &= T_{\mathrm{AE}}^{(\ell)}\mathbf{e}_4^{(1)}e^{+ir_1x} + T_{\mathrm{EE}}^{(\ell)}\mathbf{e}_2^{(1)}e^{+iq_1x}, \ \text{for } x > x_1.
\end{aligned} \tag{2.2}$$

As already discussed in section 1.5.1, Eqs (2.1) and (2.2) are continuous at the interfaces $x = x_1$, *i.e.*

$$\boldsymbol{\eta}_{\mathrm{A}}^{(2),\ell}(x)\Big|_{x=x_1^-} = \boldsymbol{\eta}_{\mathrm{A}}^{(1),\ell}(x)\Big|_{x=x_1^+} \text{ and } \boldsymbol{\eta}_{\mathrm{E}}^{(2),\ell}(x)\Big|_{x=x_1^-} = \boldsymbol{\eta}_{\mathrm{E}}^{(1),\ell}(x)\Big|_{x=x_1^+}. \tag{2.3}$$

Equations (2.3) yield

$$\begin{aligned}
\mathbf{e}_4^{(2)}e^{+ir_2x_1} + R_{\mathrm{EA}}^{(\ell)}\mathbf{e}_1^{(2)}e^{-iq_2x_1} + R_{\mathrm{AA}}^{(\ell)}\mathbf{e}_3^{(2)}e^{-ir_2x_1} &= T_{\mathrm{EA}}^{(\ell)}\mathbf{e}_2^{(1)}e^{+iq_1x_1} + T_{\mathrm{AA}}^{(\ell)}\mathbf{e}_4^{(1)}e^{+ir_1x_1}, \\
\mathbf{e}_2^{(2)}e^{+iq_2x_1} + R_{\mathrm{AE}}^{(\ell)}\mathbf{e}_3^{(2)}e^{-ir_2x_1} + R_{\mathrm{EE}}^{(\ell)}\mathbf{e}_1^{(2)}e^{-iq_2x_1} &= T_{\mathrm{AE}}^{(\ell)}\mathbf{e}_4^{(1)}e^{+ir_1x_1} + T_{\mathrm{EE}}^{(\ell)}\mathbf{e}_2^{(1)}e^{+iq_1x_1}.
\end{aligned} \tag{2.4}$$

Similarly, for waves incident from the right, we obtain

$$\begin{aligned}
T_{\mathrm{EA}}^{(r)}\mathbf{e}_1^{(2)}e^{-iq_2x_1} + T_{\mathrm{AA}}^{(r)}\mathbf{e}_3^{(2)}e^{-ir_2x_1} &= R_{\mathrm{EA}}^{(r)}\mathbf{e}_2^{(1)}e^{+iq_1x_1} + R_{\mathrm{AA}}^{(r)}\mathbf{e}_4^{(1)}e^{+ir_1x_1} + \mathbf{e}_3^{(1)}e^{-ir_1x_1}, \\
T_{\mathrm{AE}}^{(r)}\mathbf{e}_3^{(2)}e^{-ir_2x_1} + T_{\mathrm{EE}}^{(r)}\mathbf{e}_1^{(2)}e^{-iq_2x_1} &= R_{\mathrm{EE}}^{(r)}\mathbf{e}_2^{(1)}e^{+iq_1x_1} + R_{\mathrm{AE}}^{(r)}\mathbf{e}_4^{(1)}e^{+ir_1x_1} + \mathbf{e}_1^{(1)}e^{-iq_1x_1}.
\end{aligned} \tag{2.5}$$

Solving the systems associated with Eqs (2.4) and (2.5) gives, respectively

$$\hat{R}_\ell = \begin{pmatrix} R_{\mathrm{AA}}^{(\ell)} & R_{\mathrm{AE}}^{(\ell)} \\ \\ R_{\mathrm{EA}}^{(\ell)} & R_{\mathrm{EE}}^{(\ell)} \end{pmatrix}, \ \hat{T}_\ell = \begin{pmatrix} T_{\mathrm{AA}}^{(\ell)} & T_{\mathrm{AE}}^{(\ell)} \\ \\ T_{\mathrm{EA}}^{(\ell)} & T_{\mathrm{EE}}^{(\ell)} \end{pmatrix}, \tag{2.6}$$

and

$$\hat{R}_r = \begin{pmatrix} R_{\mathrm{AA}}^{(r)} & R_{\mathrm{AE}}^{(r)} \\ \\ R_{\mathrm{EA}}^{(r)} & R_{\mathrm{EE}}^{(r)} \end{pmatrix}, \quad \hat{T}_r = \begin{pmatrix} T_{\mathrm{AA}}^{(r)} & T_{\mathrm{AE}}^{(r)} \\ \\ T_{\mathrm{EA}}^{(r)} & T_{\mathrm{EE}}^{(r)} \end{pmatrix}, \tag{2.7}$$

which are the reflection and transmission matrices. The reflection and transmission matrices act on the two-dimensional subspace generated by the "acoustic" (A) and "electromagnetic" (E) eigenmodes which are incident from the left (ℓ) or from the right (r). The explicit expressions of the entries of the reflection matrix in (2.6) are

$$\begin{aligned}
R_{\mathrm{AA}}^{(\ell)} &= -\frac{ie^{2ir_2x_1}}{\mathscr{D}}\left[p^2\left(\frac{e_1}{\varepsilon_1}-\frac{e_2}{\varepsilon_2}\right)^2+(G_1r_1-G_2r_2)\left(\frac{q_1}{\varepsilon_1}+\frac{q_2}{\varepsilon_2}\right)\right], \\
R_{\mathrm{AE}}^{(\ell)} &= -\frac{2i}{\mathscr{D}}e^{+i(q_2+r_2)x_1}p\sqrt{G_2r_2}\sqrt{\frac{q_2}{\varepsilon_2}}\left(\frac{e_1}{\varepsilon_1}-\frac{e_2}{\varepsilon_2}\right), \\
R_{\mathrm{EE}}^{(\ell)} &= -\frac{ie^{2iq_2x_1}}{\mathscr{D}}\left[p^2\left(\frac{e_1}{\varepsilon_1}-\frac{e_2}{\varepsilon_2}\right)^2+(G_1r_1+G_2r_2)\left(\frac{q_1}{\varepsilon_1}-\frac{q_2}{\varepsilon_2}\right)\right], \\
R_{\mathrm{EA}}^{(\ell)} &= \frac{2i}{\mathscr{D}}e^{+i(q_2+r_2)x_1}p\sqrt{G_2r_2}\sqrt{\frac{q_2}{\varepsilon_2}}\left(\frac{e_1}{\varepsilon_1}-\frac{e_2}{\varepsilon_2}\right),
\end{aligned} \tag{2.8}$$

and the entries of the transmission matrix (2.6)

$$\begin{aligned}
T_{\mathrm{AA}}^{(\ell)} &= \frac{2}{\mathscr{D}}e^{-i(r_1-r_2)x_1}\sqrt{G_1r_1}\sqrt{G_2r_2}\left(\frac{q_1}{\varepsilon_1}+\frac{q_2}{\varepsilon_2}\right), \\
T_{\mathrm{AE}}^{(\ell)} &= -\frac{2}{\mathscr{D}}e^{+i(q_2-r_1)x_1}p\sqrt{G_1r_1}\sqrt{\frac{q_2}{\varepsilon_2}}\left(\frac{e_1}{\varepsilon_1}-\frac{e_2}{\varepsilon_2}\right), \\
T_{\mathrm{EE}}^{(\ell)} &= \frac{2}{\mathscr{D}}e^{-i(q_1-q_2)x_1}(G_1r_1+G_2r_2)\sqrt{\frac{q_1}{\varepsilon_1}}\sqrt{\frac{q_2}{\varepsilon_2}}, \\
T_{\mathrm{EA}}^{(\ell)} &= \frac{2}{\mathscr{D}}e^{-i(q_1-r_2)x_1}p\sqrt{G_2r_2}\sqrt{\frac{q_1}{\varepsilon_1}}\left(\frac{e_1}{\varepsilon_1}-\frac{e_2}{\varepsilon_2}\right),
\end{aligned} \tag{2.9}$$

where we have introduced the following notation

$$\mathscr{D} = p^2\left(\frac{e_1}{\varepsilon_1}-\frac{e_2}{\varepsilon_2}\right)^2+(G_1r_1+G_2r_2)\left(\frac{q_1}{\varepsilon_1}+\frac{q_2}{\varepsilon_2}\right). \tag{2.10}$$

The explicit expressions of the entries of the matrices $\hat{R}_r$ and $\hat{T}_r$ are

$$\begin{aligned}
R_{\mathrm{AA}}^{(r)} &= \frac{ie^{-2ir_1x_1}}{\mathscr{D}}\left[p^2\left(\frac{e_1}{\varepsilon_1}-\frac{e_2}{\varepsilon_2}\right)^2-(G_1r_1-G_2r_2)\left(\frac{q_1}{\varepsilon_1}+\frac{q_2}{\varepsilon_2}\right)\right],\\
R_{\mathrm{AE}}^{(r)} &= -\frac{2i}{\mathscr{D}}e^{-i(q_1+r_1)x_1}p\sqrt{G_1r_1}\sqrt{\frac{q_1}{\varepsilon_1}}\left(\frac{e_1}{\varepsilon_1}-\frac{e_2}{\varepsilon_2}\right),\\
R_{\mathrm{EE}}^{(r)} &= \frac{ie^{-2iq_1x_1}}{\mathscr{D}}\left[p^2\left(\frac{e_1}{\varepsilon_1}-\frac{e_2}{\varepsilon_2}\right)^2-(G_1r_1+G_2r_2)\left(\frac{q_1}{\varepsilon_1}-\frac{q_2}{\varepsilon_2}\right)\right],\\
R_{\mathrm{EA}}^{(r)} &= \frac{2i}{\mathscr{D}}e^{-i(q_1+r_1)x_1}p\sqrt{G_1r_1}\sqrt{\frac{q_1}{\varepsilon_1}}\left(\frac{e_1}{\varepsilon_1}-\frac{e_2}{\varepsilon_2}\right),
\end{aligned} \tag{2.11}$$

and

$$\begin{aligned}
T_{\mathrm{AA}}^{(r)} &= \frac{2}{\mathscr{D}}e^{-i(r_1-r_2)x_1}\sqrt{G_1r_1}\sqrt{G_2r_2}\left(\frac{q_1}{\varepsilon_1}+\frac{q_2}{\varepsilon_2}\right),\\
T_{\mathrm{AE}}^{(r)} &= -\frac{2}{\mathscr{D}}e^{-i(q_1-r_2)x_1}p\sqrt{G_2r_2}\sqrt{\frac{q_1}{\varepsilon_1}}\left(\frac{e_1}{\varepsilon_1}-\frac{e_2}{\varepsilon_2}\right),\\
T_{\mathrm{EE}}^{(r)} &= \frac{2}{\mathscr{D}}e^{-i(q_1-q_2)x_1}(G_1r_1+G_2r_2)\sqrt{\frac{q_1}{\varepsilon_1}}\sqrt{\frac{q_2}{\varepsilon_2}},\\
T_{\mathrm{EA}}^{(r)} &= \frac{2}{\mathscr{D}}e^{+i(q_2-r_1)x_1}p\sqrt{G_1r_1}\sqrt{\frac{q_2}{\varepsilon_2}}\left(\frac{e_1}{\varepsilon_1}-\frac{e_2}{\varepsilon_2}\right).
\end{aligned} \tag{2.12}$$

Single layer. Here we focus on the calculation of the scattering matrices for a single layer of piezoelectric material (1) immersed in material (2). We assume that the interfaces delimiting the layer are located at $x=x_1$ and $x=x_2$, with $b=x_2-x_1>0$. In order to distinguish the two sets of scattering matrices at the two interfaces, the reflection and transmission matrix evaluated at $x=x_2$ are denoted by $\hat{R}_r'$, $\hat{T}_r'$, $\hat{R}_\ell'$, $\hat{R}_\ell'$. The reflection and transmission matrices for a single layer can be evaluated by summing up the contributions coming from the multiple scattering between the interfaces at $x=x_1$ and $x=x_2$. Formally, for waves incident from the left the multiple scattering gives

$$\hat{\mathscr{R}}_1^{(\ell)}=\hat{R}_\ell+\hat{T}_r\hat{R}_\ell'\hat{T}_\ell+\hat{T}_r\hat{R}_\ell'\hat{R}_r\hat{R}_\ell'\hat{T}_\ell+\cdots=\hat{R}_\ell+\hat{T}_r\left(\hat{I}-\hat{R}_\ell'\hat{R}_r\right)^{-1}\hat{R}_\ell'\hat{T}_\ell\ , \tag{2.13}$$

$$\hat{\mathscr{T}}_1^{(\ell)}=\hat{T}_\ell'\hat{T}_\ell+\hat{T}_\ell'\hat{R}_r\hat{R}_\ell'\hat{T}_\ell+\hat{T}_\ell'\hat{R}_r\hat{R}_\ell'\hat{R}_r\hat{R}_\ell'\hat{T}_\ell+\cdots=\hat{T}_\ell'\left(\hat{I}-\hat{R}_r\hat{R}_\ell'\right)^{-1}\hat{T}_\ell\ . \tag{2.14}$$

Similarly, the scattering matrices for waves incident from the right are

$$\hat{\mathscr{R}}_1^{(r)}=\hat{R}_r'+\hat{T}_\ell'\left(\hat{I}-\hat{R}_r\hat{R}_\ell'\right)^{-1}\hat{R}_r\hat{T}_r'\ , \tag{2.15}$$

$$\hat{\mathscr{T}}_1^{(r)}=\hat{T}_r\left(\hat{I}-\hat{R}_\ell'\hat{R}_r\right)^{-1}\hat{T}_\ell'\ . \tag{2.16}$$

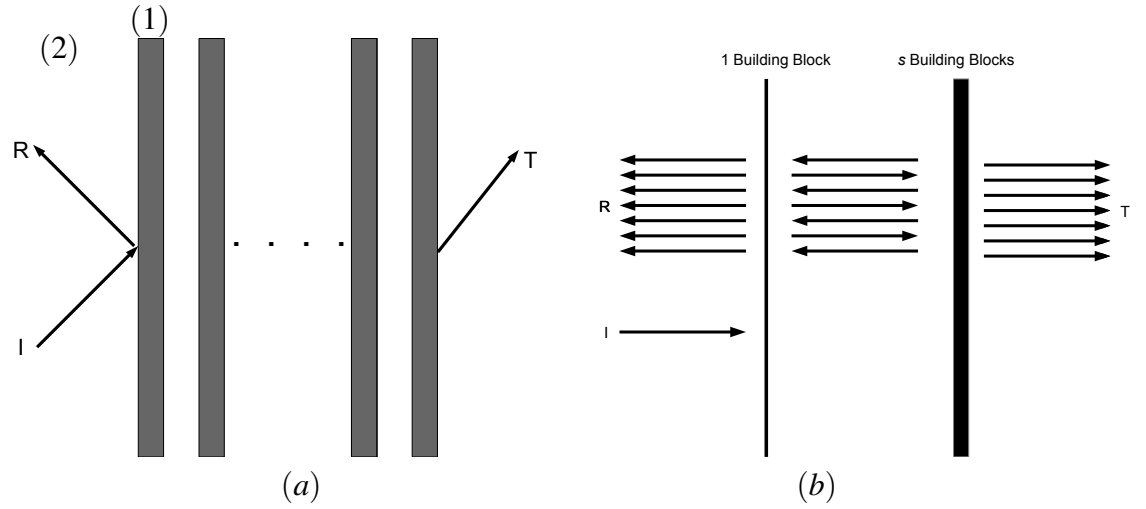

Fig. 2.1 *Panel (a) shows a finite stack of piezoelectric layers comprising material (1) (black areas of width b) hosted by a material (2) (white area). Both the materials are out-of-plane polarised 6mm piezoelectrics. Incident (I), reflected (R) and transmitted (T) waves are indicated. The black layers of width b and spaced at a distance β, are infinite in the vertical direction. In panel (b) is schematically shown the multiple scattering method which is at the basis of the recurrence procedure approach.*

2.2 Scattering from a finite number of piezoelectric layers

The reflection and transmission matrices associated with an arbitrary and finite number of building blocks, as the one depicted in Fig. 2.1(a), can be calculated using the multiple scattering method. A similar method was used, among others, by Botten *et al.* [9] for electromagnetic gratings and by Platts *et al.* [73] for elastic gratings. The thick vertical line on the right hand side of Fig. 2.1(b), schematically denotes s piezoelectric bi-layers made of material (1), immersed in a hosting piezoelectric (2). The associated reflection and transmission matrices for waves incident from the left will be denoted by $\hat{\mathscr{R}}_s^{(\ell)}$ and $\hat{\mathscr{T}}_s^{(\ell)}$. The thin vertical line represents a single layer added to the left of the stack. The associated scattering matrices are given in Eqs (2.6) and (2.7). Similarly to what we have done for the single layer in section 2.1, the scattering matrices associated with a stack comprising $(s+1)$-layers are

$$\hat{\mathscr{R}}_{s+1}^{(\ell)} = \hat{\mathscr{R}}_1^{(\ell)} + \hat{\mathscr{T}}_1^{(r)} \left(\hat{I}_2 - \hat{\mathscr{P}} \hat{\mathscr{R}}_s^{(\ell)} \hat{\mathscr{P}} \hat{\mathscr{R}}_1^{(r)} \right)^{-1} \hat{\mathscr{P}} \hat{\mathscr{R}}_s^{(\ell)} \hat{\mathscr{P}} \hat{\mathscr{T}}_1^{(\ell)}, \tag{2.17}$$

$$\hat{\mathscr{T}}_{s+1}^{(\ell)} = \hat{\mathscr{P}}\,\hat{\mathscr{T}}_{s}^{(\ell)}\,\hat{\mathscr{P}}\left(\hat{I}_2 - \hat{\mathscr{R}}_1^{(r)}\,\hat{\mathscr{P}}\,\hat{\mathscr{R}}_s^{(\ell)}\,\hat{\mathscr{P}}\right)^{-1}\hat{\mathscr{T}}_1^{(\ell)}, \tag{2.18}$$

with

$$\hat{\mathscr{P}} = \begin{pmatrix} e^{+ir_2\beta} & 0 \\ 0 & e^{+iq_2\beta} \end{pmatrix}. \tag{2.19}$$

The recurrence matrix relations (2.17) and (2.18) define the reflection and transmission matrices for $(s+1)$ layers, assuming that the s-stack matrices are known. We observe that the recurrence matrices $\hat{\mathscr{R}}_s^{(\ell)}$ and $\hat{\mathscr{T}}_s^{(\ell)}$ have a phase-shift origin at $x = x_1$. Before being used in the expression for the $(s+1)$-stack matrices in the next step of the recurrence relation, the phase origin must be shifted to $x = x_1 + \beta$. This is taken into account by the *propagation matrix* $\hat{\mathscr{P}}$ in Eq. (2.19) which appears in Eqs (2.17) and (2.18).

2.2.1 Transmittance and reflectance in the elastic frequency regime

In the elastic frequency regime, that is in the frequency range in Eq. (1.110), electromagnetic waves cannot propagate. This can be formally seen by looking at the conservation of the energy flux through the piezoelectric stack, as done below. Assuming an elastic incident wave from the left and using Eq. (1.112) the physical fields on the left and on the right of the stack can be written respectively as

$$\begin{aligned} \eta^{(\ell)}(x) &= \left[\hat{\mathscr{R}}_{\mathscr{N}}^{(\ell)}\right]_{\mathrm{EA}} \mathbf{e}_1^{(2)}\, e^{-iq_2x} + \left[\hat{\mathscr{R}}_{\mathscr{N}}^{(\ell)}\right]_{\mathrm{AA}} \mathbf{e}_3^{(2)} e^{-ir_2x} + \mathbf{e}_4^{(2)}\, e^{+ir_2x}, \;\; x < x_1, \\ \eta^{(r)}(x) &= \left[\hat{\mathscr{T}}_{\mathscr{N}}^{(\ell)}\right]_{\mathrm{EA}} \mathbf{e}_2^{(2)} e^{+iq_2x} + \left[\hat{\mathscr{T}}_{\mathscr{N}}^{(\ell)}\right]_{\mathrm{AA}} \mathbf{e}_4^{(2)} e^{+ir_2x}, \;\; \text{for } x > x_1 + (\mathscr{N}-1)\beta + b, \end{aligned} \tag{2.20}$$

where $\hat{\mathscr{R}}_{\mathscr{N}}^{(\ell)}$ and $\hat{\mathscr{T}}_{\mathscr{N}}^{(\ell)}$ are 2×2 reflection and transmission matrices constructed in Eqs (2.17) and (2.18). The energy flux in Eq. (1.104) can be evaluated using the physical fields in Eqs (2.20). From the conservation of the energy flux through the structure it follows that

$$\frac{1}{4}\boldsymbol{\eta}^{(\ell)}(x)^{\dagger}\,\hat{\mathscr{E}}\,\boldsymbol{\eta}^{(\ell)}(x) = \mathscr{F}_i - \mathscr{F}_r = \mathscr{F}_t = \frac{1}{4}\boldsymbol{\eta}^{(r)}(x)^{\dagger}\,\hat{\mathscr{E}}\,\boldsymbol{\eta}^{(r)}(x) \;\;\Rightarrow\;\; \mathscr{F}_r + \mathscr{F}_t = \mathscr{F}_i, \tag{2.21}$$

where

$$\mathscr{F}_i = 1, \quad \mathscr{F}_r = \left|\left[\hat{\mathscr{R}}_{\mathscr{N}}^{(\ell)}\right]_{\mathrm{AA}}\right|^2 \quad \text{and} \quad \mathscr{F}_t = \left|\left[\hat{\mathscr{T}}_{\mathscr{N}}^{(\ell)}\right]_{\mathrm{AA}}\right|^2. \tag{2.22}$$

We obtained Eqs (2.21) and (2.22) using the identities (1.106) , (1.107) and (1.108). The second and third relation in Eq. (2.22) represent the reflectance and transmittance of the piezoelectric stack in the elastic frequency regime.

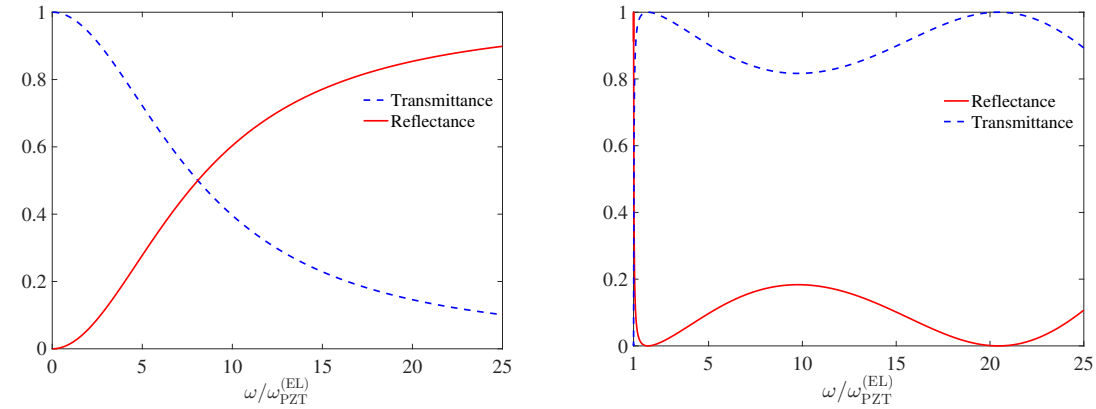

Fig. 2.2 *Transmittance (blue dashed line) and reflectance (red solid line) for a single* $BaTiO_3$ *slab in a PZT environment in the elastic frequency regime (see Eqs* (2.22)*). The width of the layer is* $b = 0.33$ mm*. Panel (a) has been obtained at* $k_y = 0$ *while panel (b) at* $k_y = 1/\beta$*. Note that in panel (b), the horizontal axis restricts to* $\omega/\omega_{\rm PZT}^{\rm (EL)} > 1$ *to avoid the non-physical region of frequencies.*

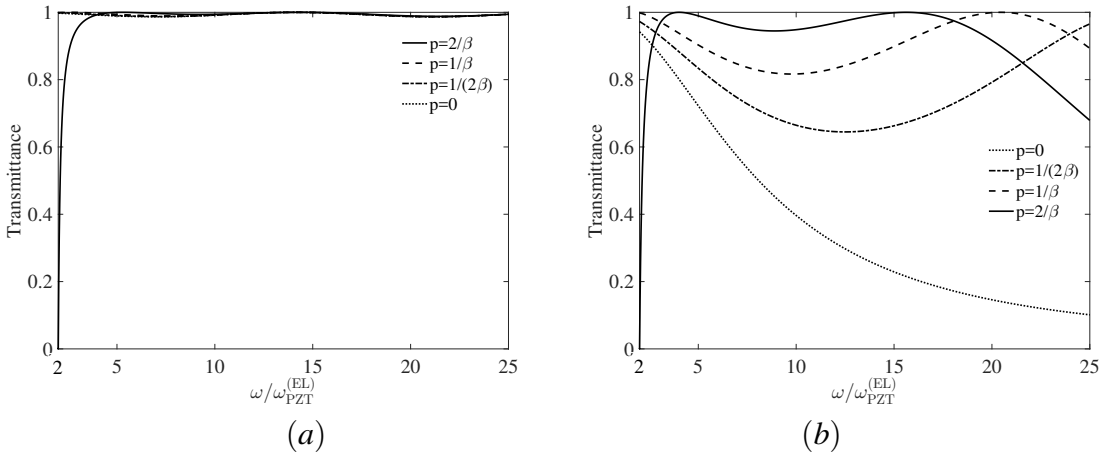

Fig. 2.3 *Both panels are transmittance calculations for elastic waves through a* $BaTiO_3$ *slab surrounded by PZT. The width of the layer is* $b = 0.33$ mm*. Panel (a) shows transmittance curves for several values of* $p = k_y$*, when the piezoelectric effect is ignored (*i.e. *when the piezoelectric couplings* e_{15} *in Table 1.2 are set to zero). Panel (b) shows transmittance curves for several values of* k_y*, when the piezoelectric effect is taken into account.*

Single layer. In Fig. 2.2 we plot the reflectance and transmittance ($\mathscr{F}_r$ and $\mathscr{F}_t$ in Eq. (2.22)), respectively) for a single layer ($\mathscr{N} = 1$). The results are obtained using reflection and transmission matrices (2.13) and (2.14), respectively. We fix the geometrical parameters of the slab to be $\beta = 1$ mm and $b = (2/3)\beta$. Material (1) in Fig. 2.1(a) is filled with $BaTiO_3$ while the hosting material is PZT (see Table 1.2). Panel (b) clearly shows that an elastic threshold frequency is positive at $k_y \neq 0$ while is zero at $k_y = 0$ (Panel (a)). This is consistent

with Eq. (1.109).

In Fig. 2.3 we show transmittance results obtained using Eq. (2.22) for several k_y (the transverse component of the incident wave vector)through a single layer. The physical parameters are the same used in Fig. 2.2. Panel (a) has been obtained ignoring piezoelectric effect, *i.e.* setting the piezoelectric coupling equal to zero. In Panel (b) the piezoelectric coupling is restored. The wide range of p investigated gives a better insight of the transmission properties of the piezoelectric slab. The effect of different angles of incidence is minute when the piezoelectric effect is ignored but is when the piezoelectric effect is restored.

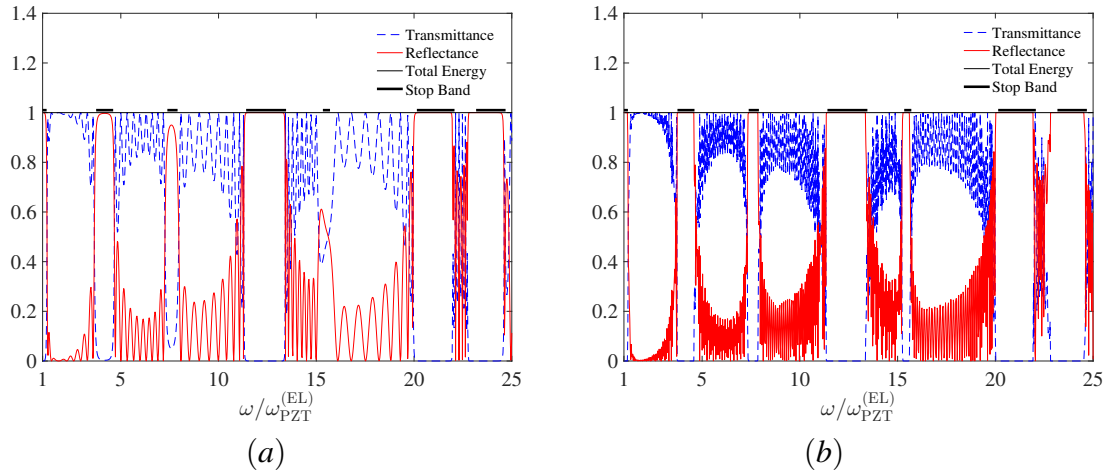

Fig. 2.4 *Reflectance (red solid lines) and transmittance (blue dotted lines) obtained by the recurrence procedures derived in Eqs (2.17) and (2.18). The building block has the same parameters as those used in Fig. 2.2. The thin black line confirms the conservation of energy according to Eq. (2.21). The thick black segments represent stop bands for the infinite structure, whose unit cell coincides with current building block. Panel (a) refers to* $\mathscr{N} = 10$ *and panel (b)* $\mathscr{N} = 50$.

Multiple layers. Fig. 2.4 shows the transmittance (blue dashed lines) and reflectance (solid red line) in the elastic frequency regime from a stack of piezoelectric layers. The results are obtained evaluating Eqs (2.22). The parameters are the same as the one used in Fig. 2.2. Panels (a) and (b) refer to $\mathscr{N} = 10$ and $\mathscr{N} = 50$, respectively. The thin black horizontal lines confirm the conservation of energy. The thick black horizontal lines denote band gap frequency regions of the corresponding periodic structure (see Fig. (1.3)(b)) whose unit cell is assumed to be the building block of the stack. The band gap frequency width has been obtained by solving Eq. (1.119). Forbidden regions for wave propagation correspond to total reflection regions (reflectance close to 1). In fact, even the result for $\mathscr{N} = 10$ shows high reflectance.

2.2.2 Transmittance and reflectance in the electromagnetic frequency regime

In the electromagnetic frequency regime (1.111), both elastic and electromagnetic waves propagate. For elastic incident waves, the physical fields reflected and transmitted by the stack can be written as in Eq. (2.20). However, since now the electromagnetic waves propagate the conservation of energy imposes

$$\mathscr{F}_i^{(\mathrm{A})} = 1, \quad \mathscr{F}_r^{(\mathrm{A})} = \left|\left[\hat{\mathscr{R}}_{\mathscr{N}}^{(\ell)}\right]_{\mathrm{AA}}\right|^2 + \left|\left[\hat{\mathscr{R}}_{\mathscr{N}}^{(\ell)}\right]_{\mathrm{EA}}\right|^2, \quad \mathscr{F}_t^{(\mathrm{A})} = \left|\left[\hat{\mathscr{T}}_{\mathscr{N}}^{(\ell)}\right]_{\mathrm{AA}}\right|^2 + \left|\left[\hat{\mathscr{T}}_{\mathscr{N}}^{(\ell)}\right]_{\mathrm{EA}}\right|^2, \tag{2.23}$$

and

$$\mathscr{F}_r^{(\mathrm{A})} + \mathscr{F}_t^{(\mathrm{A})} = 1. \tag{2.24}$$

Similarly, for incident electromagnetic waves the conservation of energy imposes

$$\mathscr{F}_i^{(\mathrm{E})} = 1, \quad \mathscr{F}_r^{(\mathrm{E})} = \left|\left[\hat{\mathscr{R}}_{\mathscr{N}}^{(\ell)}\right]_{\mathrm{EE}}\right|^2 + \left|\left[\hat{\mathscr{R}}_{\mathscr{N}}^{(\ell)}\right]_{\mathrm{AE}}\right|^2 \quad \text{and} \quad \mathscr{F}_t^{(\mathrm{E})} = \left|\left[\hat{\mathscr{T}}_{\mathscr{N}}^{(\ell)}\right]_{\mathrm{EE}}\right|^2 + \left|\left[\hat{\mathscr{T}}_{\mathscr{N}}^{(\ell)}\right]_{\mathrm{AE}}\right|^2 \tag{2.25}$$

and

$$\mathscr{F}_r^{(\mathrm{E})} + \mathscr{F}_t^{(\mathrm{E})} = 1. \tag{2.26}$$

The presence of cross-terms in Eqs (2.23) and (2.25) is the main difference with respect to the elastic frequency regime. It can be demonstrated that the cross terms are identical, *i.e.*

$$\left|\left[\hat{\mathscr{T}}_{\mathscr{N}}^{(\ell)}\right]_{\mathrm{EA}}\right|^2 = \left|\left[\hat{\mathscr{T}}_{\mathscr{N}}^{(\ell)}\right]_{\mathrm{AE}}\right|^2 \quad \text{and} \quad \left|\left[\hat{\mathscr{T}}_{\mathscr{N}}^{(\ell)}\right]_{\mathrm{EA}}\right|^2 = \left|\left[\hat{\mathscr{T}}_{\mathscr{N}}^{(\ell)}\right]_{\mathrm{AE}}\right|^2. \tag{2.27}$$

Illustrative examples. From a physical point of view, Eq. (2.27) predicts that the ratio of the cross-term contribution to the transmitted energy is the same for both elastic and electromagnetic incident waves.

Fig. 2.5 shows reflectance and transmittance through a single layer in the electromagnetic frequency regime. In panel (a) an elastic incident wave is assumed while panel (b) refers to an electromagnetic incident wave. The physical parameters of the slab are the same as those used in Fig. 2.3.

The possibility to transduce an elastic wave into an electromagnetic wave (or vice versa) is investigated in Fig. 2.6. The transmitted cross-term in Eq. (2.27) is analysed for a structure whose building block is the same as in Fig. 2.2. Fig. 2.6(a) refers to $\mathscr{N} = 1$ while Fig. 2.6(b) to $\mathscr{N} = 10$. The cross-term transmitted energy through a single slab is limited to $\approx 5\%$ of the incident energy. A stack of $\mathscr{N} = 10$ building blocks affects the cross-term

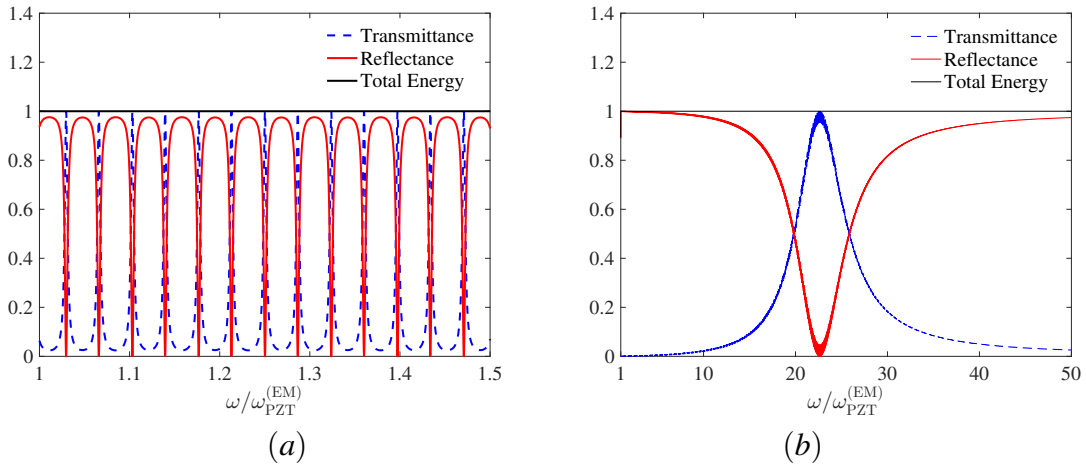

Fig. 2.5 *Reflectance (red solid line) and transmittance (blue dashed lines) at oblique incidence ($k_y = 1/\beta$) and $\mathscr{N} = 1$. We used the same building block as in Fig. 2.3. Panel (a) refers to an elastic incident wave while panel (b) refers to an electromagnetic incident wave. The frequency of the incident waves is in the electromagnetic frequency regime.*

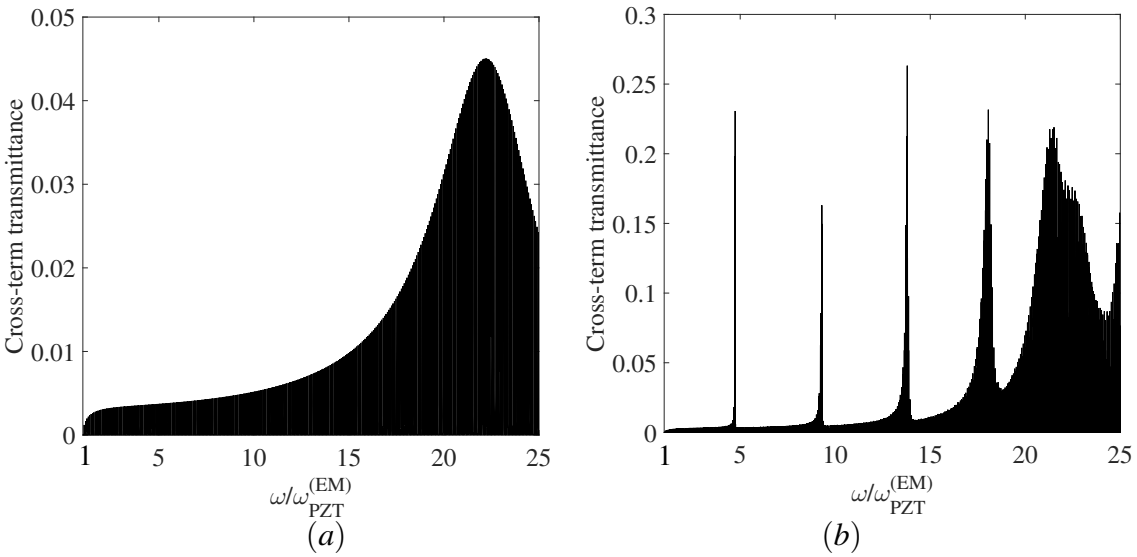

Fig. 2.6 *Cross-term contributions to the transmittance spectrum at oblique incidence ($k_y = 1/\beta$). The parameters are the same as those used in Fig. 2.2. Panel (a) refers to $\mathscr{N} = 1$ while panel (b) to $\mathscr{N} = 10$.*

transmittance. Specifically, transmission resonances of $\approx 25\%$ efficiency contribute to the transmitted spectrum.

The cross-term transmittance is typical of the electromagnetic frequency regime where elastic and electromagnetic wave propagate, coupled by the boundary conditions. Its careful

calculation is a significant result in the quantification of elastic-into-electromagnetic-wave energy conversion. This is further investigated in section 2.3.

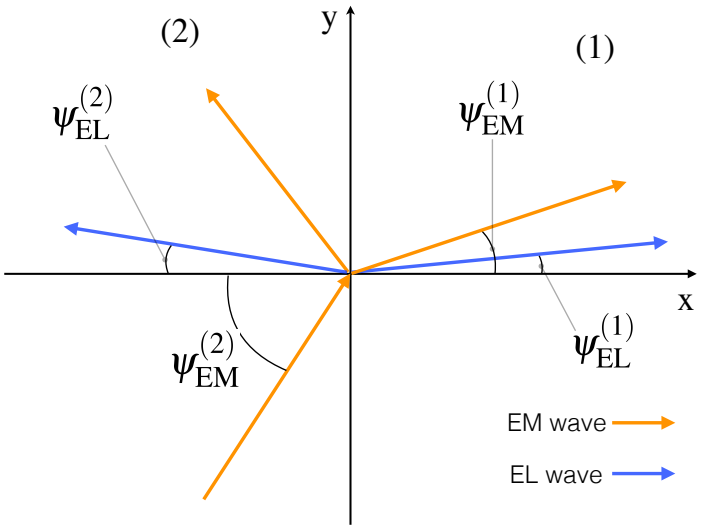

Fig. 2.7 *The diagram illustrates the decomposition of an incident electromagnetic wave into elastic (EL, blue arrows) and electromagnetic (EM, orange arrows), reflected and transmitted contributions. The angle of the propagating waves with respect to the normal to the interface are schematically reported off-scale.*

2.3 Additional remarks on oblique incidence

In experiments, it is common practice to set the angle of incidence with respect to the normal to an interface rather than k_y, the parallel component to the interface of the wave vector. A possible configuration is represented in Fig. 2.7, where two semi-infinite piezoelectric media are distinguished by the symbols "(1)" (right) and "(2)" (left). The angle of incidence and refraction of a transverse magnetic wave are denoted by $\psi_{EM}^{(2)}$, $\psi_{EM}^{(1)}$, respectively. Similarly the angles of propagation in media (1) and (2) of the generated shear elastic wave are $\psi_{EL}^{(2)}$,$\psi_{EL}^{(1)}$. Given the configuration in Fig. 2.7, the angle of refraction is related to the angle of incidence via the Snell laws

$$\frac{\sin(\psi_{EL}^{(2)})}{\sin(\psi_{EL}^{(1)})} = \frac{v_2}{v_1}, \quad \text{and} \quad \frac{\sin(\psi_{EM}^{(2)})}{\sin(\psi_{EM}^{(1)})} = \frac{c_2}{c_1}, \tag{2.28}$$

where c_i and v_i, $i = \{1,2\}$, are the shear elastic and transverse magnetic wave speeds (1.20), respectively, in material (j). The assumption underlying Eqs (2.28) is the conservation of k_y at the interface in Fig. 2.7 (see *e.g.* Born and Wolf [7]). The initial Ansätze (1.97) assume

that k_y is the same for electromagnetic and elastic waves. This implies that

$$\frac{k_y}{\omega} = \frac{\sin(\psi_{\mathrm{EM}}^{(j)})}{c_j} = \frac{\sin(\psi_{\mathrm{EL}}^{(j)})}{v_j} \Longrightarrow \frac{\sin(\psi_{\mathrm{EL}}^{(j)})}{\sin(\psi_{\mathrm{EM}}^{(j)})} = \frac{v_j}{c_j} \ll 1. \tag{2.29}$$

From the definitions (1.20), for PZT we estimate $v_2/c_2 \approx 2.3 \times 10^{-4}$ and for $BaTiO_3$ we estimate $v_1/c_1 \approx 3.9 \times 10^{-3}$. A consequence of Eq. (2.29) is that the propagation angles of elastic waves can be assumed to be zero, for every $\psi_{\mathrm{EM}}^{(2)} \neq 0$. The x components of the wave vectors, given in Eq. (1.102), can be rewritten using Eqs (2.28) and (2.29). The substitution gives

$$\begin{aligned} r_i &= \frac{\omega}{v_i}\cos(\psi_{\mathrm{EL}}^{(i)}) \approx \frac{\omega}{v_i}, \;\; i = \{1,2\}, \\ q_1 &= \frac{\omega}{c_1}\cos(\psi_{\mathrm{EM}}^{(1)}) = \frac{\omega}{c_1}\sqrt{1 - \left(\frac{c_1}{c_2}\right)^2 \sin^2(\psi_{\mathrm{EM}}^{(2)})}, \quad q_2 = \frac{\omega}{c_2}\cos(\psi_{\mathrm{EM}}^{(2)}). \end{aligned} \tag{2.30}$$

In order to simplify the notation, we introduce the definition

$$\alpha = \psi_{\mathrm{EL}}^{(2)}. \tag{2.31}$$

We emphasise that the plus sign in front of the square root in the expression for q_1 (Eqs (2.30)) is the only physically acceptable option. In fact, for $\alpha > \psi_{\mathrm{th}}$ where

$$\sin\psi_{\mathrm{th}} = \frac{c_2}{c_1}, \quad \text{and} \;\; c_2/c_1 < 1, \tag{2.32}$$

q_1 in Eqs (2.30) is purely imaginary. A minus sign would lead to growing transmitted field as the distance from the interface is increased. The angle ψ_{th} in (2.32) is the angle of total reflection for electromagnetic waves from an interface between two media with $c_2 < c_1$ (see *e.g.* [7]). In the case $c_2 > c_1$, $\mathrm{Im}(q_1) = 0$ in Eq. (2.30) and transverse magnetic waves propagate in the structure.

Fresnel-like formulae. Our aim here is to express the reflection and transmission coefficients (2.8) and (2.9) in term of the angle of incidence α of electromagnetic waves. This is the only angle needed in the formulation of the problem as it follows from Eqs (2.29) and (2.30). The entries of the reflection and transmission matrices in Eqs (2.8) and (2.9) in terms

of the angle of incidence α, yield

$$
\begin{aligned}
R_{\mathrm{AA}}^{(\ell)} &= -\frac{ie^{2i\omega x_1/v_2}}{\tilde{\mathscr{D}}}\left[\frac{\sin^2\alpha}{c_2^2}\left(\frac{e_1}{\varepsilon_1}-\frac{e_2}{\varepsilon_2}\right)^2+\left(\frac{G_1}{v_1}-\frac{G_2}{v_2}\right)\right.\\
&\qquad\left.\left(\frac{1}{\varepsilon_1 c_1}\sqrt{1-\left(\frac{c_1}{c_2}\right)^2\sin^2\alpha}+\frac{\cos\alpha}{\varepsilon_2 c_2}\right)\right],\\
R_{\mathrm{AE}}^{(\ell)} &= -R_{\mathrm{EA}}^{(\ell)} = -\frac{2i}{\tilde{\mathscr{D}}}e^{+i\omega(\cos\alpha/c_2+1/v_2)x_1}\frac{\sin\alpha}{c_2}\sqrt{\frac{G_2}{v_2}}\sqrt{\frac{\cos\alpha}{\varepsilon_2 c_2}}\left(\frac{e_1}{\varepsilon_1}-\frac{e_2}{\varepsilon_2}\right),\\
R_{\mathrm{EE}}^{(\ell)} &= -\frac{ie^{2i\omega\cos\alpha\ x_1/c_2}}{\tilde{\mathscr{D}}}\left[\frac{\sin^2\alpha}{c_2^2}\left(\frac{e_1}{\varepsilon_1}-\frac{e_2}{\varepsilon_2}\right)^2+\left(\frac{G_1}{v_1}+\frac{G_2}{v_2}\right)\right.\\
&\qquad\left.\left(\frac{1}{\varepsilon_1 c_1}\sqrt{1-\left(\frac{c_1}{c_2}\right)^2\sin^2\alpha}-\frac{\cos\alpha}{\varepsilon_2 c_2}\right)\right],
\end{aligned}
\tag{2.33}
$$

where we have introduced

$$
\tilde{\mathscr{D}} = \mathscr{D}/\omega^2 = \frac{\sin^2\alpha}{c_2^2}\left(\frac{e_1}{\varepsilon_1}-\frac{e_2}{\varepsilon_2}\right)^2+\left(\frac{G_1}{v_1}+\frac{G_2}{v_2}\right)\left(\frac{1}{\varepsilon_1 c_1}\sqrt{1-\left(\frac{c_1}{c_2}\right)^2\sin^2\alpha}+\frac{\cos\alpha}{\varepsilon_2 c_2}\right). \tag{2.34}
$$

The entries of the transmission matrix in (2.6) for waves incident from the left are

$$
\begin{aligned}
T_{\mathrm{AA}}^{(\ell)} &= \frac{2}{\tilde{\mathscr{D}}}e^{-i\omega(1/v_1-1/v_2)x_1}\sqrt{\frac{G_1}{v_1}}\sqrt{\frac{G_2}{v_2}}\left(\frac{1}{\varepsilon_1 c_1}\sqrt{1-\left(\frac{c_1}{c_2}\right)^2\sin^2\alpha}+\frac{\cos\alpha}{\varepsilon_2 c_2}\right),\\
T_{\mathrm{AE}}^{(\ell)} &= -\frac{2}{\tilde{\mathscr{D}}}e^{+i\omega(\cos\alpha/c_2-1/v_1)x_1}\frac{\sin\alpha}{c_2}\sqrt{\frac{G_1}{v_1}}\sqrt{\frac{\cos\alpha}{\varepsilon_2 c_2}}\left(\frac{e_1}{\varepsilon_1}-\frac{e_2}{\varepsilon_2}\right),\\
T_{\mathrm{EE}}^{(\ell)} &= \frac{2}{\tilde{\mathscr{D}}}e^{-i\omega(q_1(\alpha)/\omega-\cos\alpha/c_2)x_1}\left(\frac{G_1}{v_1}+\frac{G_2}{v_2}\right)\\
&\quad\times\sqrt{\frac{1}{\varepsilon_1 c_1}}\left(1-\left(\frac{c_1}{c_2}\right)^2\sin^2\alpha\right)^{\frac{1}{4}}\sqrt{\frac{\cos\alpha}{\varepsilon_2 c_2}},\\
T_{\mathrm{EA}}^{(\ell)} &= \frac{2}{\tilde{\mathscr{D}}}e^{-i(q_1(\alpha)-\omega/v_2)x_1}\frac{\sin\alpha}{c_2}\sqrt{\frac{G_2}{v_2}}\sqrt{\frac{1}{\varepsilon_1 c_1}}\left(1-\left(\frac{c_1}{c_2}\right)^2\sin^2\alpha\right)^{\frac{1}{4}}\left(\frac{e_1}{\varepsilon_1}-\frac{e_2}{\varepsilon_2}\right),
\end{aligned}
\tag{2.35}
$$

where $q_1(\alpha)$ denotes the expression for q_1 in Eqs (2.30) as a function of the angle of incidence α. The expressions (2.33) and (2.35) are the entries of the reflection and transmission matrices (2.6) for waves incident from the left in term of the angle of incident of electromagnetic waves α, shear modulus G_i, dielectric constant ε_i, piezoelectric constants e_i, shear

elastic wave speeds v_i and electromagnetic wave speeds c_i, $i = 1,2$. It is useful to compare (2.33) and (2.35) with the well known Fresnel formulae for TM electromagnetic waves [7] and elastic shear waves [49] at the boundary between homogeneous materials. In the limit $e_1 = e_2 = 0$, equations (2.33) become

$$\begin{aligned}
R_{\mathrm{AA}}^{(\ell)}\Big|_{e_1=e_2=0} &= -ie^{2i\omega x_1/v_2}\frac{G_1v_2 - G_2v_1}{G_1v_2 + G_2v_1},\\
R_{\mathrm{AE}}^{(\ell)}\Big|_{e_1=e_2=0} &= R_{\mathrm{EA}}^{(\ell)}\Big|_{e_1=e_2=0} = 0,\\
R_{\mathrm{EE}}^{(\ell)}\Big|_{e_1=e_2=0} &= -ie^{2i\omega\cos\alpha\; x_1/c_2}\left(\frac{\frac{1}{\varepsilon_1 c_1}\sqrt{1-\left(\frac{c_1}{c_2}\right)^2\sin^2\alpha} - \frac{\cos\alpha}{\varepsilon_2 c_2}}{\frac{1}{\varepsilon_1 c_1}\sqrt{1-\left(\frac{c_1}{c_2}\right)^2\sin^2\alpha} + \frac{\cos\alpha}{\varepsilon_2 c_2}}\right),
\end{aligned} \tag{2.36}$$

and Eqs (2.35) become

$$\begin{aligned}
T_{\mathrm{AA}}^{(\ell)}\Big|_{e_1=e_2=0} =& 2e^{-i\omega(1/v_1-1/v_2)x_1}\frac{\sqrt{G_1v_1}\sqrt{G_2v_2}}{G_1v_2+G_2v_1},\\
T_{\mathrm{AE}}^{(\ell)}\Big|_{e_1=e_2=0} &= T_{\mathrm{EA}}^{(\ell)}\Big|_{e_1=e_2=0} = 0,\\
T_{\mathrm{EE}}^{(\ell)}\Big|_{e_1=e_2=0} =& e^{-i\omega(q_1(\alpha)/\omega-\cos\alpha/c_2)x_1}\left(\frac{G_1}{v_1}+\frac{G_2}{v_2}\right)\\
&\times\frac{\sqrt{\frac{1}{\varepsilon_1 c_1}}\left(1-\left(\frac{c_1}{c_2}\right)^2\sin^2\alpha\right)^{\frac{1}{4}}\sqrt{\frac{\cos\alpha}{\varepsilon_2 c_2}}}{\frac{1}{\varepsilon_1 c_1}\sqrt{1-\left(\frac{c_1}{c_2}\right)^2\sin^2\alpha}+\frac{\cos\alpha}{\varepsilon_2 c_2}}.
\end{aligned} \tag{2.37}$$

By substituting $\alpha = \psi_{\mathrm{th}}$ (where ψ_{th} is defined in Eq. (2.32)) in the last of relations in (2.36) and (2.37), we retrieve the classic result according to which the reflection and transmission coefficients of transverse magnetic have modulus one and zero, respectively. In the presence of piezoelectric effect, the reflectance obtained from the last of (2.33) is not one because an elastic wave is generated at the same time.

2.4 Summarising remarks on chapter 2

In summary, by using the multiple scattering method, we derived the expressions for the transmission and reflection matrices for out-of-plane shear elastic waves and transverse magnetic waves.

The threshold frequencies identified in chapter 1 allowed us to study the scattering problem in two frequency regimes: the elastic frequency regime, addressed in section 2.2.1, where only elastic energy propagates and the electromagnetic field is localised; and the electromagnetic frequency regime, analysed in section 2.2.2, where both elastic and electromagnetic waves propagate.

Reflectance and transmittance have been evaluated via a recurrence procedure (see Eqs (2.17)). The conceptual steps are as follows: first we calculate the reflection and transmission matrices associated with an interface between two semi-infinite piezoelectric materials; we then obtain the reflection and transmission matrices for a single piezoelectric layer embedded in a infinite hosting material; given the reflection and transmission matrices for (s)-layers, the reflection and transmission matrices for $(s+1)$-layers then are evaluated from Eqs (2.17).

For a sufficiently large s, at a frequency corresponding to a stop band in the corresponding periodic system, the transmission across the piezoelectric interface becomes negligibly small.

The cross-term transmittance, corresponding to conversion of elastic energy into electromagnetic and vice versa, has been analysed in detail.

In section 2.3, the scattering problem is expressed there in terms of the incidence angle α for electromagnetic waves.

The cross-term contributions to the propagating energy is produced by the piezoelectric effect via the interface continuity (2.3). This effect is illustrated in Fig. 2.6 at a fixed transverse component of the wave vector k_y.

Chapter 3

Bloch-Floquet waves in checkerboard piezoelectric structures

In this chapter, we study a 2D periodic piezoelectric checkerboard structure, where "white" rectangles are made of an isotropic material and the "black" ones of a piezoelectric material belonging to the hexagonal symmetry class. For the axis of symmetry lying in the plane of the checkerboard, we derive the coupled partial differential equations and interface conditions for elastic and electromagnetic quantities. Bloch-Floquet quasi-periodicity conditions are used to reduce the problem to a single unit cell. In addition, perfect contact conditions and charge-free conditions are set at the interfaces between the materials. The corresponding dispersion curves for Bloch-Floquet waves are obtained solving the partial differential equations with the use of a finite element package. Several configurations of the in-plane polarisation vectors are taken into account.

3.1 Formulation of the problem

A piezoelectric doubly-periodic structure is schematically shown Fig. 3.1, where the lattice vectors are

$$\boldsymbol{r}_1 = L_x \begin{pmatrix} 1 \\ 0 \end{pmatrix} \quad \text{and} \quad \boldsymbol{r}_2 = L_y \begin{pmatrix} 0 \\ 1 \end{pmatrix}, \tag{3.1}$$

and the unit cell is the yellow semitransparent region of sides L_x and L_y. Using Eq. (3.1) into Eq. (1.34), the lattice vectors for the reciprocal lattice are

$$\boldsymbol{A}_1 = \frac{2\pi}{L_x} \begin{pmatrix} 1 \\ 0 \end{pmatrix}, \text{ and } \boldsymbol{A}_2 = \frac{2\pi}{L_y} \begin{pmatrix} 0 \\ 1 \end{pmatrix}. \tag{3.2}$$

In this chapter, a Bloch vector $\boldsymbol{k}$ belongs to the first Brillouin zone for the checkerboard-like structure, *i.e.*

$$\boldsymbol{k} = \alpha_1 \boldsymbol{A}_1 + \alpha_2 \boldsymbol{A}_2, \ \text{ with } \ (\alpha_1, \alpha_2)^{\mathrm{T}} \in [-1/2, 1/2] \times [-1/2, 1/2], \tag{3.3}$$

where $\boldsymbol{A}_1$ and $\boldsymbol{A}_2$ have been introduced in Eq. (3.2). Representative points within the first

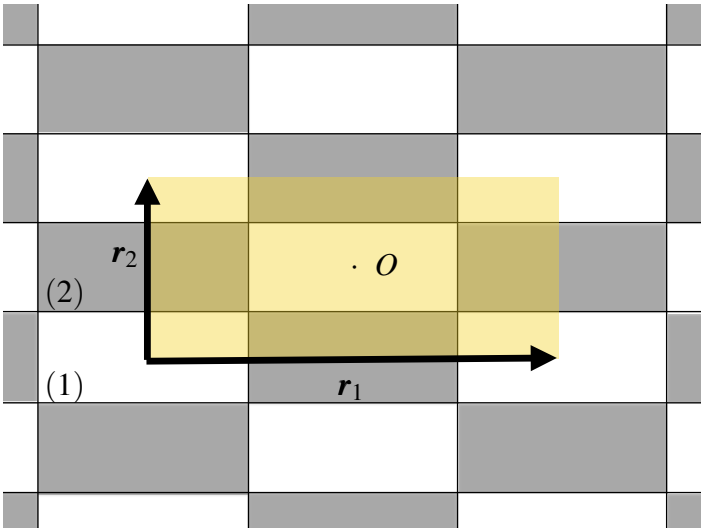

Fig. 3.1 *A checkerboard-like periodic structure where white and grey rectangles are different materials, denoted by indices (1) and (2), respectively. Material (1) is an isotropic dielectric and material (2) is piezoelectric. The yellow semi-transparent region encloses the unit cell delimited by the lattice vectors $\boldsymbol{r}_1$ and $\boldsymbol{r}_2$ in Eq.* (3.5) *(black arrows). The point O represents the origin of a Cartesian system of coordinates, with its $x-$axis and $y-$axis parallel to $\boldsymbol{r}_1$ and $\boldsymbol{r}_2$, respectively, and the $z-$axis pointing out of plane.*

Brillouin zone of the checkerboard are

$$\Gamma = \begin{pmatrix} 0 \\ 0 \end{pmatrix}, \ \mathrm{X} = -\mathrm{A} = \pi \begin{pmatrix} 1/L_x \\ 1/L_y \end{pmatrix}, \ \mathrm{M} = \pi \begin{pmatrix} 1/L_x \\ 0 \end{pmatrix}, \ \mathrm{B} = -C = \pi \begin{pmatrix} 1/L_x \\ -1/L_y \end{pmatrix}. \tag{3.4}$$

The points X and M introduced in Eq. (3.4) should not be confused with those introduced in Eq. (1.62) in the context of a triangular lattice. We denote by $\boldsymbol{r} = (x, y)^{\mathrm{T}}$ a 2D Cartesian system of coordinates whose origin is located at the point O in Fig. (3.1). The areas enclosing

$$\boldsymbol{r} \in \mathrm{X}_1^{(\boldsymbol{n})} = \left[\left(n_1 - \frac{1}{4} \right) L_x, \left(n_1 + \frac{1}{4} \right) L_x \right] \times \left[\left(n_2 - \frac{1}{4} \right) L_y, \left(n_2 + \frac{1}{4} \right) L_y \right], \ \boldsymbol{n} = (n_1, n_2)^{\mathrm{T}} \in \mathbb{Z}^2, \tag{3.5}$$

are the white rectangles of Fig. 3.1; and the areas enclosing

$$\boldsymbol{r} \in \mathrm{X}_2^{(\boldsymbol{n})} = \left[\left(n_1+\frac{1}{4}\right)L_x, \left(n_1+\frac{3}{4}\right)L_x\right] \times \left[\left(n_2+\frac{1}{4}\right)L_y, \left(n_2+\frac{3}{4}\right)L_y\right], \;\; \boldsymbol{n} = (n_1,n_2)^{\mathrm{T}} \in \mathbb{Z}^2, \tag{3.6}$$

are the grey rectangles of Fig. 3.1. White and grey rectangles in Fig. 3.1 denote two different materials with indices (1) and (2), respectively. We assume that (1) is a dielectric isotropic material and (2) is a piezoelectric material.

Transformation under rotations of constituitive tensors. With reference to the stress-charge constituitive relations (1.10), we would like to remind the general transformation rules which apply to the stiffness matrix $\hat{c}$, piezoelectric coupling matrix $\hat{e}$ and the dielectric matrix $\hat{\boldsymbol{\varepsilon}}$, when the symmetry axis of a 6*mm* piezoelectric material is rotated. We introduce the Euler angles

$$\boldsymbol{\alpha} = (\alpha_1, \alpha_2, \alpha_3)^{\mathrm{T}}, \tag{3.7}$$

where α_i, $i = \{1,2,3\}$, are elementary rotation angles around the x, y and z axes of a 3D Cartesian system of coordinates. Denoting by a superscript "$\prime$" the transformed tensors, the transformation equations are [3]

$$\hat{c}' = \hat{M}(\boldsymbol{\alpha})\, \hat{c}\, (\hat{M}(\boldsymbol{\alpha}))^{\mathrm{T}}, \;\; \hat{e}' = \hat{R}(\boldsymbol{\alpha})\, \hat{e}\, \hat{M}^{\mathrm{T}}(\boldsymbol{\alpha}), \;\; \hat{\boldsymbol{\varepsilon}}' = \hat{R}(\boldsymbol{\alpha})\, \hat{\boldsymbol{\varepsilon}}\, \hat{R}^{\mathrm{T}}(\boldsymbol{\alpha}), \tag{3.8}$$

where

$$\hat{R}(\boldsymbol{\alpha}) = \hat{R}_1(\alpha_1)\hat{R}_2(\alpha_2)\hat{R}_3(\alpha_3), \;\; \text{with} \;\; \hat{R}_1(\alpha_1) = \begin{pmatrix} 1 & 0 & 0 \\ 0 & \cos\alpha_1 & -\sin\alpha_1 \\ 0 & \sin\alpha_1 & \cos\alpha_1 \end{pmatrix},$$
$$\hat{R}_2(\alpha_2) = \begin{pmatrix} \cos\alpha_2 & 0 & -\sin\alpha_2 \\ 0 & 1 & 0 \\ \sin\alpha_2 & 0 & \cos\alpha_2 \end{pmatrix}, \hat{R}_3(\alpha_3) = \begin{pmatrix} \cos\alpha_3 & -\sin\alpha_3 & 0 \\ \sin\alpha_3 & \cos\alpha_3 & 0 \\ 0 & 0 & 1 \end{pmatrix}, \tag{3.9}$$

and

$$\hat{M}(\boldsymbol{\alpha}) = \begin{pmatrix} R_{11}^2 & R_{12}^2 & R_{13}^2 & 2R_{23}R_{13} & 2R_{13}R_{11} & 2R_{11}R_{12} \\ R_{21}^2 & R_{22}^2 & R_{23}^2 & 2R_{22}R_{23} & 2R_{23}R_{21} & 2R_{21}R_{22} \\ R_{31}^2 & R_{32}^2 & R_{33}^2 & 2R_{32}R_{33} & 2R_{33}R_{31} & 2R_{31}R_{32} \\ R_{21}R_{31} & R_{22}R_{32} & R_{23}R_{33} & R_{22}R_{33}+R_{23}R_{32} & R_{21}R_{33}+R_{23}R_{31} & R_{22}R_{31}+R_{21}R_{32} \\ R_{31}R_{11} & R_{32}R_{12} & R_{33}R_{13} & R_{12}R_{33}+R_{13}R_{32} & R_{13}R_{31}+R_{11}R_{33} & R_{11}R_{32}+R_{12}R_{31} \\ R_{11}R_{21} & R_{12}R_{22} & R_{13}R_{23} & R_{12}R_{23}+R_{13}R_{22} & R_{13}R_{21}+R_{11}R_{23} & R_{11}R_{22}+R_{12}R_{21} \end{pmatrix}, \tag{3.10}$$

with $R_{ij} = (\hat{R}(\boldsymbol{\alpha}))_{ij}$.

For example, for a spontaneous polarisation of the piezoelectric material pointing towards positive x-coordinates, the Euler angles in the transformation (3.8) are $\boldsymbol{\alpha} = (0, -\pi/2, 0)^{\mathrm{T}}$, yielding

$$\hat{c}_x = \begin{pmatrix} c_{33} & c_{13} & c_{13} & 0 & 0 & 0 \\ c_{13} & c_{11} & c_{12} & 0 & 0 & 0 \\ c_{13} & c_{12} & c_{11} & 0 & 0 & 0 \\ 0 & 0 & 0 & \frac{1}{2}(c_{11}-c_{12}) & 0 & 0 \\ 0 & 0 & 0 & 0 & c_{44} & 0 \\ 0 & 0 & 0 & 0 & 0 & c_{44} \end{pmatrix}, \quad \hat{e}_x = \begin{pmatrix} e_{33} & e_{31} & e_{31} & 0 & 0 & 0 \\ 0 & 0 & 0 & 0 & 0 & e_{15} \\ 0 & 0 & 0 & 0 & e_{15} & 0 \end{pmatrix},$$

$$\hat{\varepsilon}_x = \mathrm{diag}(\varepsilon_{33}, \varepsilon_{11}, \varepsilon_{11}), \tag{3.11}$$

where the subscript x denotes the direction along which the polarisation points. Similarly, for the spontaneous polarisation being directed towards positive $y-$coordinates, the Euler angles in the transformations (3.8) are $\boldsymbol{\alpha} = (\pi/2, 0, 0)^{\mathrm{T}}$, yielding

$$\hat{c}_y = \begin{pmatrix} c_{11} & c_{13} & c_{12} & 0 & 0 & 0 \\ c_{13} & c_{33} & c_{13} & 0 & 0 & 0 \\ c_{12} & c_{13} & c_{11} & 0 & 0 & 0 \\ 0 & 0 & 0 & c_{44} & 0 & 0 \\ 0 & 0 & 0 & 0 & \frac{1}{2}(c_{11}-c_{12}) & 0 \\ 0 & 0 & 0 & 0 & 0 & c_{44} \end{pmatrix}, \quad \hat{e}_y = \begin{pmatrix} 0 & 0 & 0 & 0 & 0 & e_{15} \\ e_{31} & e_{33} & e_{31} & 0 & 0 & 0 \\ 0 & 0 & 0 & e_{15} & 0 & 0 \end{pmatrix},$$

$$\hat{\varepsilon}_y = \mathrm{diag}(\varepsilon_{11}, \varepsilon_{33}, \varepsilon_{11}), \tag{3.12}$$

where the subscript y denotes the direction towards which the polarisation points.

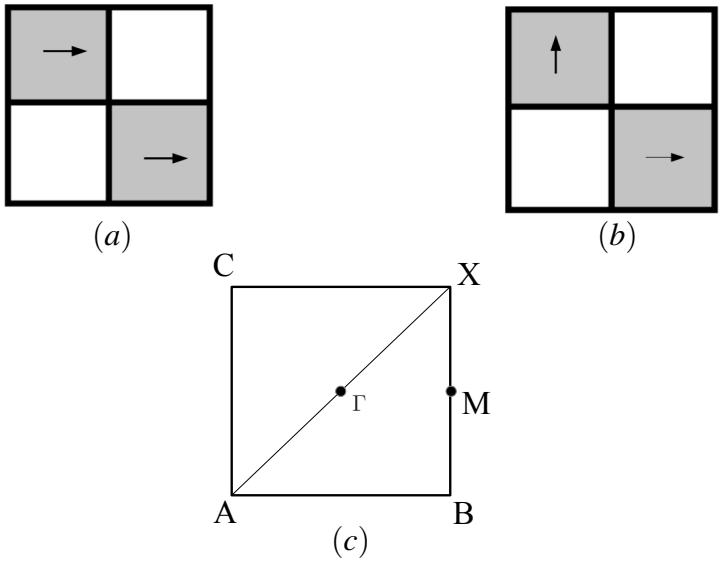

Fig. 3.2 *Arrows in panels (a) and (b) represent the direction of the piezoelectric polarisation vectors within the unit cell of a square ($L_x = L_y$) checkerboard. Panel (a) is referred to as* parallel polarisations *and panel (b) as* perpendicular polarisations*. Panel (c) shows the first Brillouin zone for a square checkerboard together with its representative points* (3.4)*.*

3.1.1 Governing equations

The in-plane vector problem of elasticity in a bulk piezoelectric medium has been formulated in section 1.1.2. It has been shown there that the equations for in-plane elasticity are coupled to that for the transverse electric field. In this section we formulate the Bloch-Floquet problem for a doubly-periodic checkerboard-like structure represented in Fig. 3.1. Both elastic and electromagnetic waves propagate through the structure. The Newton equations (1.1) are rewritten under the plain-strain assumption

$$s_{xz} = s_{yz} = s_{zz} = 0, \tag{3.13}$$

which apply to the strain components (1.9). The full set of Maxwell equations in Eq. (1.3) is assumed. We study two configurations of the polarisation vectors in the unit cell, schematically shown in Fig. 3.2(a) (parallel polarisations) and 3.2(b) (perpendicular polarisations). The orientation of the polarisation vectors are parallel to the $x-$axis and $y-$axis, and the corresponding constituitive tensors are given in Eqs (3.11) and (3.12).

***x*−polarised piezoelectric material.** Under the plain-strain assumption (3.13) and using the constituitive tensors in Eq. (3.11), the stress-strain constituitive relation in Eq. (1.14)

gives

$$\begin{aligned}
&\sigma_{xx} = c_{33}\frac{\partial u_x}{\partial x} + c_{13}\frac{\partial u_y}{\partial y} - e_{33}E_x, \;\; \sigma_{yy} = c_{13}\frac{\partial u_x}{\partial x} + c_{11}\frac{\partial u_y}{\partial y} - e_{31}E_x,\\
&\sigma_{zz} = c_{13}\frac{\partial u_x}{\partial x} + c_{12}\frac{\partial u_y}{\partial y} - e_{31}E_x, \;\; \sigma_{yz} = 0,\\
&\sigma_{xz} = -e_{15}E_z, \;\; \sigma_{xy} = c_{44}\left(\frac{\partial u_y}{\partial x} + \frac{\partial u_x}{\partial y}\right) - e_{15}E_y;
\end{aligned} \tag{3.14}$$

while the constituitive relation for the electric displacement in Eq. (1.14) yields

$$\boldsymbol{D} = \begin{pmatrix} e_{33}\frac{\partial u_x}{\partial x} + e_{31}\frac{\partial u_y}{\partial y} + \varepsilon_{33}E_x \\ \\ e_{15}\left(\frac{\partial u_x}{\partial y} + \frac{\partial u_y}{\partial x}\right) + \varepsilon_{11}E_y \\ \\ \varepsilon_{11}E_z \end{pmatrix}. \tag{3.15}$$

Because of transverse isotropy, all the derivatives with respect to the $z-$coordinate are zero in the Newton equations (1.1). After using Eqs (3.14), the first, second and third equations (1.1), yield the following governing equations for a 6*mm* x-polarised piezoelectric material

$$\begin{aligned}
c_{33}\frac{\partial^2 u_x}{\partial x^2} + c_{44}\frac{\partial^2 u_x}{\partial y^2} + (c_{13}+c_{44})\frac{\partial^2 u_y}{\partial x \partial y} - e_{15}\frac{\partial E_y}{\partial y} - e_{33}\frac{\partial E_x}{\partial x} &= -\rho\omega^2 u_x,\\
c_{44}\frac{\partial^2 u_y}{\partial x^2} + c_{11}\frac{\partial^2 u_y}{\partial y^2} + (c_{13}+c_{44})\frac{\partial^2 u_x}{\partial x \partial y} - e_{15}\frac{\partial E_y}{\partial x} - e_{31}\frac{\partial E_x}{\partial y} &= -\rho\omega^2 u_y,\\
\frac{\partial E_z}{\partial x} &= 0,
\end{aligned} \tag{3.16}$$

respectively. Since we seek for time-harmonic solutions of angular frequency ω, in Eqs (3.16) we used $\partial/\partial t(\cdot) = -i\omega$. The last equation (3.16) into the Maxwell equations (1.3) gives

$$\begin{aligned}
\frac{\partial E_y}{\partial x} - \frac{\partial E_x}{\partial y} &= i\mu\omega H_z,\\
\frac{\partial H_z}{\partial y} &= -i\omega D_x,\\
\frac{\partial H_z}{\partial x} &= i\omega D_y.
\end{aligned} \tag{3.17}$$

Using the constituitive equations (3.15) and the second and third relations in Eqs. (3.17), we can express the in-plane components of the electric field (E_x and E_y) in terms of the

transverse component of the magnetic field (H_z), yielding

$$E_x = \frac{1}{\varepsilon_{33}}\left(\frac{i}{\omega}\frac{\partial H_z}{\partial y} - e_{33}\frac{\partial u_x}{\partial x} - e_{31}\frac{\partial u_y}{\partial y}\right), \quad E_y = -\frac{1}{\varepsilon_{11}}\left[e_{15}\left(\frac{\partial u_x}{\partial x} + \frac{\partial u_y}{\partial y}\right) + \frac{i}{\omega}\frac{\partial H_z}{\partial x}\right]. \tag{3.18}$$

By substituting the expressions (3.18) in the left side of the first equation (3.17), we get

$$\left(\frac{1}{\varepsilon_{11}}\frac{\partial^2}{\partial x^2} + \frac{1}{\varepsilon_{33}}\frac{\partial^2}{\partial y^2}\right)H_z + \mu\omega^2 H_z = i\omega\frac{e_{15}}{\varepsilon_{11}}\left(\frac{\partial^2 u_y}{\partial x^2} + \frac{\partial^2 u_x}{\partial x\partial y}\right) - \frac{i\omega}{\varepsilon_{33}}\left(e_{33}\frac{\partial^2 u_x}{\partial x\partial y} + e_{31}\frac{\partial^2 u_y}{\partial y^2}\right). \tag{3.19}$$

Similarly, the substitutions of Eqs (3.18) into the first two Newton equations (3.16) gives

$$\begin{aligned}
&\left(c_{33} + \frac{e_{33}^2}{\varepsilon_{33}}\right)\frac{\partial^2 u_x}{\partial x^2} + \left(c_{44} + \frac{e_{15}^2}{\varepsilon_{11}}\right)\frac{\partial^2 u_x}{\partial y^2} + \left(c_{44} + c_{13} + \frac{e_{15}^2}{\varepsilon_{11}} + \frac{e_{33}e_{31}}{\varepsilon_{33}}\right)\frac{\partial^2 u_y}{\partial x\partial y} + \rho\omega^2 u_x \\
&= \frac{i}{\omega}\left(\frac{e_{15}}{\varepsilon_{11}} - \frac{e_{33}}{\varepsilon_{33}}\right)\frac{\partial^2 H_z}{\partial x\partial y}, \\
&\left(c_{44} + \frac{e_{15}^2}{\varepsilon_{11}}\right)\frac{\partial^2 u_y}{\partial x^2} + \left(c_{11} + \frac{e_{31}^2}{\varepsilon_{33}}\right)\frac{\partial^2 u_y}{\partial y^2} + \left(c_{44} + c_{13} + \frac{e_{15}^2}{\varepsilon_{11}} + \frac{e_{33}e_{31}}{\varepsilon_{33}}\right)\frac{\partial^2 u_x}{\partial x\partial y} + \rho\omega^2 u_y \\
&= \frac{i}{\omega}\left(\frac{e_{31}}{\varepsilon_{33}}\frac{\partial^2}{\partial y^2} - \frac{e_{15}}{\varepsilon_{11}}\frac{\partial^2}{\partial x^2}\right)H_z.
\end{aligned} \tag{3.20}$$

Eqs (3.19) and (3.20) are coupled partial differential equations which govern the in-plane problem of elasticity and transverse magnetic field for a $x-$polarised piezoelectric material.

***y*−polarised piezoelectric material.** We deduct here coupled partial differential equations which govern the transverse magnetic field and the in-plane components of the displacement for a $y-$polarised piezoelectric material. Exchanging the $x-$ and $y-$coordinates in Eqs (3.19) and (3.20), we obtain

$$\left(\frac{1}{\varepsilon_{11}}\frac{\partial^2}{\partial y^2} + \frac{1}{\varepsilon_{33}}\frac{\partial^2}{\partial x^2}\right)H_z + \mu\omega^2 H_z = i\omega\frac{e_{15}}{\varepsilon_{11}}\left(\frac{\partial^2 u_x}{\partial y^2} + \frac{\partial^2 u_y}{\partial x\partial y}\right) - \frac{i\omega}{\varepsilon_{33}}\left(e_{33}\frac{\partial^2 u_y}{\partial x\partial y} + e_{31}\frac{\partial^2 u_x}{\partial x^2}\right), \tag{3.21}$$

and

$$\left(c_{33}+\frac{e_{33}^2}{\varepsilon_{33}}\right)\frac{\partial^2 u_y}{\partial y^2}+\left(c_{44}+\frac{e_{15}^2}{\varepsilon_{11}}\right)\frac{\partial^2 u_y}{\partial x^2}+\left(c_{44}+c_{13}+\frac{e_{15}^2}{\varepsilon_{11}}+\frac{e_{33}e_{31}}{\varepsilon_{33}}\right)\frac{\partial^2 u_x}{\partial x\partial y}+\rho\omega^2 u_y$$
$$=\frac{i}{\omega}\left(\frac{e_{15}}{\varepsilon_{11}}-\frac{e_{33}}{\varepsilon_{33}}\right)\frac{\partial^2 H_z}{\partial x\partial y},$$
$$\left(c_{44}+\frac{e_{15}^2}{\varepsilon_{11}}\right)\frac{\partial^2 u_x}{\partial y^2}+\left(c_{11}+\frac{e_{31}^2}{\varepsilon_{33}}\right)\frac{\partial^2 u_x}{\partial x^2}+\left(c_{44}+c_{13}+\frac{e_{15}^2}{\varepsilon_{11}}+\frac{e_{33}e_{31}}{\varepsilon_{33}}\right)\frac{\partial^2 u_y}{\partial x\partial y}+\rho\omega^2 u_x$$
$$=\frac{i}{\omega}\left(\frac{e_{31}}{\varepsilon_{33}}\frac{\partial^2}{\partial x^2}-\frac{e_{15}}{\varepsilon_{11}}\frac{\partial^2}{\partial y^2}\right)H_z, \tag{3.22}$$

respectively.

Linear elastic material. The in-plane equations for a linear elastic material with first and second Lamé parameters λ and η, respectively, and density ρ' is the Lamé equation

$$\eta\nabla^2\boldsymbol{u}+(\lambda+\eta)\nabla(\nabla\cdot\boldsymbol{u})+\rho'\omega^2\boldsymbol{u}=\boldsymbol{0}. \tag{3.23}$$

By assuming that the material is a dielectric with dielectric constant ε and denoting by μ the magnetic permeability of the vacuum, the governing equation for the magnetic field $\boldsymbol{H}$ are

$$\nabla^2\boldsymbol{H}+\mu\varepsilon\omega^2\boldsymbol{H}=\boldsymbol{0}. \tag{3.24}$$

3.1.2 Interface conditions

In the previous section, we have shown that the governing equations for elastic and electromagnetic quantities for in-plane polarised piezoelectric materials can be reduced to a system of three coupled partial differential equations. Specifically, Eqs (3.19) and (3.20) govern a $x-$polarised piezoelectric; and Eqs (3.21) and (3.22) govern a $y-$polarised piezoelectric. In a periodic checkerboard-like metamaterial as that represented in Fig. 3.1 the following Bloch-Floquet boundary conditions apply

$$\boldsymbol{u}(\boldsymbol{r}+n_1\boldsymbol{r}_1+n_2\boldsymbol{r}_2)=e^{i\boldsymbol{k}(n_1\boldsymbol{r}_1+n_2\boldsymbol{r}_2)}\boldsymbol{u}(\boldsymbol{r}),\ \ \hat{\boldsymbol{\sigma}}(\boldsymbol{r}+n_1\boldsymbol{r}_1+n_2\boldsymbol{r}_2)=e^{i\boldsymbol{k}(n_1\boldsymbol{r}_1+n_2\boldsymbol{r}_2)}\hat{\boldsymbol{\sigma}}(\boldsymbol{r}),$$
$$\boldsymbol{H}(\boldsymbol{r}+n_1\boldsymbol{r}_1+n_2\boldsymbol{r}_2)=e^{i\boldsymbol{k}(n_1\boldsymbol{r}_1+n_2\boldsymbol{r}_2)}\boldsymbol{H}(\boldsymbol{r}),\ \ \boldsymbol{D}(\boldsymbol{r}+n_1\boldsymbol{r}_1+n_2\boldsymbol{r}_2)=e^{i\boldsymbol{k}(n_1\boldsymbol{r}_1+n_2\boldsymbol{r}_2)}\boldsymbol{D}(\boldsymbol{r}), \tag{3.25}$$

where $\boldsymbol{r}=(x,y)^{\mathrm{T}}$, $n_1,\ n_2\in\mathbb{Z}$, $\boldsymbol{r}_1$ and $\boldsymbol{r}_2$ are the lattice vectors (3.1), and $\boldsymbol{k}$ is the Bloch vector (3.3). At vertical interfaces $x=n_1L_x/2$, $n_1\in\mathbb{Z}$, perfect contact conditions (1.5) and

charge-free conditions (1.4) yield

$$\begin{aligned} u_x(x,y)|_{x=(n_1L_x/2)^+} - u_x(x,y)|_{x=(n_1L_x/2)^-} &= 0, \quad u_y(x,y)|_{x=(n_1L_x/2)^+} - u_y(x,y)|_{x=(n_1L_x/2)^-} = 0, \\ \sigma_{xx}(x,y)|_{x=(n_1L_x/2)^+} - \sigma_{xx}(x,y)|_{x=(n_1L_x/2)^-} &= 0, \quad \sigma_{xy}(x,y)|_{x=(n_1L_x/2)^+} - \sigma_{xy}(x,y)|_{x=(n_1L_x/2)^-} = 0, \\ H_z(x,y)|_{x=(n_1L_x/2)^+} - H_z(x,y)|_{x=(n_1L_x/2)^-} &= 0, \quad D_x(x,y)|_{x=(n_1L_x/2)^+} - D_x(x,y)|_{x=(n_1L_x/2)^-} = 0, \end{aligned} \tag{3.26}$$

for $y \in (-\infty,\infty)$. At horizontal interfaces $y = n_2L_y/2$, $n_2 \in \mathbb{Z}$, perfect contact conditions (1.5) and charge-free conditions (1.4), give

$$\begin{aligned} u_x(x,y)|_{y=(n_2L_y/2)^+} - u_x(x,y)|_{y=(n_2L_x/2)^-} &= 0, \quad u_y(x,y)|_{y=(n_2L_y/2)^+} - u_y(x,y)|_{y=(n_2L_y/2)^-} = 0, \\ \sigma_{yy}(x,y)|_{y=(n_2L_y/2)^+} - \sigma_{yy}(x,y)|_{y=(n_2L_y/2)} &= 0, \quad \sigma_{xy}(x,y)|_{y=(n_2L_y/2)} - \sigma_{xy}(x,y)|_{y=(n_2L_y/2)^-} = 0, \\ H_z(x,y)|_{y=(n_2L_y/2)^+} - H_z(x,y)|_{y=(n_2L_y/2)^-} &= 0, \quad D_y(x,y)|_{y=(n_2L_y/2)^+} - D_y(x,y)|_{y=(n_2L_y/2)^-} = 0, \end{aligned} \tag{3.27}$$

for $x \in (-\infty,\infty)$.

3.2 Bloch-Floquet waves

We solve here the Bloch-Floquet problem formulated in the previous section. The unit cells in Figs 3.2(a) and 3.2(b) is made of Lead Zirconate Titanate (also known as “PZT", grey areas), a 6*mm* piezoelectric material, and Nylon 66 (also known as “PA66”, white areas), a synthetic macromolecule with isotropic elastic and dielectric responses: the dielectric permittivity is $\varepsilon/\varepsilon_0 = 3.2$, the first and second Lamé parameters are $\lambda = 7.93 \times 10^8$ N/m^2 and $\eta = 3.7 \times 10^8$ N/m^2, respectively, and the mass density is $\rho' = 1150$Kg/m^3. The material properties of PZT are listed in Table 3.1. The polarisation directions represented in Fig. (3.2)(a) and Fig. (3.2)(b) are here investigated. The dispersion diagrams for

Elastic Stiffness ([10^{10} N/m^2])	**Piezoelectric Coupling** ([C/m^2])	**Relative Permittivity**	**Density** ([Kg/m^3])
$c_{11} = 13.89$	$e_{31} = -5.2$	$\varepsilon_{11}/\varepsilon_0 = 762.5$	$\rho = 7500$
$c_{12} = 7.78$	$e_{33} = 15.1$	$\varepsilon_{33}/\varepsilon_0 = 663.2$	
$c_{13} = 7.43$	$e_{15} = 12.7$		
$c_{33} = 11.54$			
$c_{44} = 2.56$			

Table 3.1 *Material properties of the piezoelectric material Lead Zirconate Titanate (PZT).*

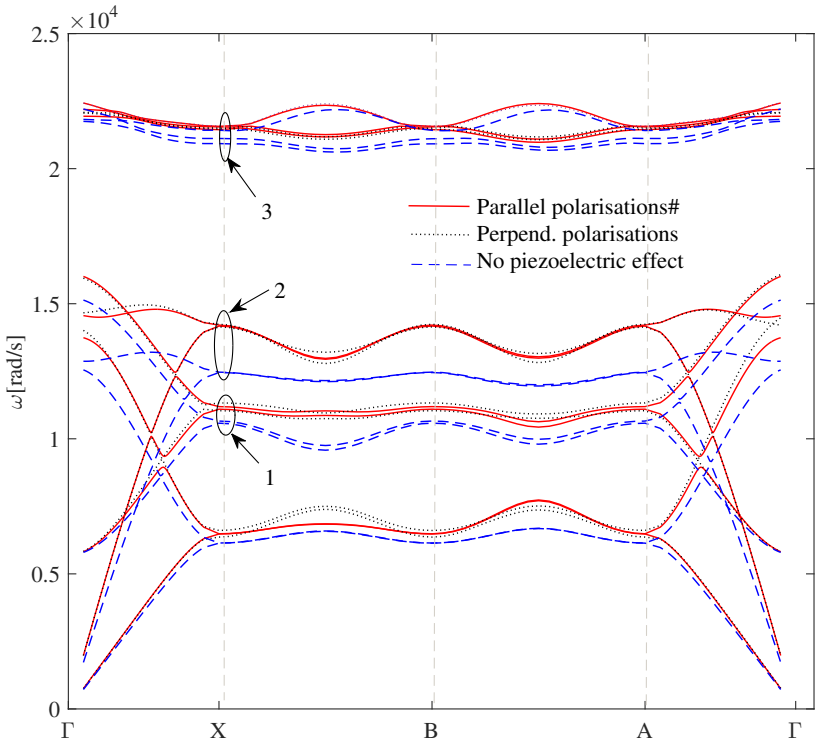

Fig. 3.3 *Dispersion diagrams along the* ΓXMBAΓ *path within the first Brillouin. With reference to Fig. 3.2(a) and 3.2(b), black dotted lines correspond to perpendicular polarisations and red solid lines refer to parallel polarisations. The dashed blue curves correspond to the perpendicular polarisation checkerboard for which piezoelectric coupling tensor has been set to zero, while leaving stiffness and dielectric matrices unchanged. The materials used in these computations are PZT (the physical parameters are listed in Table 3.1) and PA66. The side of the square is* $L = 0.5$ m.

Bloch-Floquet waves are performed along the path ΓXBAΓ of Fig. 3.2(c).

For parallel polarisations (solid red lines), the dispersion curves along XB do not coincide with those along BA. This is due to the symmetry properties of the unit cell with parallel polarisations in Fig. 3.2(a). Specifically, the unit cell in Fig. 3.2(a) is symmetric with respect to the diagonal passing through the white squares. In addition to this symmetry, the unit cell with perpendicular polarisations (see Fig. 3.2(b)) exhibits $\pi-$ rotational symmetry around its centre. Finally, the configuration in which the piezoelectric effect has been set to zero is symmetric with respect to both diagonals and is $\pi-$rotationally invariant around the centre. These symmetries are responsible for the identity of the dispersion curves along XB and BA for unit cells with perpendicular polarisations and absence of polarisation.

The high contrast between mechanical properties of the two materials produces a total band gap in Fig. 3.3. In addition, we emphasise that the relative orientation of the piezoelectric polarisations influences the opening of partial band gaps along ΓX and $A\Gamma$ paths - *cf.* red solid and black dotted lines.

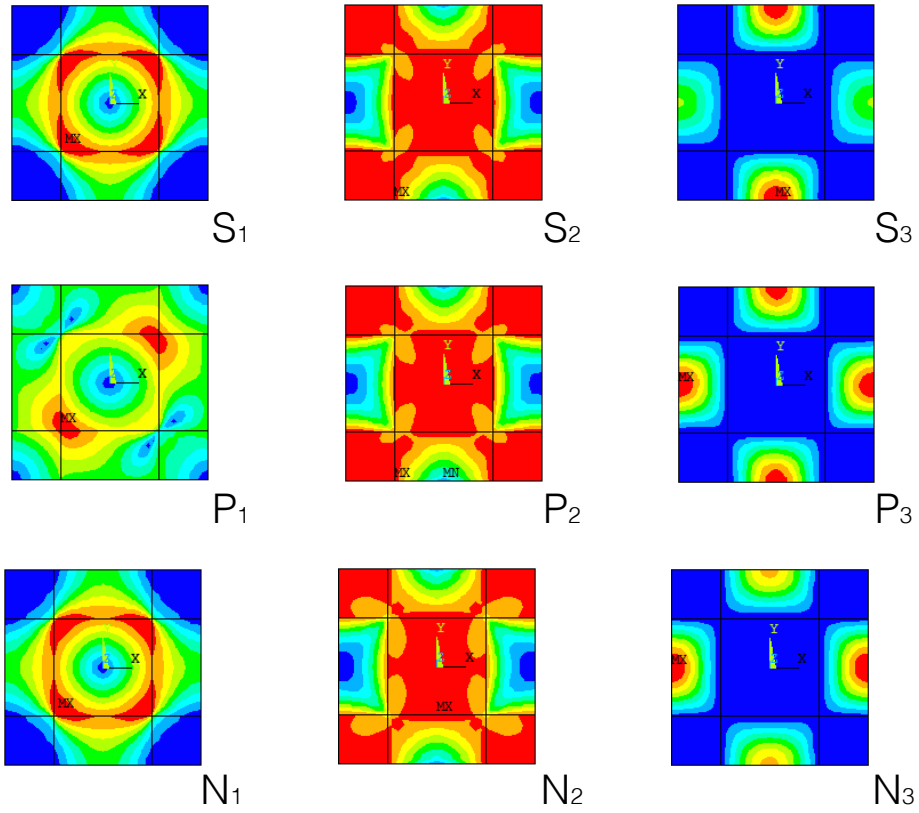

Fig. 3.4 *Moduli of the displacement of Bloch waves over the unit cell. The colour map spans from blue for minimum values to deep red to maximum values. S (perpendicular polarisations), P (parallel polarisations) and N (no piezoelectric effect) refer to the cases in Fig. 3.3. The indices* $j = \{1,2,3\}$ *correspond to the frequency regions marked in Fig. 3.3 (b) in correspondence of the X point within the Brillouin zone. For region 1 and 2 we here report eigenmodes corresponding to the lowest eigenfrequencies; for region 3 the eigenmodes corresponding to the highest eigenfrequencies are selected. Specifically for* S_j *with* $j = \{1,2,3\}$ *the angular frequencies are* $\omega = 11090.8(6), 14165.7(3), 21555.8(5)$ rad/s*, respectively; for* P_j *with* $j = \{1,2,3\}$ *the angular frequencies are* $\omega = 11047.0(8), 14134.1(0),$ $21566.7(1)$ rad/s*, respectively; for* N_j *with* $j = \{1,2,3\}$ *the angular frequencies are* $\omega = 10572.6(4), 12446.1(4), 21393.7(6)$ rad/s*, respectively.*

In Fig. 3.4, we show the modulus of Bloch-Floquet displacement waves, supported by the checkerboard piezoelectric structure. The labels S_j,P_j, N_j with $j = \{1,2,3\}$ are used here to identify the three representative groups of Bloch-Floquet waves, which correspond to the frequency regions marked as 1,2,3, in the dispersion diagram 3.3. Here S_j eigenmodes correspond to orthogonal polarisation configurations, P_j waveforms correspond to the case of parallel polarisation, whereas the N_j waveforms are obtained in the absence of piezoelectric effect, and with stiffness and dielectric matrices as in the case of perpendicular polarisations.

For the low-frequency region ($j = 1$), the identified waveforms for non-polarised materials (N_1) and for the checkerboard with the orthogonal polarisation (S_1), apart from piezoelectric stiffening resulting in the higher frequency of waveform S_1, are very similar. The similarity is due to the fact that, although the piezoelectric coupling has been set to zero in N_j, the remaining stiffness tensors are the same as in S_j. The case of parallel polarisation (P_j) shows significant differences, clearly indicating preferential directions linked to the choice of the polarisation vectors.

In Fig. 3.4, it is also shown that the piezoelectric effect depends on the frequency range. In particular, the group S_2, P_2, N_2 includes waveforms of similar shape for parallel polarisations and absence of piezoelectric effect, whereas the change is more pronounced in the transition from the orthogonal polarisation (S_2) to the parallel polarisation (P_2). The higher frequency group of eigenmodes (S_3, P_3, N_3) shows examples of waveforms concentrated in the non-piezoelectric phase.

3.3 Summarising remarks on chapter 3

In summary, we studied the in-plane vector problem of elasticity of a checkerboard-like periodic piezoelectric structure with different configurations of the polarisation vectors lying in-plane. In section 3.1 we have derived the partial differential equations for the in-plane elasticity problem coupled to the out-of-plane magnetic field for $x-$polarised and $y-$polarised piezoelectric materials. The partial differential equations are complemented with perfect contact conditions, charge-free interface conditions and Bloch-Floquet conditions.

The Bloch-Floquet frequency dispersion curves and corresponding examples of Bloch-Floquet waves have been evaluated and analysed in section 1.3. The focus was there on qualitative and quantitative differences in the dispersive properties and eigenmodes of periodic checkerboard structures with different orientations and magnitudes of the polarisation vectors.

In the next chapter we propose a novel doubly periodic lattice system which contains chiral resonators. This provides a mechanism of coupling between the dilatational and shear wave forms.

Chapter 4

Shear and pressure waves in lattices with tilted inertial resonators

In this chapter, we consider a vibrating triangular mass-truss lattice whose unit cell contains a resonator of a triangular shape. A representation of the lattice is given in Fig. 4.1(a) and details of the geometry of the resonators are represented in Fig. 4.1(b). The resonators are connected to the triangular lattice by trusses. Each resonator is tilted, *i.e.* it is rotated with respect to the triangular lattice's unit cell through an angle ϑ_0. This geometrical parameter is responsible for the emergence of a resonant mode in the Bloch spectrum for elastic waves and strongly influences the dispersive properties of the lattice.

The formulation of the spectral problem together with the governing equations for Bloch-Floquet waves are described in section 4.1.

In section 4.2 we specify the chiral geometry of the resonator and analyse its dynamic behaviour. Static degeneracy for a single resonator is identified as linked to the $\vartheta_0 = 0$ (untilted) configuration. Possible ways to overcome this limitation are described, including finite tilting ($\vartheta_0 \neq 0$) and the introduction of flexible links.

Section 4.3 is primarily concerned with the derivation of the dispersion equations and its solution. Specifically, a detailed analysis of the dispersion diagrams, which show the radian frequency as a function of the Bloch vector is provided. We identify standing waves and examine the effects of the orientation of the resonator on the dispersive properties of the lattice. Slowness contours and results concerning dynamic anisotropy are also presented in section 4.3.

In section 4.4 we examine the dynamic behaviour of the lattice in which the orientation of the resonators is non-uniform. Specifically, we compare the dispersive properties of the triangular lattice with one resonator per unit cell with those of an oblique lattice whose unit

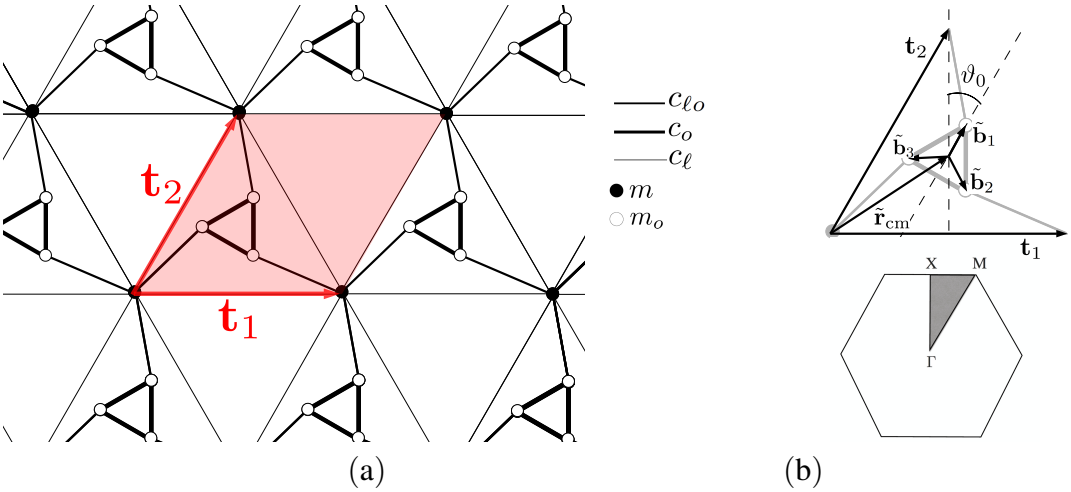

(a) (b)

Fig. 4.1 *Panel (a): A schematic representation of the triangular elastic lattice containing resonators; the unit cell of the lattice is highlighted in red. Panel (b), top: The vectors $\boldsymbol{t}_1$ and $\boldsymbol{t}_2$ are the primitive vectors of the triangular mass-truss lattice; the vector $\tilde{\boldsymbol{r}}_{\mathrm{cm}}$ describes the rest position of the centre of mass of the resonator; the tilting angle ϑ_0 describes the rotation of the resonator about $\tilde{\boldsymbol{r}}_{\mathrm{cm}}$; the vectors $\tilde{\boldsymbol{b}}_1$, $\tilde{\boldsymbol{b}}_2$ and $\tilde{\boldsymbol{b}}_3$ identify the rest positions for the masses m_o, relative to $\tilde{\boldsymbol{r}}_{\mathrm{cm}}$. Panel (b), bottom: The first Brillouin zone for the triangular lattice and the irreducible region (grey shaded region).*

cell contains two tilted resonators. A difference in the tilting angles of the unit cell of the oblique lattice is studied as an additional tuning parameter of the dispersive properties.

4.1 Formulation of the problem and description of geometry

Before studying the dynamical properties of the lattice system, it is necessary to introduce some notation, the geometry and the equations of motion. For the sake of simplicity, we restrict ourselves to the study of triangular lattices; such lattices are particularly interesting as they are statically isotropic but exhibit strong dynamic anisotropy at finite frequencies, as already outlined in 1.4.1. Subsequently, we specify the geometry and physical parameters of the resonators embedded in the triangular lattice unit cell - see Fig. 4.1. We conclude this section by stating the form of the equation of motion for a general two-dimensional micro-structured lattice made of point masses and massless trusses.

4.1.1 Geometry of a resonator

The centre of mass of the triangular resonator is located at the point with position vector $\tilde{\boldsymbol{r}}_{\mathrm{cm}}$, as in Eq. (1.72), relative to the bottom left nodal point of the unit cell (Fig. 4.1(a)). The

vector is schematically reported in Fig. 4.1(b). The vector $\tilde{\boldsymbol{b}}_i$ with $i=\{1,2,3\}$ shown in Fig. 4.1(b), is the position vector of the i^{th} mass relative to the centre of mass $\tilde{\boldsymbol{r}}_{\text{cm}}$ in Eq. (1.72). The explicit expression is

$$\tilde{\boldsymbol{b}}_i = b\hat{\mathscr{R}}_i\tilde{\boldsymbol{\beta}}_1 = b\hat{\mathscr{R}}_i\begin{pmatrix}\sin\vartheta_0\\ \cos\vartheta_0\end{pmatrix},\quad \text{with}\quad \hat{\mathscr{R}}_i=\hat{\mathscr{R}}_\vartheta\big|_{\vartheta=2\pi(i-1)/3}, \tag{4.1}$$

where ϑ_0 is the tilting angle, $b=\ell/\sqrt{3}$, and

$$\hat{\mathscr{R}}_\vartheta=\begin{pmatrix}\cos\vartheta & \sin\vartheta\\ -\sin\vartheta & \cos\vartheta\end{pmatrix}, \tag{4.2}$$

is the clockwise rotation matrix. It follows that the i^{th} mass belonging to the *tilted inertial resonator* (TIR), embedded in an arbitrarily chosen unit cell $\boldsymbol{n}$, is located at

$$\tilde{\boldsymbol{x}}_i^{(\boldsymbol{n})}=\tilde{\boldsymbol{x}}_0^{(\boldsymbol{n})}+\tilde{\boldsymbol{r}}_{\text{cm}}+\tilde{\boldsymbol{b}}_i, \tag{4.3}$$

where $\tilde{\boldsymbol{x}}_0^{(\boldsymbol{n})}$ are the nodal point of the hosting triangular lattice, and $\tilde{\boldsymbol{r}}_{\text{cm}}$ and $\tilde{\boldsymbol{b}}_i$, $i=\{1,2,3\}$, are given in Eqs (1.72) and (4.1) respectively.

The vector linking the triangular lattice to the i^{th} mass of the TIR (abbreviation for "Tilted Inertial Resonator") in the reference cell $\boldsymbol{n}=\boldsymbol{0}$ is

$$\tilde{\boldsymbol{\alpha}}_i=\hat{\mathscr{R}}_i\tilde{\boldsymbol{\alpha}}_1,\ \text{with}\ \tilde{\boldsymbol{\alpha}}_1=\boldsymbol{t}_2-\tilde{\boldsymbol{x}}_1^{(\boldsymbol{0})}=\begin{pmatrix}b\sin\vartheta_0\\ b\cos\vartheta_0-B\end{pmatrix}, \tag{4.4}$$

where $B=L/\sqrt{3}$ and the matrix $\hat{\mathscr{R}}_i$ is introduced in Eq. (4.1). For every $i=\{1,2,3\}$, the norm of the vectors in Eq. (4.4) is

$$\ell_r=||\tilde{\boldsymbol{\alpha}}_i||=\frac{1}{\sqrt{3}}\sqrt{L^2+\ell^2-2\ell L\cos(\vartheta_0)}. \tag{4.5}$$

Given the set of vectors (4.1) and (4.4), we introduce the corresponding projector matrices along the link directions of the lattice

$$\begin{aligned}&\hat{\pi}_1=\frac{1}{\ell^2}\left(\tilde{\boldsymbol{b}}_3-\tilde{\boldsymbol{b}}_2\right)\otimes\left(\tilde{\boldsymbol{b}}_3-\tilde{\boldsymbol{b}}_2\right),\quad \hat{\pi}_2=\frac{1}{\ell^2}\left(\tilde{\boldsymbol{b}}_1-\tilde{\boldsymbol{b}}_3\right)\otimes\left(\tilde{\boldsymbol{b}}_1-\tilde{\boldsymbol{b}}_3\right),\quad \hat{\pi}_3=\frac{1}{\ell^2}\left(\tilde{\boldsymbol{b}}_1-\tilde{\boldsymbol{b}}_3\right)\otimes\left(\tilde{\boldsymbol{b}}_1-\tilde{\boldsymbol{b}}_3\right),\\ &\hat{\Pi}_i=\frac{1}{\ell_r^2}\tilde{\boldsymbol{\alpha}}_i\otimes\tilde{\boldsymbol{\alpha}}_i,\quad i=\{1,2,3\}.\end{aligned} \tag{4.6}$$

In addition, the projector matrices $\hat{\tau}_i$, $i=\{1,2,3\}$, along the triangular lattice link directions $\boldsymbol{t}_1$, $\boldsymbol{t}_2$ and $\boldsymbol{t}_3=\boldsymbol{t}_1-\boldsymbol{t}_2$ in Eq. (1.60) have been introduced in Eq. (1.65).

4.1.2 Truss structure

The triangular lattice is formed from an array of point masses located at $\tilde{\boldsymbol{x}}_0^{(\boldsymbol{n})}$ and connected to neighboring masses by thin elastic rods. The rods are assumed to be massless and extensible, with longitudinal stiffness c_ℓ, but not flexible, *i.e.* they are trusses. The links are represented in Fig. 4.1(a) by thin solid lines. Additionally, each mass is connected to three resonators by rods of the same type as the ambient lattice and longitudinal stiffness $c_{\ell o}$; these links are denoted by the solid lines of intermediate thickness in Fig. 4.1(a).

The resonators themselves are composed of three point masses of magnitude m_o, located at vertices of a smaller equilateral triangle, and connected by massless trusses of longitudinal stiffness c_o; these trusses are indicated by the thick solid lines in Fig. 4.1(a). The TIRs are constrained such that they do not cross the links of the exterior lattice or those connecting the resonator to the ambient lattice. It is easy to demonstrate that the constraints

$$0 < \frac{\ell}{L} < \frac{1}{2} \quad \text{and} \quad |\vartheta_0| < \vartheta_{\max} = \arccos\left(\frac{\ell}{L}\right), \tag{4.7}$$

are sufficient to ensure the aforementioned conditions.

The solution to the Bloch-Floquet problem associated with a general lattice unit cell was studied in [56]. For the case of massless trusses studied here, the Bloch-Floquet problem for time-harmonic waves of angular frequency ω can be reduced [56] to the algebraic system

$$\left[\hat{\Sigma}'(\boldsymbol{k}) - \omega^2 \hat{\mathscr{M}}'\right] \boldsymbol{U}'_{\boldsymbol{k}} = \boldsymbol{0}, \tag{4.8}$$

where $\hat{\Sigma}'_{\boldsymbol{k}}$ is a Hermitian positive semi-definite matrix containing information about the geometry of the lattice and stiffness of the links and depends on the Bloch vector $\boldsymbol{k}$. The eigenvector $\boldsymbol{U}'(\boldsymbol{k}) \in \mathbb{C}^{dq}$ defines the displacement amplitudes of the masses; for a lattice with truss-like links d is the spatial dimension and q is the number of masses per unit cell. The matrix $\hat{\mathscr{M}}'$ is diagonal with entries corresponding to the magnitude of the masses in the unit cell. Finally, the multiplicative factor $e^{-i\omega t}$ is omitted but understood.

For the geometry considered here, and shown in Fig. 4.1(a), $d = 2$ and $q = 4$. Therefore the algebraic problem (4.8) is eight-dimensional. The column vector $\boldsymbol{U}'(\boldsymbol{k})$, introduced in (4.8) may be written in the form

$$\boldsymbol{U}'(\boldsymbol{k}) = \left(\boldsymbol{u}_0^{\mathrm{T}}(\boldsymbol{k}), \quad \boldsymbol{u}_1^{\mathrm{T}}(\boldsymbol{k}), \quad \boldsymbol{u}_2^{\mathrm{T}}(\boldsymbol{k}), \quad \boldsymbol{u}_3^{\mathrm{T}}(\boldsymbol{k})\right)^{\mathrm{T}}, \tag{4.9}$$

where $\boldsymbol{u}_i(\boldsymbol{k})$ with $i = \{0,1,2,3\}$ are the displacement amplitude vectors of the masses.

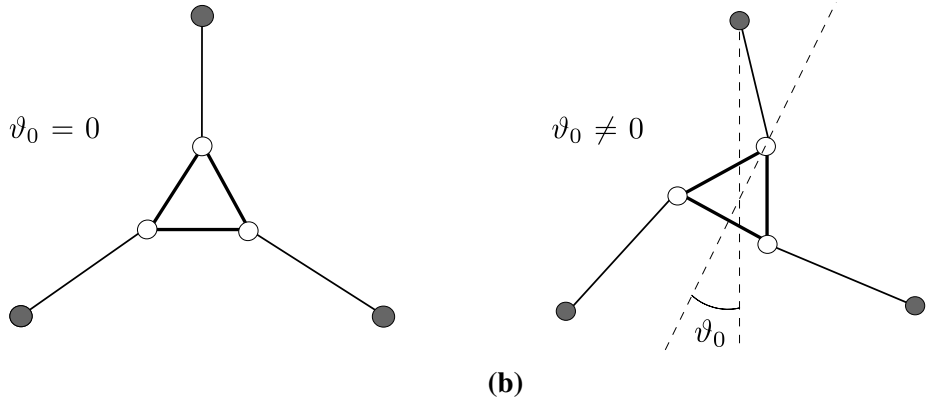

Fig. 4.2 *Schematic representations of a single hinged resonator. In each panel, the hinges are represented by grey circles, located at the vertices of a equilateral triangle of side L. In each panel, the resonators form an equilateral triangle of side ℓ, whose masses m_o (empty circles) are located at its vertices. Panel (a) represents the degenerate case corresponding to $\vartheta_0 = 0$; and panel (b) shows the non-degenerate case corresponding to $\vartheta_0 \neq 0$.*

4.2 A single resonator: rotational wave-forms

In this section, we analyse a single hinged resonator (see Fig. 4.2). In this context, we identify a degeneracy associated with $\vartheta_0 = 0$, shown in Fig 4.2(a). We show that the degeneracy disappears when a non-zero tilting angle is considered - see the chiral geometry in Fig. 4.2(b). We assume that the resonator is a rigid-body and present the corresponding natural frequencies. We conclude this section with a physical interpretation of the degeneracy corresponding to non-tilted resonators.

We consider a single TIR and assume hinged conditions at the vertices of an equilateral triangle of side length L (see Fig. 4.2(a)). The equations of motion for the time-harmonic displacements of the masses at the vertices of the TIR are

$$\left[\hat{\sigma}' - \omega^2 m_0 \hat{I}_6\right] \boldsymbol{U} = \boldsymbol{0}, \tag{4.10}$$

where $\boldsymbol{U} = (\boldsymbol{u}_1, \boldsymbol{u}_2, \boldsymbol{u}_3)^{\mathrm{T}}$ contains the aforementioned displacement amplitudes, m_o is the mass at every vertex, ω is the angular frequency, $\hat{\sigma}'$ is the stiffness matrix, and $\hat{I}_6$ is the 6×6 identity matrix. In Eq. (4.10), the stiffness matrix is

$$\hat{\sigma}' = \begin{pmatrix} c_{\ell o}\hat{\Pi}_1 + c_o\hat{\pi}_2 + c_o\hat{\pi}_3 & -c_o\hat{\pi}_3 & -c_o\hat{\pi}_2 \\ -c_o\hat{\pi}_3 & c_{\ell o}\hat{\Pi}_2 + c_o\hat{\pi}_1 + c_o\hat{\pi}_3 & -c_o\hat{\pi}_1 \\ -c_o\hat{\pi}_2 & -c_o\hat{\pi}_1 & c_{\ell o}\hat{\Pi}_3 + c_o\hat{\pi}_2 + c_o\hat{\pi}_1 \end{pmatrix}, \tag{4.11}$$

where the projectors $\hat{\Pi}_i$ and $\hat{\pi}_i$, are given in Eq. (4.6).

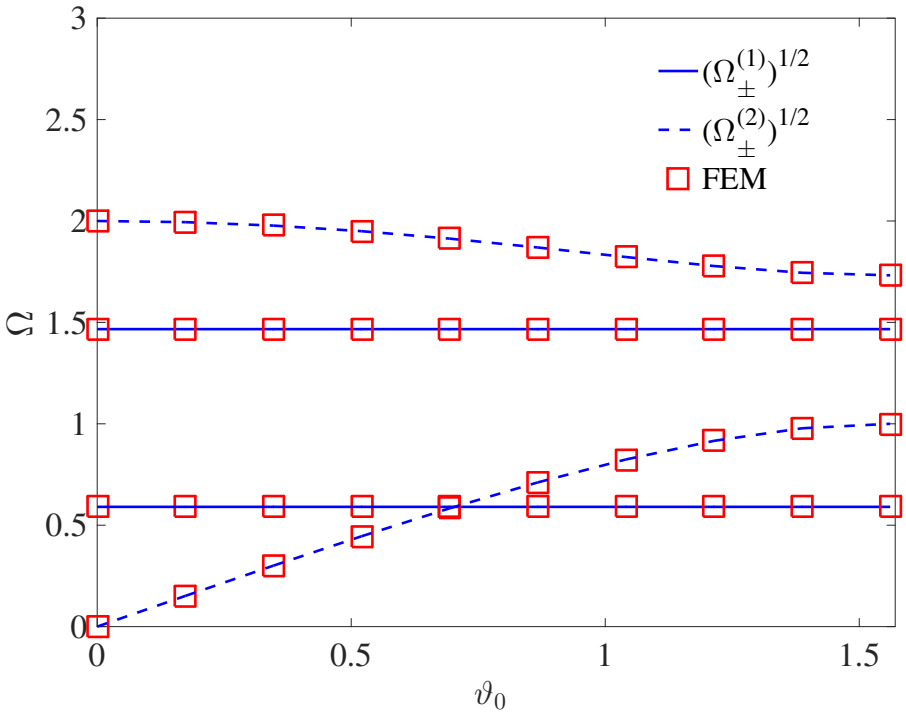

Fig. 4.3 *The natural frequencies of a single resonator where we compare Eqs. (4.12) (blue lines) with FEM results (red squares). We take small ℓ and vary ϑ_0. The remaining parameters are $m_o = 1$, $L = 1$, $c_o = c_{\ell o} = 1$.*

4.2.1 Non-degenerate case

We use the notation $\Omega = \omega^2$. For $\vartheta_0 \neq 0$, solving the eigenvalue problem (4.10) with stiffness matrix (4.11) gives

$$\begin{aligned}
\Omega_\pm^{(1)} &= \frac{1}{2}\frac{c_{\ell o}}{m_o}\left[1+\frac{3}{2}\frac{c_o}{c_{\ell o}} \pm \sqrt{1+\frac{9}{4}\left(\frac{c_o}{c_{\ell o}}\right)^2}\right], \\
\Omega_\pm^{(2)} &= \frac{1}{2}\frac{c_{\ell o}+3c_o}{m_o}\left[1 \pm \sqrt{1-4\frac{L^2}{\ell_r^2}\frac{c_o c_{\ell o}}{(c_{\ell o}+3c_o)^2}\sin^2\vartheta_0}\right],
\end{aligned} \tag{4.12}$$

where the first two eigenvalues have multiplicity two, and the last two eigenvalues are of multiplicity one; ℓ_r is given by (4.5). This demonstrates that for $\vartheta_0 \neq 0$ both the structure and the corresponding stiffness matrix are non-degenerate. For very small resonators $\ell/L \to 0$,

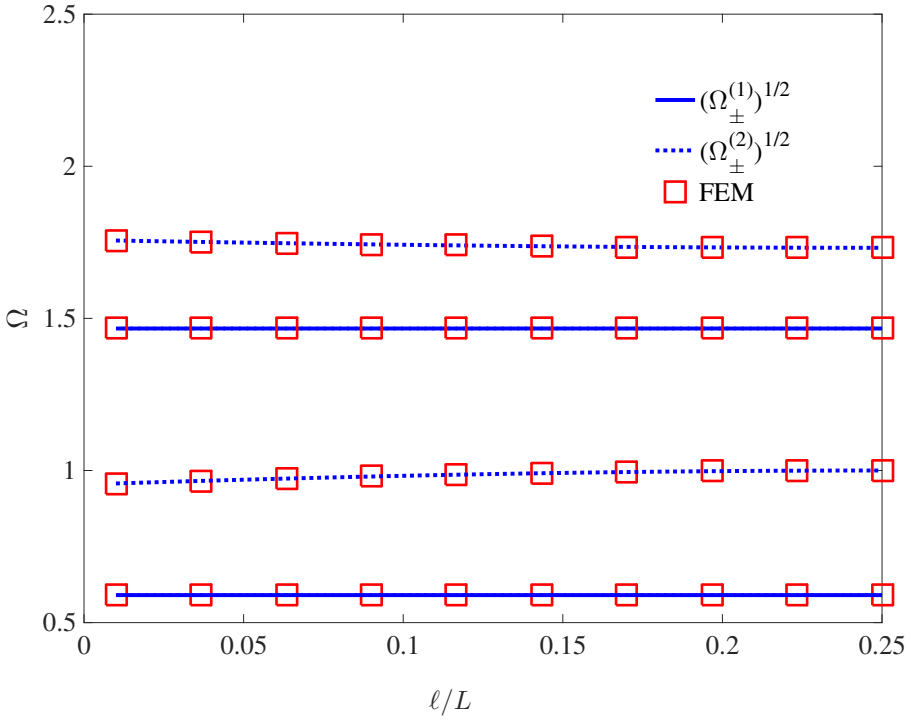

Fig. 4.4 *The natural frequencies of a single resonator. We compare Eqs. (4.12) (blue lines) with FEM results (red squares). We fix* $\vartheta_0 \approx 1.32$ *and vary* ℓ*. The remaining parameters are* $m_o = 1$*,* $L = 1$*,* $c_o = c_{\ell o} = 1$*.*

$\Omega_{\pm}^{(2)}$ has the limit

$$\lim_{\ell/L\to 0} \Omega_{\pm}^{(2)} = \frac{1}{2}\frac{c_{\ell o}+3c_o}{m_o}\left[1 \pm \sqrt{1-\frac{12c_o c_{\ell o}}{(c_{\ell o}+3c_o)^2}\sin^2\vartheta_0}\right], \tag{4.13}$$

whereas $\Omega_{\pm}^{(1)}$ is independent of ℓ/L. The absence of degeneracy at non-zero tilting angles and as ℓ is varied, is illustrated by Figs 4.3 and 4.4, respectively. In Fig. 4.3, we compare the frequencies (4.12) (blue lines) with FEM numerical results obtained using COMSOL Multiphysics® (red squares), as a function of ϑ_0 and for at a fixed small value of ℓ. In Fig. 4.4, a similar comparison is done by fixing $\vartheta_0 \simeq 1.32$ and varying ℓ.

4.2.2 Degenerate case

For $\vartheta_0 = 0$, we observe that $\Omega_-^{(2)} = 0$, as illustrated in Fig. 4.3. Therefore, the structure represented in Fig. 4.2(a) is degenerate, that is

$$\det\left(\hat{\sigma}'\right) = 0, \tag{4.14}$$

where the stiffness matrix $\hat{\sigma}'$ is introduced in Eq. (4.11). Degeneracy is obtained also in the trivial limits for a very soft resonator, *i.e.* $c_o/c_{\ell o} \to 0$, and non-zero tilting angle. In this case, we get $\Omega_-^{(1)} = \Omega_-^{(2)} = 0$.

4.2.3 Rigid-body approximation

Here we assume that

$$c_o/c_{\ell o} \gg 1 \quad \text{and} \quad c_o/c_\ell \gg 1, \tag{4.15}$$

i.e. the TIR's trusses are inextensible. In turn, this implies that the lengths of the links connecting the vertices of the TIR are fixed to ℓ. Specifically, three spatial degrees of freedom, corresponding to the relative motion of the three vertices of the TIRs, do not contribute to the propagation of Bloch-Floquet waves. Therefore, in the limit (4.15), Eq. (4.10) can be simplified further. In fact, the motion of a single rigid hinged resonator can be described by a time-harmonic in-plane displacement of the centre of mass and an angular displacement about the centre of mass. The natural frequencies of the system are

$$\Omega_{\text{cm}} = \frac{3}{2}\frac{c_{\ell o}}{M} \text{ and } \Omega_\vartheta = \frac{c_{\ell o}\ell^2}{I}\frac{\sin^2\vartheta_0}{1+\ell^2/L^2-2\ell/L\cos\vartheta_0}, \tag{4.16}$$

where $M = 3m_o$ and $I = m_o\ell^2$. In Eq. (4.16), Ω_{cm} corresponds to the displacement of the centre of mass and is consistent with Eq. (1.79), *i.e.* the natural frequency of a single point resonator of mass $m_b = M = 3m_o$ considered in section 1.4.1.The role of the resonator's microstructure emerges in the eigenfrequency Ω_ϑ, which describes the angular displacement about the centre of mass. We observe that

$$\Omega_{\text{cm}} = \lim_{c_o\to+\infty}\Omega_\pm^{(1)}, \quad \Omega_\vartheta = \lim_{c_o\to+\infty}\Omega_-^{(2)} \text{ and } \lim_{c_o\to+\infty}\Omega_+^{(2)} = +\infty, \tag{4.17}$$

where $\Omega_\pm^{(1)}$ and $\Omega_\pm^{(2)}$ are eigenvalues given in Eq. (4.12) for the hinged single resonator with soft ligaments. Eqs (4.17) show that the eigenvalues for a single rigid hinged resonator can be retrieved as a limiting case from the eigenvalues in Eqs (4.12). The additional diverging eigenvalue corresponds to the limiting case of high stiffness between the TIR's vertices

and thus can be disregarded in the dynamics of the problem. In addition, we note that the degeneracy at zero tilting angle persists, as $\Omega_\vartheta = 0$ for $\vartheta_0 = 0$. This observation further emphasises the fact that a chiral geometry of the ligaments is a necessary condition to avoid degeneracy, if thin and non-bendable links are assumed. We finally observe that the eigenvalues (4.16) coincide for the tilting angle

$$\vartheta_0^* = \arccos \frac{1}{2}\left(\frac{\ell}{L}+1\right). \tag{4.18}$$

4.2.4 Flexible links

We would like to remark that the degeneracy corresponding to Eq. (4.14), arises from neglecting bending deformations of the hinged links. Conversely, a finite bending stiffness $B = E\mathscr{I}$, where E represents the Young's modulus and $\mathscr{I}$ is the second moment of inertia of the beam, would lead to a different frequency calculated as follows. We allow the links between the hinges and the TIR to be flexible beams, with a given bending stiffness B. We assume that the longitudinal elongations of the links are negligible. The TIR is assumed to be a rigid-body. We fix the y-axis of a Cartesian coordinate system to be parallel to the top link in Fig. 4.2(a), pointing downwards. We fix the origin to coincide with the top hinge. By symmetry considerations, each link produces the same torque on the rigid resonator. Hence, without loss of generality, it is sufficient to study a single beam, *e.g.* the one along the y-axis. The massless beam assumption implies that the flexural displacement is

$$\boldsymbol{w}(y) = w(y)\hat{\boldsymbol{x}} = \left(\mathscr{A}_0 + \mathscr{A}_1 y + \mathscr{A}_2 y^2 + \mathscr{A}_3 y^3\right)\hat{\boldsymbol{x}}, \tag{4.19}$$

where $\hat{\boldsymbol{x}}$ denote the unit vector along the x-axis and $\mathscr{A}_i$ are real constants to be determined from the conditions at the ends of the beam. Hinged junction conditions at $y = 0$ read

$$w(0) = w''(0) = 0 \Longrightarrow \mathscr{A}_0 = \mathscr{A}_2 = 0. \tag{4.20}$$

We denote by $\vartheta(t)$ the angular oscillation of the resonator around $\vartheta_0 = 0$ and assume positive angles in the clockwise direction. At the junction between the resonator and the beam, located at $y = (L-\ell)/\sqrt{3}$, clamped conditions apply. Clamped conditions can be expressed to leading order in $\vartheta(t)$ as

$$w(y)\big|_{y=(L-\ell)/\sqrt{3}} \simeq \frac{\vartheta(t)\ell}{\sqrt{3}} \quad \text{and} \quad w'(y)\big|_{y=(L-\ell)/\sqrt{3}} = -\vartheta(t). \tag{4.21}$$

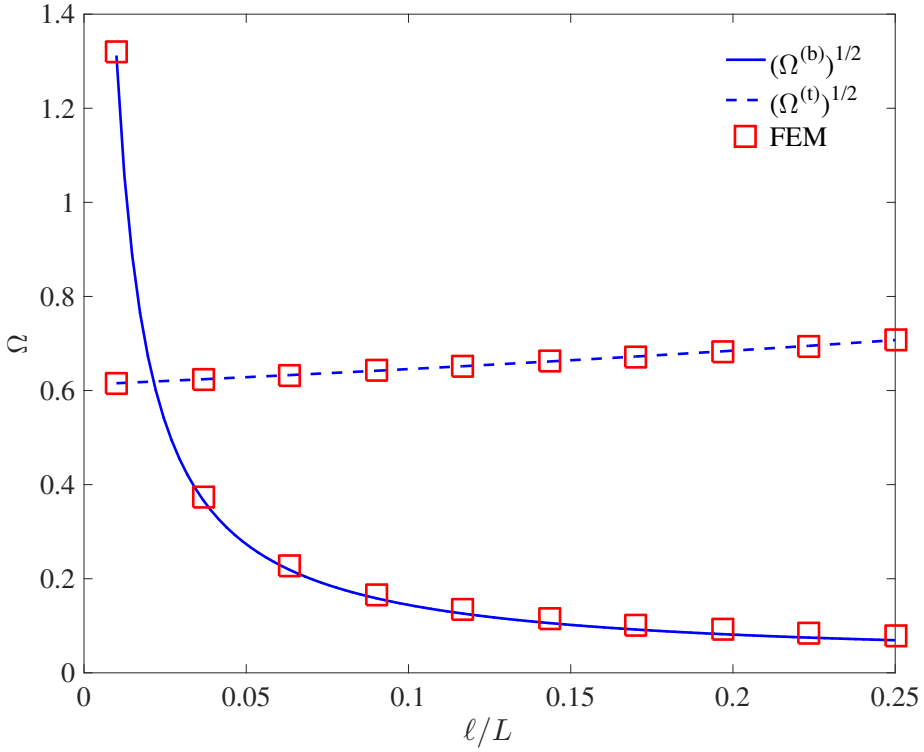

Fig. 4.5 *The natural frequencies of a single resonator. In panels (a) and (b) we compare Eqs. (4.12) (blue lines) with FEM results (red squares). We compare the analytical predictions (4.25) and (4.26) (solid blue and dashed blue line, respectively) with FEM results (red squares) as a function of ℓ. We fix the Young's modulus to be $E_0 \approx 1.38 \times 10^3$ and the cross-sectional radius $r \approx 0.01$. The other parameters are $m_o = 1$ and $L = 1$.*

By substituting the expression (4.19) into Eqs (4.20) and (4.21), we get

$$\mathscr{A}_3 = -\frac{3}{2}\frac{L}{(L-\ell)^3}\vartheta(t) \quad \text{and} \quad \mathscr{A}_1 = \frac{L/2+\ell}{L-\ell}\vartheta(t). \tag{4.22}$$

The Newton equation for the small angular oscillations of the resonator is

$$I\frac{d^2\vartheta(t)}{dt^2} = 3\mathscr{M}, \tag{4.23}$$

where we have introduced the moment

$$\mathscr{M} = Bw''(y)\big|_{(L-\ell)/\sqrt{3}} = -\frac{3\sqrt{3}LB}{(L-\ell)^2}\vartheta(t), \tag{4.24}$$

exerted on the resonators by each of the three beams. The substitution of Eq. (4.24) into Eq. (4.23) gives time-harmonic solutions of angular frequency squared

$$\Omega^{(\mathrm{b})} = 9\sqrt{3}\frac{L}{\ell^2(L-\ell)^2}\frac{B}{m_o}. \tag{4.25}$$

Eq. (4.25) is a non-zero frequency at zero tilting angle, corresponding to the rotational motion of the resonator in Fig. 4.2(a) with flexible hinged links. Fig. 4.5 shows agreement between Eq. (4.25) (solid blue line) and FEM numerical results (red squares), as ℓ is varied. The translational frequency for a rigid resonator with hinged flexible links of Young's modulus E and cross-sectional surface $S = \pi r^2$ can be directly obtained from the first of Eqs (4.16). Its expression is

$$\Omega^{(\mathrm{t})} = \frac{\sqrt{3}}{2}\frac{S}{L-\ell}\frac{E}{m_o}, \tag{4.26}$$

and it is compared in Fig. 4.5 (blue dashed line) against FEM computations (red squares) as a function of ℓ.

4.3 Bloch-Floquet waves in a lattice with tilted resonators

Having examined the behaviour of a single resonator in the previous section, we now proceed to consider the dispersive properties of a two-dimensional triangular lattice with resonators; the geometry is shown in Fig. 4.1(a).

Equations of motion. The primary object of study is the algebraic system (4.8), which can be derived using the Newton equations for the nodal points of the structured lattice in Fig. 4.1(a). The displacements of the masses which compose the TIR (white hollow circles

in Fig. 4.1(a)) obey the following Newton equations

$$\begin{aligned}
m_o\omega^2\boldsymbol{u}_1^{(\boldsymbol{n})}(\boldsymbol{k}) &= c_{\ell o}\,\hat{\Pi}_1\left(\boldsymbol{u}_1^{(\boldsymbol{n})}(\boldsymbol{k})-\boldsymbol{u}_0^{(\boldsymbol{n}+\boldsymbol{p}_2)}(\boldsymbol{k})\right)\\
&\quad + c_o\hat{\pi}_3\left(\boldsymbol{u}_1^{(\boldsymbol{n})}(\boldsymbol{k})-\boldsymbol{u}_2^{(\boldsymbol{n})}(\boldsymbol{k})\right)+c_o\hat{\pi}_2\left(\boldsymbol{u}_1^{(\boldsymbol{n})}(\boldsymbol{k})-\boldsymbol{u}_3^{(\boldsymbol{n})}(\boldsymbol{k})\right),\\
m_o\omega^2\boldsymbol{u}_2^{(\boldsymbol{n})}(\boldsymbol{k}) &= c_{\ell o}\,\hat{\Pi}_2\left(\boldsymbol{u}_2^{(\boldsymbol{n})}(\boldsymbol{k})-\boldsymbol{u}_0^{(\boldsymbol{n}+\boldsymbol{p}_1)}(\boldsymbol{k})\right)\\
&\quad + c_o\hat{\pi}_3\left(\boldsymbol{u}_2^{(\boldsymbol{n})}(\boldsymbol{k})-\boldsymbol{u}_1^{(\boldsymbol{n})}(\boldsymbol{k})\right)+c_o\hat{\pi}_1\left(\boldsymbol{u}_2^{(\boldsymbol{n})}(\boldsymbol{k})-\boldsymbol{u}_3^{(\boldsymbol{n})}(\boldsymbol{k})\right),\\
m_o\omega^2\boldsymbol{u}_3^{(\boldsymbol{n})}(\boldsymbol{k}) &= c_{\ell o}\,\hat{\Pi}_3\left(\boldsymbol{u}_3^{(\boldsymbol{n})}(\boldsymbol{k})-\boldsymbol{u}_0^{(\boldsymbol{n})}(\boldsymbol{k})\right),\\
&\quad + c_o\hat{\pi}_2\left(\boldsymbol{u}_3^{(\boldsymbol{n})}(\boldsymbol{k})-\boldsymbol{u}_1^{(\boldsymbol{n})}(\boldsymbol{k})\right)+c_o\hat{\pi}_1\left(\boldsymbol{u}_3^{(\boldsymbol{n})}(\boldsymbol{k})-\boldsymbol{u}_2^{(\boldsymbol{n})}(\boldsymbol{k})\right).
\end{aligned} \tag{4.27}$$

The displacement for the nodal point $\boldsymbol{n}$ of the triangular lattice (solid circles in Fig. 4.1(a)) is

$$\begin{aligned}
-m\omega^2\boldsymbol{u}_0^{(\boldsymbol{n})}(\boldsymbol{k}) &= c_\ell\,\hat{\tau}_1\left(\boldsymbol{u}_0^{(\boldsymbol{n}+\boldsymbol{p}_1)}(\boldsymbol{k})+\boldsymbol{u}_0^{(\boldsymbol{n}-\boldsymbol{p}_1)}(\boldsymbol{k})-2\boldsymbol{u}_0^{(\boldsymbol{n})}(\boldsymbol{k})\right)\\
&+ c_\ell\,\hat{\tau}_2\left(\boldsymbol{u}_0^{(\boldsymbol{n}+\boldsymbol{p}_2)}(\boldsymbol{k})+\boldsymbol{u}_0^{(\boldsymbol{n}-\boldsymbol{p}_2)}(\boldsymbol{k})-2\boldsymbol{u}_0^{(\boldsymbol{n})}(\boldsymbol{k})\right)\\
&+ c_\ell\,\hat{\tau}_3\left(\boldsymbol{u}_0^{(\boldsymbol{n}+\boldsymbol{p}_1-\boldsymbol{p}_2)}(\boldsymbol{k})+\boldsymbol{u}_0^{(\boldsymbol{n}+\boldsymbol{p}_2-\boldsymbol{p}_1)}(\boldsymbol{k})-2\boldsymbol{u}_0^{(\boldsymbol{n})}(\boldsymbol{k})\right)\\
&+ c_{\ell o}\,\hat{\Pi}_1\left(\boldsymbol{u}_1^{(\boldsymbol{n}-\boldsymbol{p}_2)}(\boldsymbol{k})-\boldsymbol{u}_0^{(\boldsymbol{n})}(\boldsymbol{k})\right)\\
&+ c_{\ell o}\,\hat{\Pi}_2\left(\boldsymbol{u}_2^{(\boldsymbol{n}-\boldsymbol{p}_1)}(\boldsymbol{k})-\boldsymbol{u}_0^{(\boldsymbol{n})}(\boldsymbol{k})\right)\\
&+ c_{\ell o}\,\hat{\Pi}_3\left(\boldsymbol{u}_3^{(\boldsymbol{n})}(\boldsymbol{k})-\boldsymbol{u}_0^{(\boldsymbol{n})}(\boldsymbol{k})\right).
\end{aligned} \tag{4.28}$$

In Eqs (4.27) and (4.28) we introduce the notation $\boldsymbol{p}_1=(1,0)^{\mathrm{T}}$ and $\boldsymbol{p}_2=(0,1)^{\mathrm{T}}$.

Bloch-Floquet conditions. Bloch-Floquet conditions for the displacements are

$$\boldsymbol{u}_i^{(\boldsymbol{n}+\boldsymbol{m})}(\boldsymbol{k})=e^{i\boldsymbol{k}\cdot\hat{\mathscr{T}}\boldsymbol{m}}\boldsymbol{u}_i^{(\boldsymbol{n})}(\boldsymbol{k}), \tag{4.29}$$

where $i=\{0,1,2,3\}$ and $\hat{\mathscr{T}}$ is the matrix whose columns coincide with the primitive vectors of the triangular lattice, $\boldsymbol{t}_1$ and $\boldsymbol{t}_2$ in Eq. (1.60). After imposing the Bloch-Floquet conditions

(4.29), Eqs (4.27) and (4.28) depend on nodal points in the cell $\boldsymbol{n}$, yielding

$$\begin{aligned}
m_o\omega^2\boldsymbol{u}_1(\boldsymbol{k}) &= c_{\ell o}\,\hat{\Pi}_1\left(\boldsymbol{u}_1(\boldsymbol{k})-e^{i\boldsymbol{k}\cdot\boldsymbol{t}_2}\boldsymbol{u}_0(\boldsymbol{k})\right)\\
&\quad + c_o\hat{\pi}_3\left(\boldsymbol{u}_1(\boldsymbol{k})-\boldsymbol{u}_2(\boldsymbol{k})\right)+c_o\hat{\pi}_2\left(\boldsymbol{u}_1(\boldsymbol{k})-\boldsymbol{u}_3(\boldsymbol{k})\right),\\
m_o\omega^2\boldsymbol{u}_2(\boldsymbol{k}) &= c_{\ell o}\,\hat{\Pi}_2\left(\boldsymbol{u}_2(\boldsymbol{k})-e^{i\boldsymbol{k}\cdot\boldsymbol{t}_1}\boldsymbol{u}_0(\boldsymbol{k})\right)\\
&\quad + c_o\hat{\pi}_3\left(\boldsymbol{u}_2(\boldsymbol{k})-\boldsymbol{u}_1^{(\boldsymbol{n})}(\boldsymbol{k})\right)+c_o\hat{\pi}_1\left(\boldsymbol{u}_2(\boldsymbol{k})-\boldsymbol{u}_3(\boldsymbol{k})\right),\\
m_o\omega^2\boldsymbol{u}_3(\boldsymbol{k}) &= c_{\ell o}\,\hat{\Pi}_3\left(\boldsymbol{u}_3(\boldsymbol{k})-\boldsymbol{u}_0(\boldsymbol{k})\right)\\
&\quad + c_o\hat{\pi}_2\left(\boldsymbol{u}_3(\boldsymbol{k})-\boldsymbol{u}_1(\boldsymbol{k})\right)+c_o\hat{\pi}_1\left(\boldsymbol{u}_3(\boldsymbol{k})-\boldsymbol{u}_2(\boldsymbol{k})\right).
\end{aligned}\tag{4.30}$$

and

$$\begin{aligned}
-m\omega^2\boldsymbol{u}_0(\boldsymbol{k}) &= 2c_\ell\;\hat{\tau}_1\left(\cos(\boldsymbol{k}\cdot\boldsymbol{t}_1)-1\right)\boldsymbol{u}_0(\boldsymbol{k})+2c_\ell\;\hat{\tau}_2\left(\cos(\boldsymbol{k}\cdot\boldsymbol{t}_2)-1\right)\boldsymbol{u}_0(\boldsymbol{k})\\
&\quad +2c_\ell\;\hat{\tau}_3\left(\cos(\boldsymbol{k}\cdot(\boldsymbol{t}_1-\boldsymbol{t}_2))-1\right)\boldsymbol{u}_0(\boldsymbol{k})+c_{\ell o}\,\hat{\Pi}_1\left(e^{-i\boldsymbol{k}\cdot\boldsymbol{t}_2}\boldsymbol{u}_1(\boldsymbol{k})-\boldsymbol{u}_0(\boldsymbol{k})\right)\\
&\quad +c_{\ell o}\,\hat{\Pi}_2\left(e^{-i\boldsymbol{k}\cdot\boldsymbol{t}_1}\boldsymbol{u}_2(\boldsymbol{k})-\boldsymbol{u}_0(\boldsymbol{k})\right)+c_{\ell o}\,\hat{\Pi}_3\left(\boldsymbol{u}_3(\boldsymbol{k})-\boldsymbol{u}_0(\boldsymbol{k})\right).
\end{aligned}\tag{4.31}$$

We emphasise that the index $(\boldsymbol{n})$ in Eqs (4.27) and (4.28) has been suppressed after the substitution of the Bloch-Floquet conditions (4.29). From Eqs. (4.30) and (4.31) follows the secular equation (4.8). Moreover the limit $m\to+\infty$ in Eq. (4.31) implies $\boldsymbol{u}_0(\boldsymbol{k})=\boldsymbol{0}$. From the substitution of $\boldsymbol{u}_0(\boldsymbol{k})=\boldsymbol{0}$ into (4.30), we obtain the equation of motion (4.10) for a single resonator whose stiffness matrix is given in Eq. (4.11).

Stiffness matrix. With reference to (4.8), the 8×8 stiffness matrix has the form

$$\hat{\boldsymbol{\Sigma}}'(\boldsymbol{k})=\begin{pmatrix}
\hat{\Sigma}_0(\boldsymbol{k}) & -c_{\ell o}\hat{\Pi}_1e^{-i\boldsymbol{k}\cdot\boldsymbol{t}_2} & -c_{\ell o}\hat{\Pi}_2e^{-i\boldsymbol{k}\cdot\boldsymbol{t}_1} & -c_{\ell o}\hat{\Pi}_3\\
-c_{\ell o}\hat{\Pi}_1e^{i\boldsymbol{k}\cdot\boldsymbol{t}_2} & \hat{\Sigma}_1 & -c_o\hat{\pi}_3 & -c_o\hat{\pi}_2\\
-c_{\ell o}\hat{\Pi}_2e^{i\boldsymbol{k}\cdot\boldsymbol{t}_1} & -c_o\hat{\pi}_3 & \hat{\Sigma}_2 & -c_o\hat{\pi}_1\\
-c_{\ell o}\hat{\Pi}_3 & -c_o\hat{\pi}_2 & -c_o\hat{\pi}_1 & \hat{\Sigma}_3
\end{pmatrix},\tag{4.32}$$

where we have introduced the following notation for the diagonal blocks

$$\begin{aligned}
\hat{\Sigma}_0(\boldsymbol{k}) &= -\sum_{i=1}^{3}\left[2c_\ell(\cos\boldsymbol{k}\cdot\boldsymbol{t}_i-1)\hat{\tau}_i-c_{\ell o}\hat{\Pi}_i\right]=\hat{\Sigma}_{\boldsymbol{k}}^{(\mathrm{TL})}+c_{\ell o}\sum_{i=1}^{3}\hat{\Pi}_i,\\
\hat{\Sigma}_1 &= c_{\ell o}\hat{\Pi}_1+c_o(\hat{\pi}_2+\hat{\pi}_3),\;\;\hat{\Sigma}_2=c_{\ell o}\hat{\Pi}_2+c_o(\hat{\pi}_1+\hat{\pi}_3),\;\;\text{and,}\\
\hat{\Sigma}_3 &= c_{\ell o}\hat{\Pi}_3+c_o(\hat{\pi}_1+\hat{\pi}_2).
\end{aligned}\tag{4.33}$$

The 2×2 stiffness matrix $\hat{\boldsymbol{\Sigma}}_{\boldsymbol{k}}^{(\mathrm{TL})}$ in Eq. (4.33) is the stiffness matrix for a triangular lattice (*c.f.* Eq. (1.68)). We emphasise that each element is a 2×2 block matrix, as defined in (4.6).

Degeneracy of the untilted lattice. We note that the submatrix obtained by removing the first column and row of block matrices in (4.32) is precisely the stiffness matrix of a single hinged resonator (4.11). Expanding the determinant of (4.32) over the first column results in a sum of four terms: three of them being proportional to $\det(\hat{\Pi}_i)$ and the fourth one to $\det(\hat{\sigma}')$. Recalling that the matrices $\hat{\sigma}'$ and $\hat{\Pi}_i$ (c.f. (4.6) and (4.11)) are degenerate when $\vartheta_0 = 0$, it is clear that (4.11) is also degenerate when $\vartheta_0 = 0$.

4.3.1 Rigid resonators

The limit case of a single rigid resonators, that is $c_o/c_{\ell o} \gg 1$ and $c_o/c_\ell \gg 1$, has been analysed in detail in section 4.2.3. Here we formulate the problem for a triangular lattice containing tilted resonators, where

$$c_o/c_{\ell o} \gg 1, \ \text{ and } \ c_o/c_\ell \gg 1. \tag{4.34}$$

Equations of motion. We write here the equations of motion for time-harmonic in-plane waves under the rigid-body assumptions (4.34) for the tilted resonators. The governing equations for the displacements of the masses which compose the TIR (black solid dots in Fig. 4.1(a)) can be rewritten from (4.27), yielding

$$\begin{aligned}
-m_o\omega^2\boldsymbol{u}_1^{(\boldsymbol{n})}(\boldsymbol{k}) &= c_{\ell o}\,\hat{\Pi}_1\left(\boldsymbol{u}_0^{(\boldsymbol{n}+\boldsymbol{p}_2)}(\boldsymbol{k}) - \boldsymbol{u}_1^{(\boldsymbol{n})}(\boldsymbol{k})\right) - \boldsymbol{s}_{12}(\boldsymbol{k}) + \boldsymbol{s}_{31}(\boldsymbol{k}),\\
-m_o\omega^2\boldsymbol{u}_2^{(\boldsymbol{n})}(\boldsymbol{k}) &= c_{\ell o}\,\hat{\Pi}_2\left(\boldsymbol{u}_0^{(\boldsymbol{n}+\boldsymbol{p}_1)}(\boldsymbol{k}) - \boldsymbol{u}_2^{(\boldsymbol{n})}(\boldsymbol{k})\right) + \boldsymbol{s}_{12}(\boldsymbol{k}) - \boldsymbol{s}_{23}(\boldsymbol{k}),\\
-m_o\omega^2\boldsymbol{u}_3^{(\boldsymbol{n})}(\boldsymbol{k}) &= c_{\ell o}\,\hat{\Pi}_3\left(\boldsymbol{u}_0^{(\boldsymbol{n})}(\boldsymbol{k}) - \boldsymbol{u}_3^{(\boldsymbol{n})}(\boldsymbol{k})\right) + \boldsymbol{s}_{23}(\boldsymbol{k}) - \boldsymbol{s}_{31}(\boldsymbol{k}).
\end{aligned} \tag{4.35}$$

In Eq. (4.35) we introduce the force $\boldsymbol{s}_{ij}(\boldsymbol{k})$ on mass i due to mass $j \neq i$ with $i,j = \{1,2,3\}$. Since $\boldsymbol{s}_{ij}(\boldsymbol{k}) = -\boldsymbol{s}_{ji}(\boldsymbol{k})$, it follows that the forces can be rewritten as

$$\boldsymbol{s}_{12}(\boldsymbol{k}) = \frac{s_1(\boldsymbol{k})}{\ell}(\tilde{\boldsymbol{b}}_2 - \tilde{\boldsymbol{b}}_1),\ \ \boldsymbol{s}_{23}(\boldsymbol{k}) = \frac{s_2(\boldsymbol{k})}{\ell}(\tilde{\boldsymbol{b}}_3 - \tilde{\boldsymbol{b}}_2),\ \ \boldsymbol{s}_{31}(\boldsymbol{k}) = \frac{s_3(\boldsymbol{k})}{\ell}(\tilde{\boldsymbol{b}}_1 - \tilde{\boldsymbol{b}}_3), \tag{4.36}$$

where $s_i(\boldsymbol{k}) = |\boldsymbol{s}_{ij}(\boldsymbol{k})|$ are the moduli of the tension forces along the equilibrium position of the trusses. In Eq. (4.35), $\boldsymbol{p}_1 = (1,0)^{\mathrm{T}}$ and $\boldsymbol{p}_2 = (0,1)^{\mathrm{T}}$.

The displacement of the nodal point $\boldsymbol{n}$ of the triangular lattice (see solid circles in Fig. 4.1(a)) is

$$\begin{aligned}
-m\omega^2\boldsymbol{u}_0^{(\boldsymbol{n})}(\boldsymbol{k}) &= c_\ell\ \hat{\tau}_1\left(\boldsymbol{u}_0^{(\boldsymbol{n}+\boldsymbol{p}_1)}(\boldsymbol{k})+\boldsymbol{u}_0^{(\boldsymbol{n}-\boldsymbol{p}_1)}(\boldsymbol{k})-2\boldsymbol{u}_0^{(\boldsymbol{n})}(\boldsymbol{k})\right)\\
&+ c_\ell\ \hat{\tau}_2\left(\boldsymbol{u}_0^{(\boldsymbol{n}+\boldsymbol{p}_2)}(\boldsymbol{k})+\boldsymbol{u}_0^{(\boldsymbol{n}-\boldsymbol{p}_2)}(\boldsymbol{k})-2\boldsymbol{u}_0^{(\boldsymbol{n})}(\boldsymbol{k})\right)\\
&+ c_\ell\ \hat{\tau}_3\left(\boldsymbol{u}_0^{(\boldsymbol{n}+\boldsymbol{p}_1-\boldsymbol{p}_2)}(\boldsymbol{k})+\boldsymbol{u}_0^{(\boldsymbol{n}+\boldsymbol{p}_2-\boldsymbol{p}_1)}(\boldsymbol{k})-2\boldsymbol{u}_0^{(\boldsymbol{n})}(\boldsymbol{k})\right)\\
&+ c_{\ell o}\ \hat{\Pi}_1\left(\boldsymbol{u}_1^{(\boldsymbol{n}-\boldsymbol{p}_2)}(\boldsymbol{k})-\boldsymbol{u}_0^{(\boldsymbol{n})}(\boldsymbol{k})\right)+c_{\ell o}\ \hat{\Pi}_2\left(\boldsymbol{u}_2^{(\boldsymbol{n}-\boldsymbol{p}_1)}(\boldsymbol{k})-\boldsymbol{u}_0^{(\boldsymbol{n})}(\boldsymbol{k})\right)\\
&+ c_{\ell o}\ \hat{\Pi}_3\left(\boldsymbol{u}_3^{(\boldsymbol{n})}(\boldsymbol{k})-\boldsymbol{u}_0^{(\boldsymbol{n})}(\boldsymbol{k})\right). \qquad (4.37)
\end{aligned}$$

We observe that the displacement vector for the centre-of-mass of the TIR in the cell $\boldsymbol{n}$ is

$$\boldsymbol{u}_{\rm cm}^{(\boldsymbol{n})}(\boldsymbol{k})=\frac{1}{3}\left(\boldsymbol{u}_1^{(\boldsymbol{n})}(\boldsymbol{k})+\boldsymbol{u}_2^{(\boldsymbol{n})}(\boldsymbol{k})+\boldsymbol{u}_3^{(\boldsymbol{n})}(\boldsymbol{k})\right), \qquad (4.38)$$

where the displacement $\boldsymbol{u}_i(\boldsymbol{k})$, $i=\{1,2,3\}$ are given in Eqs (4.35).

Linearised rotations. Eqs (4.35) can be simplified further, under the assumption of the angular displacements $\vartheta_{\boldsymbol{n}}(\boldsymbol{k})$ being small for every $\boldsymbol{n}$. The displacements of the vertices of rigid TIRs (4.35) can written as

$$\begin{aligned}
\boldsymbol{u}_i^{(\boldsymbol{n})}(\boldsymbol{k}) &= \boldsymbol{u}_{\rm cm}^{(\boldsymbol{n})}(\boldsymbol{k})+\left(\hat{\mathscr{R}}_{\frac{2\pi}{3}(i-1)+\vartheta_{\boldsymbol{n}}(\boldsymbol{k})}-\hat{\mathscr{R}}_{\frac{2\pi}{3}(i-1)}\right)\tilde{\boldsymbol{b}}_1\\
&\approx \boldsymbol{u}_{\rm cm}^{(\boldsymbol{n})}(\boldsymbol{k})+\vartheta_{\boldsymbol{n}}(\boldsymbol{k})\left(\left.\frac{d\hat{\mathscr{R}}_\vartheta}{d\vartheta}\right|_{\vartheta=2\pi(i-1)/3}\right)\tilde{\boldsymbol{b}}_1, \qquad (4.39)
\end{aligned}$$

where the last approximate equality follows from a Taylor expansion of the first rotation matrix in the small parameter $\vartheta_{\boldsymbol{n}}(\boldsymbol{k})$. By substituting Eq. (4.39) into Eqs. (4.35) and summing the result term-by-term as prescribed by Eq. (4.38), we get

$$\begin{aligned}
-\omega^2 M\boldsymbol{u}_{\rm cm}^{(\boldsymbol{n})}(\boldsymbol{k}) &= c_{\ell o}\ \hat{\Pi}_1\left(\boldsymbol{u}_0^{(\boldsymbol{n}+\boldsymbol{p}_2)}(\boldsymbol{k})-\boldsymbol{u}_{\rm cm}^{(\boldsymbol{n})}(\boldsymbol{k})-\hat{\mathscr{R}}_1'\tilde{\boldsymbol{b}}_1\vartheta_{\boldsymbol{n}}(\boldsymbol{k})\right)\\
&+ c_{\ell o}\ \hat{\Pi}_2\left(\boldsymbol{u}_0^{(\boldsymbol{n}+\boldsymbol{p}_1)}(\boldsymbol{k})-\boldsymbol{u}_{\rm cm}^{(\boldsymbol{n})}(\boldsymbol{k})-\hat{\mathscr{R}}_2'\tilde{\boldsymbol{b}}_1\vartheta_{\boldsymbol{n}}(\boldsymbol{k})\right)\\
&+ c_{\ell o}\ \hat{\Pi}_3\left(\boldsymbol{u}_0^{(\boldsymbol{n})}(\boldsymbol{k})-\boldsymbol{u}_{\rm cm}^{(\boldsymbol{n})}(\boldsymbol{k})-\hat{\mathscr{R}}_3'\tilde{\boldsymbol{b}}_1\vartheta_{\boldsymbol{n}}(\boldsymbol{k})\right), \qquad (4.40)
\end{aligned}$$

where $M = 3m_o$ is the total mass of the TIR. In Eq. (4.40), we have introduced

$$\mathscr{R}'_i = \left(\frac{d\hat{\mathscr{R}}_\vartheta}{d\vartheta}\bigg|_{\vartheta=2\pi(i-1)/3} \right), \quad i = \{1,2,3\}. \tag{4.41}$$

After the linearisation (4.39), we project each of the equations (4.35), on the vectors $\tilde{\boldsymbol{b}}_3 - \tilde{\boldsymbol{b}}_2$, $\tilde{\boldsymbol{b}}_1 - \tilde{\boldsymbol{b}}_3$ and $\tilde{\boldsymbol{b}}_2 - \tilde{\boldsymbol{b}}_1$, respectively. Summing the resulting equations term-by-term and performing algebraic simplifications, we obtain

$$\begin{aligned} -\omega^2 I \vartheta_{\boldsymbol{n}}(\boldsymbol{k}) &= -\frac{1}{\sqrt{3}} c_{\ell o}\, (\tilde{\boldsymbol{b}}_3 - \tilde{\boldsymbol{b}}_2)^{\mathrm{T}} \hat{\Pi}_1 \left(\boldsymbol{u}_0^{(\boldsymbol{n}+\boldsymbol{p}_2)}(\boldsymbol{k}) - \boldsymbol{u}_{\mathrm{cm}}^{(\boldsymbol{n})}(\boldsymbol{k}) - \hat{\mathscr{R}}'_1 \tilde{\boldsymbol{b}}_1 \vartheta_{\boldsymbol{n}}(\boldsymbol{k}) \right) \\ &- \frac{1}{\sqrt{3}} c_{\ell o}\, (\tilde{\boldsymbol{b}}_1 - \tilde{\boldsymbol{b}}_3)^{\mathrm{T}} \hat{\Pi}_2 \left(\boldsymbol{u}_0^{(\boldsymbol{n}+\boldsymbol{p}_1)}(\boldsymbol{k}) - \boldsymbol{u}_{\mathrm{cm}}^{(\boldsymbol{n})}(\boldsymbol{k}) - \hat{\mathscr{R}}'_2 \tilde{\boldsymbol{b}}_1 \vartheta_{\boldsymbol{n}}(\boldsymbol{k}) \right) \\ &- \frac{1}{\sqrt{3}} c_{\ell o}\, (\tilde{\boldsymbol{b}}_2 - \tilde{\boldsymbol{b}}_1)^{\mathrm{T}} \hat{\Pi}_3 \left(\boldsymbol{u}_0^{(\boldsymbol{n})}(\boldsymbol{k}) - \boldsymbol{u}_{\mathrm{cm}}^{(\boldsymbol{n})}(\boldsymbol{k}) - \hat{\mathscr{R}}'_3 \tilde{\boldsymbol{b}}_1 \vartheta_{\boldsymbol{n}}(\boldsymbol{k}) \right), \end{aligned} \tag{4.42}$$

where $I = 3m_o b^2 = m_o \ell^2$ is the moment of inertia with respect to the centre-of-mass reference frame. Using the following rotation matrix identities

$$\hat{\mathscr{R}}_3 - \hat{\mathscr{R}}_2 = -\sqrt{3}\hat{\mathscr{R}}'_1, \;\; \hat{\mathscr{R}}_2 - \hat{\mathscr{R}}_1 = -\sqrt{3}\hat{\mathscr{R}}'_3 \text{ and } \hat{\mathscr{R}}_1 - \hat{\mathscr{R}}_3 = -\sqrt{3}\hat{\mathscr{R}}'_2, \tag{4.43}$$

into (4.42), we get

$$\begin{aligned} -\omega^2 I \vartheta_{\boldsymbol{n}}(\boldsymbol{k}) &= c_{\ell o}\, (\hat{\mathscr{R}}'_1 \tilde{\boldsymbol{b}}_1)^{\mathrm{T}} \hat{\Pi}_1 \left(\boldsymbol{u}_0^{(\boldsymbol{n}+\boldsymbol{p}_2)}(\boldsymbol{k}) - \boldsymbol{u}_{\mathrm{cm}}^{(\boldsymbol{n})}(\boldsymbol{k}) - \hat{\mathscr{R}}'_1 \tilde{\boldsymbol{b}}_1 \vartheta_{\boldsymbol{n}}(\boldsymbol{k}) \right) \\ &+ c_{\ell o}\, (\hat{\mathscr{R}}'_2 \tilde{\boldsymbol{b}}_1)^{\mathrm{T}} \hat{\Pi}_2 \left(\boldsymbol{u}_0^{(\boldsymbol{n}+\boldsymbol{p}_1)}(\boldsymbol{k}) - \boldsymbol{u}_{\mathrm{cm}}^{(\boldsymbol{n})}(\boldsymbol{k}) - \hat{\mathscr{R}}'_2 \tilde{\boldsymbol{b}}_1 \vartheta_{\boldsymbol{n}}(\boldsymbol{k}) \right) \\ &+ c_{\ell o}\, (\hat{\mathscr{R}}'_3 \tilde{\boldsymbol{b}}_1)^{\mathrm{T}} \hat{\Pi}_3 \left(\boldsymbol{u}_0^{(\boldsymbol{n})}(\boldsymbol{k}) - \boldsymbol{u}_{\mathrm{cm}}^{(\boldsymbol{n})}(\boldsymbol{k}) - \hat{\mathscr{R}}'_3 \tilde{\boldsymbol{b}}_1 \vartheta_{\boldsymbol{n}}(\boldsymbol{k}) \right), \end{aligned} \tag{4.44}$$

Bloch-Floquet conditions. Bloch-Floquet conditions on the displacement fields are

$$\begin{gathered} \boldsymbol{u}_{\mathrm{cm}}^{(\boldsymbol{n}+\boldsymbol{m})}(\boldsymbol{k}) = e^{i\boldsymbol{k}\cdot\hat{\mathscr{T}}\boldsymbol{m}} \boldsymbol{u}_{\mathrm{cm}}^{(\boldsymbol{n})}(\boldsymbol{k}), \;\; \boldsymbol{u}_0^{(\boldsymbol{n}+\boldsymbol{m})}(\boldsymbol{k}) = e^{i\boldsymbol{k}\cdot\hat{\mathscr{T}}\boldsymbol{m}} \boldsymbol{u}_0^{(\boldsymbol{n})}(\boldsymbol{k}), \\ \vartheta_{\boldsymbol{n}+\boldsymbol{m}}(\boldsymbol{k}) = e^{i\boldsymbol{k}\cdot\hat{\mathscr{T}}\boldsymbol{m}} \vartheta_{\boldsymbol{n}}(\boldsymbol{k}), \end{gathered} \tag{4.45}$$

where the matrix $\hat{\mathscr{T}}$ has as column the primitive vectors of the lattice, and $\boldsymbol{m}$ and $\boldsymbol{n}$ are integer vectors.

By using the Bloch-Floquet conditions (4.45), Eqs. (4.37), (4.40), and (4.44) become

$$\begin{aligned}
-m\omega^2\boldsymbol{u}_0(\boldsymbol{k}) &= 2c_\ell\ \hat{\tau}_1\left(\cos(\boldsymbol{k}\boldsymbol{t}_1)-1\right)\boldsymbol{u}_0(\boldsymbol{k})+2c_\ell\ \hat{\tau}_2\left(\cos(\boldsymbol{k}\cdot\boldsymbol{t}_2)-1\right)\boldsymbol{u}_0(\boldsymbol{k})\\
&+ 2c_\ell\ \hat{\tau}_3\left(\cos(\boldsymbol{k}\cdot(\boldsymbol{t}_1-\boldsymbol{t}_2))-1\right)\boldsymbol{u}_0(\boldsymbol{k})\\
&+ c_{\ell o}\ \hat{\Pi}_1\left(e^{-i\boldsymbol{k}\cdot\boldsymbol{t}_2}\boldsymbol{u}_{\rm cm}(\boldsymbol{k})+e^{-i\boldsymbol{k}\cdot\boldsymbol{t}_2}\hat{\mathscr{R}}_1'\tilde{\boldsymbol{b}}_1\vartheta(\boldsymbol{k})-\boldsymbol{u}_0(\boldsymbol{k})\right)\\
&+ c_{\ell o}\ \hat{\Pi}_2\left(e^{-i\boldsymbol{k}\cdot\boldsymbol{t}_1}\boldsymbol{u}_{\rm cm}(\boldsymbol{k})+e^{-i\boldsymbol{k}\cdot\boldsymbol{t}_1}\hat{\mathscr{R}}_2'\tilde{\boldsymbol{b}}_1\vartheta(\boldsymbol{k})-\boldsymbol{u}_0(\boldsymbol{k})\right)\\
&+ c_{\ell o}\ \hat{\Pi}_3\left(\boldsymbol{u}_{\rm cm}(\boldsymbol{k})+\hat{\mathscr{R}}_3'\tilde{\boldsymbol{b}}_1\vartheta(\boldsymbol{k})-\boldsymbol{u}_0(\boldsymbol{k})\right),
\end{aligned}\tag{4.46}$$

$$\begin{aligned}
-M\omega^2\boldsymbol{u}_{\rm cm}(\boldsymbol{k}) &= c_{\ell o}\ \hat{\Pi}_1\left(e^{i\boldsymbol{k}\boldsymbol{t}_2}\boldsymbol{u}_0(\boldsymbol{k})-\boldsymbol{u}_{\rm cm}(\boldsymbol{k})-\hat{\mathscr{R}}_1'\tilde{\boldsymbol{b}}_1\vartheta(\boldsymbol{k})\right)\\
&+ c_{\ell o}\ \hat{\Pi}_2\left(e^{i\boldsymbol{k}\boldsymbol{t}_1}\boldsymbol{u}_0(\boldsymbol{k})-\boldsymbol{u}_{\rm cm}(\boldsymbol{k})-\hat{\mathscr{R}}_2'\tilde{\boldsymbol{b}}_1\vartheta(\boldsymbol{k})\right)\\
&+ c_{\ell o}\ \hat{\Pi}_3\left(\boldsymbol{u}_0(\boldsymbol{k})-\boldsymbol{u}_{\rm cm}(\boldsymbol{k})-\hat{\mathscr{R}}_3'\tilde{\boldsymbol{b}}_1\vartheta(\boldsymbol{k})\right)\ ,
\end{aligned}\tag{4.47}$$

and

$$\begin{aligned}
\omega^2 I\vartheta(\boldsymbol{k}) &= c_{\ell o}\ \tilde{\boldsymbol{b}}_1^{\rm T}\hat{\mathscr{R}}_1'\ \hat{\Pi}_1\left(e^{i\boldsymbol{k}\boldsymbol{t}_2}\boldsymbol{u}_0(\boldsymbol{k})-\boldsymbol{u}_{\rm cm}(\boldsymbol{k})-\hat{\mathscr{R}}_1'\tilde{\boldsymbol{b}}_1\vartheta(\boldsymbol{k})\right)\\
&+ c_{\ell o}\ \tilde{\boldsymbol{b}}_1^{\rm T}\hat{\mathscr{R}}_2'\ \hat{\Pi}_2\left(e^{i\boldsymbol{k}\boldsymbol{t}_1}\boldsymbol{u}_0(\boldsymbol{k})-\boldsymbol{u}_{\rm cm}(\boldsymbol{k})-\hat{\mathscr{R}}_2'\tilde{\boldsymbol{b}}_1\vartheta(\boldsymbol{k})\right)\\
&+ c_{\ell o}\ \tilde{\boldsymbol{b}}_1^{\rm T}\hat{\mathscr{R}}_3'\ \hat{\Pi}_3\left(\boldsymbol{u}_0(\boldsymbol{k})-\boldsymbol{u}_{\rm cm}(\boldsymbol{k})-\hat{\mathscr{R}}_3'\tilde{\boldsymbol{b}}_1\vartheta(\boldsymbol{k})\right),
\end{aligned}\tag{4.48}$$

where we suppress the cell index $\boldsymbol{n}$ after using the Bloch-Floquet conditions (4.45).

Eqs (4.46), (4.47) and (4.48) can be recast in the matrix form

$$\left[\hat{\Sigma}(\boldsymbol{k})-\omega^2\hat{\mathscr{M}}\right]\boldsymbol{U}(\boldsymbol{k})=\boldsymbol{0},\quad\text{with}\quad\boldsymbol{U}(\boldsymbol{k})=\left(\boldsymbol{u}_0^{\rm T}(\boldsymbol{k}),\quad\boldsymbol{u}_{\rm cm}^{\rm T}(\boldsymbol{k}),\quad\vartheta(\boldsymbol{k})\right)^{\rm T},\tag{4.49}$$

and where $\vartheta(\boldsymbol{k})$ and $\boldsymbol{u}_{\rm cm}(\boldsymbol{k})$ denote the amplitude of rotation and displacement of the TIR's centre of mass, respectively. The stiffness matrix in (4.49) is

$$\hat{\Sigma}(\boldsymbol{k})=\sum_{i=1}^{3}\begin{pmatrix}
-2c_\ell(\cos(\boldsymbol{k}\cdot\boldsymbol{t}_i)-1)\hat{\tau}_i+c_{\ell o}\hat{\Pi}_i & -c_{\ell o}\varphi_i(\boldsymbol{k})\hat{\Pi}_i & -c_{\ell o}\varphi_i(\boldsymbol{k})\hat{\Pi}_i\hat{\mathscr{R}}_i'\tilde{\boldsymbol{b}}_1\\
-c_{\ell o}\varphi_i^*(\boldsymbol{k})\hat{\Pi}_i & c_{\ell o}\hat{\Pi}_i & c_{\ell o}\hat{\Pi}_i\hat{\mathscr{R}}_i'\tilde{\boldsymbol{b}}_1\\
-c_{\ell o}(\varphi_i(\boldsymbol{k})\hat{\Pi}_i\hat{\mathscr{R}}_i'\tilde{\boldsymbol{b}}_1)^\dagger & c_{\ell o}(\hat{\Pi}_i\hat{\mathscr{R}}_i'\tilde{\boldsymbol{b}}_1)^\dagger & c_{\ell o}\tilde{\boldsymbol{b}}_1^{\rm T}\cdot(\hat{\mathscr{R}}_i'\hat{\Pi}_i\hat{\mathscr{R}}_i'\tilde{\boldsymbol{b}}_1)
\end{pmatrix},\tag{4.50}$$

where we introduce the functions $\varphi_1(\boldsymbol{k})=\exp(-\boldsymbol{k}\cdot\boldsymbol{t}_2)$, $\varphi_2(\boldsymbol{k})=\exp(-\boldsymbol{k}\cdot\boldsymbol{t}_1)$ and $\varphi_3(\boldsymbol{k})=1$; and $\mathscr{R}_i'$, $i=\{1,2,3\}$, are introduced in Eq. (4.41). The inertia matrix which appears in (4.49)

is

$$\hat{\mathscr{M}} = \mathrm{diag}(m,m,M,M,I), \tag{4.51}$$

where $M = 3m_o$ is the total mass of the TIR, $I = m_o\ell^2$ is its moment of inertia, and m is the mass of the nodal points in the ambient lattice. The results presented here correspond to triangular resonators with point masses placed at their vertices. These results can be easily generalised to the case of resonators with the mass distributed over the entire triangular region provided that the appropriate moment of inertia is used in Eq. (4.51). For example, for a uniform rigid equilateral triangular resonator of the same total mass, the moment of inertia about its centre of mass is $I = m_o\ell^2/8$.

Consider the 3×3 block independent of $\boldsymbol{k}$ which appears in Eq. (4.50). We observe that

$$\sigma = \begin{pmatrix} \hat{\Sigma}_{\mathrm{cm,cm}} & \boldsymbol{\Sigma}_{\mathrm{cm},\vartheta} \\ \\ \boldsymbol{\Sigma}^{\dagger}_{\mathrm{cm},\vartheta} & \Sigma_{\vartheta,\vartheta} \end{pmatrix} = \begin{pmatrix} 3c_{\ell o}/2\ \hat{I}_{2\times 2} & \boldsymbol{0} \\ \\ \boldsymbol{0}^{\mathrm{T}} & c_{\ell o}\ell^2\sin^2\vartheta_0/(1+\ell^2/L^2-2\ell/L\cos(\vartheta_0)) \end{pmatrix}, \tag{4.52}$$

exactly coincide with the stiffness matrix of a single resonator. The solvability condition for the algebraic system (4.49) yields the dispersion equation for Bloch-Floquet waves in the triangular lattice with TIRs

$$\mathscr{D}(\boldsymbol{k},\omega) = \det\left(\hat{\Sigma}(\boldsymbol{k}) - \omega^2\hat{\mathscr{M}}\right) = 0. \tag{4.53}$$

The remainder of this section will be devoted to the analysis and interpretation of the roots of this equation.

4.3.2 Effective group velocity

It is interesting to examine the dynamic behaviour of the lattice containing TIRs in the long-wave regime. In particular, the effect of the resonator on the quasi-static response will be examined. We consider the non-degenerate case of $\vartheta_0 \neq 0$ and expand $\mathscr{D}(\boldsymbol{k},\omega)$ in a MacLaurin series assuming $0 < \omega \ll 1$ and $0 < L|\boldsymbol{k}| \ll 1$. In the low frequency regime, Eq. (4.53) can be written as

$$\mathscr{D}(\boldsymbol{k},\omega) = \mathscr{D}_\Gamma(\boldsymbol{k},\omega) + o(\omega^6). \tag{4.54}$$

We then search for solutions of the form $\omega_{\boldsymbol{k}} = v|\boldsymbol{k}|$, where v is the effective group velocity. Consequently, in Eq. (4.54) we can write

$$\mathscr{D}_\Gamma(\boldsymbol{k},\omega) = \mathscr{D}_\Gamma^{(4)}(\boldsymbol{k})\omega^4 + \mathscr{D}_\Gamma^{(2)}(\boldsymbol{k})\omega^2 + \mathscr{D}_\Gamma^{(0)}(\boldsymbol{k}) + o(|\boldsymbol{k}|^6). \tag{4.55}$$

The determinant of the matrix equation (4.49) is a polynomial function of fifth degree in the variable ω^2, *i.e.*

$$\mathscr{D}(\boldsymbol{k},\omega)=\sum_{j=0}^{5}\mathscr{D}^{(2j)}(\boldsymbol{k})(\omega)^{2j}, \tag{4.56}$$

where the coefficients $\mathscr{D}^{(2j)}(\boldsymbol{k})$ are analytical functions of $\boldsymbol{k}$. From analyticity it follows that the order in which the $\boldsymbol{k}\to\boldsymbol{0}$ and $\omega\to 0$ are taken, does not affect the result. We deliberately assume $\vartheta_0\neq 0$, *i.e.* a statically determined lattice. In Eq. (4.56) we retain only the terms up to fourth order in ω and expand $\mathscr{D}^{(2j)}(\boldsymbol{k})$ in Maclaurin series for small $\boldsymbol{k}$ around Γ. To leading order, the coefficients of Eq. (4.55) are

$$\begin{aligned}
\mathscr{D}^{(0)}_{\Gamma}(\boldsymbol{k})&=-\frac{3^5}{2^8}\frac{L^6\ell^2}{\ell_r^2}c_\ell^2c_{\ell o}^3\sin^2(\vartheta_0)\,|\boldsymbol{k}|^4,\\
\mathscr{D}^{(2)}_{\Gamma}(\boldsymbol{k})&=\frac{3^3}{2^3}\frac{L^4\ell^2}{\ell_r^2}c_\ell c_{\ell o}^3\sin^2(\vartheta_0)(m+3m_o)\,|\boldsymbol{k}|^2,\\
\mathscr{D}^{(4)}_{\Gamma}(\boldsymbol{k})&=-\frac{3^2}{2^2}\frac{L^2\ell^2}{\ell_r^2}c_{\ell o}^3\sin^2(\vartheta_0)(m+3m_o)^2.
\end{aligned} \tag{4.57}$$

In Eqs. (4.57), the index "Γ" indicates Taylor expansion in $\boldsymbol{k}$ around Γ. The effective long-waves group velocities in Eq. (4.59) follow from

$$v^2=\frac{1}{2|\boldsymbol{k}|^2\mathscr{D}^{(4)}_{\Gamma}(\boldsymbol{k})}\left(-\mathscr{D}^{(2)}_{\Gamma}(\boldsymbol{k})\pm\sqrt{(\mathscr{D}^{(2)}_{\Gamma}(\boldsymbol{k}))^2-4\mathscr{D}^{(4)}_{\Gamma}(\boldsymbol{k})\mathscr{D}^{(0)}_{\Gamma}(\boldsymbol{k})}\right). \tag{4.58}$$

The long-wave and low-frequency pressure v_{p} and shear v_{s} *group velocities* for Bloch-Floquet waves in a triangular lattice containing TIRs are

$$v_{\mathrm{p}}=\sqrt{3}v_{\mathrm{s}}\ \text{ and }\ v_{\mathrm{s}}=\frac{1}{2}\sqrt{\frac{3}{2}}L\sqrt{\frac{c_\ell}{m+3m_o}}. \tag{4.59}$$

According to equations (4.59), the low-frequency and long-wave dispersion surfaces are conical and isotropic. In addition, we remark that the group velocities depend on the total mass of the cell, on the inter-cell stiffness c_ℓ and on the triangular lattice nearest-neighbour distance L. The intra-cell physical parameters ϑ_0, $c_{\ell o}$ and ℓ, do not appear in this regime because they characterise sub-wavelength structures. Moreover, equations (4.59) suggest that the low-frequency and long-wave dispersion of elastic waves in a lattice with TIRs is equivalent to the behaviour associated with a simple monatomic triangular lattice with mass per unit cell

$$m_{\mathrm{TL}}=m+3m_o, \tag{4.60}$$

and ligaments with stiffness c_ℓ.

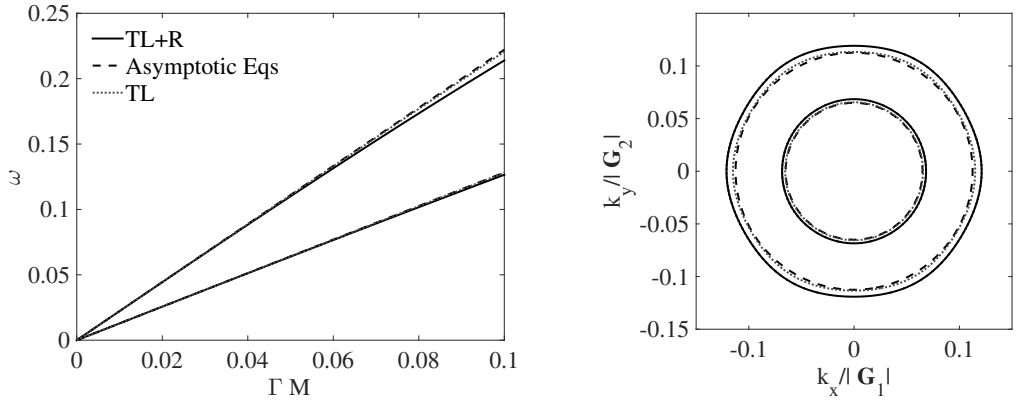

(a) **(b)**

Fig. 4.6 *Panel (a) shows dispersion diagrams and panel (b) the corresponding slowness contours. Black solid lines refer to a triangular lattice with tilted TIRs (see Eq. (4.49)) for $\vartheta_0 = \vartheta_{\max}$ with the remaining parameters as listed in Table 4.1; black dashed lines correspond to the effective group velocities (4.59); grey dotted lines refer to a monatomic triangular lattice (see Eq. (1.68)) mass per site as in Eq.* (4.60) *and other parameters as listed in Table 4.1.*

These effects are illustrated in Fig. 4.6, where we examine the dispersion curves in the low-frequency and long-wave regime. The solid lines correspond to the dispersion curves for a triangular lattice with TIRs. The numerical parameters have been chosen as detailed in Table (4.1) and the tilting angle is $\vartheta_0 = \vartheta_{\max}$. The dashed lines correspond to the asymptotic dispersion relation $\omega_{\boldsymbol{k}} \sim vk$, evaluated using the effective group velocities in Eq. (4.59). The dotted lines refer to a triangular lattice (studied in section section 1.4.1) whose dispersion curves have been obtained by solving (1.68), with the mass m_{TL} at the nodal points as in Eq. (4.60). The matrix $\hat{I}_2$ is the 2×2 identity matrix and the remaining parameters are listed in Table 4.1. We observe that Eq. (1.68) can be retrieved from the stiffness matrix (4.50) in the limit $c_{\ell o} \to 0$, for which the resonators do not influence the motion of the nodal points of the triangular lattice.

Fig. 4.6(a) shows that the dispersion curves for a triangular lattice containing non-degenerate ($\vartheta_0 = \vartheta_{\max}$) TIRs are linear and equivalent to a monatomic triangular lattice with renormalised mass in the long-wavelength and low-frequency regime. Fig. 4.6(b) shows slowness contours for the same three examples at a fixed frequency of $\omega = 0.25$. We observe that the slowness contours for the triangular lattice with TIRs (solid lines) are approximately circular, indicating that the lattice with TIRs is isotropic in the long-wave, low-frequency regime.

In the non-degenerate case, the unit cell in Fig. 4.1(a) is chiral, in a similar sense as considered by Spadoni *et al.* in [85]. However, we note that the geometry and the effective dispersion properties derived here are different from those studied in [85]. The difference arises due to the fact that the chirality, associated with the topology of the TIRs, emerges at length scales shorter than the unit cell width L. Therefore, the chiral effects are likely to emerge at higher frequencies, as it is illustrated below.

c_ℓ	$c_{\ell o}$	L	ℓ	m	m_o	$\vartheta_{\max}$
1	1	1	$1/4$	1	1	1.318

Table 4.1 *Parameters used in Eq. (4.49) in order to model the triangular lattice with TIRs. The threshold angle $\vartheta_{0\max}$ has been introduced in Eq.* (4.7).

4.3.3 Effect of the tilting angle ϑ_0 on the dispersion properties

In this subsection, we study the role of the rotational parameter ϑ_0 on the dispersion of Bloch-Floquet elastic waves in a triangular lattice containing TIRs.

Band gaps in the dispersion diagrams for Bloch-Floquet waves. In Fig. 4.7 we compare the dispersion surfaces, over the square set of Bloch vectors introduced in Eq. (1.63). The set comprises the hexagonal Brillouin zone represented in Fig. 1.7(b). Fig. 4.7(a) corresponds to a monatomic triangular lattice whose physical parameters coincide with those used in Fig. 4.6. Fig. 4.7(b), shows the dispersion surfaces for the degenerate ($\vartheta_0 = 0$) triangular lattice with resonators. Fig. 4.7(c) and Fig. 4.7(d) correspond to the the choices of the tilting angles $\vartheta_0 = \vartheta_{\max}/5$ and $\vartheta_0 = \vartheta_{\max}$, respectively. The remaining parameters for the aforementioned examples are listed in Table 4.1. The monatomic triangular lattice (panel (a)) exhibits two *acoustic branches* corresponding to the degrees of freedom for the in-plane displacement of the mass in the unit cell. The insertion of a *non-tilted* resonator, which preserves the symmetry of the elementary cell, results in the two *optical branches* shown in panel (b). These additional surfaces are associated with the motion of the centre-of-mass of the resonator and are separated from the acoustic branches by a complete band gap. Tilting the resonator, and thus breaking the symmetry of the elementary cell, induces a new dispersion surface, as shown in panels (c) and (d). This new surface is associated with the rotational motion of the resonator. For a sufficiently small ϑ_0 (see panel (c)), the novel dispersion surface intersects the acoustic branches of the dispersion diagram. Interestingly, for the maximum angle achievable $\vartheta_0 = \vartheta_{\max}$, panel (d) shows that the novel resonant branch completely decouples from the acoustic branches. Both the position and shape of this surface,

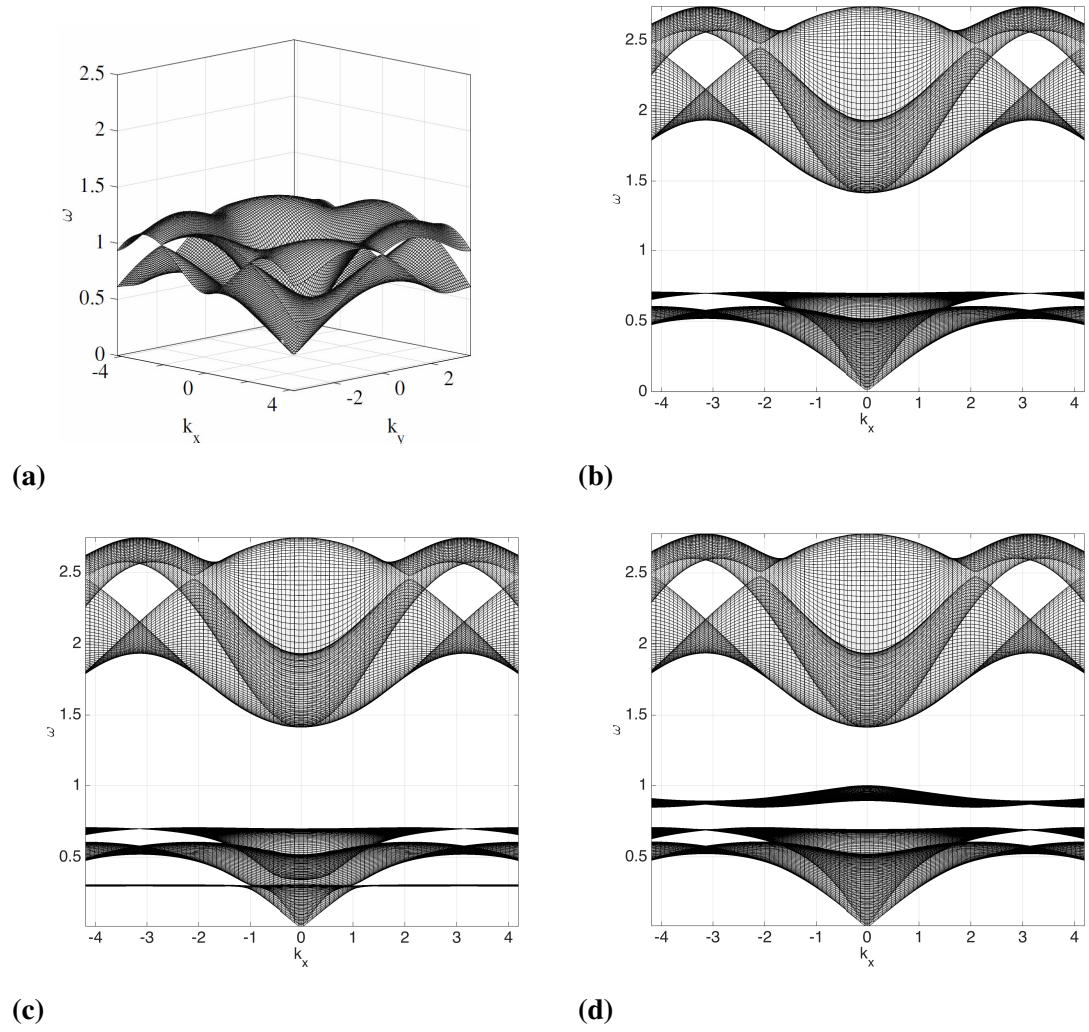

Fig. 4.7 *Bloch dispersion surfaces over a wave vector region which includes the first Brillouin zone for the triangular lattice - see Fig. (4.1)(c). Panel (a): The dispersion surfaces for a monatomic triangular lattice whose parameters are the same as for Fig. 4.6, grey dotted lines. Panel (b): The dispersion surfaces for the triangular lattice with resonator and* $\vartheta_0 = 0$*. Panel (c): The dispersion surfaces for the triangular lattice with TIR at* $\vartheta_0 = 0.2\ \vartheta_{\max}$*, as defined in Eq. (4.7). Panel (d): The triangular lattice with TIR at* $\vartheta_0 = \vartheta_{\max}$*. The remaining parameters are listed in Table 4.1.*

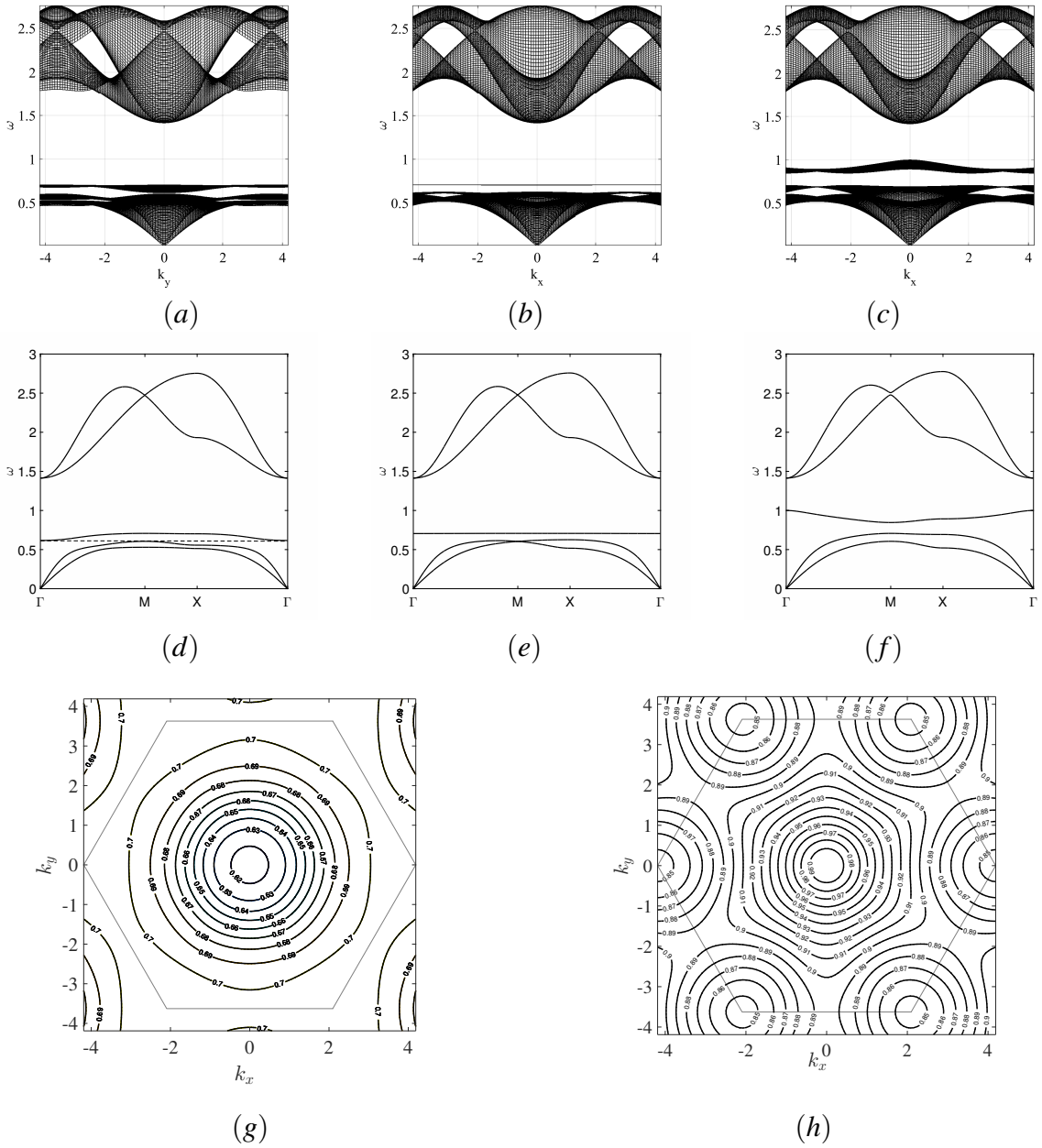

Fig. 4.8 *Panels (a), (b) and (c) show dispersion surfaces corresponding to the tilting angles* $\vartheta_0 = 0.51, 0.61, 1.32$ rad*, respectively. In the same order, figures (d), (e) and (f) show the corresponding dispersion curves plotted over the the boundary of the irreducible Brillouin zone. The isofrequency diagrams in panels (g) and (h) show the slowness contours corresponding to the dispersion surfaces (a) and (c), for the tilting angles* $\vartheta_0 = 0.51, 1.32$ rad *respectively.*

associated with the rotational motion of the resonator, can be controlled by tuning the *tilting angle* ϑ_0 as it is further illustrated in the next section.

Localisation and standing waves. Fig. 4.8 shows the dispersion surfaces, diagrams and slowness contours for a range of tilting angles ϑ_0. The parameters used in this set of computations are listed in Table 4.1. The pairs of panels (a) and (d), (b) and (e), and (c) and (f) correspond to $\vartheta_0 \approx 0.51$ rad, $\vartheta_0 \approx 0.61$ rad and $\vartheta_0 \approx 1.32$ rad, respectively. This choice illustrates the influence exerted by the angle ϑ_0 on the dispersive properties of the Bloch resonant mode. In particular, for $\vartheta_0 \approx 0.51$, the frequency band gap between the acoustic and the rotational mode closes (c.f. panels (a) and (d)). On the other hand, for $\vartheta_0 = \vartheta_{\max} \approx 1.32$, the band gap between the rotational mode and the highest acoustic branch is maximal - see panels (c) and (f). Moreover, for $\vartheta_0 \approx 0.61$, there is a resonant rotational mode, and the corresponding dispersion surface becomes flat.

It is clear that the dispersive properties of the rotational mode depend on the tilting angle ϑ_0. This is illustrated in panels (g) and (h), where the slowness contours for the rotational band in panels (a) and (c) are shown. In panel (g), the group velocities points outwards in the vicinity of Γ; this can be identified with a positive effective mass in the sense of [32]. Conversely, in panel (h), the group velocity points inwards in the neighbourhood of Γ, corresponding to a negative group velocity. Finally, we observe that the frequency of the standing wave reported in panel (b) exactly coincides with the single resonator rotational frequency, already introduced in Eq. (4.16) (see also panel (e)). We also observe that the resonances of the rotational mode at Γ, coincide with the single resonator frequency; for panel (a), this corresponds to the lower boundary of the rotational band, whilst in (f) it corresponds the the upper boundary of the rotational band.

4.3.4 Triple eigenvalue at the Γ point and the Dirac-like dispersion

Here we refer to the point Γ in Fig. 4.1(b). At $\boldsymbol{k} = \boldsymbol{0}$, the roots of fifth-degree polynomial equation in $\Omega = \omega^2$ (4.53) can be found in their closed forms. Introducing the notation $\Omega_\Gamma^{(i)} = \Omega_{\boldsymbol{k}}^{(i)}\Big|_{\boldsymbol{k}=\boldsymbol{0}}$, with i indexing the root, we find

$$\Omega_\Gamma^{(1)} = 0,\ \Omega_\Gamma^{(2)} = \Omega_{\rm cm}\left(1+\frac{3m_o}{m}\right) \text{ and } \Omega_\Gamma^{(3)} = \Omega_\vartheta = \Omega_{\rm cm}\frac{2\sin^2\vartheta_0}{1+\ell^2/L^2-2\ell/L\cos\vartheta_0}, \quad (4.61)$$

where the frequencies $\Omega_{\rm cm}$ and Ω_ϑ are given in Eq. (4.16). The first and second eigenvalues in Eqs. (4.61) have multiplicity two, and the last one has multiplicity one.

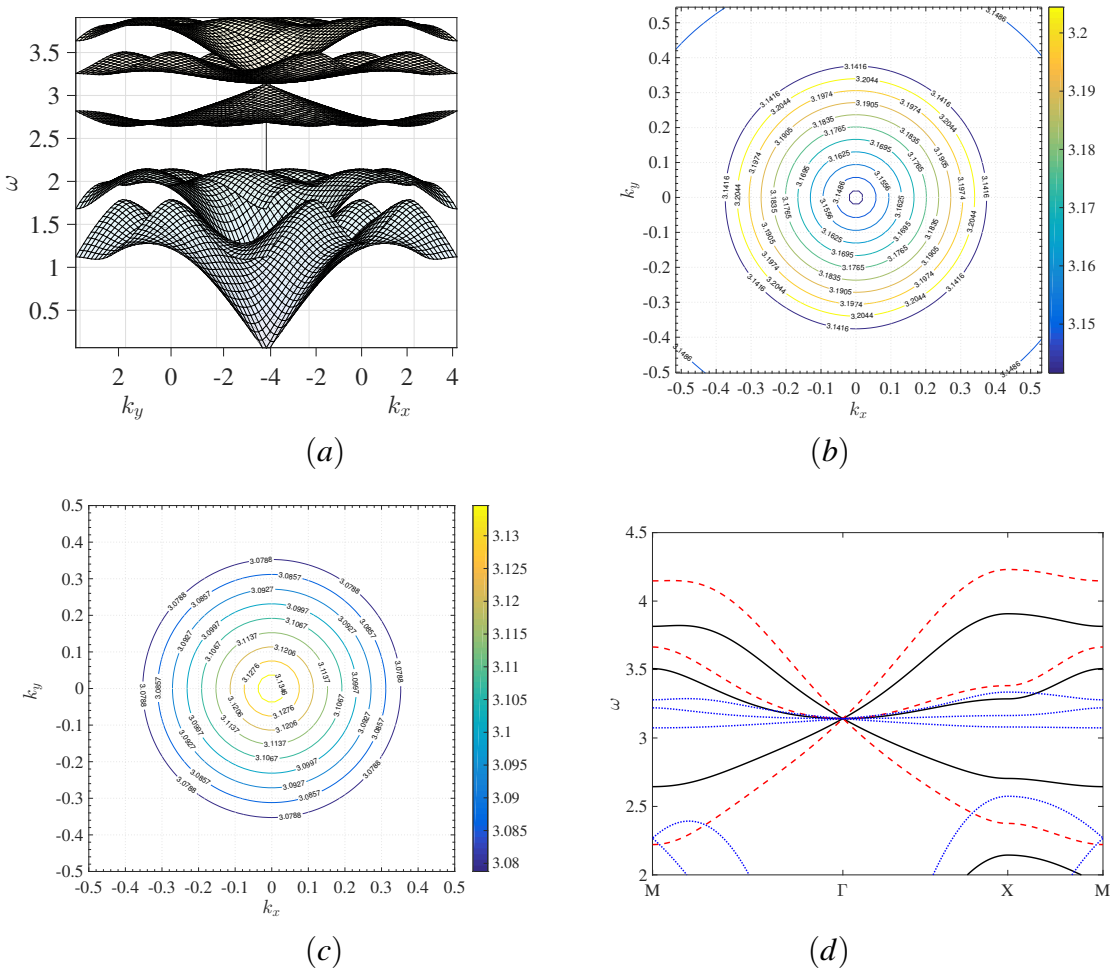

Fig. 4.9 *In panel (a) we report the Bloch-Floquet dispersion surfaces for a triangular lattice with resonators whose lattice parameters are listed in set 1 of Table 4.1. Panels (b) and (c) are slowness contours of panel (a) and their colour maps represent Bloch-Floquet frequencies ω. The frequencies represented here lie just above (panel (b)) and just below (panel (c)) $\omega = \pi$, corresponding to the Dirac-like point. Panel (d) shows the dispersion curves of the optical modes for three set of lattice parameters. The solid black line correspond to the lattice parameters used in panel (a); red dashed lines and blue dotted lines correspond to "set 2" and "set 3" in Table 4.1, respectively.*

Given $\bar{\ell} = \ell/L$ and ϑ_0 in the intervals (4.7), we observe that it is possible to obtain a triple eigenvalue corresponding to $\Omega_\Gamma^{(2)} = \Omega_\Gamma^{(3)}$, if there exists

$$\bar{m} = \frac{\cos 2\vartheta_0 + \bar{\ell}^2 - 2\bar{\ell}\cos\vartheta_0}{2\bar{\ell}\cos\vartheta_0 - \bar{\ell}^2 - 1} > 0, \tag{4.62}$$

with $\bar{m} = 3m_o/m$. We observe that

$$\bar{m} > 0 \iff \cos\vartheta_0 - |\sin\vartheta_0| < \bar{\ell} < \cos\vartheta_0 + |\sin\vartheta_0|. \tag{4.63}$$

The substitution of the expression (4.62) for m_o into the the expression for $\Omega_\Gamma^{(2)}$ (Eq. (4.61)) gives the frequency squared for the triple eigenvalue

$$\Omega_\Gamma^{(\mathrm{te})} = -\frac{3c_{\ell o}}{m}\frac{\sin^2\vartheta_0}{\bar{\ell}^2 - 2\bar{\ell}\cos\vartheta_0 + \cos 2\vartheta_0}, \tag{4.64}$$

which is a positive quantity if the condition on $\bar{\ell}$ and ϑ_0 of Eq. (4.63) is satisfied.

Fig. 4.9(a) represents the frequency dispersion surfaces for a TLR as a function of a set of Bloch wave vectors which comprise the first Brillouin zone (see Fig. 4.1(b)). The lattice parameters have been chosen in such a way that Eq. (4.62) is satisfied. This yields the occurrence of a triple eigenvalue at Γ, as it can be seen by direct inspection of the optical part of the dispersion diagram. Specifically, we choose $\bar{\ell} = 0.21$ and $\vartheta_0 = 0.82$, which gives $\bar{m} = 0.41$. We take $L = 1$, $c_\ell = 1$ and $m = 0.8$. This influences the maximum frequency of the acoustic modes. Finally, the choice $c_{\ell o} = 1.53$ guarantees that the triple-eigenvalue's frequency is

$$\sqrt{\Omega_\Gamma^{(\mathrm{te})}} = \pi. \tag{4.65}$$

Figs 4.9(b) and 4.9(c) show the slowness contours of Fig. 4.9(a) around the triple-eigenvalue's frequency $\omega = \pi$. Fig. 4.9(b) (Fig. 4.9(c)) refers to frequencies slightly above (slightly below) $\omega = \pi$. Figs 4.9(b) and 4.9(c) show that the dispersion in the vicinity of the triple-eigenvalue is isotropic. In Fig. 4.9(d) we compare (along the path MΓXM) the optical branches of three different TLRs whose lattice parameters are listed in the table 4.2. The black solid line refers to set 1 in Tab. 4.2 (same as in Fig. 4.9(a)). The dispersion around the triple-eigenvalue's frequency $\omega = \pi$ is linear, suggesting that the triple eigenvalue is a Dirac-like point. Other choices of the parameters are possible resulting in different group velocities at Γ. In Fig. 4.9(d) we use the set 2 (red dashed line) and set 3 (blue dotted line) listed in the table 4.2. The chosen sets of parameters satisfy (4.65), which corresponds to the occurrence of a triple eigenvalue at Γ and $\omega = \pi$. We observe that Dirac-like dispersion is robust over the chosen sets of the lattice parameters.

	c_ℓ	m	L	ℓ	$c_{\ell o}$	m_o	ϑ_0
set 1	1	0.8	1	0.21	1.534	0.11	0.82
set 2	1	0.8	1	0.25	2.6319	0.27	1.32
set 3	1	0.8	1	0.1	0.2722	0.0145	0.74

Table 4.2 *Sets of parameters for selected triangular lattices with resonators whose frequency dispersion (see Fig. 4.9) is Dirac-like at $\omega = \pi$. SI units of measurement are understood.*

4.3.5 Dispersion and eigenmodes in the neighbourhood of a Dirac point

We now examine the Dirac cones and the opening of a partial band gap at the high-symmetry point M, shown in Fig. 4.1(b). Fig. 4.10 (b) shows the dispersion curves, in the vicinity of M, for the triangular lattice with TIRs; the solid, dotted and dashed lines correspond to $\vartheta_0 \approx 0.51$ rad, $\vartheta_0 \approx 0.61$ rad and $\vartheta_0 \approx 1.32$ rad, respectively, and the material parameters are detailed in Table 4.1. The two dispersion surfaces intersect and form a pair of Dirac cones for the special value $\vartheta \approx 0.61$ rad, which was shown to give rise to a flat resonance in the dispersion diagrams 4.8(b) and 4.8(e); these surfaces separate and form a partial band gap (see, also, Fig. 4.8) for values of the tilting angle greater or less than the special value $\vartheta_0 \approx 0.61$ rad. Fig. 4.10(b) shows the dependence of the optical frequencies at M as a function of the tilting angle ϑ_0; the special value of $\vartheta_0 \approx 0.61$ corresponds to the angle at which the curves intersect. The figure highlights the fact that one of the two optical frequencies at M does not depend on the tilting angle. This observation suggests that, at M, there exists an eigenmode where the resonator does not contribution to the motion of the lattice and waves propagate purely through the ambient triangular lattice. Fig. 4.11 shows the displacement amplitude fields for the triangular lattice with TIRs for two different tilting angles. We note that the two modes are identical, up to an arbitrary phase shift, and the displacements of the resonators are small compared with those of the ambient lattice. The red empty circles indicate the equilibrium positions of the masses, whilst the blue solid lines denote their orbits; the black solid lines indicate the trusses.The displacement fields are obtained by finding the eigenvalues of (4.49) and their corresponding eigenvectors.

4.4 Non-uniform vortex-type lattice

The variation in tilting angle can be conveniently accommodated by introducing the macro-cell illustrated in Fig. 4.12, where the primitive lattice vectors are marked (c.f. Eq. (1.60)). In this case, the oblique unit cell comprises two masses m (black solid dots) and two triangular resonators of side ℓ. The same assumptions made for the resonator introduced in Sec. 4.1 are applied here, that is $c_o/c_{\ell o} \gg 1$ and $c_o/c_\ell \gg 1$. The two masses are located at the basis vectors

$$\boldsymbol{d}_0 = \boldsymbol{0} \qquad \text{and} \qquad \boldsymbol{d}_1 = L\begin{pmatrix}1\\0\end{pmatrix}, \tag{4.66}$$

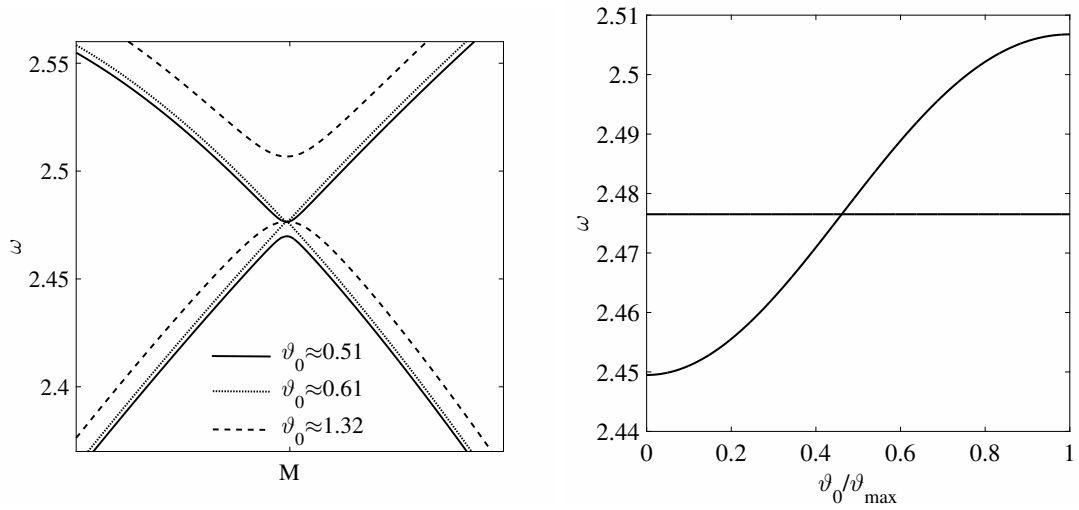

(a) **(b)**

Fig. 4.10 *Panel (a): The dispersion diagram in the vicinity of M for different choices of the tilting angle. Panel (b): The optical mode eigenfrequencies evaluated at point M in the first Brillouin zone as a function of* ϑ_0.

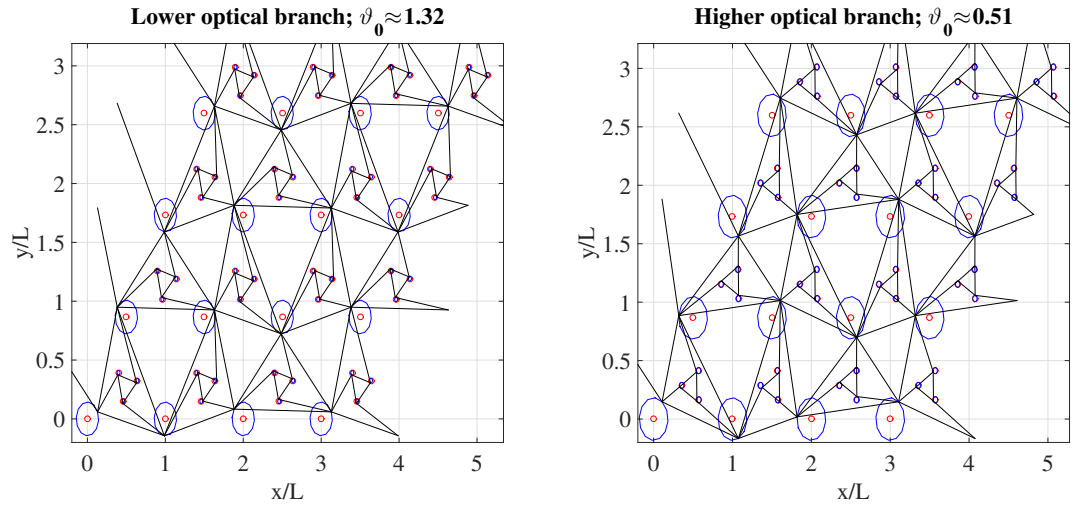

(a) **(b)**

Fig. 4.11 *Illustrations of the Bloch eigenmodes at M. Red empty dots are the equilibrium positions of the masses in the lattice; blue lines represent the orbits of the masses in the lattice and are obtained by solving* (4.53). *Black solid lines are trusses. Panels (a) and (b) refer to* $\vartheta_0 \approx 0.51$ *and* $\vartheta_0 \approx \vartheta_{\max} \approx 1.32$, *respectively.*

respectively. Similarly, the rest positions of the centres of mass of the resonators are

$$\tilde{\boldsymbol{r}}_{\mathrm{cm},i} = \tilde{\boldsymbol{r}}_{\mathrm{cm}} + \boldsymbol{d}_i, \tag{4.67}$$

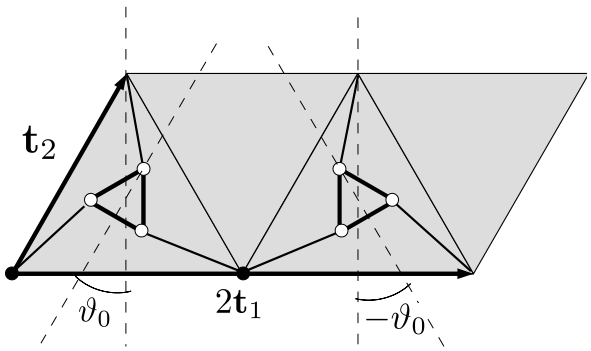

Fig. 4.12 *A schematic representation of a macrocell where a specific variation of the tilting angle is introduced.*

where the vector $\tilde{\boldsymbol{r}}_{\rm cm}$ represents the position vector of the centre of mass of a resonator in a triangular lattice (Eq. (1.72)), and the vectors $\boldsymbol{d}_i$ with $i = \{0,1\}$ are given in Eq. (4.66). The left resonator in Fig. 4.12 is tilted by an angle ϑ_0 and the right one of an angle $-\vartheta_0$. Since our aim is to compare the dispersion properties associated with the unit cells in Figs 4.1(a) and 4.12, it is necessary to choose a common region in which to perform the comparison.

In this section, we present results for the frequency surfaces as a function of the Bloch vector

$$\boldsymbol{k} = \alpha_1 \boldsymbol{G}_1^* + \alpha_2 \boldsymbol{G}_2^*, \tag{4.68}$$

where $(\alpha_1, \alpha_2) \in [-1/2, 1/2]^2$ and $\boldsymbol{G}_1^*$ and $\boldsymbol{G}_1^*$ are the reciprocal lattice vectors for the oblique lattice introduced in Eq. (1.87). In particular, Fig. 4.13 shows the dispersion surfaces over the set of Bloch wave vectors (4.68) and eigenmodes for two cases. Panel (a) shows the dispersion surfaces for the case when the two resonators in the macro-cell, shown in Fig. 4.12, are tilted by the same angle $\vartheta_0 = \vartheta_{\rm max}$. In panel (b), the two resonators are rotated by opposite angles. The physical parameters used are listed in Table 4.1. We observe that a partial band gap between the two optical surfaces, opens when the two resonators are tilted in the opposite directions.

In section 4.3.5, we highlighted some features of Bloch-Floquet waves at the point M. The corresponding point for the macro-cell shown in Fig. 4.12 is

$$\mathrm{M}' = \frac{\pi}{3L}\begin{pmatrix} 1 \\ \sqrt{3} \end{pmatrix}. \tag{4.69}$$

When the resonators in the macro-cell are rotated in the same direction, it is natural to expect the same Bloch eigenmodes at M′ that we would have had at M for a single-resonator

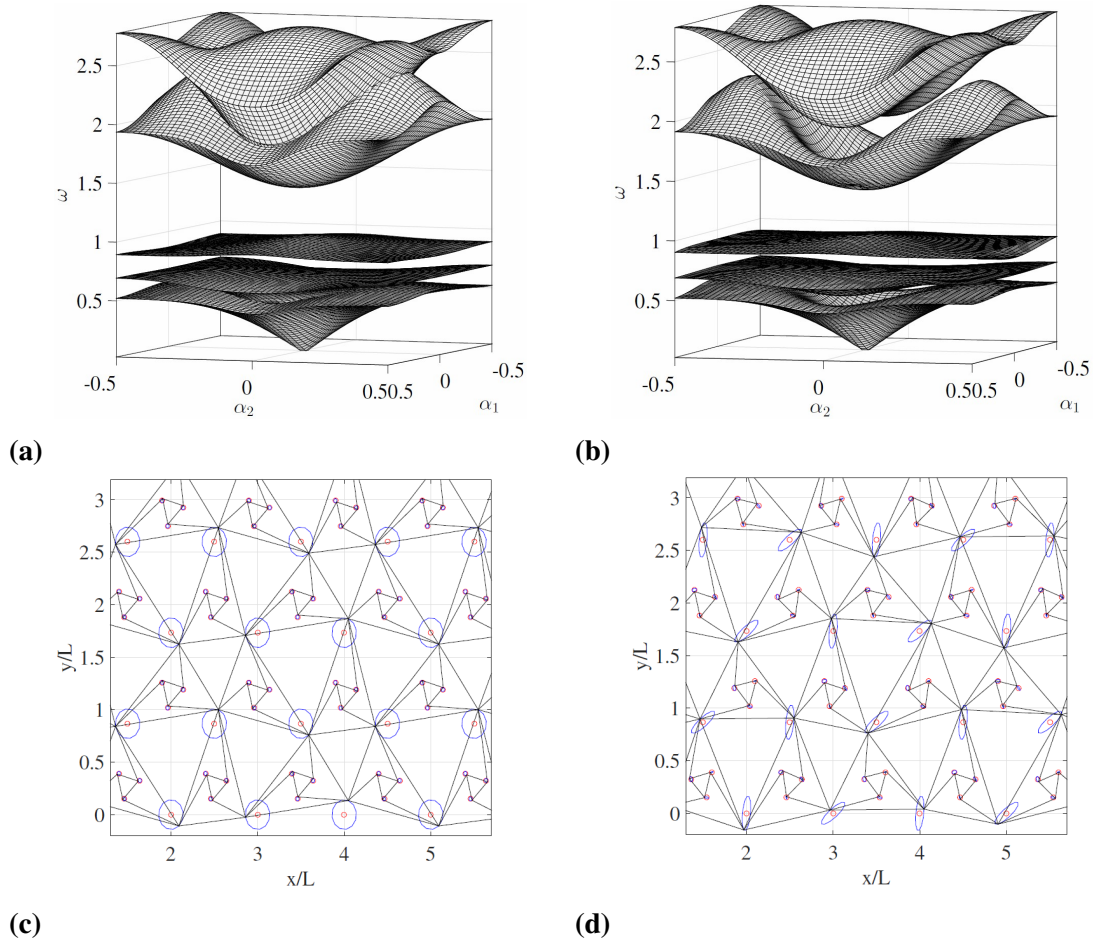

Fig. 4.13 *Panels (a) and (b) are dispersion surfaces for two different macro-cells. Panel (a) corresponds to a macro-cell whose resonators are rotated though the same angle* $\vartheta_0 = \vartheta_{\max}$*. In Panel (b), a resonator is rotated of an angle* $\vartheta_0 = \vartheta_{\max}$ *and the other one though the angle* $\vartheta_0 = -\vartheta_{\max}$*, as shown in Fig. 4.12(a). The remaining parameters are fixed as listed in Table 4.1. Panels (c) and (d) are illustrations of Bloch waves at* M' *which correspond to the macro-cells considered in panels (a) and (b), respectively. Symbols are the same as in Fig. 4.11. In panel (c) and (d) the Bloch frequencies at* M' *are* $\omega \approx 2.75$ rad/s *and* $\omega \approx 2.82$ rad/s*, respectively.*

cell. Fig. 4.13(c) shows the displacement amplitude field at M' for the structure whose dispersion surface is given in Fig. 4.13(a). We observe that the eigenmode shown in Fig. 4.13(c) is equivalent, up to an arbitrary phase shift, to that shown in Fig. 4.11(b) for a single-resonator cell corresponding to the point M. Fig. 4.13(d) shows the Bloch eigenmode at M' corresponding to a macro-cell with resonators rotated in the opposite directions; the corresponding dispersion surfaces are shown in Fig. 4.13(b). In this case, we observe that the orbits described by the triangular lattice nodes are elliptic. As in the previous case of single resonator unit cells, the resonators do not contribute to the propagation of elastic Bloch waves, at the chosen frequency.

4.5 Summarising remarks on chapter 4

In summary, the main focus of this chapter was on a new chiral lattice which exhibit a range of interesting dynamic properties, including dynamic anisotropy, Dirac, and Dirac-like dispersion. The chiral lattice, introduced in section 4.1, is modelled as a periodic array of triangular resonators embedded within an infinite uniform triangular lattice.

The lattice is statically undetermined in its untitled configuration. This degeneracy can be cured by assuming non-zero tilting or flexible links, as highlighted in section 4.2.

The dispersive properties of the chiral lattice have been studied in section 4.3. The geometric chirality arises from *tilting* the resonator and thus breaking the mirror symmetry of the ambient lattice. The introduction of the resonator results in the appearance of several additional modes that interact with the modes corresponding to the triangular lattice without resonators.

In particular, the resonators give rise to a novel rotationally dominant mode, which we refer to as the "chiral branch". In section 4.3.4 we have shown that the chiral branch frequency can be tuned to form Dirac-like dispersion with the optical modes at Γ.

The effect of introducing a non-uniform tilting angle (see section 4.4) has also been examined and it has been shown that it affects the dispersive properties and the polarisation of vortex-like modes around standing wave frequencies.

Generalisations are envisaged to the cases of high contrast between nodal masses of resonators and nodal masses of the ambient lattice. Similarly, high contrast between the stiffness of elastic ligaments within the resonators and the stiffness of the ambient lattice brings interesting dynamic features.

In the next chapter, we use the chiral branch to design and implement a flat lens for mechanical waves in a triangular lattice and to influence the crack speed in a thermoelastic lattice.

Chapter 5

Structured interfaces containing tilted resonators: focussing and wave-guiding

In this chapter we focus on scattering of in-plane elastic waves by lattice interfaces containing tilted resonators.

Transmission problems across slabs of finite width are of particular interest, as they enable us to evaluate the effect of coupling of pressure and shear waves in such metamaterials.

In section 5.1 a geometrically chiral interface is illustrated which incorporates a structured layer with rotational resonators of a special design, and shows negative refraction. Details on the design of the "flat lens" are also reported. Specifically, as already highlighted in the introduction to this thesis, the estimation of local dispersive properties of the lattice is of paramount importance in order to achieve focussing via negative refraction.

In the present chapter, we are primarily concerned with the range of frequencies corresponding to the chiral branch of the dispersion surfaces which is associated with the chiral effects of the resonator.

Here we give a special attention to micro-structured solids containing cracks, and we show how a coating, built of a tilted resonator lattice, can absorb vibrations, or otherwise can channel the energy away from the crack tip.

An additional focus of this chapter is on the effect of geometric chirality to the edge waves propagating along structured interfaces. In this context, we would like to mention the earlier work [38] where asymptotics for elastic waves propagating along line defects in triangular and square lattices were investigated. Here we analyse the propagation of edge waves along an interface around a "coated" crack, where the coating is introduced as a multi-scale structure of tilted resonators. Illustrative examples are provided in section 5.3.

An adaptive finite element computation has been performed to model a transient propagation of a crack inside a channel of the micro-structured material. The earlier work [92]

has addressed the question of a transient advance of a crack subjected to a dynamic load. The influence of a geometrically chiral multi-scale lattice on the field around the crack is addressed in section 5.4.

5.1 Focussing of elastic waves by a slab of TIRs

Dynamic anisotropy in a triangular lattice containing tilted resonators. We start by examining the forced problem for the triangular lattice both with and without TIRs. Similar problems have been extensively studied in the literature, with the classical reference text being the book by Maradudin *et al.* [54]. We also mention the papers by Martin [55] and Movchan and Slepyan [66], which analyse the properties of the dynamic Green's functions for a square lattice in the pass and stop band, respectively. The dynamic Green's functions for square and triangular elastic lattices were examined by Colquitt *et al.* in [20], with a particular emphasis on the resonances associated with dynamic anisotropy and *primitive waveforms*. These primitive waveforms have also been examined in the papers by Langley [47], Ruzzene *et al.* [77], Ayzenberg-Stepanenko and Slepyan [4], and Osharovich *et al.* [68], among others.

	c_ℓ	$c_{\ell o}$	L	ℓ	m	m_o
TLR	9 N/m	1.35 c_ℓ	1 m	$1/4\,L$	1 Kg	1 Kg
TL	9 N/m		1 m		4 Kg	

Table 5.1 *Physical parameters used in* COMSOL Multiphysics® *to model the structured interface containing tilted resonators.*

The Green's function for a lattice with triangular periodicity can be written in the form of a Fourier integral over the first Brillouin zone

$$\mathbf{G}_{mn}(\omega) = \frac{\sqrt{3}L^2}{8\pi^2} \int_{\boldsymbol{k}\in \mathrm{BZ}} \mathrm{d}\boldsymbol{k}\; \mathbf{g}_{mn}(\boldsymbol{k},\omega) e^{-i\mathbf{k}\cdot(n\mathbf{t}_1+m\mathbf{t}_2)}, \tag{5.1}$$

where $\mathbf{t}_1$ and $\mathbf{t}_2$ are the triangular lattice vectors (1.60), and m and n are integers. The influence of the rigid TIRs is captured by the Fourier transformed Green's function

$$\mathbf{g}_{mn}(\boldsymbol{k},\omega) = \left(\hat{\Sigma}_{\boldsymbol{k}} - \omega^2 \hat{\mathscr{M}}\right)^{-1} \mathbf{F}, \tag{5.2}$$

where the stiffness matrix $\hat{\Sigma}_{\boldsymbol{k}}$ is given in Eq. (4.50) and the inertia matrix $\hat{\mathscr{M}}$ in Eq. (4.51). In Eq. (5.2), $\mathbf{F}$ represents the amplitude of the time-harmonic force applied at the origin. So-

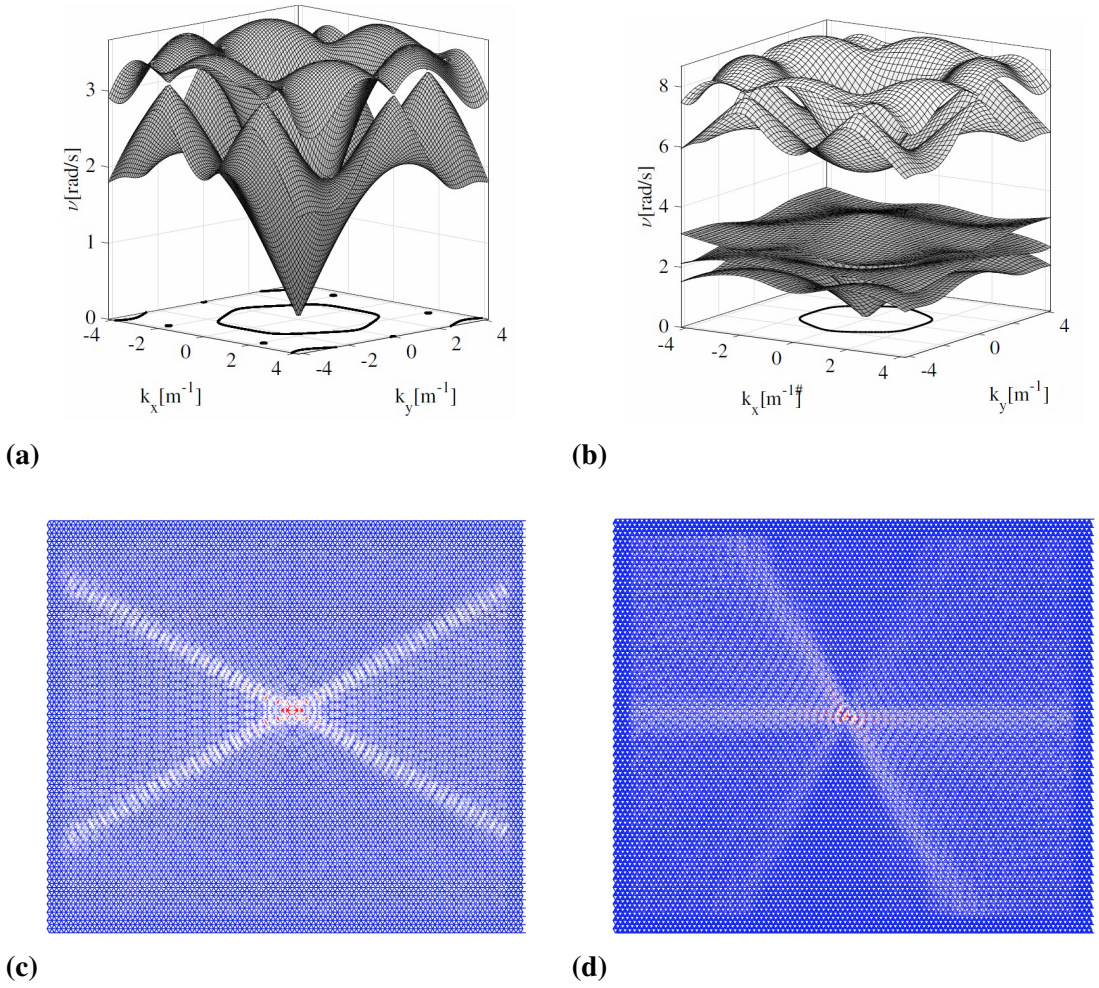

Fig. 5.1 *Panel (a) and (b) are dispersion surfaces for a monatomic triangular lattice (TL) and a triangular lattice with TIRs (TLR), respectively. The slowness contours at* $\omega = \pi$ rad/s *are also reported as projections onto the plane* $\omega = 0$*. The parameters used are listed in Table 5.1. Panel (c) and (d) are elastic responses of the TL and TLR, respectively considered in panels (a) and (b). The source of the excitation has amplitude as in Eq. (5.3), with* $F = 0.1$ N *and angular frequency* $\omega = \pi$ rad/s.

lutions of Eq. (5.1) are obtained using COMSOL Multiphysics®. The numerical parameters used for the illustrative computations presented in this section, are listed in table 5.1. Figs 5.1 (a) and 5.1(b) show the dispersion surfaces for a triangular lattice and a triangular lattice with TIRs, respectively. The slowness contours at $\omega = \pi$ rad/s are also shown as projections onto the $\omega = 0$ plane. Figs 5.1(c) and 5.1(d) show the magnitude of the displacement field generated by an harmonic point load. In particular, panels (c) and (d) show the fields for a triangular lattice and a triangular lattice with TIRs, respectively. The source of the excitation is a point, time-harmonic loading exerted at the centre of the computational window. The orientation of the applied load is chosen to be parallel to the horizontal x-axis and of unit amplitude, so that

$$\mathbf{F} = F\,(1,0,0,0,0)^{\mathrm{T}}. \tag{5.3}$$

The angular frequency of the excitation is $\omega = \pi$ rad/s. Figs 5.1(c) and 5.1(d) show the expected strong dynamic anisotropy. In particular, panel (c) shows a cross-like propagation pattern with the arms of the cross at $\pi/6$ radians with respect to the horizontal direction. This is consistent with the slowness contour in panel (a) with the waves propagating in the directions normal to the hexagon-like slowness contour. No wave propagation is observed in the vertical direction because the source is polarised in the x direction. Panel (d) shows a similar star-like shape for the displacement field. The slowness contour shown in panel (b) arises from the mode associated with the TIRs. Again, we observe that the displacement field shown in panel (d) is consistent with the associated slowness contour, and waves propagate in the directions parallel to the normals of the slowness contours.

Focussing via negative refraction. We now proceed to consider the scattering problem associated with a thin strip of triangular lattice with TIRs embedded within an ambient triangular lattice. Fig. 5.2(a) shows the slowness curves which also appear in Figs 5.1(a) and 5.1(b), at $\omega = \pi$ rad/s. We choose this frequency to isolate the effect of the Bloch mode associated with the geometric chirality of the lattice. We observe that the concavity of the dispersion surface in correspondence of $\omega = \pi$ rad/s is negative (see Fig. 5.1(b)). Since the group velocity points towards growing frequencies, at $\omega = \pi$ rad/s along the preferential directions of the lattice with TIRs points inwards the first Brillouin zone. On the other hand, the group velocity associated with the triangular ambient lattice points outwards, because the concavity of the dispersion surfaces is positive at $\omega = \pi$ rad/s (see Fig. 5.1(a)). The group velocity vectors are qualitatively represented in Fig. 5.2(a). The two-dimensional hexagonal slowness contours in Fig. 5.2(a) are rotated, by $\pi/6$, with respect to each other. These two properties - opposite group velocities along the preferential directions and rotated slowness contours - are here used to design a flat lens capable of utilising negative refraction

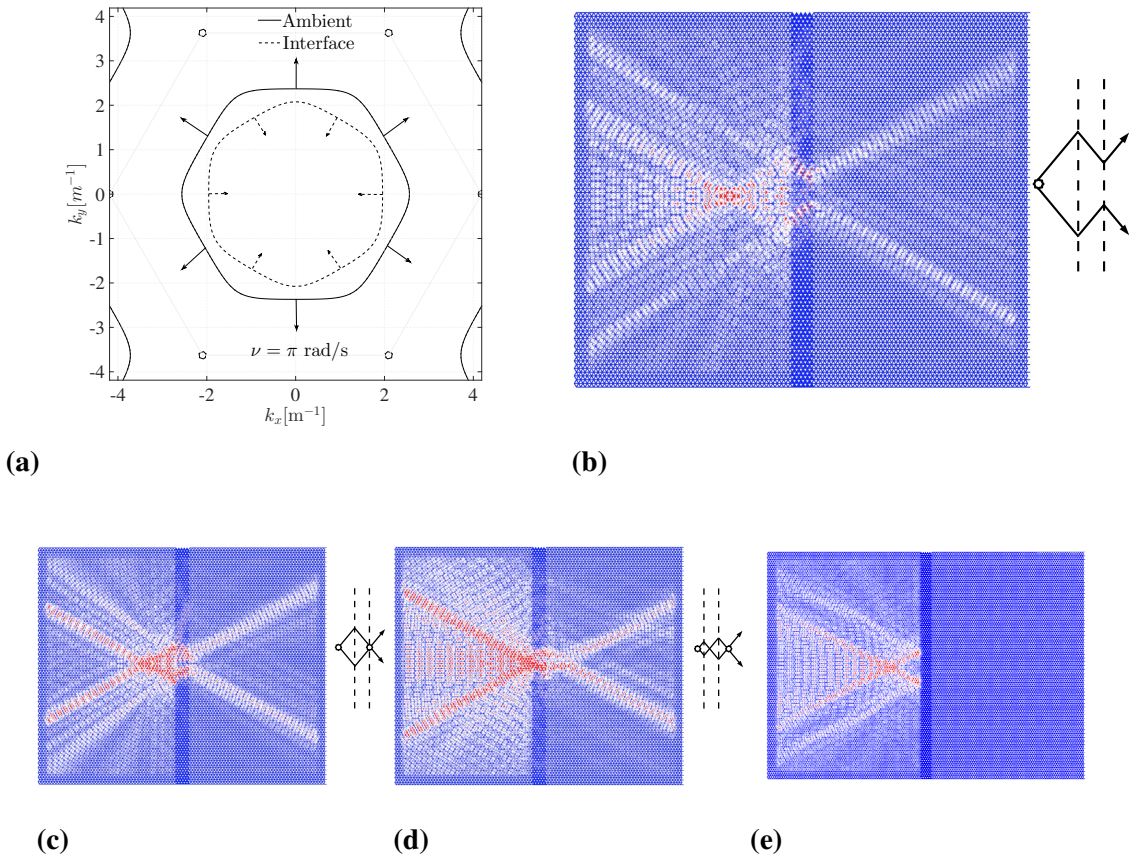

Fig. 5.2 *Panel (a): A comparison of slowness curves presented in Fig. 5.1; the slowness curves are plotted at the same frequency as the one of the harmonic excitation, that is* $\omega = \pi$ rad/s. *The dashed and solid arrows schematically represent the directions of the group velocities in the corresponding lattice. Panels (b), (c) and (d): Numerical simulations of a negative refractive flat lense containing TIRs surrounded by a TL; the physical parameters for the TL and TLR are as in Table 5.1. The time-harmonic force is horizontal and has amplitude* $F = 0.1$ N *and angular frequency* $\omega = \pi$ rad/s. *In panels (b), (c) and (d), the distance of the point source away from from the left interface is 20, 10 and 1 lattice sites. In panel (e) the tilting angle is set to zero, leading to total reflection.*

to focus elastic waves in a triangular lattice. This effect is illustrated in Fig. 5.2(b). The excitation source is the same as the one used to generate Fig. 5.1(c) and the parameter values are described in Table 5.1.

At the chosen frequency $\omega = \pi$ rad/s, exciting the triangular lattice with a point source results in a cross-like displacement field, as already discussed for Fig. 5.1(c); the angle between the beams and the x-axis is $\pi/6$. This is consistent with the slowness contours for the ambient lattice shown in Fig. 5.2(a). The slowness contours for the interface are rotated by $\pi/6$ with respect to those of the ambient lattice, as shown in Fig. 5.2(a). This explains the negative refraction evident at the interfaces between the triangular lattice and the lattice

with TIRs, shown in panel (b). A virtual image of the source can be observed on the right side of the ambient lattice. The formation of the virtual image is illustrated in the inset diagram. Panel (b) is obtained locating the point source twenty lattice spaces away from the left interface of the lens. In panel (c), we move the source closer (ten lattice spaces). We observe that the position of the virtual image moves closer to the right interface of the flat interface (see also inset diagram). In panel (d), we locate the source one lattice site away from the flat lens. This results in the formation of a *real* image of the source on the right side of the diagram, and demonstrates focussing of elastic waves by means of negative refraction. In Fig. 5.2(e), the resonators in the structured interface are not tilted. As illustrated in the context of Fig. 4.7, at zero tilting angle the Bloch branch associated with the geometrical chirality annihilates. Elastic waves propagating from the ambient lattice experience a frequency stop band and, in turn, total reflection as shown in panel (e). This results in the disappearance of any negative refractive effect.

5.2 Localisation and wave-guiding at the Dirac-like point

In this section, we analyse the wave forms, which correspond to the frequencies in the neighbourhood of the Dirac-like point discussed in section 4.3.4. In addition, we study the propagation of edge waves along interfaces obtained by modifying the bulk homogeneous lattices.

The dynamic response of the periodic lattice to point loads of different orientations is studied using COMSOL Multiphysics. In the computations we truncate the lattice retaining a $N \times N$ cluster of TLR's cells, where $N \approx 50$. In order to reduce spurious reflections from the boundaries of the computational window, the dynamic equations of the nodal points close to the sides of the grid include a damping term. The damping layer is approximately four lattice spacings wide. The harmonic responses shown in this section are triggered by a point force of frequency $\omega = \pi$ rad/s, linear polarisation and amplitude $F = 0.1$ N. We assume that the force is exerted on a triangular lattice node, located at the centre of the cluster. The lattice parameters considered here are listed in Table 4.2, where SI units of measurement and angles in unit of radiant are understood. These parameters have been chosen to reproduce a triple-eigenvalue at Γ and frequency $\omega = \pi$ rad/s at the Dirac-like point (see section 4.3.4).

5.2.1 Dynamic response and edge waves

The effective properties of the dispersion surfaces emanating from the Dirac-like point (see section 4.3.4 and Figs 4.9) strongly influence the harmonic response of the structure. Special

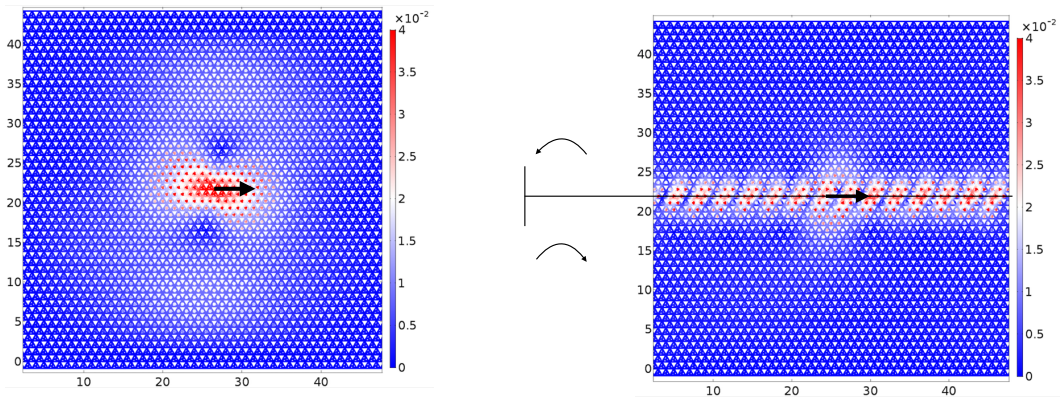

Fig. 5.3 *Panel (a) is the time-harmonic response of a homogeneous lattice with tilted resonators to a time-harmonic force of amplitude $F = 0.1$ N, frequency $\omega = \pi$ rad/s and applied at a triangular lattice nodal point. The force is oriented in the horizontal direction (black arrow). The lattice parameters are reported in set 1 of Table 4.2. In panel (b), leaving the lattice parameters in set 1 of Table 4.2 and loading conditions unchanged, an inhomogeneity is introduced: above the thin horizontal line, the resonators are tilted in the counter-clockwise direction and below the thin line they are tilted clockwise. Both angles are of the same magnitude ϑ_0.*

attention is given to the influence of the effective mass (see Eq. (**??**)) of the parabolic-in-**k** mode, and to the group velocity at the conical mode, on the localisation patterns and on the amplitude and wavelength of the edge waves propagating along interfaces obtained from the bulk triangular lattice with resonators.

Edge waves along an interface between oppositely tilted half-spaces. Figure 5.3 shows the harmonic responses of a homogeneous (panel (a)) and inhomogeneous (panel (b)) lattice with tilted resonators to a harmonic force of amplitude $F = 0.1$ N, frequency $\omega = \pi$ rad/s and applied to a triangular lattice nodal point. The lattice parameters are reported in set 1 of Table 4.2. The inhomogeneity considered in Fig. 5.3(b) arises from the tilting angle which is oriented in the counter-clockwise and clockwise directions above and below the thin horizontal line, respectively. The thin line represents therefore an interface separating two homogeneously tilted half-spaces. Since the modulus of the tilting angle is the same, the dispersion surfaces associated with the two configurations are the same and coincide with Fig. 4.9(a). For the time being, the force is in the horizontal direction (black arrow). In the homogeneous lattice (panel (a)) we observe a localised mode as one would expect in correspondence of the parabolic-in-$\boldsymbol{k}$ mode at $\omega = \pi$ in Fig. 4.9(a) (see the black line in Fig. 4.9(d) for the corresponding dispersion curve). The harmonic response changes

dramatically as the inhomogeneous tilting is introduced (panel (b)) leading to a propagating mode travelling along the interface, which we refer to as “edge wave”.

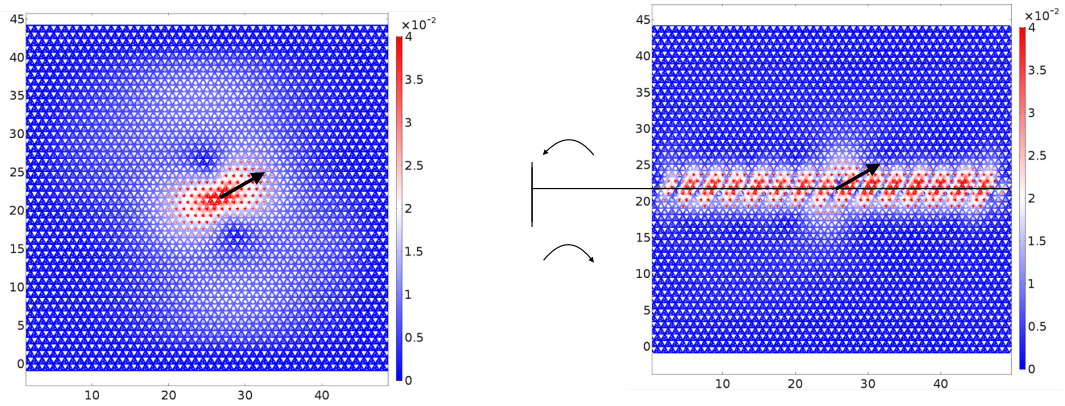

Fig. 5.4 *Panel (a) is the time-harmonic response of a homogeneous lattice with tilted resonators to a time-harmonic force of amplitude* $F = 0.1$ N, *frequency* $\omega = \pi$ rad/s *and applied to a triangular lattice nodal point. The force is oriented at* 30 *degrees angle with respect to the horizontal direction (black arrow). The lattice parameters are reported in set 1 of Table 4.2. In panel (b), leaving the lattice parameters in set 1 of Table 4.2 and loading conditions unchanged, an inhomogeneity is introduced: above the thin horizontal line, the resonators are tilted by an angle* ϑ_0, *and below the thin line they are tilted of an angle* $-\vartheta_0$.

Role of the direction of the force. We here investigate the role of the orientation of the force on the dynamic response of systems which are identical to those introduced in Fig. 5.3. The computations are shown in Figs 5.4 and 5.5. In Fig. 5.4(a) we consider a lattice identical to the one introduced in Fig. 5.3(a). The force (black arrow in Fig. 5.4(a)) is oriented at 30 degrees with respect to the horizontal direction. The same orientation is assumed in Fig. 5.4(b) where a inhomogeneously tilted lattice is considered, similarly to Fig. 5.3(b). The lattices considered in Figs 5.5(a) and 5.5(b) are the same as in Figs 5.4(a) and 5.4(b). The harmonic loadings considered in Fig. 5.5 is at sixty degrees with respect to the horizontal direction (see black arrows). By comparing Figs 5.3(a), 5.4(a) and 5.5(a), we observe that the symmetry axis of the localisation pattern follows the polarisation angle of the force. Moreover, comparing Figs 5.3(b), 5.4(b) and 5.5(b), the intensity of the modes changes, being larger for larger angles. A possible physical interpretation may be found in the polarisation of the propagating mode. The in-plane displacement field in Figs 5.3(b), 5.4(b) and 5.5(b) is “bubble like" or, more formally, is elliptically polarised, with the polarisation axis aligned with the lattice vectors $\boldsymbol{t}_1$ and $\boldsymbol{t}_2$. Therefore, when the direction of the force matches 60 degrees the mode has maximum amplitude compared to the other orientations.

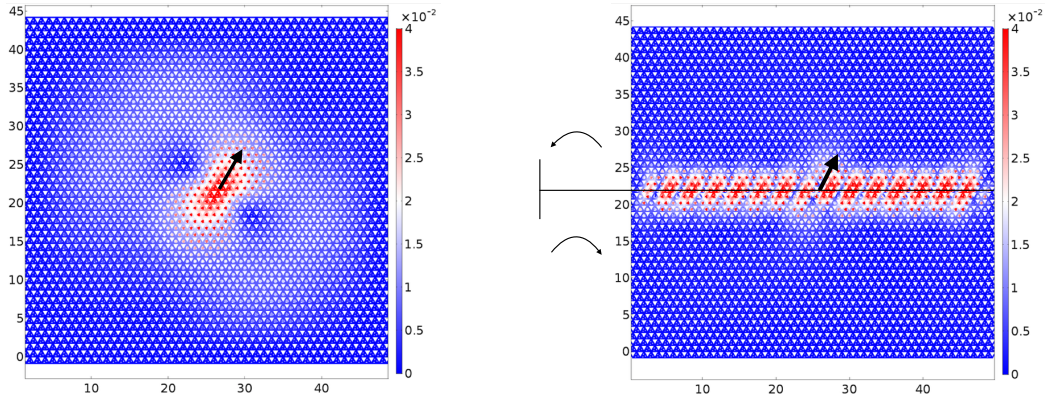

Fig. 5.5 *Panel (a) is the time-harmonic response of a homogeneous lattice with tilted resonators to a harmonic force of amplitude* $F = 0.1$ N, *frequency* $\omega = \pi$ rad/s *and applied to a triangular lattice nodal point. The force is oriented at* 60 *degrees angle with respect to the horizontal direction (black arrow). The lattice parameters are reported in set 1 of Table 4.2. In panel (b), setting the lattice parameters and loading condition as in panel (a), an inhomogeneity is introduced: above the thin horizontal line, the resonators are tilted by an angle* ϑ_0, *and below the thin line they are tilted of an angle* $-\vartheta_0$.

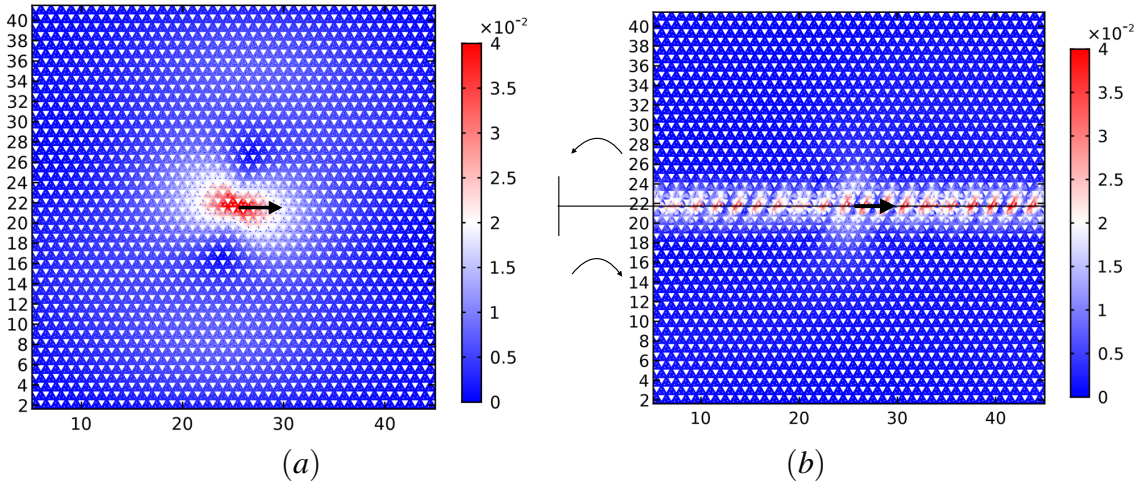

Fig. 5.6 *Panel (a) is the harmonic response of a homogeneous lattice with tilted resonators to a harmonic force of amplitude* $F = 0.1$ N, *frequency* $\omega = \pi$ rad/s *and applied to a triangular lattice nodal point. The force is oriented at* 0 *degrees angle with respect to the horizontal direction (black arrow). The lattice parameters are reported in set 1 of Table 4.2. In panel (b), leaving the lattice parameters in set 2 of Table 4.2 and loading conditions unchanged, an inhomogeneity is introduced: above the thin horizontal line, the resonators are tilted by an angle* ϑ_0, *and below the thin line they are tilted of an angle* $-\vartheta_0$.

Role of different group velocities at the Dirac-like point. A deeper insight into the dynamic properties of the localised waves and edge waves described in Figs 5.3(b), 5.4(b)

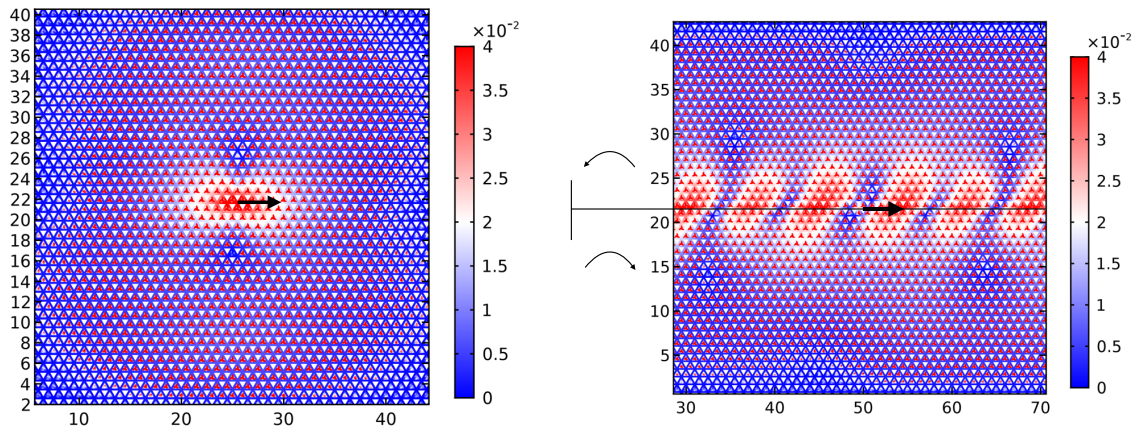

Fig. 5.7 *Panel (a) is the harmonic response of a homogeneous lattice with tilted resonators to a harmonic force of amplitude $F = 0.1$ N, frequency $\omega = \pi$ rad/s and applied to a triangular lattice nodal point. The force is oriented in the horizontal direction (black arrow). The lattice parameters are reported in set 1 of Table 4.2. In panel (b), taking the lattice parameters of set 2 of Table 4.2 and loading conditions unchanged, an inhomogeneity is introduced: above the thin horizontal line, the resonators are tilted by an angle ϑ_0, and below the thin line they are tilted by an angle $-\vartheta_0$.*

and 5.5(b) is proposed here. In order to assess the dynamic nature of the mode, we consider here different lattice parameters compared to those used earlier. In the same spirit as in Figs 5.3, 5.4 and 5.5, in Figs 5.6 and 5.7 we show the harmonic responses of clusters whose lattice parameters are listed in set 2 and set 3 of Table 4.2, respectively. Although the lattice parameters are different, they have been chosen in order to reproduce a Dirac-like dispersion at $\omega = \pi$. The corresponding dispersion surfaces are represented in Fig. 4.9(d) by the red and blue lines, respectively. Different dispersive properties near the Dirac-like point affect the harmonic responses of homogeneously tilted clusters (panels (a) and (c)) and inhomogeneously tilted clusters (panels (b) and (d)). The inhomogeneity considered here has the same meaning as in Fig. 5.3. Figs 5.6(a) and 5.7(a) show localised patterns similar to that encountered in Fig. 5.3(a). Figs 5.6(b) and 5.7(b) show an edge wave travelling across the interface. We remark that the wavelength of the edge waves is larger for smaller effective group velocities at the Dirac-like point $\omega = \pi$ rad/s. This suggests that the dynamics of the edge waves, *e.g.* its wavelength, can be controlled by harnessing the group velocities at the Dirac-like point, with shorter wavelength corresponding to higher group velocities.

Edge wave along a strongly damaged interface. Figure 5.8 shows the modulus of the displacement field for a forced triangular lattice with resonators containing a defect which consists of a missing line of resonators, as shown in the magnifying inset highlighted in

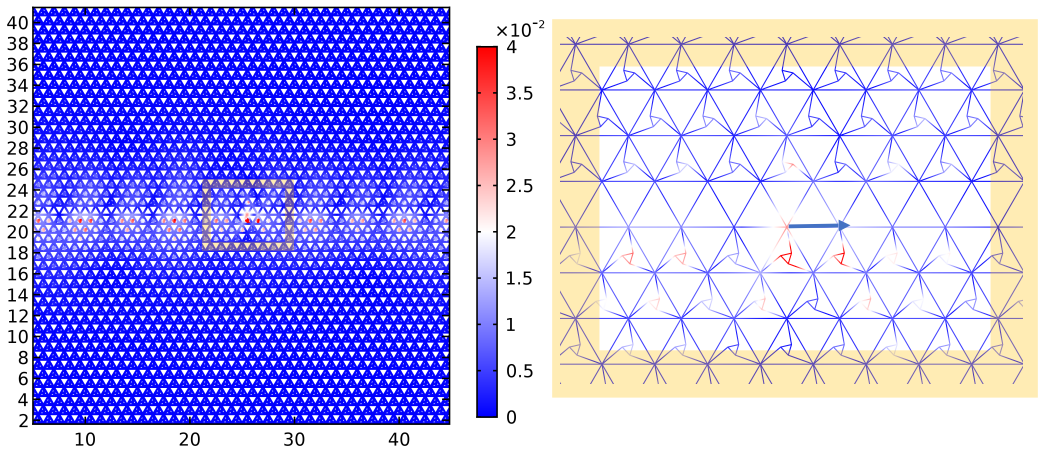

Fig. 5.8 *Response of a defective triangular lattice with resonators to a time-harmonic point force. The defect consists of a missing line of resonators, as highlighted in the yellow magnifying inset on the right. The point force is represented in the inset by the blue arrow and has amplitude* $F = 0.1$ N *and frequency* $\omega = \pi$ rad/s. *The parameters used in this computation are listed in set 1 of Table 4.2.*

yellow on the right side of the figure. The lattice parameters used in this computation are listed in set 1 of Table 4.2. The harmonic force is identical to the one used in Fig. 5.3(a) and is exerted on a triangular lattice nodal point below the line defect (see blue arrow in the inset). We observe that the defect acts as a wave guide for an edge wave whose wavelength differs from the one in Fig. 5.3(b). We emphasise again that the wave-guiding behaviour in Fig. 5.8 differs significantly from the localisation pattern in Fig. 5.3(a), the bulk homogeneous counterpart.

5.3 Wave-forms around a crack surrounded by a micro-structured coating

In this section we study a special coating for one-dimensional cracks inside a triangular lattice. We consider a shear plane wave of angular frequency $\omega = \pi$ rad/s impinging on the crack. The coating is obtained by introducing resonators around the crack.

The physical parameters of the exterior triangular lattice in which the plane wave propagates, can be chosen in such a away as to guarantee an isotropic dynamic response at a given frequency. For example, the stiffness of the links $c_{\mathrm{TL}} = 50$ N/m and the mass of the nodal points $m_{\mathrm{TL}} = m + 3m_o = 1.43$ Kg (see set 1 in Table 4.2) guarantee an isotropic dynamic response at $\omega = \pi$ rad/s. We observe that the aforementioned choice of the mass minimises

spurious scattering effects associated with a contrast in inertia. Fig. 5.9(a) shows a shear plane wave of frequency $\omega = \pi$ rad/s propagating through the isotropic triangular lattice. In Fig. 5.9(b), a crack, created by removing some links from the triangular lattice, scatters the shear plane wave.

In this section, the lattice parameters of the structured coating are given in set 1 of Table 4.2. The corresponding dispersion surfaces are reported in Fig. 4.9(a). The different frequency regimes are discussed via the analysis of the scattered displacement fields: we address first the frequencies close to the Dirac-like point and later we focus on a band gap regime.

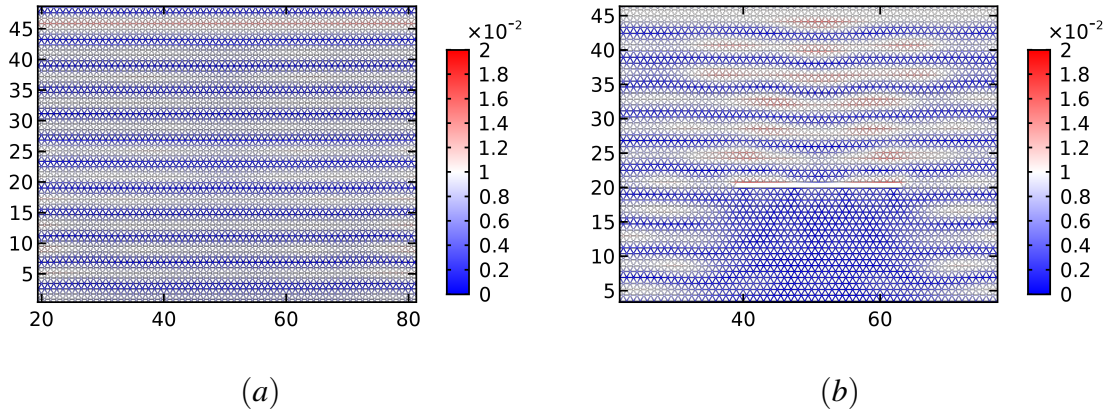

Fig. 5.9 *Panel (a) shows a shear plane wave of angular frequency $\omega = \pi$ rad/s travelling through an homogeneous triangular lattice. In panel (b) the same shear wave is scattered by a one dimensional uncoated crack.*

Dirac-like regime. In Fig. 5.10 we compare the modulus of the displacement field resulting from the interaction of an elastic shear wave with a cluster of resonators (panel (a)) and with a cluster of resonators containing a crack (panel (b)). The source of the excitation is a plane wave of frequency $\omega = \pi$ rad/s which corresponds to the Dirac-like point for the periodic TLR (see Fig. 4.9). Panel (a) shows that scattering of elastic waves is highly anisotropic, the displacement field being concentrated on the right side of the cluster. It is worthwhile noting that if the resonators are rotated in the counter-clockwise direction ($\vartheta_0 = -0.82$) the displacement field is mirror-symmetric compared to that of Fig. 5.10(a). The introduction of a crack within the cluster (Fig. 5.10(b)) triggers the propagation of elastic waves around the crack itself. The displacement field and the corresponding stresses are still visibly concentrated around the right tip of the crack. This suggests that a coating of resonators in the Dirac-like regime is likely to lead to a left-right asymmetry in the propagation of the crack.

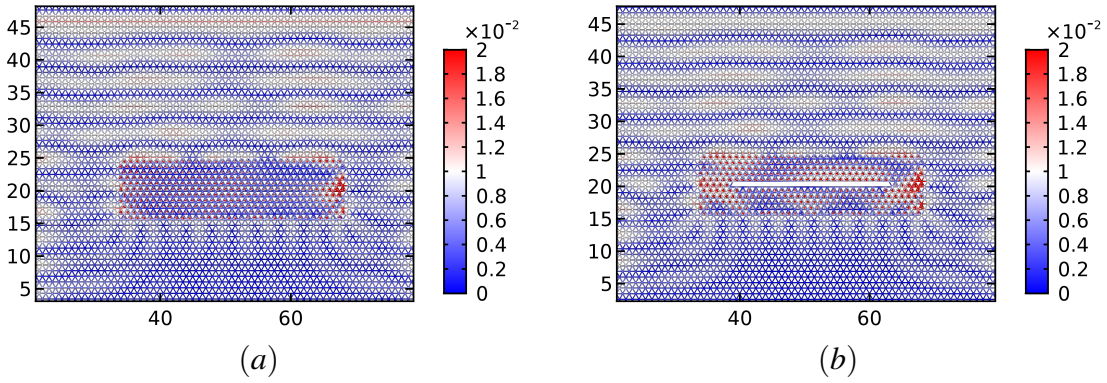

Fig. 5.10 *The time-harmonic responses to a shear plane wave of frequency* $\omega = \pi$ rad/s *corresponding to the Dirac-like point for the triangular lattice with resonators. Panels (a) and (b) represent a cluster of resonators and a crack surrounded by a cluster of resonators, respectively. The parameters used to model the clusters are listed in set 1 of Table 4.2.*

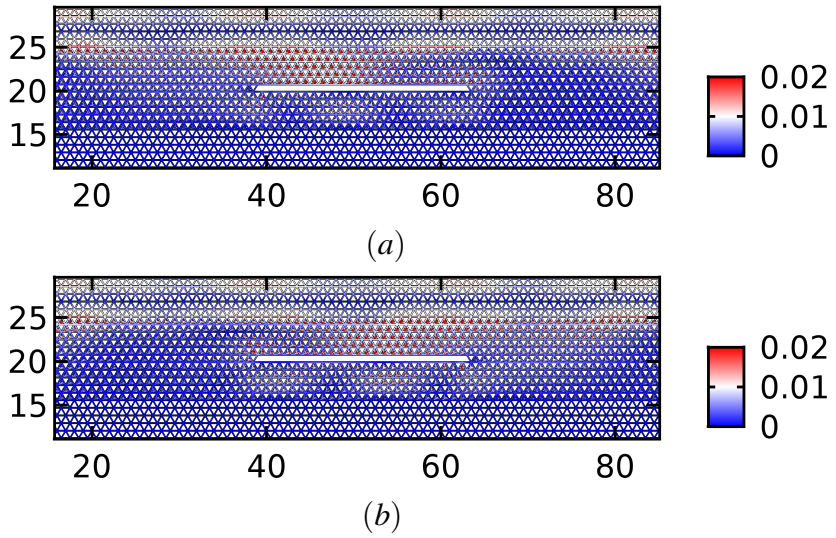

Fig. 5.11 *The harmonic responses to a shear plane wave of frequency* $\omega = \pi$ rad/s *corresponding to the Dirac point for the triangular lattice with resonators. In panels (a) and (b), we substitute the cluster of Fig. 5.10(b), which is finite in the horizontal direction, with an infinite strip. In panels (a) and (b), the tilting is clockwise and counter-clockwise, respectively. The parameters used to model the clusters are listed in set 1 of Table 4.2.*

In Figs 5.11, a long strips of resonators containing a crack interact with a shear plane wave impinging on the strip from above. Several arrangements for the resonators are considered. In panel (a) (panel (b)) the resonators in the strip are homogeneously tilted in the clockwise (counter-clockwise) direction. Similarly to Fig. 5.10(a), this leads to an enhancement of the displacement field close to the tips of the crack. Moreover, the results are mirror-symmetric

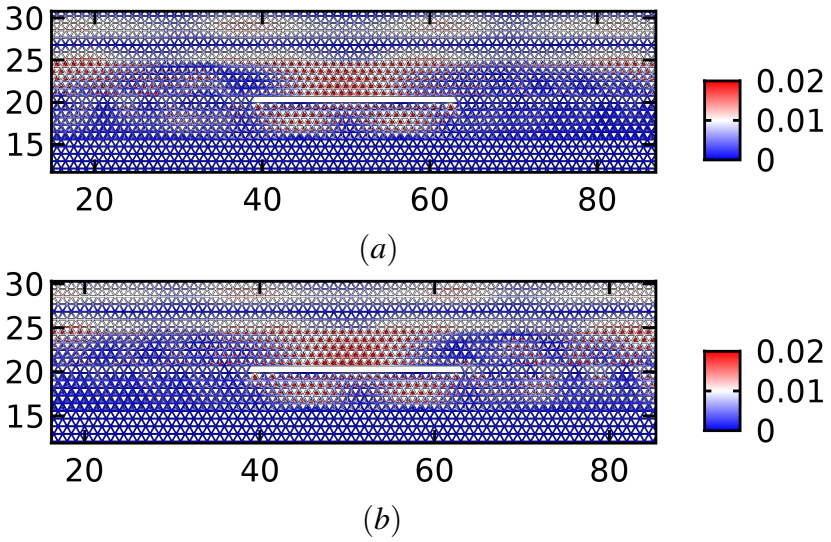

Fig. 5.12 *The time-harmonic responses to a shear plane wave of frequency $\omega = \pi$ rad/s corresponding to the Dirac point for the triangular lattice with resonators. In panels (a) and (b), we substitute the cluster of Figs 5.11 with a strongly damaged one, where an infinite line of resonators is missing along the line of the crack. In panels (a) the tilting is homogeneous. ln panel (b) the tilting is counter-clockwise above and clockwise below the line defect. The parameters used to model the clusters are listed in set 1 of Table 4.2.*

about the vertical line passing through the centre of the crack. This is consistent with what we observe in Fig. 5.10(b).

In Fig. 5.12, the homogeneously tilted strip analysed in Fig. 5.11(a) has been replaced by a strip with an interface. The interface is represented by a line of missing resonators. The stiffness of the triangular lattice links, which define the interface, is assumed to be $c_{\mathrm{TL}} = 50$ N/m, as in the exterior triangular lattice. In Fig. 5.12(b), the strip is similar to the one of Fig. 5.12(a) but counter-clockwise tilting above the line and clockwise tilting below the line is implemented. In Figs 5.12(c) and 5.12(d) the displacement field is mirror-symmetric with respect to a vertical line passing through the centre of the crack.

Band gap regime. In Fig. 5.13, a shear plane wave coming from above impinges at normal incidence on a cluster of resonators (panel (a)) and on a cluster of resonators containing a crack (panels (b),(c) and (d)). The frequency of the excitation is $\omega = 2.4$ rad/s corresponding to the band gap of Fig. 4.9(a). It is remarked that the incident wave does not penetrate the coating. In particular, panel (b) shows that the structured cluster acts as a protective layer for the crack, as one would expect from the analysis of the dispersion diagram for Bloch-Floquet waves. In Figs 5.13(c) and 5.13(d) we introduce a defect consisting of a missing line of resonators along the extension of the crack. In Fig. 5.13(c) the tilting angle is

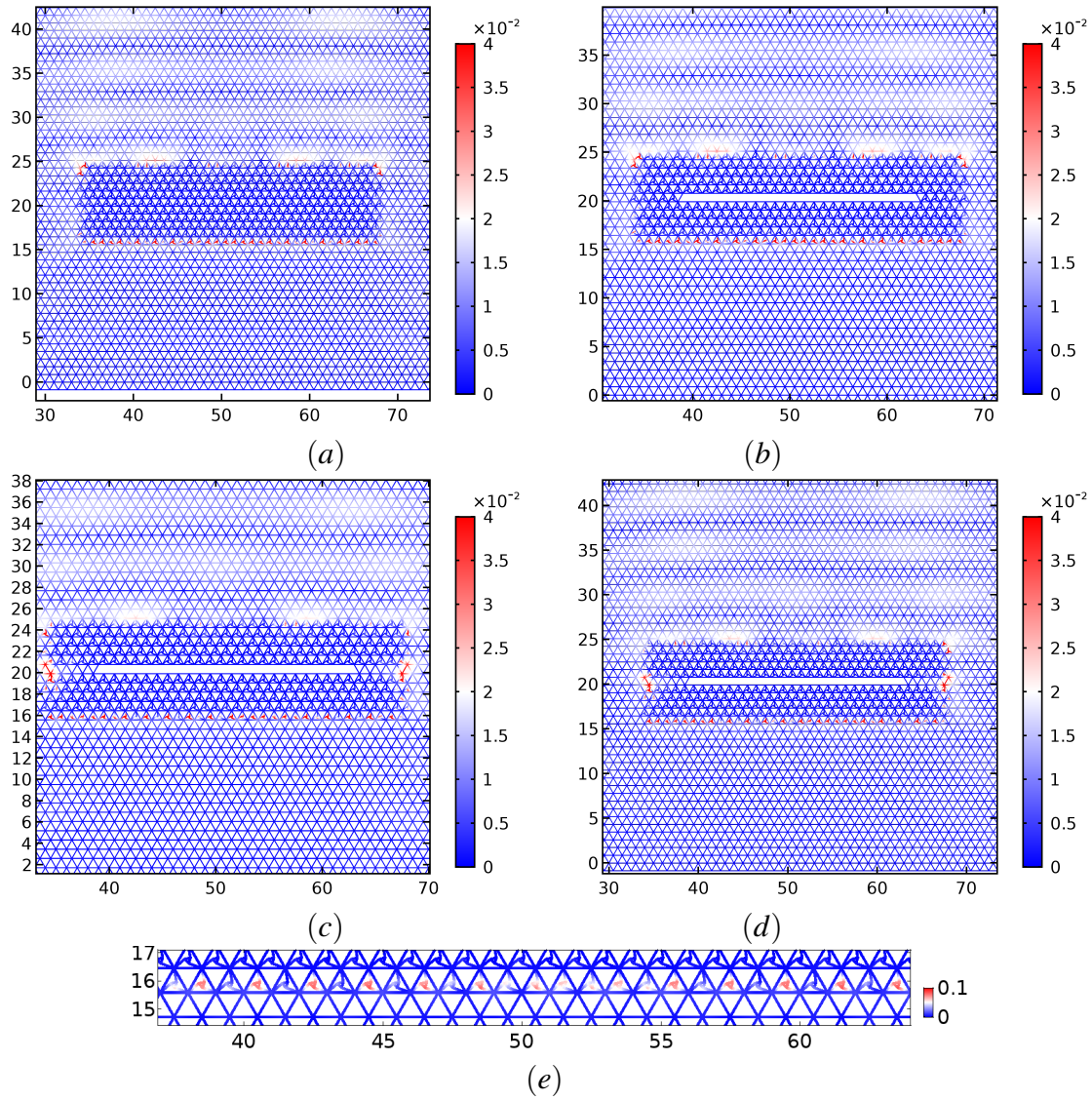

Fig. 5.13 *The harmonic response of a cluster of resonators to a shear plane wave of frequency* $\omega = 2.4$ rad/s *inside the stop band for the TLR. Panel (a) and (b) are with and without a crack. Panels (c) and (d) include a line of resonators missing along the extension of the crack. In panel (c) the tilting angle is homogeneous, whereas in panel (d) the resonators are tilted through opposite angles above and below the crack. Panel (e) is a detail of the lower boundary of the cluster in panel (a) showing an edge wave. The lattice parameters are as in Figs 5.10.*

homogeneous, whereas in panel 5.13(d) the resonators are tilted in opposite directions above and below the line defect. The stiffness of the links of the line defects is the same as of the exterior triangular lattice. Figs 5.13(c) and 5.13(d) show a displacement enhancement at the perimeter of the cluster, however away from the crack tip. Fig. 5.13(e) highlights an edge wave travelling along the boundary of the cluster.

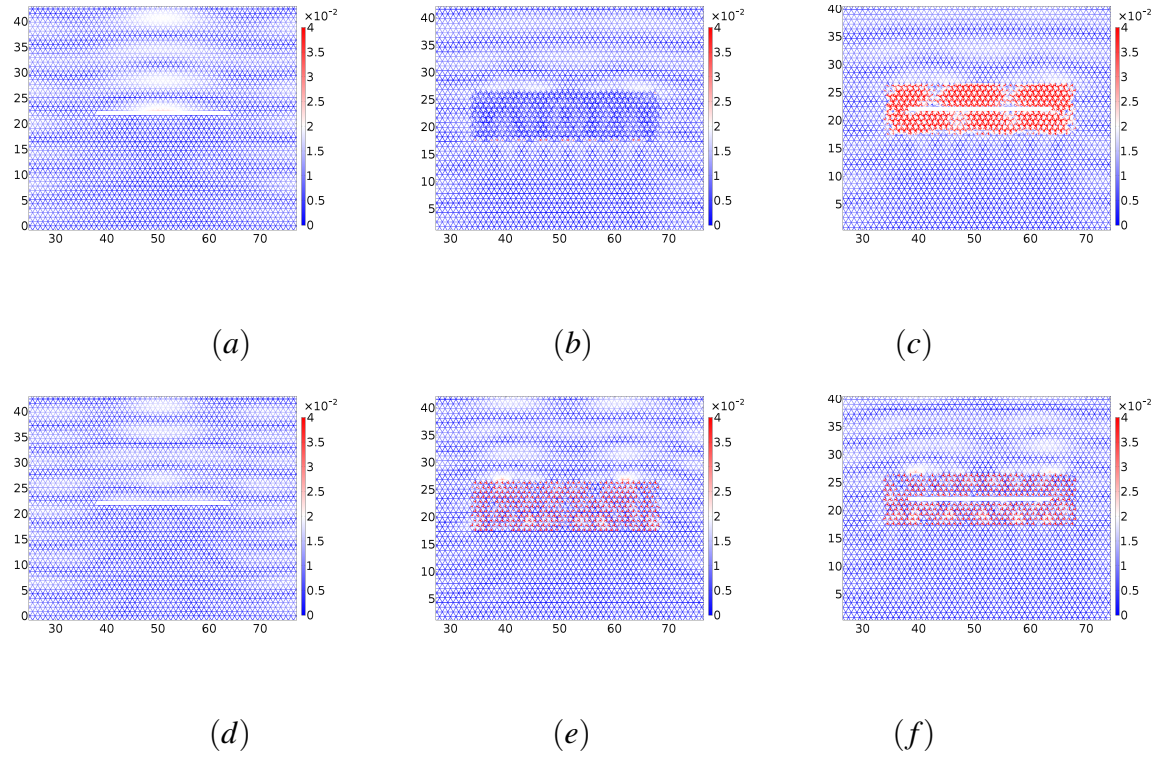

Fig. 5.14 *The time-harmonic response to a shear plane wave. Panels (a) and (d), (b) and (e), (c) and (f), comprise a crack, a cluster of resonators and a crack surrounded by a cluster of resonators, respectively. The angular frequency for panels (a), (b) and (c) is* $\omega = 2.1$ rad/s *corresponding to the lower edge of the band gap of Fig. 4.9(a). The angular frequency of the shear waves in panels (d), (e) and (f) is* $\omega = 2.7$ rad/s*, corresponding to the upper edge of the band gap of Fig. 4.9(a).*

In Figs 5.14(a), 5.14(b) and 5.14(c), the angular frequency $\omega = 2.1$ rad/s of the plane wave corresponds to the lower edge of the band gap of Fig. 4.9(a). In Figs 5.14(d), 5.14(e) and 5.14(f), the frequency $\omega = 2.7$ rad/s corresponds to the upper edge of the band gap. For the lower edge frequency, although the cluster is partially protective (see panel (b)), the introduction of the one-dimensional defect increases the stress concentration around the crack (panels (c)), compared to the uncoated configuration (panels (a)). A similar effect is reported for the upper edge of the band gap in Figs 5.14(e) and 5.14(f). In the vicinity of the band gap edges, the coating of resonators enhances the displacement field around the crack, increasing the chances for the crack to propagate.

5.4 Edge crack subjected to a transient thermal load

The governing equations, loading configuration and the fracture criterion are the same as in the earlier computations for the thermoelastic crack advancing through a homogeneous triangular

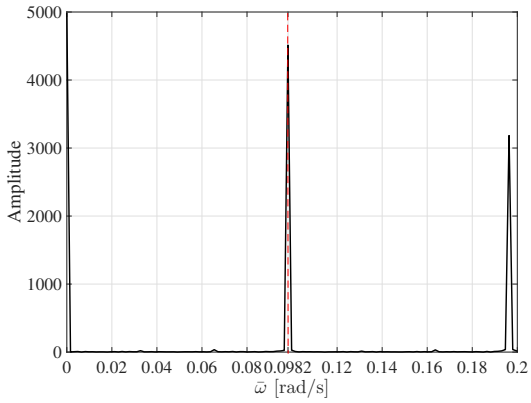

Fig. 5.15 *The Fast Fourier Transform of the input pulsating load has identified a countable number of spikes at different frequencies. Two spikes in the low frequency regime are shown here.*

	c_ℓ [N/m]	m [Kg]	L [m]	ℓ [m]	$c_{\ell o}$ [N/m]	m_o [Kg]	ϑ_0 [deg]	$\alpha[\mathrm{C}^{-1}]$
set 1, TLR	1	181.82	1	0.21	1	90.91	47	10^{-3}
set 2, TLR	1	181.82	1	0.21	1	90.91	78	10^{-3}
TL	1	1	1					10^{-3}

Table 5.2 *Thermoelastic parameters for the ambient triangular lattice (third row) and for triangular lattices with resonators (first and second rows). The parameter $\alpha = (\mathrm{d}L/\mathrm{d}T)/L$ is the longitudinal coefficient of thermal expansion which applies to the triangular lattice links only. The remaining links are such that $\alpha = 0$.*

lattice [92]. Here, a geometrically chiral coating surrounding the crack is introduced into the model. An elastic wave is generated as a result of a rapid variation of the boundary temperature. The fracture criterion is based on a normalised threshold elongation $\varepsilon = \Delta L/L$. The crack advances when the ligament at the crack tip reaches the critical threshold elongation. The loading configuration is made of square pulses applied to the left edge of the computational domain. The period of the load is $\theta = 4\tau$, where $\tau = 16$ s is the duration of a single pulse. The radian frequency of the pulse is therefore $\omega_s = 0.0982$ rad/s, where the subscript s stands for “striping". The duration of the pulse is 60 τ. Fig. 5.15 shows the Fourier spectrum of the temperature loading. We observe that the spectrum is dominated by spikes occurring at multiples of ω_s. We limited the plot to $\bar{\omega} \in [0, 2.1\omega_s]$, where the most pronounced spikes of the spectrum appear.

Tilted resonators are added as four layers (two above and two below the crack). The trusses which link the resonators to the nodal points of the triangular lattice are thermally insulated. The mass of the unit cell containing a resonator is not equal to the mass of the exterior triangular lattice nodal points. In Table 5.2, we list the thermoelastic parameters

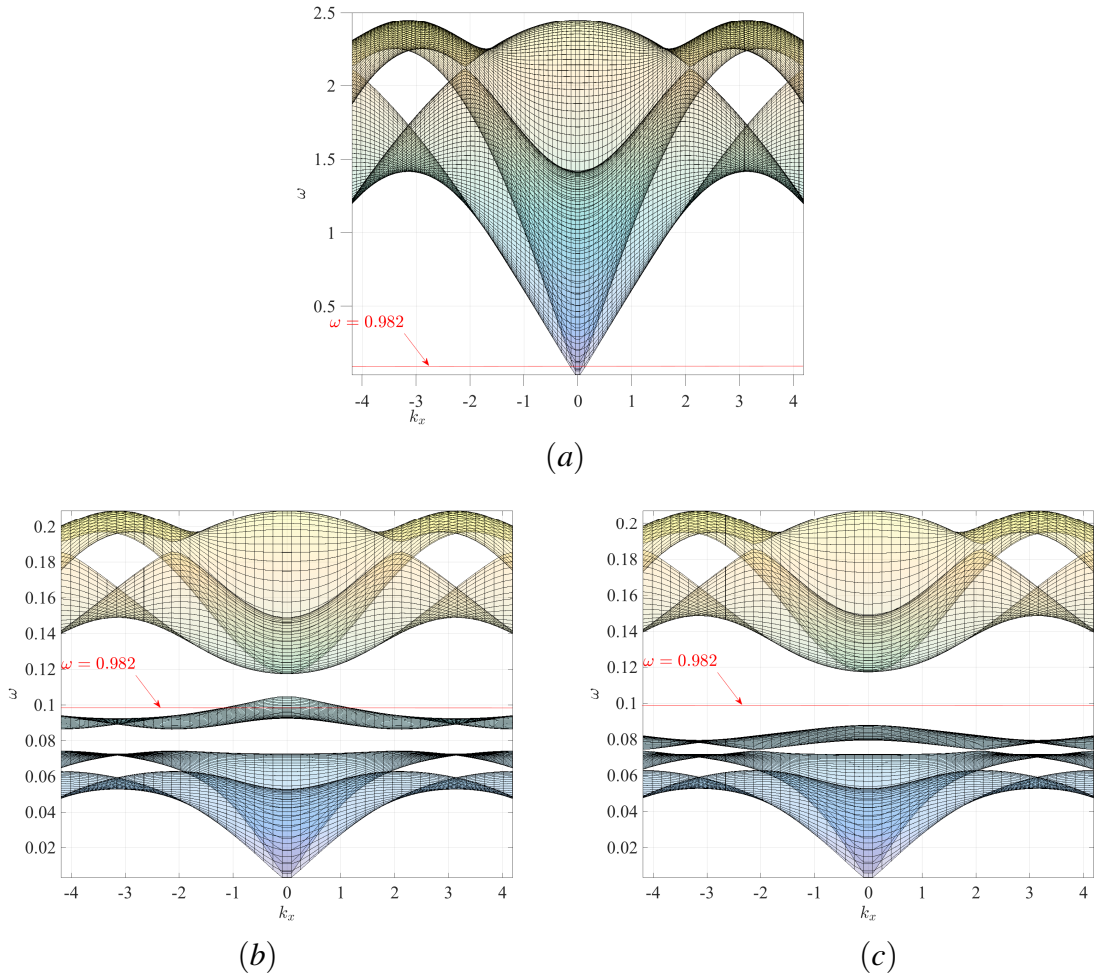

Fig. 5.16 *Dispersion surfaces for a TL (panel (a)) and for two TLRs (panels (b) and (c)). Panel (a) has been obtained using the parameters listed in the third row of Table 5.2. Panels (b) and (c) correspond to the parameters listed in the second and first rows of Table 5.2, respectively.*

used in the transient non-linear simulations. The dispersion diagrams corresponding to the periodic lattices are presented in Fig. 5.16. Fig. 5.16(a) presents the dispersion surfaces for the triangular lattice outside the cracked strip. Figs 5.16(b) and 5.16(c) show the dispersion diagrams for two triangular lattices with resonators which differ from each other by the tilting angle (47 deg and 78 deg, respectively). The structured lattices are deliberately designed in such a way that ω_s lies in the pass band of Fig. 5.16(b) and in the stop band of Fig. 5.16(c), as highlighted by the horizontal red lines.

From the transient solution of the thermoelastic problem described above, we extracted the crack length L_c at several time intervals. The results are presented in Fig. 5.17 for different normalised elongation thresholds ε. Panel (a) corresponds to the lower tilting angle and panel (b) to the bigger one. At the same elongation threshold, the average crack speeds in

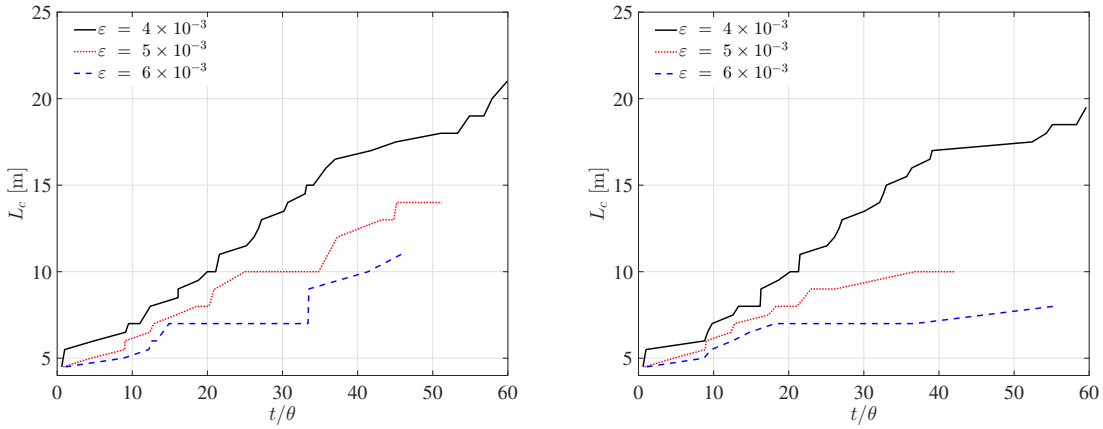

Fig. 5.17 *Crack length L_c as a function of time for two configurations corresponding to two tilting angles. The hosting triangular lattice and the the parameters for the two lattices with resonators are reported in Table 5.2.*

panel (a) are slightly higher than those in panel (b). We provide a qualitative interpretation of this phenomenon as follows. The thermal shocks at the left edge of the computational window trigger elastic waves whose Fourier spectrum (amplitude in arbitrary units *vs* frequency) is represented in Fig. 5.15. When ω_s is in the pass band, *i.e.* when $\vartheta_0 = 78$ deg, elastic waves can propagate along the strip of tilted resonators (see Fig. 5.16), resulting in a reduction of strain concentration at the crack tip compared to the $\vartheta_0 = 47$ deg configuration. Equivalently, for $\vartheta_0 = 78$ deg the strip of resonators acts as a structured waveguide which channels the energy away from the crack tip, as illustrated in Fig. 5.18. On the contrary, when $\vartheta_0 = 47$ deg, the waveguide action is being suppressed, which leads to the field localisation around the crack and hence a stronger advance of the fracture through the lattice.

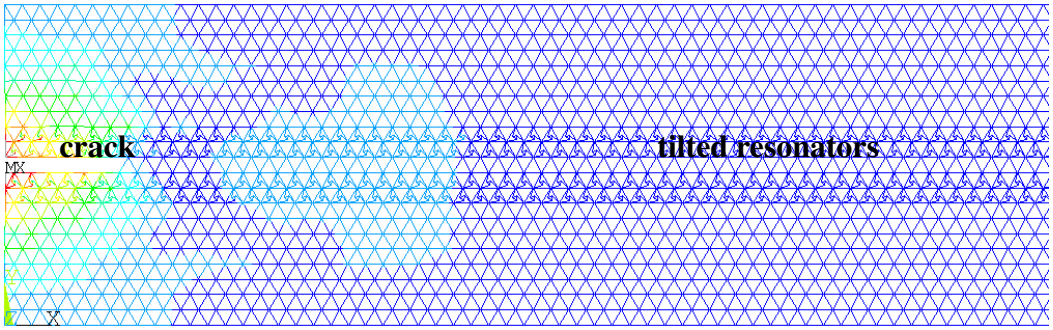

Fig. 5.18 *Instantaneous modulus of the displacement for the time step $t/\theta \approx 10$ in the transient simulation represented in Fig. 5.17(b) for the elongation threshold $\varepsilon = 5 \times 10^{-3}$ (red dotted line). The crack tip "emits" elastic waves which propagate along the structured coating.*

5.5 Summarising remarks on chapter 5

In this chapter we have studied several applications of lattices containing tilted resonators, whose dispersive properties have been analysed in chapter 4. The effects of the resonators are most significant in the dynamic regime and give rise to many interesting phenomena, such as dynamic anisotropy, spatial localisation and Dirac cones. We have identified several important applications of a novel geometrically chiral micro-structure in the design of advanced materials, used as filters/polarisers of elastic waves.

In section 5.1 we have used the chiral branch to design and implement a flat lens for mechanical waves in a triangular lattice. In our model, we have chosen the mass of the unit cell of the structured lattice to coincide with the mass of the unit cell of the ambient triangular lattice. This allows us to deal with statically equivalent lattices, as it has been demonstrated in section 4.3.2. The differences in dispersive properties (existence of a chiral branch for the triangular lattice with tilted resonators, dynamic anisotropy, concavity of the dispersion surface) emerge in the dynamic regime.

A transient advance of a crack, whose instantaneous snapshot is given in Fig. 5.18, has been studied in a micro-structured layer where tilted resonators in the lattice are present. The analysis of the transient crack advance illustrated by Figs 5.17(a) and 5.17(b) is linked to the tunable dispersion properties of the lattices (see Fig. 5.16) and to the guiding features of the structured coating around the crack, as shown in Fig. 5.18.

The Dirac-like dynamic regime has been achieved and studied here in relation to the wave-guiding and wave-defect interaction problems. Asymmetries in the scattered elastic field have been identified for waves at the Dirac-like frequency.

Shielding of a defect from an incident elastic shear wave have been achieved in the band-gap regime of the triangular lattice with resonators. In addition to the usual low penetration of external waves within the protecting coating, we emphasise that edge waves occur around the perimeter of the coating in our model (see Fig. 5.13). This is a “finger-print" of the lattice’s geometric chirality, and cannot be achieved by the straightforward adjustment of the triangular lattice parameters, *e.g.* by introducing a contrast in the inertia or stiffness.

Chapter 6

Conclusions and future work

In this chapter, we highlight the main findings of this thesis and their contributions to the diverse research fields investigated. The research line drawn by this thesis is also linked to future scientific investigations.

In chapter 2 we derived the transmission and reflection matrices for the out-of-plane shear elastic waves and transverse magnetic waves scattered by a finite piezoelectric layered medium. The identification of threshold frequencies (discussed in chapter 1) allowed us to formulate the scattering problem in two regimes: the elastic frequency regime, addressed in section 2.2.1, where only elastic energy propagates and the electromagnetic field is localised; and the electromagnetic frequency regime, analysed in section 2.2.2, where both elastic and electromagnetic waves propagate. The electromagnetic regime deserves a special mention. Given an elastic (electromagnetic) incident wave an electromagnetic (elastic) response develops at the same frequency. In section 2.3, it is further emphasised how oblique incidence plays a major role in the scattering problem. The cross-term contributions to the propagating energy are driven by the piezoelectric effect via the boundary conditions as discussed in 2.2.2.

In chapter 3, we studied the in-plane vector problem of elasticity for a checkerboard-like periodic piezoelectric structure. The governing equations and the continuity and Bloch-Floquet conditions have been investigated for the polarisation vectors lying in the plane of the checkerboard. The dispersion surfaces for Bloch-Floquet waves have been presented and several dynamic effects have been mentioned. We believe that the solution of the transmission problem through a finite checkerboard-like structure, will be important for a deeper understanding of the aforementioned physical phenomena. The modelling approach developed here is generic, and it is readily extendible to the case of imperfect interfaces, where jump conditions are imposed on displacement and tractions.

In chapter 4, our main focus was on a new chiral lattice which exhibits a range of interesting dynamic properties, including dynamic anisotropy, and Dirac and Dirac-like dispersion. The chiral lattice is created by the inclusion of a periodic array of triangular resonators embedded within an infinite uniform triangular lattice.

The dispersive properties of the chiral lattice are traced back to the *tilting* of the resonator. Specifically, the introduction of the resonator results in the appearance of several additional modes that interact with the modes corresponding to the triangular lattice without resonators. In particular, the resonators give rise to a novel rotationally dominant mode, which we refer to as the "chiral branch" (see section 4.3). The chiral branch frequency can be tuned to form Dirac-like dispersion with the optical modes at Γ, as discussed in section 4.3.4. The effect of introducing a non-uniform tilting angle has also been examined in section 4.4, where it has been shown that vortex-like modes can be obtained by alternating the tilting angle from one cell to the next. The plan of future studies includes breaking the spatial periodicity of the lattice by random perturbations of the tilting angles - adding a small random distribution to the tilting angles around a given value ϑ_0 may influence considerably the propagation of elastic waves.

In chapter 5 we investigate structured interfaces containing tilted resonators. In section 5.4, a transient advance of a crack has been studied in a micro-structured layer with tilted resonators. The analysis of the transient crack advance is linked to the tunable dispersive properties of the lattices and to the guiding features of the structured coating around the crack.

The Dirac-like dynamic regime has been studied in sections 5.2 and 5.3 in relation to the wave-guiding and wave-defect interaction problems. Asymmetries in the scattered elastic field have been identified for waves at the Dirac-like frequency. This in turn empowers further studies in the context of asymmetric crack initiation mechanisms.

Here we have proposed the design of a structured interface which contains tilted resonators and acts as a flat lens for mechanical waves in a triangular lattice. As it has been demonstrated in section 4.3.2 and further remarked in chapter 5, our analysis focuses on lattices which are statically equivalent, by imposing the masses of the unit cells to be the same. In a future work, it would be interesting to include a contrast in inertia between the ambient lattice and the interface. This will allow, for example, to investigate wave scattering by a dynamically anisotropic interface placed in a dynamically isotropic lattice.

Future research will address the effect of pre-stress on the distribution of tilting angles within a finite cluster of resonators. This may have interesting applications in structural engineering, both in static and dynamic problems. In addition, an extension of the work

which has been done in section 5.4, where only the triangular lattice links are thermally conductive, may include heat-conductive resonator links.

References

[1] Agranovich, V.M. *Surface polaritons*. Vol. 1. Elsevier, 2012.

[2] Anton, S.R. and Sodano, H.A. "A review of power harvesting using piezoelectric materials (2003–2006)". In: *Smart Materials and Structures* 16.3 (2007), R1. URL: http://stacks.iop.org/0964-1726/16/i=3/a=R01.

[3] Auld, B.A. *Acoustic fields and waves in solids (vol. 1)*. New York: Wiley, 1973.

[4] Ayzenberg-Stepanenko, M.V. and Slepyan, L.I. "Resonant-frequency primitive waveforms and star waves in lattices". In: *J. Sound Vibration* 313 (2008), pp. 812–821.

[5] Babiker, M., Constantinou, N.C., and Cottam, M.G. "General linear response theory of polaritons in binary superlattices". In: *Journal of Physics C: Solid State Physics* 20.28 (1987), p. 4581.

[6] Bigoni, D., Guenneau, S., Movchan, A.B., and Brun, M. "Elastic metamaterials with inertial locally resonant structures: Application to lensing and localization". In: *Physical Review B* 87.174343 (2014).

[7] Born, M. and Wolf, E. *Principles of optics: electromagnetic theory of propagation, interference and diffraction of light*. Elsevier, 1980.

[8] Botten, L.C., Nicorovici, N.A., Asatryan, A.A., McPhedran, R.C., Sterke, C.M. de, and Robinson, P.A. "Formulation for electromagnetic scattering and propagation through grating stacks of metallic and dielectric cylinders for photonic crystal calculations. Part I. Method". In: *J. Opt. Soc. Am.* 17.12 (2000), pp. 2165–2176.

[9] Botten, L.C., Nicorovici, N.A., Asatryan, A.A., McPhedran, R.C., Sterke, C.M. de, and Robinson, P.A. "Formulation for electromagnetic scattering and propagation through grating stacks of metallic and dielectric cylinders for photonic crystal calculations. Part II. Properties and applications". In: *J. Opt. Soc. Am.* 17.12 (2000), pp. 2177–2190.

[10] Botten, L.C., Nicorovici, N.A., McPhedran, R.C., Sterke, C.M. de, and Asatryan, A.A. "Photonic band structure calculations using scattering matrices". In: *Physical Review E* 64.046603 (18pp) (2001).

[11] Brillouin, L. *Wave propagation in periodic structures: electric filters and crystal lattices*. Courier Corporation, 2003.

[12] Brun, M., Jones, I.S., and Movchan, A.B. "Photonic band structure calculations using scattering matrices". In: *Proc. R. Soc. A* 468 (2012), pp. 3027–3046.

[13] Busch, K., Von Freymann, G., Linden, S., Mingaleev, S.F., Tkeshelashvili, L., and Wegener, M. "Periodic nanostructures for photonics". In: *Physics reports* 444.3 (2007), pp. 101–202.

[14] Carta, G., Brun, M., Movchan, A.B., Movchan, N.V., and I.S., Jones. "Dispersion equations in vortex-type monoatomic lattices". In: *International Journal of Solids and Structures* 51.2213 (2014).

[15] Carta, G., Giaccu, G.F., and Brun, M. "A phononic band gap model for long bridges. The 'Brabau' bridge case". In: *Journal of Engineering Structures* 140 (2017), pp. 66–76.

[16] Castro Neto, A.H., Guinea, F., Peres, N.M.R., Novoselov, K.S., and Geim, A.K. "The electronic properties of graphene". In: *Reviews of Modern Physics* 81.1 (2009), p. 109.

[17] Chan, C.T., Yu, Q.L., and Ho, K.M. "Order-N spectral method for electromagnetic waves". In: *Physical Review B* 51.23 (1995), p. 16635.

[18] Chen, J.C. *Introduction to scanning tunneling microscopy, second edition*. Oxford, UK: Oxford University Press, 2008.

[19] Colquitt, D.J., Jones, I.S., Movchan, N.V., and Movchan, A.B. "Dispersion and localization of elastic waves in materials with microstructure". In: *Proc. R. Soc. A* 467 (2011), pp. 2874–2895.

[20] Colquitt, D.J., Jones, I.S., Movchan, N.V., Movchan, A.B., and McPhedran, R.C. "Dynamic anisotropy and localization in elastic lattice systems". In: *Waves Random Complex Media* 22.2 (2012), pp. 143–159.

[21] Colquitt, D.J., Makwana, M., and Craster, R.V. "High-frequency homogenisation for lattices". In: *Q. J. Mech. Appl. Math.* 68.2 (2015), pp. 203–230.

[22] Colquitt, D.J., Movchan, N.V., and Movchan, A.B. “Parabolic metamaterials and Dirac bridges”. In: *Journal of the Mechanics and Physics of Solids* 95 (2016), pp. 621–631.

[23] Craster, R.V., Kaplunov, J., and Pichugin, A.V. “High-frequency homogenisation for periodic media”. In: *Proc. R. Soc. A* 466 (2010), pp. 2341–2362.

[24] Craster, R.V., Kaplunov, J., and Postnova, J. “High-frequency asymptotics, homogenisation and localisation for lattices”. In: *Q. J. Mech. Appl. Math.* 63.4 (2013), pp. 497–519.

[25] Darinskii, A.N., Le Clezio, E., and Feuillard, G. “The role of electromagnetic waves in the reflection of acoustic waves in piezoelectric crystals”. In: *Wave motion* 45 (2008), pp. 428–444.

[26] Dobson, D.C. “An Efficient Method for Band Structure Calculations in 2D Photonic Crystals”. In: *Journal of Computational Physics* 149.2 (1999), pp. 363–376.

[27] *Five-hundred-meter aperture spherical radio telescope*. http://fast.bao.ac.cn/en/. Accessed: 2017-05-02.

[28] Fu, Z., Schlier, L., Travitzky, N., and Greil, P. “Three-dimensional printing of SiSiC lattice truss structures”. In: *Materials Science and Engineering: A* 560 (2013), pp. 851–856.

[29] Ho, K.M., Chan, C.T., and Soukoulis, C.M. “Existence of a photonic gap in periodic dielectric structures”. In: *Physical Review Letters* 65.25 (1990), p. 3152.

[30] Hou, Z., Wu, F., and Liu, Y. “Phononic crystals containing piezoelectric material”. In: *Solid State Communications* 130.11 (2004), pp. 745–749.

[31] Hu, X., Shen, X., Liu, X., Fu, R., and Zi, J. “Superlensing effect in liquid surface waves”. In: *Physical Review E* 69.3 (2004), p. 030201.

[32] Huang, H.H., Sun, C.T., and Huang, G.L. “On the negative effective mass density in acoustic metamaterials”. In: *Int. J. Eng. Sci.* 47.4 (2009), pp. 610–617.

[33] Huang, K. “Lattice vibrations and optical waves in ionic crystals”. In: *Nature* 167.4254 (1951), pp. 779–780.

[34] Huber, S.D. “Topological mechanics”. In: *Nature Physics* 12.7 (2016), pp. 621–623.

[35] Hussein, M.I. “Reduced Bloch mode expansion for periodic media band structure calculations”. In: *Proceedings of the Royal Society of London A: Mathematical, Physical and Engineering Sciences*. Vol. 465. 2109. The Royal Society. 2009, pp. 2825–2848.

[36] Jackson, J.D. *Electrodynamics*. Wiley Online Library, 1975.

[37] Johnson, S.G. and Joannopoulos, J.D. "Block-iterative frequency-domain methods for Maxwell's equations in a planewave basis". In: *Optics Express* 8.3 (2001), pp. 173–190.

[38] Joseph, L.M. and Craster, R.V. "Asymptotics for Rayleigh-Bloch Waves along Lattice Line Defects". In: *Multiscale Modeling & Simulation* 1.3 (2013), pp. 871–889.

[39] Ke, M., Liu, Z., Qiu, C., Wang, W., Shi, J., Wen, W., and Sheng, P. "Negative-refraction imaging with two-dimensional phononic crystals". In: *Physical Review B* 72.6 (2005), p. 064306.

[40] Kittel, C. *Introduction to solid state physics - 8th ed.* John Wiley & Sons, 2005.

[41] Kohn, W. and Rostoker, N. "Solution of the Schrödinger equation in periodic lattices with an application to metallic lithium". In: *Physical Review* 94.5 (1954), p. 1111.

[42] Korringa, J. "On the calculation of the energy of a Bloch wave in a metal". In: *Physica* 13.6-7 (1947), pp. 392–400.

[43] Kozlov, V., Maz'ya, V., and Movchan, A.B. *Asymptotic analysis of fields in multi-structures*. Oxford, UK: Claredon Press, 1999.

[44] Krowne, C. M and Zhang, Y. *Physics of negative refraction and negative index materials*. Springer, 2007.

[45] Kyame, J.J. "Wave Propagation in Piezoelectric Crystals". In: *The Journal of the Acoustical Society of America* 21.3 (1949), pp. 159–167.

[46] Langley, R.S. "A variational principle for periodic structures". In: *Journal of Sound and Vibration* 135.1 (1989), pp. 135–142.

[47] Langley, R.S. "The response of two-dimensional periodic structures to point harmonic forcing". In: *Journal of Sound and Vibration* 197.4 (1996), pp. 447–469.

[48] Laude, V., Wilm, M., Benchabane, S., and Khelif, S.A. "Full band gap for surface waves in two-dimensional phononic crystal consisting of materials with general anisotropy". In: *Phys. Rev. E* 69.094301 (7pp) (2004).

[49] Lekner, J. *Theory of reflection*. Springer, 1987.

[50] Leung, K.M. and Qiu, Y. "Multiple-scattering calculation of the two-dimensional photonic band structure". In: *Physical Review B* 48.11 (1993), p. 7767.

[51] Lu, Bingwei, Chen, Ying, Ou, Dapeng, Chen, Hang, Diao, Liwei, Zhang, Wei, Zheng, Jun, Ma, Weiguo, Sun, Lizhong, and Feng, Xue. "Ultra-flexible piezoelectric devices integrated with heart to harvest the biomechanical energy". In: *Scientific reports* 5 (2015), p. 16065.

[52] Lu, Y., Zhu, Y., Chen, Y., Zhu, S., Ming, N., and Feng, Y. "Optical properties of an ionic-type phononic crystal". In: *Science* 284.5421 (1999), pp. 1822–1824.

[53] Luo, C., Johnson, S.G., Joannopoulos, J.D., and Pendry, J.B. "All-angle negative refraction without negative effective index". In: *Phys. Rev. B* 65.201104(R (2002).

[54] Maradudin, A.A., Montroll, E.W., and Weiss, G.H. *Theory of lattice dynamics in the harmonic approximation*. New York, USA: Academic Press, 1963.

[55] Martin, P.A. "Discrete scattering theory: Green's function for a square lattice." In: *Wave Motion* 43 (2006), pp. 619–629.

[56] Martinsson, P.G. and Movchan, A.B. "Vibrations of lattice structures and phononic band gaps". In: *Q. J. Mech. Appl. Math.* 56.1 (2003), pp. 45–64.

[57] McPhedran, R.C., Movchan, A.B., and Movchan, N.V. "Platonic crystals: Bloch bands, neutrality and defects". In: *Mechanics of materials* 41.4 (2009), pp. 356–363.

[58] Mead, D.J. "A general theory of harmonic wave propagation in linear periodic systems with multiple coupling". In: *Journal of Sound and Vibration* 27.2 (1973), pp. 235–260.

[59] Meade, R.D., Rappe, A.M., Brommer, K.D., Joannopoulos, J.D., and Alerhand, O.L. "Accurate theoretical analysis of photonic band-gap materials". In: *Phys. Rev. B* 48 (11 1993), pp. 8434–8437.

[60] Mei, J., Wu, Y., Chan, C.T., and Zhang, Z. "First-principles study of Dirac and Dirac-like cones in phononic and photonic crystals". In: *Physical Review B* 86.3 (2012), p. 035141.

[61] Mills, D.L. and Burstein, E. "Polaritons: the electromagnetic modes of media". In: *Reports on Progress in Physics* 37.7 (1974), p. 817.

[62] Montroll, E.W. and Potts, R.B. "Effect of defects on lattice vibrations". In: *Physical Review* 100.2 (1955), p. 525.

[63] Moreno, E., Erni, D., and Hafner, C. "Band structure computations of metallic photonic crystals with the multiple multipole method". In: *Physical Review B* 65.15 (2002), p. 155120.

[64] Movchan, A.B., Movchan, N.V., and McPhedran, R.C. "Bloch–Floquet bending waves in perforated thin plates". In: *Proceedings of the Royal Society of London A: Mathematical, Physical and Engineering Sciences* 463.2086 (2007), pp. 2505–2518.

[65] Movchan, A.B., Movchan, N.V., and Poulton, C.G. *Asymptotic models of fields in dilute and densely packed composites*. World Scientific, 2002.

[66] Movchan, A.B. and Slepyan, L.I. “Band gap Green’s functions and localized oscillations”. In: *Proceedings of the Royal Society of London A: Mathematical, Physical and Engineering Sciences* 463.2086 (2007), pp. 2709–2727.

[67] Novoselov, K.S., Geim, A. K., Morozov, S.V., Jiang, D., Zhang, Y., Dubonos, S. V., Grigorieva, I. V., and Firsov, A. A. “Electric field effect in atomically thin carbon films”. In: *Science* 306.5696 (2004), pp. 666–669.

[68] Osharovich, G., Ayzenberg-Stepanenko, M., and Tsareva, O. “Wave propagation in elastic lattices subjected to a local harmonic loading II. Two-dimensional problems”. In: *Continuum Mech.Therm.* 22 (2010), pp. 599–616.

[69] Pendry, J.B. “Negative refraction makes a perfect lens”. In: *Physical review letters* 85.18 (2000), p. 3966.

[70] Piliposian, G.T., Avetisyan, A.S., and Ghazaryan, K.B. “Shear wave propagation in periodic phononic/photonic piezoelectric medium”. In: *Wave Motion* 49.1 (2012), pp. 125–134.

[71] Piliposyan, D.G., Ghazaryan, K.B., and Piliposian, G.T. “Shear Bloch waves and coupled phonon–polariton in periodic piezoelectric waveguides”. In: *Ultrasonics* 54.2 (2014), pp. 644–654.

[72] Piliposyan, D.G., Piliposian, G.T., and Ghazaryan, K.B. “Propagation and control of shear waves in piezoelectric composite waveguides with metallized interfaces”. In: *International Journal of Solids and Structures* 106 (2017), pp. 119–128.

[73] Platts, S.B., Movchan, N.V., McPhedran, R.C., and Movchan, A.B. “Two dimensional phononic crystals and scattering of elastic waves by an array of voids”. In: *Proc. R. Soc. A* 458 (2009), pp. 2327–2347.

[74] Plihal, M. and Maradudin, A.A. “Photonic band structure of two-dimensional systems: The triangular lattice”. In: *Physical Review B* 44.16 (1991), p. 8565.

[75] Poulton, C.G., McPhedran, R.C., Movchan, N.V., and Movchan, A.B. “Convergence properties and flat bands in platonic crystal band structures using the multipole formulation”. In: *Waves in Random and Complex Media* 20.4 (2010), pp. 702–716.

[76] Rayleigh, Lord. “XXXI. Investigations in optics, with special reference to the spectroscope”. In: *The London, Edinburgh, and Dublin Philosophical Magazine and Journal of Science* 8.49 (1879), pp. 261–274.

[77] Ruzzene, M., Scarpa, F., and Soranna, F. “Wave beaming effects in two-dimensional cellular structures”. In: *Smart Mater. Struct.* 12 (2003), pp. 363–372.

[78] Sabina, F.J. and Movchan, A.B. “Interfacial effects in electromagnetic coupling within piezoelectric phononic crystals”. In: *Acta Mech. Sin.* 25 (2009), pp. 95–99.

[79] Sharma, N.D., Landis, C.M., and Sharma, P. “Piezoelectric thin-film superlattices without using piezoelectric materials”. In: *Journal of Applied Physics* 108.2 (2010), p. 024304.

[80] Sheng, P., Mei, J., Liu, Z., and Wen, W. “Dynamic mass density and acoustic metamaterials”. In: *Physica B: Condensed Matter* 394.2 (2007), pp. 256–261.

[81] Shuvalov, A.L. and Gorkunova, A.S. “Transverse acoustic waves in piezoelectric and ferroelectric antiphase superlattices”. In: *Physical Review B* 59.14 (1999), p. 9070.

[82] Sigalas, M and Economou, Eleftherios N. “Band structure of elastic waves in two dimensional systems”. In: *Solid state communications* 86.3 (1993), pp. 141–143.

[83] Sigalas, M.M. and Economou, E.N. “Elastic and acoustic wave band structure”. In: *Journal of sound and vibration* 158.2 (1992), pp. 377–382.

[84] Spadoni, A. and Ruzzene, M. “Elasto-static micropolar behaviour of a chiral auxetic lattice”. In: *Journal of the Mechanics and Physics of Solids* 60 (2012), pp. 156–171.

[85] Spadoni, A., Ruzzene, M., Gonnella, S., and Scarpa, F. “Phononic properties of hexagonal chiral lattices”. In: *Wave Motion* 46 (2009), pp. 435–450.

[86] Sukhovich, A, Merheb, B, Muralidharan, K, Vasseur, JO, Pennec, Y, Deymier, PA, and Page, JH. “Experimental and theoretical evidence for subwavelength imaging in phononic crystals”. In: *Physical review letters* 102.15 (2009), p. 154301.

[87] Süsstrunk, R. and Huber, S.D. “Observation of phononic helical edge states in a mechanical topological insulator”. In: *Science* 349.6243 (2015), pp. 47–50.

[88] Tagantsev, A.K., Meunier, V., and Sharma, P. “Novel electromechanical phenomena at the nanoscale: phenomenological theory and atomistic modeling”. In: *MRS bulletin* 34.09 (2009), pp. 643–647.

[89] Tallarico, D., Movchan, N.V., Movchan, A.B., and Camposaragna, M. “Propagation and filtering of elastic and electromagnetic waves in piezoelectric composite structures”. In: *Mathematical Methods in the Applied Sciences* (2016).

[90] Tallarico, D., Movchan, N.V., Movchan, A.B., and Colquitt, D.J. “Tilted resonators in a triangular elastic lattice: chirality, Bloch waves and negative refraction”. In: *Journal of the Mechanics and Physics of Solids* (2017).

[91] Thomson, Lord Kelvin W. *Baltimore lectures on molecular dynamics and the wave theory of light*. La Vergne, USA: Kessinger Publishing, 2009.

[92] Trevisan, A., Borzi, G.P., Movchan, N.V., Movchan, A.B., and Brun, M. "Thermal shock driven fracture in a structured solid: dynamic crack growth and nucleation". In: *Int. J. Fract.* 202 (2016), pp. 167–177.

[93] Truby, R.L. and Lewis, J.A. "Printing soft matter in three dimensions". In: *Nature* 540.7633 (Dec. 2016), pp. 371–378.

[94] Veselago, V.G. "The electrodynamics of substances with simultaneously negative values of ε and μ". In: *Soviet Physics Uspekhi* 10.4 (1968), p. 509.

[95] Wang, P., Casadei, F., Shan, S., Weaver, J.C., and Bertoldi, K. "Harnessing buckling to design tunable, locally resonant acoustic metamaterials". In: *Physical Review Letters* 113.014301 (2014).

[96] Wei, C. and Jing, X. "A comprehensive review on vibration energy harvesting: Modelling and realization". In: *Renewable and Sustainable Energy Reviews* 74 (2017), pp. 1–18.

[97] Wu, T.T., Huang, Z.G., and Lin, S. "Surface and Bulk acoustic waves in two-dimensional phononic crystal consisting of materials with general anysotropy". In: *Phys. Rev. B* 69.094301 (10pp) (2007).

[98] Yang, H.Y.D. "Finite difference analysis of 2-D photonic crystals". In: *IEEE Transactions on Microwave Theory and Techniques* 44.12 (1996), pp. 2688–2695.

[99] Yang, J. *Special topics in the theory of piezoelectricity*. Dorderecht, Heidelberg, London, New York: Springer, 2009.

[100] Yang, J. and Wang, J. "Dynamic anti-Plane problems of piezoceramics and applications in ultrasonics - a review". In: *Acta Mechanica Solida Sinica* 21.3 (2008), pp. 207–218.

[101] Yu, P.Y. and Cardona, M. *Fundamentals of semiconductors: physics and materials properties*. Springer Science & Business Media, 2010.

[102] Zhang, V. and Djafari-Rouhani, B.A. "A general model for analysis of acoustic phonons in piezoelectric superlattices. Application to (111)-ALAs/GaAs superlattice." In: *J. Phys: Condensed Matter* 19.186209 (17pp) (2007).

[103] Zhang, X., Zhu, R., Zhao, J., Chen, Y., and Zhu, Y. "Phonon-polariton dispersion and the polariton-based photonic band gap in piezoelectric superlattices". In: *Phys. Rev. B* 69 (8 2004), p. 085118.

[104] Zhang, Z. and Satpathy, S. “Electromagnetic wave propagation in periodic structures: Bloch wave solution of Maxwell’s equations”. In: *Physical review letters* 65.21 (1990), p. 2650.

[105] Zhu, Y., Zhang, X., Lu, Y., Chen, Y., Zhu, S., and Ming, N. “New Type of Polariton in a Piezoelectric Superlattice”. In: *Phys. Rev. Lett.* 90 (5 2003), p. 053903.